Development of a simulation tool for MHD flows under nuclear fusion conditions

Elisabet Mas de les Valls

DOCTORAL DISSERTATION
October 2011

THESIS SUPERVISOR: LLUÍS BATET

Dept. of Physics and Nuclear Engineering
Universitat Politècnica de Catalunya

A las hadas y duendes del bosque...

Executive Summary

In Nuclear Fusion Technology, MHD flows can be encountered in liquid metal (LM) breeding blankets, the part of a fusion reactor where tritium, one of the fusion fuels, is to be produced. LM breeding blankets can be classified into three types, according to the fraction of the thermal load extracted by the LM. In the first BB type, called separately-cooled blanket, the LM (usually PbLi) is to be used only for breeding purposes and a primary coolant (typically helium or water) is required to extract the heat deposited both in the structure and in the LM zone. In separately-cooled BBs, LM flows at low velocities ($\sim$ mm/s), what makes buoyancy the predominant force. In the second BB type, called dual-coolant blanket, the LM acts as a secondary coolant by extracting the thermal load deposited in the LM zone, whereas the primary coolant only extracts the heat deposited in the structure. In this case, the LM must travel at higher velocities ($\sim 10\,$cm/s) and inertia and buoyancy are of the same order of magnitude. In the third and last BB type, called self-cooled blanket, the LM is the primary and unique cooling fluid for the entire blanket and, hence, its velocity must be even higher than in the dual-coolant type ($\sim 0.5\,$m/s), what makes inertia to dominate over buoyancy.

The flow inside breeding blanket channels can be very complex, particularly in those blanket types where buoyancy plays a relevant role. The understanding of the flow nature, including the possible instabilities that might appear, the exact knowledge of flow profiles for tritium control purposes, and the prediction of thermal fluxes for thermal efficiency analysis are of great interest for blanket design optimisation.

In this direction, a thermal-MHD coupled simulation tool has been implemented in the OpenFOAM toolkit. The resultant code can be understood as a preliminary predictive tool for liquid metal breeding blanket channel design. The developed code is a transient 3D tool that accounts for thermal-MHD coupling and can deal with several layers of materials.

The development process of this tool consists of a first MHD phase and a second thermal-MHD coupling phase. Along the MHD phase, various MHD modelling strategies have been studied, starting with the implementation of an induced magnetic field

formulation and continuing with an electric potential formulation based on the low magnetic Reynolds approximation, in this case using the conservative formula of the Lorentz force proposed by Ni *et al.* (2007). Two pressure-velocity couplings have been analysed. The first one is based on a projection method whereas the second one, which has proved to be more robust, follows a PISO-like algorithm (Weller *et al.* 1998). In the thermal-MHD coupling phase, the MHD model has been extended to account for energy transport phenomena. The coupling has been achieved by means of the Boussinesq hypothesis, and the viscous dissipation and Joule generation terms have been neglected in the energy balance. In terms of algorithm structure, the energy equation can be simply introduced sequentially in a fractional step algorithm, or as an extra equation inside the PISO loop, in a PISO-like algorithm.

The developed tool accounts for the linear wall function for Hartmann boundary layers from Leboucher (1999), which reduces substantially the CPU time of the simulations. The code also accounts for fluid-solid thermal and electrical coupling by means of coupled fluid and solid grids. The coupling is implicit at grid level, so no extra iterative process is required between both domains. Special attention has been placed in correctly coupling liquid-solid energy transport equations by means of the conservative form of the equations in both domains.

All along the development process, validation steps have been carried out with successful results. Such validations are based on both analytical and numerical solutions. Special focus has been placed in evaluating the code performance when coarse meshes are used, since, with the available CPU capacities, mesh size is a limiting constraint for breeding blanket channels simulation.

Since time step is not only crucial for stability purposes, but also for accuracy of the results, special emphasis has been placed on estimating the required time step criterion, either by means of a more conservative monotone scheme (Patankar 1980) or by a 1D linear stability von Neumann analysis.

An alternative thermal-MHD tool has also been implemented following the 2D approach from Sommeria and Moreau (1982) (SM82). Such code accounts for the 0-equation Q2D turbulence RANS model from Smolentsev and Moreau (2006).

Three application cases are considered. In the first case, the integrated effect of volumetric heating and magnetic field on tritium transport in a U-bend flow, as applied to the EU HCLL blanket concept (which is a separately-cooled blanket), is studied. The second application case corresponds to the thermal analysis of the blanket design that is being developed in the framework of the Spanish National Project on Breeding Blanket Technologies TECNO_FUS (through the CONSOLIDER-INGENIO 2010 Programme). The third and last case includes the instability analysis of a pressure-driven MHD flow

in a horizontal channel with a constant thermal load. The application cases have not only shown the code capabilities to simulate liquid metal channels in breeding blankets but, also, have provided a useful *know-how* on flow properties inside those channels.

Related to liquid metal modelling in HCLL blanket, it has been observed that the fluid-solid electromagnetic coupling is relevant since it determines, together with the Hartmann number, the magnitude of the electromagnetic damping of the flow. If the only output parameters needed from the simulation are averaged values of temperatures, Nusselt and heat fluxes, fluid-solid thermal coupling can be avoided, being replaced by the use of a thermal boundary condition based on an estimation of the overall heat transfer coefficient (from tne LM to the He cooling channels). To this aim, an accurate estimator of the heat transfer coefficient helium-Eurofer is required. Nevertheless, for buoyancy induced vortices detection, fluid-solid thermal coupling is required in the simulation. It can be anticipated that, when the correct electromagnetic damping is considered (real Ha and electric conductivity ratio), the flow in the core of the channel remains 2D except in the Hartmann boundary layers, and vortical structures are only expected to exist in the HCLL design near the gap close to the first wall. In any case, if vortical structures exist along the channel, their characteristic length is expected to be the channel height. The presence of vortical structures is related to 3D secondary motions; their effect on the main flow and on relevant design parameters (e.g. tritium permeation ratio) should be analysed.

For an accurate prediction of the tritium permeation ratio (TPR), it is urgent to develop new and precise measurements of tritium transport properties, specially tritium solubility. In the present study, a preliminary tritium analysis has been addressed by considering tritium as a passive scalar and neglecting helium influence on the flow (He is a by-product of the breeding reaction with lithium). Results show similar TPR values for electrically conducting and insulating walls, since in both cases high velocity zones exist near the walls (due to either M-shape profile or vortical structures). An important result is the influence that Hartmann walls can have on the total TPR, reaching about 10 % of the total permeated tritium, whereas their surface is 15 % of the total wall surface.

The TECNO_FUS blanket concept is of the dual-coolant type, with high LM velocities. Therefore, inertia is predominant in front of buoyancy. Correspondingly, the flow in the core of the banana-shaped (toroidal) channels is expected to be 2D, except at Hartmann boundary layers, with no vortical structures. Thus, the alternative 2D tool (SM82) can be used. Among the issues which are relevant for the simulation, MHD turbulence modelling is, probably, the most prominent aspect since flow profile is strongly dependent on it. However, there is a lack of accurate Q2D MHD turbulence models,

specially when buoyancy effects have to be considered. The thermal performance of the blanket can be defined by means of the LM temperature gain (which should be of order $\sim 300^o$C), the maximum temperature of the structural material (Eurofer, that must be kept below 550^oC), the thermal stress across the flow channel insert (FCI, an electrical and thermal insulating layer of ceramic foam), and the LM thermal gain (which depends on the temperature gain but also on the LM flow rate). From the sensitivity analysis carried out in this study, it can be predicted that, for a maximised liquid metal temperature increment with an inlet velocity of 0.2 m/s, FCI thermal conductance should be around 1 W/m^{2}K. In contrast, for a maximised LM thermal gain, what would imply a reduced thermal stress across FCI layer, and under the studied design specifications, higher velocities are preferable, what would also imply a reduced thermal stress across FCI layer. However, this second thermal strategy would result in a lower LM temperature increment, which is not desirable for efficiency reasons.

Acknowledgements

This PhD dissertation is part of a research line that has been set up basically thanks to the encouraging efforts of Dr. Luis A. Sedano who, with his enthusiasm, convinced first my supervisor, Dr. Lluís Batet and, afterwards, myself.

I would like to thank Dr. Lluís Batet for his patience, support and, above all, confidence in my work. Despite being very busy, I could always count on him. It has been a pleasure to work with him and, hopefully, we can do so in the future.

I wish to express my gratitude to people from the Department of Physics and Nuclear Engineering as well as from the CTTC Research group. Special gratitude to Marina Pérez, Roser Capdevila and Xavi Trias, for their friendship and interest in sharing knowledge.

I'm proud of having had the opportunity to work with Alban Pótherat and Vincent Dousset, from Coventry University. Working with them has been very enriching and amazing. I also want to thank Dr. Smolentsev for his valuable suggestions and interest on my work.

I must mention here my gratitude to OpenFOAM developers community. Having access to such a well structured open source CFD tool is a privilege that I had never imagined. They really do a great job.

I'm grateful to the Dept. of Applied Math. I (http://www.ma1.upc.edu), the Research and Development Laboratory of LSI Dept. (http://rdlab.lsi.upc.edu) and, specially, the GITS research group (http://www.gits.ws) for allowing me free use of their computing clusters.

I gratefully acknowledge the financial support I have received from the Technical University of Catalonia, the Institut de Tècniques Energètiques, and the Ministerio de Ciencia e Innovación (by means of a Consolider grant for TECNO_FUS project, Ref. CSD2008-079). My stay at Coventry was financed by COST P17 Action (COST-STSM-P17-03789).

Last but not least, I will never thank enough the constant assistance received from Dr. Vicente de Medina. Besides emotional support, Vicente has made very interesting contributions to the study, has solved many technical issues and has made this thesis possible. Thank you.

Contents

Nomenclature

Acronyms

BB	Breeding Blanket
CFD	Computational Fluid Dynamics
DCLL	Dual Coolant Lithium-Lead
DEMO	DEMOnstration Power Plant
DNS	Direct Numerical Simulation
EUROATOM	EURopean ATOMic Energy Community
FCI	Flow Channel Inserts
FFT	Fast Fourier Transformation
FSI	Fluid Solid Interface
FSPM	Four Step Projection Method
HCLL	Helium-Cooled Lithium-Lead
ITER	International Thermonuclear Experimental Reactor
LES	Large Eddy Simulation
LM	Liquid Metal
MHD	Magnetohydrodynamics
PISO	Pressure-Implicit Split-Operator
Q2D	Quasi-two-dimensional
RAFM	Reduced Activation Ferritic/Martensitic steel
RANS	Reynolds-Averaged Navier-Stokes
SM	Structural Material

TBM	Test Blanket Module
TBR	Tritium Breeding Ratio
TPR	Tritium Permeation Ratio

Latin Letters

$\mathbf{j}$	current density vector
$\mathbf{j}_n$	current density flux vector at face centres
$\mathbf{B_o}$	externally applied magnetic field vector
$\mathbf{B}$	magnetic field vector
$\mathbf{b}$	induced magnetic field vector
$\mathbf{b}_f$	body force vector
$\mathbf{g}$	gravity vector
$\mathbf{v}$	velocity vector
a	half channel width in magnetic field direction
C_p	heat capacity at constant pressure
C_T	tritium concentration
C_w	wall conductivity ratio
D_T	tritium diffusivity
g_o	reference gravity for Boussinesq approximation
k_s	Sievert's coefficient for tritium
L	characteristic length
p	total pressure
p_d	dynamic pressure (total pressure minus hydrostatic one)
$S_{thermal}$	heat source term
$S_{tritium}$	tritium source term
t	time
T_o	reference temperature for Boussinesq approximation
U_{eq}	equivalent overall heat transport coefficient
v_o	characteristic velocity

$v_{o,MHD}$	characteristic velocity when Lorentz forces balance buoyant forces

Greek Letters

α	thermal diffusivity
β	thermal expansion coefficient
η	magnetic viscosity
μ_m	magnetic permeability
ν	kinematic viscosity
ϕ	electric potential
ρ	density
σ_m	electric conductivity
k	thermal conductivity

Dimensionless Numbers

Gr	Grashof number
Ha	Hartmann number
Ly	Lykoudis number
Pr	Prandtl number
Pe	Peclet number
Ra	Rayleigh number
Re	Reynolds number
Ri	Richardson number
Rm	magnetic Reynolds number
Sc	Schmidt number
N	Interaction parameter or Stuart number

Part I

Introduction

1 Introduction

1.1 Overview and aim

1.1.1 Motivation

For the proper design of fusion reactors' liquid metal (LM) breeding blankets (BB), tools capable of predicting the LM flow nature, pressure drop, heat flux and average temperatures, as well as tritium inventories and the tritium permeation ratio (TPR), are required. To this aim, it is essential to have a simulation code able to take into account, if not all, at least the most relevant phenomena that occur in LM channels.

The synergy between the Department of Physics and Nuclear Engineering at the UPC (GREENER, Lluís Batet) and the National Fusion Laboratory at CIEMAT (NFL, Luis Sedano) has been instrumental in the progress towards the development of such tool. On one hand, part of the NFL research is focused on the development of predictive tools for tritium control in BB. One of the main drawbacks of the instruments at hand for tritium transport prediction is that flow is not simulated in detail so that the influence of the flow profile on tritium transport is not accounted for. On the other hand, one of the research lines at GREENER is the thermal-hydraulics of nuclear plants. Hence, their work is based on flow simulation and heat and mass transfer. As a result of such synergy, a new research line was born between both groups, within whose framework the work presented in this PhD dissertation has been developed.

Several Computational Fluid Dynamic (CFD) tools have already been developed and are continuously being validated (as soon as new experimental data is available) for

BB studies. Examples of these tools are the CFX user defined files in the KIT Research centre (in Karlsruhe, Germany, Kharicha *et al.* 2004), aimed to the study of magnetohydrodynamic (MHD) flows in blankets, or the Castem code in CEA (France, Gabriel *et al.* 2007) in which MHD is coupled with temperature. Also some in-house codes are being developed, being an example the one in UCLA (California, USA, Smolentsev *et al.* 2010), with thermal MHD coupling. None of them, however, is open source.

In GREENER's Thermal-Hydraulics Studies Group, some experience had been achieved on the open source code OpenFOAM (*http://www.openfoam.org*, Weller *et al.* 1998) so that its use was considered for the development of the present PhD thesis. OpenFOAM choice seemed appropriate, not only for code accessibility, transparency and feasibility of incorporating new models, but also for the opportunity it offers to work in collaboration with other research groups. Indeed, in recent years the use of OpenFOAM has spread within the magnetohydrodynamic (MHD) research community applied to BB technology, first at Coventry University (Alban Pothérat), and recently in KIT (Chiara Mistrangelo) and UCLA (Sergey Smolentsev).

This research line is framed in a context of international efforts to develop and validate predictive tools capable of extrapolation to DEMO conditions, as declared by the European Union's Joint Undertaking for ITER experiment, Fusion for Energy (F4E, Zmitko 2009). Thus, it can be stated that the goal of the present PhD thesis, *the development of a thermal-MHD predictive tool for liquid metal breeding blankets, based on the open source code OpenFOAM*, coincides with such Fusion for Energy milestone.

1.1.2 Scope of the research

For a basic simulation of the flow in liquid metal breeding blankets, coupling the MHD phenomenon with heat transfer is crucial. Other relevant aspects include tritium and helium production (in breeding reactions) and transport, thermal and electromagnetic stresses on the structure, and thermal loads, among others. It soon become evident that for an incipient research line and in the frame of a PhD thesis, all phenomena could not be encompassed. Thus, the scope of the present PhD research was reduced to MHD and thermal coupling phenomena. Tritium transport has been sporadically analysed considering tritium as a passive scalar. In principle, only laminar flows are considered, although a first approach to turbulent analysis has also been carried out.

Since different approaches to MHD modelling exist, more than one algorithm has been developed and validated. Comparisons between the developed algorithms are carried out when needed. All along validation phases, both analytical and numerical solutions have been used. However, a code can be always further validated, specially

regarding the complex phenomena encountered in thermal MHD coupling.

It is not the scope of the present research to optimise in terms of CPU time the developed code. Efforts have been focused on the quality of results rather than on simulation time. Nevertheless, since the OpenFOAM toolkit is largely optimised, the resulting code is quite efficient in terms of CPU costs.

The natural aim of a predictive tool is to be used in the design optimisation. However, in the present PhD dissertation, since the phenomena involved in liquid metal breeding blankets are complex, and very often the flow presents instabilities, main efforts need to be focused on understanding the nature of such flows rather than on improving the breeding blanket design. Nevertheless, in some specific cases, such design improvement is crucial, mostly in the initial breeding blanket design phases, and thus, unavoidable.

This study has been developed in the frame of the Spanish National Project on Breeding Blanket Technologies TECNO_FUS (through the CONSOLIDER-INGENIO 2010 Programme). In TECNO_FUS, a new liquid metal breeding blanket concept is being worked out, which basically is a dual-coolant design but with high liquid metal velocities and higher thermal efficiency (*http://www.tecnofus.net/*). As a consequence, the analysis of the flow in the proposed blanket design as well as a preliminary design optimisation has been required.

1.2 Document outline

This PhD dissertation is organised in five parts.

The first part includes the motivation and objectives of the PhD research, and provides an overview of the nuclear fusion technology and the concept of breeding blanket, and a classification of some of the most relevant designs (Chapter 2). MHD thermofluid phenomena occurring in breeding blanket channels and the related transport equations are also explained in this first part (Chapter 3). In order to provide the reader with a more applied definition of MHD effects, a brief introduction of main flow characteristics at high Hartmann numbers is given. Also, with the dimensionless numbers defined in Chapter 3, some of the relevant liquid metal breeding blanket designs are analysed. To end this first part of the PhD dissertation, an overview of the State of the Art is given (Chapter 4), focused basically on the key steps that allow to understand the starting point of the research.

The second part includes all the code development carried out in the frame of the present research. It is split into two chapters. In Chapter 5, the three studied MHD formulations are explained and the four implemented algorithms are described and validated. In this chapter, two different stability analyses are exposed in sections 5.2.2 and

5.2.3. Also, the implemented Hartmann wall function and the fluid-solid electromagnetic coupling strategy are shown in sections 5.2.4 and 5.2.5, respectively. In Chapter 6, the thermal MHD coupling is described and the implemented algorithm defined and validated.

The third part of this PhD dissertation consists of three application cases. In the first case (Chapter 7), the integrated effect of volumetric heating and magnetic field on tritium transport in a U-bend flow, as applied to the HCLL blanket concept, is studied. The second application case (Chapter 8) corresponds to the thermal analysis of the blanket design that is being developed in the frame of TECNO_FUS project. The third and last case (Chapter 9), includes the instability analysis of a pressure-driven MHD flow in a horizontal channel with a constant thermal load.

The fourth part of the document summarises the main conclusions and includes recommendations for further studies.

Published papers and publications related with the present research are listed in the appendices, at the end of the document.

2 Background

2.1 Nuclear Fusion Technology

In the last decades, international efforts towards the development and deployment of alternative energy sources have been steadily increasing. One promising alternative despite its technological challenges is nuclear fusion. It has the great advantage of nuclear energy, regarding the amount of energy generated, but avoids the main risk of the fission energy as no chain reaction is involved and the reaction is thermally self-limiting. However, is still in a technological development stage and will not be ready for commercial deployment within decades. In order to be feasible, there are still many technological challenges to overcome, from the creation of new high temperature resistant materials with good behaviour under irradiation, to control and remote diagnostics. Obviously, all conceptual design should be based upon safety and environmental aspects.

Several fusion nuclear reactions exist, as listed in reaction 2.1, where the fuel is restricted to deuterium ($^{2}_{1}$H), tritium ($^{3}_{1}$H) and/or helium ($^{3}_{2}$He), and the values given correspond to the total energy released (kinetic energy of products). If the required nuclear reactions were to be induced by the thermal motion of the nuclei (the so-called thermonuclear fusion) it would be necessary to achieve extremely high temperatures, probably 100 million degree K (Wesson 2006). Under such conditions, the reaction would take place at plasma state of the matter and both external heating and plasma

confinement would be required.

$$^{2}_{1}\mathrm{H} + ^{2}_{1}\mathrm{H} \rightarrow ^{3}_{2}\mathrm{He} + ^{1}_{0}\mathrm{n} + 3.3\,\mathrm{MeV} \tag{2.1a}$$

$$^{2}_{1}\mathrm{H} + ^{2}_{1}\mathrm{H} \rightarrow ^{3}_{1}\mathrm{H} + ^{1}_{1}\mathrm{H} + 4.0\,\mathrm{MeV} \tag{2.1b}$$

$$^{3}_{1}\mathrm{H} + ^{2}_{1}\mathrm{H} \rightarrow ^{4}_{2}\mathrm{He} + ^{1}_{0}\mathrm{n} + 17.6\,\mathrm{MeV} \tag{2.1c}$$

$$^{2}_{1}\mathrm{H} + ^{3}_{2}\mathrm{He} \rightarrow ^{4}_{2}\mathrm{He} + ^{1}_{1}\mathrm{H} + 18.3\,\mathrm{MeV} \tag{2.1d}$$

Since the maximum reaction rate for the deuterium-tritium (D–T) reaction 2.1c occurs at temperatures about 1-2 orders of magnitude lower than for D–D or He–D reactions, D–T reactions is considered the best alternative in the short/mid-term.

If D–T reaction is to be considered, the fuels for the fusion reaction would be deuterium and tritium. Deuterium fuel is abundant in water (30 g/m^3) and can be extracted by electrolysis, despite the required technology is not yet economically feasible. The main drawback is tritium because, despite its radioactive decay product is a low energy beta that cannot penetrate the outer dead layer of human skin, the internal exposure of tritium (from inhalation, ingestion or skin absorption) is a main hazard.

Tritium production has been limited to military industry, from what nuclear fusion technology has to remain independent, and, in few quantities, heavy water-moderated reactors (CANDU type). Despite tritium short biological half-life should prevent significant long-term accumulation in the atmosphere, the difficulty for tritium confinement makes its storage and transport not feasible due to radioactive contamination. Thus, apart from the start-up phase of the reactor, tritium should be produced inside the reactor in a proper way to ensure tritium self-sufficiency. The proposed strategy for such tritium production is the tritium breeding blanket concept, as commented in next section.

At the present stage of fusion technology development, the external heating of the plasma is achieved by means of ohmic heating, microwaves and neutral beam injection (Wesson 2006). Plasma confinement is obtained by means of a magnetic field produced by super-conducting magnets. Two different fusion reactor concepts related to plasma confinement are being developed: the tokamak reactor and the stellerator reactor. Several efforts have been carried out regarding both technologies, with great improvements, but some basic technological limitations or unknowns are still present. On one hand, stellerators could theoretically achieve higher temperatures in the plasma, what might allow to avoid the D–T reaction and tritium confinement problems. On the other hand, plasma stability and confinement is even more technologically challenging in stellerators than in tokamak designs.

The first fusion experiment took place about 1930 and, by the mid 1950s ”fusion ma-

chines" were operating in the Soviet Union, the United Kingdom, the United States, France, Germany and Japan (*http://www.iter.org/*). In 1968, researches in the Soviet Union achieved higher temperature levels and plasma confinement times than those achieved so far. From that time on, the tokamak was to become the dominant concept in fusion research, and tokamak devices multiplied across the globe. It became evident the need of unified economic and technological efforts. The Joint European Torus (JET, Wesson 2006, *http://www.jet.efda.org/*) in Culham, UK, in operation since 1983, was a first step in this direction. JET is collectively used by the EURATOM (European Atomic Energy Community) Associations of more than 20 European countries. In 1991, the JET tokamak achieved the world's first controlled release of fusion power. Other key milestones are the 6 minutes and 30 seconds of plasma confinement in the Tore Supra Tokamak (Cadarache, France, *http://www-drfc.cea.fr/*), and the highest value of fusion triple product –density, temperature and confinement time– in the Japanese JT-60 (*http://www.jt60sa.org/index.htm*). US fusion facilities have reached temperatures of several hundred million degree Celsius (TFTR and NSTX experiments, *http://nstx.pppl.gov/*). Other relevant fusion experiments include ASDEX device in Germany (*http://www.ipp.mpg.de/*), RFX in Italy (*http://www.igi.cnr.it/*) and the stellarators TJ-II in Spain (*http://www-fusion.ciemat.es/*) and W7-X in Germany (*http://www.ipp.mpg.de/*).

The fusion energy gain factor Q is defined as the ratio between fusion power contained in charged products and the required plasma heating power. Plasma energy breakeven ($Q = 1$) has never been achieved: the current record for energy release is held by JET, which succeeded in generating 70% of input power. Scientists have now designed the next-step device (ITER) which will be able to produce Q up to 10 (50 MW of input heating power and 500 MW of fusion heating power)

Beyond ITER experiment, fusion community is already working on the conceptual design of DEMO (DEMOnstration Power Plant). DEMO is defined as the predecessor to a commercial-sized fusion reactor, generating electricity at the level of a few hundred MW ($\sim$2500 MW of fusion power with $Q = 25$) and using all technologies necessary for a commercial device.

2.2 Breeding Blankets

As introduced in the previous section, in a D–T powered fusion reactor tritium must be produced – "bred" – inside the fusion reactor. A feasible option to generate such tritium is based on the interaction between the high energy (14 MeV) neutrons generated in the fusion reaction (2.1c), with lithium following reaction 2.2b. However, a more interesting

reaction would be 2.2a due to both its exothermic nature and greater tritium production cross section. Thus, for breeding purposes, the blanket (surrounding the plasma) should contain lithium $^{6}_{3}$Li. Since natural lithium is 92.44 % $^{7}_{3}$Li, enrichment techniques up to 90 % $^{6}_{3}$Li are required. Also, for energy sustainability reasons, the Tritium Breeding Ratio or TBR has to be higher than 1 (typically 1.15). To this aim, a neutron multiplier such as lead or beryllium (apart from $^{7}_{3}$Li) has to be included in the blanket.

$$\text{for thermal neutrons:} \quad {}^{1}_{0}\text{n} + {}^{6}_{3}\text{Li} \longrightarrow {}^{4}_{2}\text{He} + {}^{3}_{1}\text{H} + 4.78\ \text{MeV} \tag{2.2a}$$

$$\text{for fast neutrons:} \quad {}^{1}_{0}\text{n} + {}^{7}_{3}\text{Li} \longrightarrow {}^{4}_{2}\text{He} + {}^{3}_{1}\text{H} + {}^{1}_{0}\text{n} - 2.47\ \text{MeV} \tag{2.2b}$$

Since the blanket is located between the plasma and the magnet (see figure 2.1), one of its functions is shielding the super-conducting magnets (and the vacuum vessel that contains the entire system) against neutron and gamma radiation.

Moreover, since the energy originated in the fusion reactions must be transformed into useful heat, the blanket has to extract the nuclear power in an efficient way. This is carried out by means of coolant fluids that circulate through the blanket structure.

The three above mentioned blanket functions (breeding, shielding and heat extraction) are schematically shown in figure 2.1. It can be seen that the primary fuels for the fusion reactor are deuterium and lithium. The unburned tritium and deuterium fractions have to be refuelled into the core, together with the tritium produced in the blanket. Thus, tritium has to be extracted through the so called Tritium Extraction System (TES) before tritium refuelling. In figure 2.1, the power generation system is drawn separately from the breeding system, but in reality both systems are unified. Controlling tritium inventories is of utmost interest because of (1) tritium is one of the fusion reaction fuels and the TBR is only slightly greater than 1, and (2) tritium is radioactive and, thus, its emissions must be kept under highly restrictive limits. Such tritium control must consider not only permeation through structural materials but also trapping effects (such as fluid stagnation zones or presence of helium bubbles, for example) and inefficiencies in various tritium processing systems.

Several breeding blanket (BB) designs or conceptual proposals, classified according the use of solid or liquid breeding materials:

1. Liquid Breeder Concepts

   - Liquid breeder can be:
     - Liquid metal (high conductivity, low Prandtl number): Li or PbLi eutectic (15.7 % Li atomic fraction)

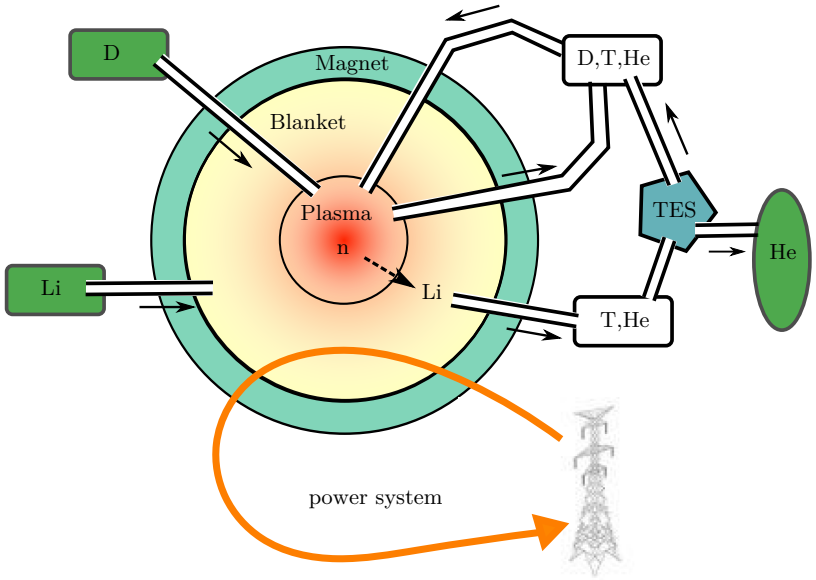

Figure 2.1: Schematic of the fuel cycle in a fusion reactor.

  - Molten salt (low conductivity, high Pr): Flibe $(LiF)_n \cdot (BeF_2)$, Flinabe ($LiF\text{-}BeF_2\text{-}NaF$)
- BB concepts can be classified depending on the cooling role played by the liquid breeder:
  - Separately cooled: A unique coolant exists and the breeder circulates at low speed for tritium extraction purposes.
  - Self-Cooled: liquid breeder is circulated at high speed to operate as primary coolant for the entire blanket
  - Dual Coolant: The primary coolant is responsible of cooling the first wall and the structure, whereas breeding zone is self-cooled.

2. Solid Breeder Concepts

- Always separately cooled
- Solid Breeder: Lithium Ceramic (Li_2O, Li_4SiO_4, Li_2TiO_3, Li_2ZrO_3)
- Coolant: Helium or Water

The lead-lithium liquid metal breeding blanket is a promising concept since lead avoids the use of beryllium (neutron multiplier) and tritium is extracted relatively easy from the alloy.

Structural material selection relays basically on reduced activation ferritic/martensitic (RAFM) steels due to their superior resistance against irradiation swelling, although some vanadium alloys and SiC composites are also considered in the mid/long-term. The choice of a RAFM steel determines the operational window of blanket structure temperature; which is limited to $\sim$300-550 ^{o}C.

In the considered BB, the coolant fluid can be helium, CO_2, pressurised water or the liquid metal breeder. Despite its low cost and availability, pressurised water is not desirable due to the production of tritiated water, from which is very difficult to extract the tritium and refuel it. At present, only Japan is considering water as cooling material (konishi 2010). Depending on the cooling relevance of the liquid metal breeder, the liquid metal BBs are classified as separately cooled, dual coolant or self-cooled, as listed in the previous classification. The separately cooled blanket is considered mainly in EU, whereas USA and Japan are basically focused on dual-coolant designs (*http://www.fds.org.cn/*). The self-cooled design, despite being the most attractive one, presents high technological challenges.

Recently, in the frame of the Spanish National Project on Breeding Blanket Technologies TECNO_FUS (through the CONSOLIDER-INGENIO 2010 Programme), a new BB concept is being worked out, which basically is a dual-coolant design but with high liquid metal velocities and higher thermal efficiency (*http://www.tecnofus.net/*).

All the proposed designs are to be finally tested before their introduction into a commercial fusion reactor. However, until now, no experimental fusion reactor has tested any breeding blanket. Thus, the testing and data collection of BBs is essential and urgent.

2.3 TBM: BB for ITER experiment

Nowadays, the main fusion experiment is ITER, the International Thermonuclear Experimental Reactor, which is being built in Cadarache, France. ITER is a joint project involving Europe (represented by EURATOM), China, India, Japan, South Korea, the Russian Federation and the United States. The goal is to demonstrate that, from a scientific and technical point of view, fusion can be used as an energy source on earth (*http://www.iter.org/*). The first plasma should be possible in ITER by June 2018 (Zmitko 2009).

Compared with current conceptual designs for future fusion power plants, ITER will include most of the necessary technology, but will be of slightly smaller dimensions and will operate at about one-sixth of the power output level. It will generate 500 MW of fusion power for extended periods of time, ten times more than the energy input needed

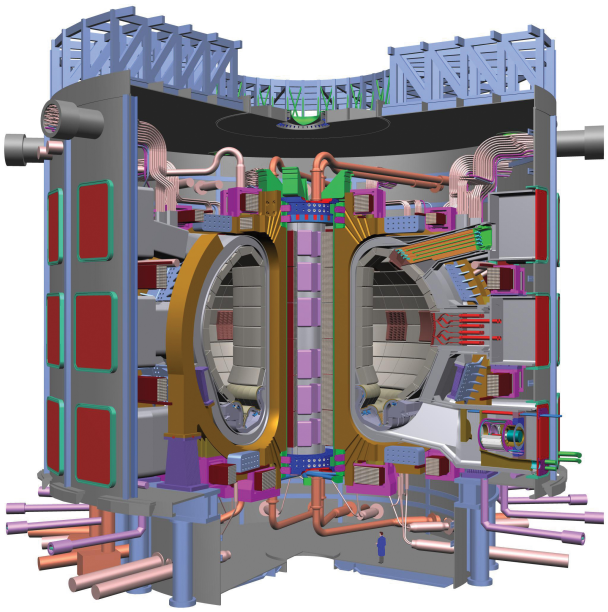

Figure 2.2: ITER experiment design

to keep the plasma at the right temperature. It will also be used to test a number of key technologies, including the heating, control, diagnostic and remote maintenance that will be needed for a real fusion power station.

ITER (figure 2.2) is a deuterium–tritium fusion reactor based on tokamak technology. Not all of the blanket is considered for breeding; instead, there are only some specific locations (in three of the so called equatorial ports) where the BB modules will be inserted. Therefore, BBs have to be designed in a modular form. Since one of the specific technical goals in ITER is to test and develop concepts for breeding tritium from lithium-containing materials inside thermally efficient high temperature blankets surrounding the plasma, the BB modules designed for being tested in ITER are called Test Blanket Modules (TBM).

Among the TBM that are being developed nowadays, the present PhD dissertation will focus on liquid metal TBM since they are the ones that involve MHD phenomena. Six liquid metal breeder TBM designs exist, listed in table 2.1, chosen by their efficiency and technological feasibility. It can be seen that three separately cooled designs, two dual coolant designs and only one self-cooled design are to be tested in ITER. In order to give a global overview, the separately cooled HCLL design and the dual coolant DCLL design are described in the next sections. For a comparison of the main MHD flow characteristics, the reader is referred to section 3.4.2.

Although almost all the designs contemplate the use of ferritic/martensitic steel as

Design	Country	Structural material	Tritium breeder	cooler
DCLL	USA	RAFM(F82H)	LiPb	LiPb/He
DFLL	CN	RAFM(CLAM)	LiPb	LiPb/He
HCLL	EU	RAFM(EUROFER)	LiPb	He
HCML	KO	RAFM(EUROFER)	LiPb	He
LLCB	IN	LAFMS	LiPb	He
LiV	RF	V-alloy	Li	Li

Table 2.1: Existing liquid breeder TBM.

structural material, Zmitko (2009) points out that such structures are expected to: (1) deform the magnetic field, (2) increase plasma instabilities, and (3) induce ions losses. Since the magnitude of the effects is unknown, detailed calculations and experiments are required. In order to reduce the expected effects, the introduction of correction coils, TBMs mass reduction or recession should be considered. No decision has already been taken to the knowledge of the author.

In the first plasma phase of ITER experiment (the electromagnetic phase, that is expected to take place from June 2018 until June 2024, -Zmitko 2009-) main objectives concerning TBMs are: (1) to asses the overall functionality of the TBM, (2) to validate the performance and predictability of heat extraction from the First Wall, (3) to validate the structural integrity, (4) to verify the impact of RAFM steel on plasma, and (5) to measure MHD effects on liquid metal (pressure drop, velocity and temperature profiles) as a function of flow rate. All aspects related to high neutron flux, including thermal efficiency, thermal stresses, tritium production and tritium permeation are considered in future ITER phases, specially in deuterium-tritium phases at the end of the ITER experiment (2027-2030).

The organisation that decides which experiments are going to take place in ITER is Fusion for Energy (F4E, *http://fusionforenergy.europa.eu/*), which is the European Union's Joint Undertaking for ITER and the Development of Fusion Energy, created in April 2007. As declared by this organisation in Zmitko (2009), one of the relevant ITER activities is the development and validation of the predictive/modelling tools capable of extrapolating to DEMO conditions. To validate such tools, some experiments in ITER and out-of ITER are being planned.

2.3.1 EU HCLL TBM

In the HCLL design, PbLi eutectic acts as tritium breeding material whereas cooling is assured by circulating pressurised helium. Eurofer is being considered as structural

material, with a special treatment based on beryllium at the first wall in order reduce the release of impurities into the plasma. The Pb-15.7Li circulates under an intense magnetic field at low velocities ($\sim$ mm/s). Such velocities are limited by the pressure drop of MHD origin derived from the coupling between the induced current and the magnetic field, due to the high electrical conductivity of the Eurofer. The liquid metal withstands an important part of the thermal power deposited by neutron radiation in the component, and transports tritium for its external recovery. The pressurised (8 MPa) helium has an inlet temperature of 300 ^{o}C and an outlet temperature of 500 ^{o}C.

The module designed for ITER (EU HCLL TBM, Salavy *et al.* 2008) consists of a 1650 mm (poloidal) $\times$ 484 mm (toroidal) $\times$ 575 mm (radial) box stiffened by the so called Stiffening Plates in order to withstand the internal pressure of 8 MPa in case of accident. The structure is cooled by helium. Each module consists of several breeder units (BU). In each breeder unit the liquid metal flows radially (towards or away from the plasma in an alternate way) . Inside the BU, the liquid metal is cooled by cooling plates where helium flows inside very thin cooling channels. The fluid travels from one BU to the next one through a narrow gap between the First Wall and the stiffening plate. At the outlet of the TBM, tritium permeated through the Eurofer wall towards the helium has to be recovered in the Tritium Extraction System (TES) and, afterwards, the purified helium is sent to the power generation system. A sketch of the TBM decomposition is showed in figure 2.3.

The design of the HCLL TBM has undergone several revisions in the last years; for instance, in figure 2.3 each BU consists of 5 cooling plates, while in a more recent design described by Aiello *et al.* (2009), only 3 cooling plates are considered and the cooling channels design is redefined. Also, in the present HCLL design, liquid metal enter the module at its bottom due to buoyant effects (Reimann *et al.* 2006).

2.3.2 US DCLL TBM

The DCLL breeding blanket design is an evolution of ARIES concept (Sze *et al.* 2000). Since DCLL is a dual-coolant design, the liquid metal flows at a higher velocity ($\sim$10 cm/s) than in the HCLL. The PbLi flows through long poloidal channels for power conversion and tritium breeding. The chosen structural material is reduced activation ferritic steel (RAFS). Helium is the coolant for the structural material, including the First Wall.

The module designed for ITER (US DCLL TBM, Wong *et al.* 2006, , Smolentsev *et al.* 2006, Smolentsev *et al.* 2010) consists of a 2 m (poloidal) $\times$ 30 cm (toroidal) $\times$ 20 cm (radial) box stiffened by the so called Stiffening Plates in order to withstand the internal helium pressure of 8 MPa in case of accident. Preliminary designs consisted of

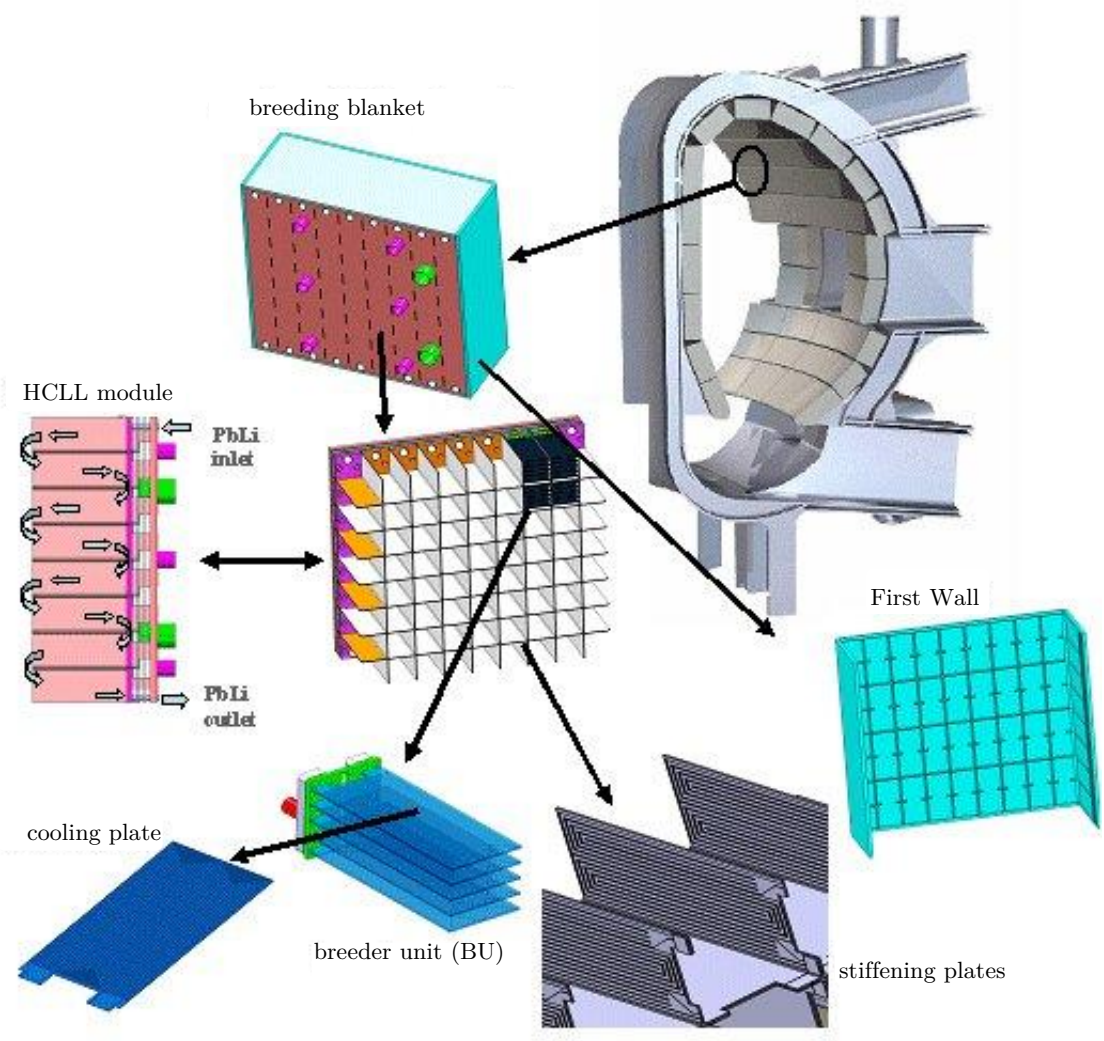

Figure 2.3: Decomposition of a EU HCLL TBM

two rows of poloidal ducts. The flow entered the module from the bottom and travelled through the front (close to the First Wall) ducts and returned downstream through the back ducts (see figure 2.5). However, with the aim of better extrapolating the DCLL concept to DEMO, in terms of thermal performance, new improvements are being defined. Indeed, in the present design, described by Wong *et al.* (2010), the liquid metal enters the upper part of the module from the back, flows down the back duct and turns at the bottom of the module before flowing up the front duct (see figure 2.4). This modification is motivated by the need of reducing the risk of hot spots due to reverse fluid currents caused by the buoyancy forces opposing to the flow.

The pressurised helium presents an inlet/outlet temperature of 350 ^{o}C–410 ^{o}C, while

lead lithium at 2 MPa lays in the range of 360 ^{o}C–470 ^{o}C, according to Wong *et al.* (2010). Such temperatures are limited by the structural material properties (maximum steel structure temperature of 550 ^{o}C and a corrosion limit of about 480 ^{o}C).

In order to reduce MHD pressure drops and increase the liquid metal maximum temperature, flow channel inserts (FCI) made of silicon carbide (SiC), either as a composite or as foam, are introduced between the structural material and the liquid metal (as seen in figure 2.5). FCI presents a very low electrical conductivity, what minimises the coupling between the induced current and the magnetic field, reducing the MHD pressure drop. This allows higher liquid metal velocities. Moreover, since the FCI material has a very small thermal conductivity, it acts as a thermal insulator and temperature limits for the structural material do not represent such a restrictive constrain.

Between the FCI (typically 5mm thick, Smolentsev *et al.* 2008) and the structural material, a thin ($\sim$2 mm) gap also filled with PbLi exists. The gap and the main flows are connected through small openings in one of the FCI walls to equalise the pressure on both sides of the FCI.

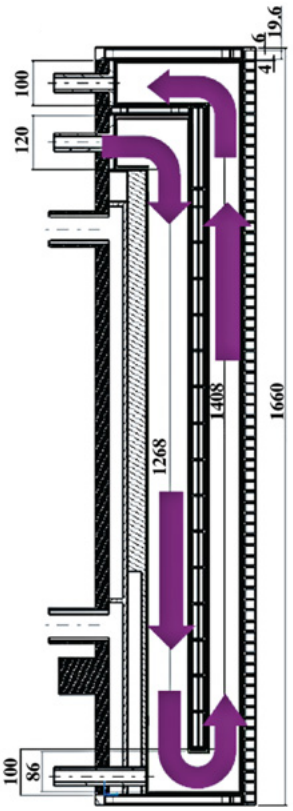

Figure 2.4: PbLi circulation in the US DCLL TBM, from Wong *et al.* (2010)

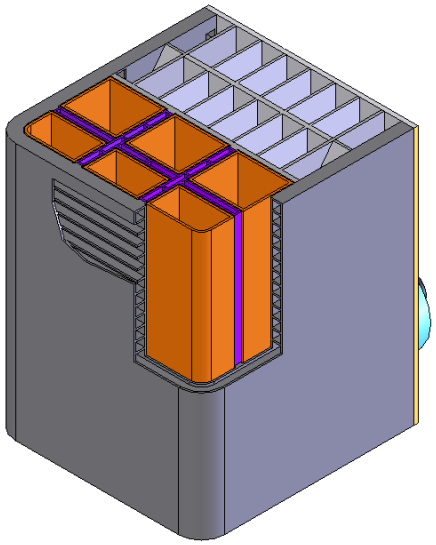

Figure 2.5: Section of the US DCLL TBM. The two rows of ducts can be seen with the surrounding FCI (in orange), from Wong *et al.* (2006)

3 Phenomena

In this chapter MHD thermofluid phenomena occurring in breeding blanket channels and the related transport equations are explained. Other phenomena also occurring in breeding blanket liquid metal channels, so as corrosion, material activation or thermal stresses, are not considered here. For the sake of clarity, only the basic concepts are explained and the final equations shown, skipping the somewhat cumbersome intermediate steps. Mainly, all concepts are extracted from four references, the book from Oliver and de Saracibar (2002), Davidson (2001), Cramer and Pai (1973) and Müller and Bühler (2001).

The explanation includes the assumed hypotheses, MHD transport equations and thermal coupling. At the end of this Chapter, a brief introduction of main flow characteristics at high Hartmann numbers is given in order to provide the reader with a more applied definition of MHD effects.

3.1 Hypotheses

The first step before starting analysing any phenomenon is defining the hypotheses needed in order to simplify (or just define) the study. All the hypotheses here mentioned are introduced along the following sections; however, it has been deemed useful for the reader to have them listed here in order to get an overview of the simplifications applied.

The main hypotheses applied in the development of the governing flow equations are:

1. continuum media
2. incompressible fluid
3. Boussinesq hypothesis
4. Newtonian fluid with the Stokes condition for the bulk viscosity
5. homogeneity and isotropy of materials
6. electrically conducting fluid
7. relativistic terms neglected in the constitutive relations for the electric displacement and the magnetic induction.
8. no magnetic monopoles
9. symmetric Maxwell stress tensor
10. low magnetic Reynolds number approximation
11. negligible expansion/contraction work, viscous dissipation and Joule generation.

All equations have been developed macroscopically, assuming a continuum medium, so that infinitesimal calculus can be applied. This could only be discussed in a microscale analysis, where all nuclear interactions can be studied in detail. In that case, a statistical analysis could be more appropriate.

Considering the fluid as incompressible is a strong simplification, specially in a non-isothermal system. However, following Boussinesq hypothesis, if in the expected temperature differences the fluid density does not vary substantially, the fluid can be considered incompressible in all terms of the momentum equation except at the buoyant term. This issue is analysed in section 3.3.

The following three hypotheses are related to material properties. Only the homogeneity and isotropy of material properties involve a simplification. Such simplification would not be acceptable if, for example, fluid properties vary considerably with temperature.

The next three hypotheses are needed in order to simplify Maxwell's equations. All of them are perfectly reasonable for liquid metal MHD flows and, hence, widely accepted.

The low magnetic Reynolds number approximation is valid when liquid metal flows at laboratory velocities are considered, which is the case in the present study. The

interest of this approximation is that it simplifies a big deal the describing equations reducing the unknowns of the final set of equations. An extended explanation of this hypothesis is included in section 3.2.

In order to simplify the energy equation, a negligible expansion/contraction work, a negligible viscous dissipation, and a negligible Joule generation are assumed. Such simplifications are perfectly reasonable under the flow conditions considered in the frame of the present study.

3.2 Magnetohydrodynamics

In the context of the present PhD dissertation, magnetohydrodynamics (MHD) refers to isothermal hydrodynamics under the influence of a magnetic field. Hence, the equations involved are Navier-Stokes equations and Maxwell equations. Navier-Stokes equations include a continuity equation and the linear momentum equation. The first one is obtained from a mass conservation balance; the second one from Newton's Second Law. Under all the hypotheses above mentioned (section 3.1), Navier-Stokes equations take the form:

$$\nabla \cdot \mathbf{v} = 0 \tag{3.1a}$$

$$\frac{\partial \mathbf{v}}{\partial t} + (\mathbf{v} \cdot \nabla)\mathbf{v} = -\frac{\nabla p}{\rho} + \nu \nabla^2 \mathbf{v} + \mathbf{b}_f \tag{3.1b}$$

where $\mathbf{v}$, p, t, ρ, ν and $\mathbf{b}_f$ stand for velocity, pressure, time, density, kinematic viscosity and body forces vector, respectively. The two terms on the left hand side (l.h.s.) of equation 3.1b are the transport of linear momentum, i.e., the transient term and the convective term. The two first terms on the right hand side (r.h.s.) of equation 3.1b correspond to surface forces: the pressure and the viscous terms. The last term corresponds to all the body forces applied, including buoyancy and Lorentz force, among others.

In order to evaluate the Lorentz force and all the magnetic variables of interest, Maxwell equations need to be manipulated. Maxwell equations presented here (equations 3.2) are simplified considering approximately grossly neutral fluid, obtaining the so called pre-Maxwell equations.

Solenoidal nature of $\mathbf{B}$	$\nabla \cdot \mathbf{B} = 0$	(3.2a)
Faraday's law of induction	$\nabla \times \mathbf{E} = -\frac{\partial \mathbf{B}}{\partial t}$	(3.2b)
Ampere's law equation	$\nabla \times \mathbf{B} = \mu_m \, \mathbf{j}$	(3.2c)
Charge conservation	$\nabla \cdot \mathbf{j} = 0$	(3.2d)
Ohm's law	$\mathbf{j} = \sigma_m(\mathbf{E} + \mathbf{v} \times \mathbf{B})$	(3.2e)
Lorentz force	$\mathbf{F} = \mathbf{j} \times \mathbf{B}$	(3.2f)

where $\mathbf{B}$, $\mathbf{E}$, $\mathbf{j}$, μ_m and σ_m stand for the magnetic field, the electric field, the electric current density, the magnetic permeability and the electric conductivity, respectively.

Using the pre-Maxwell equations (3.2), and defining $\eta = \frac{1}{\sigma_m \mu_m}$, an equation for the magnetic field $\mathbf{B}$ can be obtained:

$$\frac{\partial \mathbf{B}}{\partial t} = \nabla \times (\mathbf{v} \times \mathbf{B}) + \eta \nabla^2 \mathbf{B} \tag{3.3}$$

Also, the Lorentz force (equation 3.2f) can be developed as follows:

$$\mathbf{F} = \mathbf{j} \times \mathbf{B} = \frac{1}{\mu_m} \left(-\nabla \frac{\mathbf{B}^2}{2} + (\mathbf{B} \cdot \nabla)\mathbf{B} \right) \tag{3.4}$$

Hence, the Lorentz force is split into two parts, one corresponding to a magnetic pressure drop, the gradient term, and the other corresponding to a stress term. With all this, the system of equations to be solved for pure MHD[1] is:

$$\nabla \cdot \mathbf{v} \ = \ 0 \tag{3.5a}$$

$$\frac{\partial \mathbf{v}}{\partial t} \ + \ (\mathbf{v} \cdot \nabla)\mathbf{v} \ = \ -\frac{\nabla p}{\rho} + \nu \nabla^2 \mathbf{v} \ + \ \frac{1}{\mu_m \rho} \left(-\nabla \frac{\mathbf{B}^2}{2} + (\mathbf{B} \cdot \nabla)\mathbf{B} \right) \tag{3.5b}$$

$$\frac{\partial \mathbf{B}}{\partial t} = \nabla \times (\mathbf{v} \times \mathbf{B}) + \eta \nabla^2 \mathbf{B} \tag{3.5c}$$

$$\nabla \cdot \mathbf{B} \ = \ 0 \tag{3.5d}$$

Here, the bi-directional coupling between velocity and magnetic field is made explicit. Such coupling can be conceptually explained by artificially (but usefully) splitting the phenomenon into three steps (see Davidson (2001), section 1.1):

1. The relative movement of a conducting fluid and a magnetic field causes an electromagnetic force (of order $|\mathbf{v} \times \mathbf{B}|$) in accordance with Faraday's law of induction. At the same time, according to Ohm's law, electric currents are generated.

2. According to Ampère's law, these currents must rise to a second induced magnetic field. This adds to the original magnetic field and the effect is usually such that the fluid appears to 'drag' the magnetic field lines along with it.

3. The combined magnetic field (imposed plus induced) interacts with the induced current density, $\mathbf{j}$, to give rise to a Lorentz force (per unit volume), $\mathbf{j} \times \mathbf{B}$. This acts on the fluid and is generally directed so as to inhibit the relative movement of the magnetic field and the fluid.

[1] when the only body force $\mathbf{b}_f$ corresponds to the Lorentz force

3.2.1 Dimensionless equations

The goal of this section is to obtain the dimensionless numbers that characterise the flow. There are several strategies to do so, here, $\mathbf{v}$, t, $\mathbf{B}$, $\mathbf{j}$ and p are adimensionalised with v_o, L/v_o, B_o, $\sigma_m v_o B_o$ (from Ohm's law) and $\sigma v_o B_o^2 L$ (from Lorentz force), respectively. L is the characteristic length, being usually half of the length in the direction of the externally imposed magnetic field B_o, and v_o is the characteristic velocity such as, for example, the forced flow velocity. The $\hat{}$ symbol has been used to indicate the dimensionless variables. The dimensionless set of equations is:

$$\nabla \cdot \hat{\mathbf{v}} = 0 \tag{3.6a}$$

$$\frac{\partial \hat{\mathbf{v}}}{\partial \hat{t}} + (\hat{\mathbf{v}} \cdot \nabla)\hat{\mathbf{v}} = -N \nabla \hat{p} + \frac{1}{Re}\nabla^2 \hat{\mathbf{v}} + \frac{N}{Rm}\left(-\nabla \frac{\hat{\mathbf{B}}^2}{2} + (\hat{\mathbf{B}} \cdot \nabla)\hat{\mathbf{B}}\right) \tag{3.6b}$$

$$\frac{\partial \hat{\mathbf{B}}}{\partial \hat{t}} = \nabla \times (\hat{\mathbf{v}} \times \hat{\mathbf{B}}) + \frac{1}{Rm}\nabla^2 \hat{\mathbf{B}} \tag{3.6c}$$

$$\nabla \cdot \hat{\mathbf{B}} = 0 \tag{3.6d}$$

where:

- Reynolds number $Re = \frac{v_o L}{\nu}$ relates the inertial forces with the viscous ones.
- Interaction parameter $N = \frac{\sigma_m B_o^2 L}{\rho v_o}$ relates the magnetic forces with the inertial ones.
- Magnetic Reynolds number $Rm = \frac{v_o L}{\eta}$ (being $\eta = \frac{1}{\sigma_m \mu_m}$) relates the magnetic advection with the magnetic diffusion.

The Hartmann number is then obtained as $Ha = (NRe)^{1/2} = B_o L(\frac{\sigma_m}{\rho\nu})^{1/2}$, which relates the magnetic forces with the viscous ones.

3.2.2 Low Rm approximation

The magnetic Reynolds number, Rm, gives an idea of the freezing of the magnetic field lines. For very low Rm ($Rm << 1$), the magnetic field lines are almost frozen (the magnetic field will tend to relax towards a purely diffusive state, and inhomogeneities in the field will be smoothed out), what implies that the induced magnetic field is negligible. This reasoning leads to the inductionless approximation, also called low Rm approximation or Quasi-Static approximation, where the flow no longer affects the magnetic field. Under these conditions, and following the so called ϕ-formulation that uses ϕ, the electric potential, as the main variable, the set of equations governing the pure MHD

flow is:

$$\nabla \cdot \mathbf{v} \;=\; 0 \tag{3.7a}$$

$$\frac{\partial \mathbf{v}}{\partial t} \;+\; (\mathbf{v}\cdot\nabla)\mathbf{v} \;=\; -\frac{\nabla p}{\rho} + \nu\nabla^2\mathbf{v} \;+\; \frac{\mathbf{j}\times\mathbf{B_o}}{\rho} \tag{3.7b}$$

$$\nabla^2\phi \;=\; \nabla\cdot(\mathbf{v}\times\mathbf{B_o}) \tag{3.7c}$$

$$\mathbf{j} = \sigma_m\,(-\nabla\phi \;+\; \mathbf{v}\times\mathbf{B_o}) \tag{3.7d}$$

Notice that the total magnetic field $\mathbf{B}$ has been split into two terms, the externally applied magnetic field $\mathbf{B_o}$ and the induced magnetic field $\mathbf{b}$, being the latter negligible under the inductionless approximation. The Poisson equation for the electric potential (3.7c) has been obtained applying the divergence operator on Ohm's law.

The dimensionless form of this system of equations, with ϕ normalised with $v_o B_o L$ is:

$$\nabla \cdot \hat{\mathbf{v}} \;=\; 0 \tag{3.8a}$$

$$\frac{\partial \hat{\mathbf{v}}}{\partial \hat{t}} \;+\; (\hat{\mathbf{v}}\cdot\nabla)\hat{\mathbf{v}} \;=\; -N\,\nabla\hat{p} + \frac{1}{Re}\nabla^2\hat{\mathbf{v}} \;+\; N\,(\hat{\mathbf{j}}\times\hat{\mathbf{B}}) \tag{3.8b}$$

$$\nabla^2\hat{\phi} \;=\; \nabla\cdot(\hat{\mathbf{v}}\times\hat{\mathbf{B}}) \tag{3.8c}$$

$$\hat{\mathbf{j}} = -\nabla\hat{\phi} \;+\; \hat{\mathbf{v}}\times\hat{\mathbf{B}} \tag{3.8d}$$

where Rm no longer appears. The great advantage of this system (3.7) in front of the complete set of equations (3.5) is the simplicity of the numerical solution. That is, the three transient convective-diffusion equations for the induced magnetic field (equation 3.5c for each component $-i, j, k-$) is substituted by a Poisson equation (equation 3.7c) and an explicit evaluation of the current density (equation 3.7d), which are much easier to solve and need less computational efforts. For these reasons, the low Rm approximation (system 3.7) is the one generally solved by the community of MHD analysts working on fusion technology.

Recently, a new MHD approach has been presented by Smolentsev *et al.* (2010), where a j-formulation based on the electric current as the main electromagnetic variable is introduced. Compared to the ϕ-formulation, the j-formulation avoids some numerical errors potentially present at high Hartmann numbers, but needs to solve a vectorial j equation instead of the scalar ϕ equation, requiring more computation time.

3.3 Heat Transfer

The integral total energy equation, based on the first law of thermodynamics, is presented in equation (3.9); where ε corresponds to the total energy per unit mass defined

as the sum of the kinetic energy, the internal energy u, and the magnetic energy ω_m.

$$\begin{aligned}
\underbrace{\frac{d}{dt}\int_\Omega \rho\,\varepsilon\,dV}_{\text{total energy variation rate}} &= \frac{d}{dt}\int_\Omega \rho\left(\frac{1}{2}\mathbf{v}\cdot\mathbf{v} + u + \frac{\omega_m}{\rho}\right)dV \\
&= \underbrace{\int_{\partial\Omega}((-p\cdot\mathbf{I} + \rho\,\nu\,\nabla\mathbf{v})\cdot\mathbf{v})\cdot\mathbf{n}\,dS}_{\text{surface stresses rate}} + \underbrace{\int_\Omega \rho\,\mathbf{b}_f\cdot\mathbf{v}\,dV}_{\text{body forces rate}} \\
&- \underbrace{\int_{\partial\Omega}\mathbf{q}\cdot\mathbf{n}\,dS}_{\text{heat and e.m. energy flux}} + \underbrace{\int_\Omega \rho\,S_{thermal}\,dV}_{\text{others (reaction, radiation,...)}}
\end{aligned} \tag{3.9}$$

Note that Ω and $\partial\Omega$ are the system's volume and its surface area, correspondingly.

The development of this equation into the final one, as a function of temperature, is very complex and the exposition here of the complete process will not contribute to a deeper understanding. Thus, only the final equation is shown. However, it is important to keep in mind all the concepts that are involved in this development, which include:

- The Reynolds Transport Theorem, the continuity equation and the kinetic energy equation (from the linear momentum equation)
- The definition of the enthalpy i: $i = u + \frac{p}{\rho}$
- The relation between enthalpy and entropy s: $di = T\,ds + \frac{1}{\rho}dp$
- Maxwell's relations
- The definition of the thermal expansion coefficient β: $\beta = -\frac{1}{\rho}\left(\frac{\partial\rho}{\partial T}\right)_p$
- The magnetic energy definition $\omega_m = \frac{\mathbf{B}\cdot\mathbf{B}}{2\mu_m}$
- The Fourier law: $\mathbf{q} = -k\nabla T$, where k is the thermal conductivity

With all this, the total energy equation is written as:

$$\underbrace{\rho\,C_p\,\frac{dT}{dt}}_{\text{thermal energy gain}} - \underbrace{\beta\,T\,\frac{dp}{dt}}_{\text{exp.contractions}} = \underbrace{\frac{\mathbf{j}^2}{\sigma_m}}_{\text{Ohmic gain}} + \underbrace{(\rho\,\nu\,\nabla\mathbf{v}):\mathbf{d}}_{\text{viscous dissipation}} + \underbrace{k\,\nabla^2 T}_{\text{heat fluxes}} + \underbrace{\rho\,S_{thermal}}_{\text{other}} \tag{3.10}$$

where T, C_p and $\mathbf{d}$ stand for temperature, heat capacity at constant pressure, and the symmetric part of the velocity gradient (deformation), respectively.

If the studied fluid is a liquid, work done by expansions or contractions can be neglected. Moreover, in liquid metal MHD flows as applied to breeding blanket studies, the influence on the flow of both viscous dissipation and the Joule generation terms is

small enough, compared to other terms, that both terms can be neglected from the energy equation. Instead, the source term $S'_{thermal}$ is of great interest in BB simulations since it is related to the neutron irradiation from the plasma to the breeding material.

Applying the above mentioned assumptions, the simplified energy equation (3.11) is obtained, where $\alpha = \frac{k}{\rho C_p}$ is the thermal diffusivity.

$$\frac{\partial T}{\partial t} + \nabla \cdot (\mathbf{v}T) = \alpha \nabla^2 T + S'_{thermal} \tag{3.11}$$

3.3.1 Coupling between momentum and temperature

Coupling between momentum and temperature equations is essential for a correct flow analysis. The necessity of the coupling arises from the fact that density varies with temperature, which should be made explicit in the equation of state of the fluid. In the present case, however, as the thermal expansion coefficient, β, of the liquid metal is one order of magnitude lower than typical values for gases, and half the value for liquid water, the equation of state can be substituted by a constant density in all terms of the momentum equation except the buoyancy term, according to the Boussinesq hypothesis. This way, the flow can still be considered as incompressible, where equation 3.7a still applies. The buoyancy term is part of the body forces ($\rho\, \mathbf{b}_f$) and corresponds to ($\rho\, \mathrm{g}$), where g is the gravity vector. Several correlations between the density and the temperature can be used in the buoyancy term. Here, a linear Taylor expansion of the density is used, according to:

$$\rho = \rho_o - \left(\frac{\partial \rho}{\partial T}\right)_o (T - T_o) = \rho_o \left(1 - \beta_o \left(T - T_o\right)\right) \tag{3.12}$$

where T_o, ρ_o and β_o are the temperature, density and thermal expansion coefficient at the reference state ($\cdot_o$). Hence, the momentum equation (3.7b) is now modified as:

$$\frac{\partial \mathbf{v}}{\partial t} + (\mathbf{v} \cdot \nabla)\mathbf{v} = -\frac{\nabla p_d}{\rho_o} + \nu \nabla^2 \mathbf{v} + \frac{\mathbf{j} \times \mathbf{Bo}}{\rho_o} - \beta_o\, \mathbf{g}\, (T - T_o) \tag{3.13}$$

Note that p_d is the so called dynamic pressure, what in fact means the total pressure minus the hydrostatic one. For the sake of clarity, the complete development related to both pressure and buoyancy terms is shown in equation 3.14.

$$\begin{aligned} -\nabla p + \rho\, \mathbf{g} &= -\nabla p + \rho_o \left(1 - \beta_o \left(T - T_o\right)\right) \mathbf{g} \\ &= -\nabla (p - p_{hyd}) - \rho_o\, \beta_o\, \mathbf{g}\, (T - T_o) \\ &= -\nabla p_d - \rho_o\, \beta_o\, \mathbf{g}\, (T - T_o) \end{aligned} \tag{3.14}$$

3.3.2 Dimensionless equations

The same normalisation as in section 3.2.1 has been applied. The new variable, the temperature increment $(T - T_o)$, has been normalised by a reference temperature gradient ΔT_o, obtaining $\hat{T}$. Thus, the momentum equation yields:

$$\frac{v_o}{L}\left[\frac{\partial \hat{\mathbf{v}}}{\partial \hat{t}} + (\hat{\mathbf{v}}\cdot\nabla)\hat{\mathbf{v}}\right] = -\frac{\sigma\, v_o\, B_o^2}{\rho_o}\nabla\hat{p_d} + \frac{\nu\, v_o}{L^2}\nabla^2\hat{\mathbf{v}} + \frac{\sigma\, v_o\, B_o^2}{\rho_o}(\hat{\mathbf{j}}\times\hat{\mathbf{B}}) - \beta_o\, g_o\, \Delta T_o\, \hat{\mathbf{g}}\, \hat{T} \quad (3.15)$$

If Lorentz forces balance buoyant forces then the characteristic velocity would be $v_{o,MHD}$, shown in equation 3.16, where $Gr = \frac{g\beta\Delta T L^3}{\nu^2}$ is the Grashof number, which is a ratio of the buoyant forces to the viscous forces.

$$\frac{\sigma v_o B_o^2}{\rho_o \beta_o g_o \Delta T} = 1 \qquad \longrightarrow \qquad v_o = v_{o,MHD} = \frac{Gr}{Ha^2}\frac{\nu}{L} \quad (3.16)$$

In contrast, for non MHD flows, $v_{o,HYD} = Gr^{0.5}\nu L^{-1}$. The ratio of both numbers yields the Lykoudis number $Ly = v_{o,HYD}/v_{o,MHD} = Ha^2\, Gr^{0.5}$, which relates Lorentz and buoyant forces. Thus, for high Ly, the magnetic damping is predominant.

When $v_{o,MHD}$ is used as the characteristic velocity, the dimensionless system of equations is:

$$\nabla\cdot\hat{\mathbf{v}} = 0 \quad (3.17a)$$

$$\frac{Gr}{Ha^4}\left[\frac{\partial \hat{\mathbf{v}}}{\partial \hat{t}} + (\hat{\mathbf{v}}\cdot\nabla)\hat{\mathbf{v}}\right] = -\nabla\hat{p_d} + \frac{1}{Ha^2}\nabla^2\hat{\mathbf{v}} + (\hat{\mathbf{j}}\times\hat{\mathbf{B}}) - \hat{\mathbf{g}}\hat{T} \quad (3.17b)$$

$$\nabla^2\hat{\phi} = \nabla\cdot(\hat{\mathbf{v}}\times\hat{\mathbf{B}}) \quad (3.17c)$$

$$\hat{\mathbf{j}} = -\nabla\hat{\phi} + \hat{\mathbf{v}}\times\hat{\mathbf{B}} \quad (3.17d)$$

$$\frac{Pr\,Gr}{Ha^2}\left[\frac{\partial \hat{T}}{\partial \hat{t}} + \nabla\cdot(\hat{\mathbf{v}}\hat{T})\right] = \nabla^2\hat{T} + S'_{thermal} \quad (3.17e)$$

where Pr is the Prandtl number $Pr = \frac{\nu}{\alpha}$ and provides a relation between the hydrodynamic boundary layer depth and the thermal one. Note that the Rayleigh number is defined as $Ra = Gr\ Pr$. Comparing equation 3.17b with equation 3.8b, $Gr\,Ha^{-2}$ plays the role of Re for pure MHD flows, whereas $Ly^2 = Ha^4 Gr^{-1}$ plays the role of N. If $Ha^4 Gr^{-1} >> 1$, inertia effects can be neglected in the momentum balance (eq. 3.17b) except when high velocity jets are expected to appear at side boundary layers, as stated by Bühler (1998). Another interesting dimensionless number is the Peclet number, $Pe = Pr\,Gr\,Ha^{-2}$. For $Pe << 1$, inertia effects can be neglected in the energy balance (eq. 3.17e).

3.4 Main flow characteristics at high Hartmann numbers

MHD flows behave substantially different than pure hydrodynamic flows, being such difference even stronger when buoyancy exist. Thus, it has been considered necessary to include a brief introduction on qualitative understanding of basic MHD flow in section 3.4.1, whereas a characterisation of the flow in breeding blanket channels is exposed in section 3.4.2.

3.4.1 Basics of MHD flows

In figure 3.1 a cross-section of a square channel of side $2a$ is shown. The externally applied magnetic field is aligned with z axis while the flow travels in x direction. Here, the only body force is the Lorentz force, and no buoyancy is considered. The walls aligned with the magnetic field are called side walls, whereas the walls perpendicular to the magnetic fields are the Hartmann walls. Such type of flow has been widely studied as, for instance, by Shercliff (1953) and Hunt (1965).

Under the above mentioned pressure-driven flow specifications ($\mathbf{B} = (0, 0, B_z)$ and $\mathbf{v} = (v_x, 0, 0)$), the induced electric current at the core flow travels in the negative y axis direction, as sketched in figure 3.2. This electric current, when interacting with the magnetic field, generates a Lorentz force that acts as a damping force that opposes the pressure gradient. As a result, the velocity profile is flattened at the core region. As Ha increases, the electromagnetic damping increases. Hence, for a given Re number, the pressure drop increases with Ha.

The ratio between the electric conductivity of the walls and that of the fluid has a great influence on the flow. Such ratio, often called wall conductivity ratio, is expressed as $C_w = \sigma_w \delta_w / (\sigma a)$, where σ, δ_w and a stand for electric conductivity, wall depth and characteristic flow dimension along magnetic field lines, respectively.

If all walls are perfectly insulated ($C_{w,side} = C_{w,Ha} = 0$, see Shercliff 1953), due to charge conservation, the electric current stream lines close their path inside the fluid domain. Hence, electric current travel close to side walls first and, then, along Hartmann walls until the opposite side wall before closing the path, as shown in figure 3.2. As a result, Lorentz force is strongly reduced close to side walls whereas it is x positive near Hartmann walls. Close to side walls, the unique force is the viscous one and the so called side boundary layer develops. Such layer is of depth $\delta_{side} = a/Ha^{0.5}$. Next to Hartmann walls, the Lorentz force opposes the viscous force and the so called Hartmann boundary layer develops. As Ha increases, the Lorentz force pushes the flow further and the Hartmann boundary layer depth decreases according to $\delta_{Ha} = a/Ha$ ($\delta_{Ha} = 42\mu$m in PbLi for $B = 1$T). Thus, at high Ha numbers, Hartmann boundary

layers are much thinner than side ones. If the magnetic field is not perpendicular to a pair of walls, inner boundary layers exist. However, here, only the case with the magnetic field perpendicular to one pair of walls is considered. Results for $Ha = 300$ and $N = 9{\cdot}10^3$ are shown in figure 3.3. Due to the high Ha number, Hartmann boundary layers are hardly seen in the figure, however, the core-flattened velocity profile as well as the closed electric current path can be clearly observed.

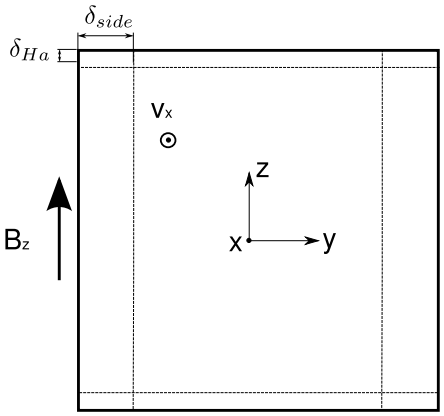

Figure 3.1: Sketch of a cross-section of a channel

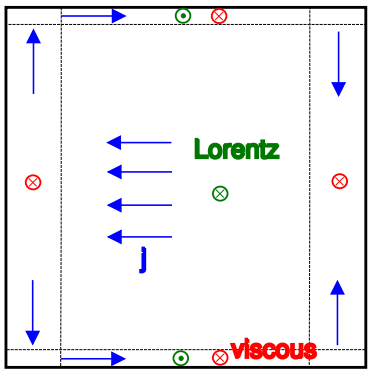

Figure 3.2: Schematic drawing of forces acting on the fluid for $C_{w,side} = C_{w,Ha} = 0$

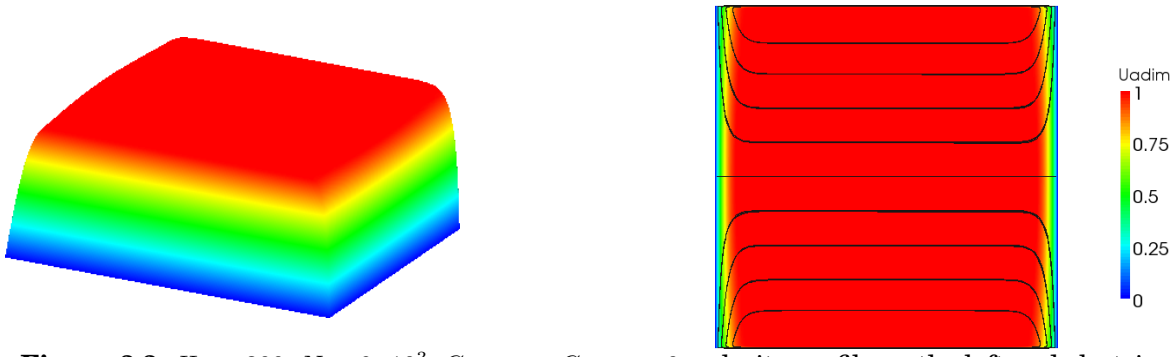

Figure 3.3: $Ha = 300$, $N = 9 \cdot 10^3$, $C_{w,side} = C_{w,Ha} = 0$, velocity profile on the left and electric current stream lines on velocity on the right.

If side walls are perfectly insulated but Hartmann walls are perfectly conducting ($C_{w,side} = 0$ and $C_{w,Ha} = \infty$, see Hunt 1965), electric currents can cross Hartman walls

and, hence, the overall electric resistivity decreases compared with the perfectly insulating case. Thus, the total amount of circulating electric current increases, causing an increase on the Lorentz force. As a result, the core velocity is reduced and the main part of the flow is carried out by side boundary layers (where almost no Lorentz force exist). Results for $Ha = 300$ are shown in figure 3.4. According on what was already predicted in Müller and Bühler (2001), the velocity at side boundary layers exceeds the average duct velocity by a factor of $(Ha/2)^{0.5}$. The obtained velocity profile is the well known M-shaped profile. If a fixed Re is imposed, when $Cw, side = 0$ and $C_{w,Ha} = \infty$ the pressure drop is higher than for the perfectly insulating case.

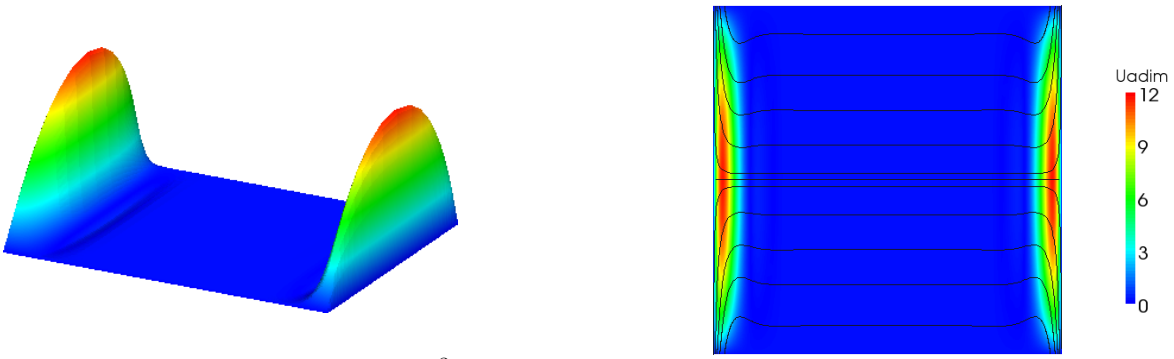

Figure 3.4: $Ha = 300$, $N = 9 \cdot 10^3$, $C_{w,side} = 0$, $C_{w,Ha} = \infty$, velocity profile on the left and electric current stream lines on velocity on the right.

For the case with perfectly conducting side and Hartmann walls ($C_{w,side} = C_{w,Ha} = \infty$, see Hunt 1965), a Lorentz force opposing the flow exists at side boundary layers, what reduces the magnitude of the jets. As the total amount of circulating electric current increases even more than the case with $Cw, side = 0$ and $C_{w,Ha} = \infty$, the flow is strongly damped and, for a given Re, the pressure drop increases substantially.

3.4.2 Fusion technology flow conditions

According to Smolentsev *et al.* (2010), typical Ha, Re and Gr values for DCLL, HCLL and Self-cooled blanket concepts, introduced in section 2.3, are listed in table 3.1 together with other characteristic dimensionless numbers. Both DCLL and HCLL values correspond to ITER TBM designs, whereas Self-cooled data is predicted for DEMO specifications considering $B_o = 10$ T, $v_o = 0.5$m/s and $L = 0.05$ m. For the estimation of the Grashof number, the characteristic temperature scale is defined as $\Delta T = \bar{S}\, a^2/k$, which is associated with the average radial thermal load $\bar{S}$, the characteristic length a and the

liquid metal conductivity k. Also, from Ha, Re and Gr values, some interesting dimensionless numbers have been calculated and included at the same table (3.1), considering lead lithium to be at 450^{o}C, hence $Pr = 0.015$ (Mas de les Valls *et al.* 2008).

For the DCLL and Self-cooled cases, the Re number is high enough for turbulence to exist. According to Re/Ha ratio, the flow would present Q2D turbulence (see section 4.1.3). Moreover, since walls have a finite electric conductivity, the M-shaped profile is retrieved and high velocity jets appear at side boundary layers. Due to the high Re, such jets could present some instabilities.

In all three cases, Gr is very high, hence, buoyancy can alter the flow. Whether the flow is buoyant predominant or not depends, basically on the ratio between the mean flow velocity and the buoyant one ($v_{o,MHD}$ in previous section). In HCLL design, this ratio, despite being of order 10^{-2}, is one order of magnitude higher than in the DCLL or Self-coled designs. In fact, according to the results by Kharicha *et al.* (2004), it can be stated that, in HCLL blanket, buoyant convection may become as relevant as forced flow. However, according to the high Lykoudis numbers, the magnetic damping has enough relevance to obtain an equivalent $Re = Gr/Ha^2$ number much below the forced one, in all three cases.

Whether the flow is unsteady or not, can be grossly predicted following the flow classification from Molokov (1997). According to this classification, both DCLL and Self-cooled flows would correspond to the unsteady inertial flow, whereas HCLL flow would be steady and inertial. However, such classification is only valid for pure MHD flows and buoyancy might cause some flow instabilities (due to Rayleigh-Bénard instability).

Relative to numerical strategies, as the equivalent interaction parameter Ha^4/Gr is very high in all three cases, inertia effects can be neglected from momentum balance. However, only for the HCLL case where $Pe << 1$, inertia effects could be removed from the energy balance.

Blanket type	Ha	Re	Gr	Re/Ha	Ly	Pe	Gr/Ha^2
DCLL (ITER TBM)	$6.5 \cdot 10^3$	$3.0 \cdot 10^4$	$7.0 \cdot 10^9$	4.6	505	2.5	165.7
HCLL (ITER TBM)	$1.1 \cdot 10^4$	670	$1.0 \cdot 10^9$	0.06	$3.8 \cdot 10^3$	0.1	8.3
Self-cooled (DEMO)	$4.5 \cdot 10^4$	$3.2 \cdot 10^4$	$2.0 \cdot 10^{12}$	0.7	$1.4 \cdot 10^3$	14.8	987.6

Table 3.1: Typical breeding blanket dimensionless numbers

In general, the following flow characterisation is widely accepted:

- In the Self-cooled blanket, as the liquid metal flows at high velocities (~ 0.5 m/s),

MHD pressure drop is the most critical issue. In order to reduce such pressure drop, electrical insulators are required. However, the technical problem related to such a good insulator is not solved yet. MHD turbulence and flow instabilities are also relevant issues.

- In the US DCLL blanket, the liquid metal flows at a moderate velocity ($\sim 0.01 - -0.1$ m/s), thus, electric insulation can be provided using SiC Flow Channel Inserts (FCI). MHD turbulence and buoyancy are also relevant aspects. Moreover, in order to keep lead lithium at a maximum temperature for thermal efficiency purposes, while fulfilling the temperature specifications for the structural material, a thermal insulator is required. FCI can act as both thermal and electrical insulators.

- In the HCLL blanket, liquid metal flows at a very low velocity (< 1 mm/s), hence low MHD pressure drops are expected (except at complex geometries as manifolds and at fringing fields). However, buoyant predominance of the flow is predicted.

Other aspects not mentioned above but also relevant would include corrosion, tritium and helium transport, interfacial slip and electromagnetic coupling between channels.

In Chapter 4, main research on critical breeding blanket MHD related aspects is summarised.

4 State of Art

The field of Physics dealing with moving electrically conducting fluids under the influence of a magnetic field was first named *Hg-dynamics*, as suggested in the pioneering work of Hartmann (1937). In that work, based on an analytical study of a Hg laminar flow in an homogeneous magnetic field, three main results were obtained: (1) For electrically insulating walls, the velocity profile only depends on a dimensionless parameter that was later named Hartmann number (Ha); it was proved that within strong magnetic fields, the original parabolic flow profile was flattened as a consequence of the so called magnetic damping. (2) Velocity profiles depend on Ha and wall electrical conductivity. (3) A high magnetic field could relaminarise an initially turbulent hydrodynamic flow.

Since then, MHD research has included analytical, experimental, asymptotic and numerical studies. Its interest not only lays on fusion technology but also includes a wide range of applications. The application of which earlier references have been reported is electromagnetic pumping, what was first observed by Northrup (1907) and, then, studied by Hartmann (1937). Control techniques for metallurgical processing also benefit from MHD effects in the stabilisation of free surfaces and in the homogenisation of solidification or casting processes (with or without electromagnetic stirring). A summary of these techniques was given by Lielpeteris and Moreau (1989) and Kolesnichenko (1990). Magnetic fields can also be used to generate levitation confinement of either small droplets of sample (for material properties measurement, Egry *et al.* 2001) or large volumes of fluid (for extreme temperatures melting, Bojarevics *et al.* 2010). For MHD power generation, gaseous MHD is a promising alternative in terms of high electric conversion efficiency and low emissions (Sporn and Kantrowitz 1959, Steg and Sut-

ton 1960 and Tillack and Morley 1998). Other relevant MHD applications are magnetic levitation in trains (Tixador 1994) and seawater MHD propulsion (Graneau 1989 and Tixador 1994).

Five main MHD issues are relevant for fusion technology: (1) liquid metal MHD flows, (2) fluid-solid electrical coupling, (3) wall functions, (4) MHD turbulence, and (5) thermal MHD coupling. In section 4.1 just a brief summary of the state-of-the-art in the first four items is introduced, whereas main landmarks obtained in the coupling between liquid metal MHD and heat transfer are introduced in section 4.2. Extended reviews are included, when required, in parts II and III.

4.1 Review of LM MHD research

Numerical MHD analysis has been carried out following four different strategies (see Müller and Bühler 2001 for a detailed explanation):

1. Analytical analysis, limited to simple channel geometries. Solutions are typically series expansions difficult to evaluate at high Ha;

2. Asymptotic analysis which consider $Ha >> 1$ for fully developed stationary conditions;

3. Full system of equations (hydrodynamics plus electrodynamics equations) considering the bidirectional interaction between the fluid and the magnetic field by means of the induced magnetic field and the Lorentz force;

4. Low magnetic Reynolds number approximation or inductionless approximation, where the induced magnetic field is neglected.

In the asymptotic analysis the flow can be divided in different regions including: (i) the core flow, (ii) Hartmann boundary layers (at walls perpendicular to the magnetic field), (iii) side boundary layers (at walls parallel to the magnetic field), (iv) corner regions, and, (v) internal layers. The core solution is obtained by neglecting the viscous effects; thus, the obtained equation is a balance between pressure gradient and Lorentz force. Core solutions must match with other region solutions and boundary conditions must be fulfilled. Some relevant examples include the circular channel with fringing magnetic field of Reed *et al.* (1987) or the channel with a sudden expansion of Bühler *et al.* (2007). However, at flow conditions relevant for fusion technology, the asymptotic analysis is complex and requires some extra simplifications. Few works in this direction have been carried out as, for instance, Bühler (1998).

The full system of equations includes, apart from the Navier-Stokes equations, a vectorial transport equation for the magnetic field and a correction for the solenoidal nature of it, see Chapter 3 and section 5.1. Thus, the resulting system of equations is quite large and its resolution is time expensive. Since liquid metals at laboratory velocities always present a low magnetic Reynolds number ($Rm \sim 10^{-6}$), the inductionless approximation, also called quasi-static approximation, is a reasonable strategy in order to reduce the number of equations to be solved. Indeed, in the inductionless approximation, the induced magnetic field is neglected so that the coupling of the velocity and the magnetic field is simplified. A comparison of the inductionless approximation with the full set of governing equations, as applied to fully developed flows, can be found in Smolentsev and Tananaev (1994), where authors concluded that the induced magnetic field formulation (with the full set of governing equations) has a better convergence behaviour. An explanation for it could be the non conservation of the current density in the studied inductionless model. Indeed, the unique drawback of the inductionless approximation is the difficulty on conserving the current density, what is critical at high Hartmann numbers. In this direction, several strategies have been proposed. For instance, for incompressible MHD flows, Sterl (1990) proposed a numerical scheme for uniform rectangular staggered meshes, but it was limited to low Hartmann numbers and simple geometries. The scheme proposed by Leboucher (1999) for nonuniform rectangular staggered meshes was limited to simple geometries and unidirectional magnetic field. More recently several proposals have been published including, among others, the schemes used by di Piazza and Bühler (2000), Aleksandrova *et al.* (2002) and Mistrangelo (2006), for collocated meshes, although none of them is fully conservative regarding current density. A recent and very attractive proposal is the one by Ni *et al.* (2007) where an alternative for obtaining consistent and conservative schemes for non-structured meshes is exposed.

The cases analysed in liquid metal MHD using CFD codes are rather simple compared with standard hydrodynamic cases. More frequently, the cases are simple channels (Shercliff 1953, Hunt 1965, Ni *et al.* 2007), U-bends (Molokov *et al.* 1995), channels with obstacles (Dousset and Pothérat 2008), channel expansions (Mistrangelo 2006) and vortex generation or damping (Sommeria 1988). Despite their simplicity, all these cases are closely related to blanket simulations. For instance, channel expansions are present in the manifolds, U-bends exist all over the breeding unit, and channel obstacles are interesting as turbulence promoters in order to increase heat transfer.

4.1.1 Fluid-solid electrical coupling

According to what was already exposed by Hartmann (1937), the ratio between the electric conductivity of the walls and that of the fluid has a great influence on the flow. Thus, the electrical coupling of several side-by-side channels, with conducting walls between them, could give rise to the multi-channel effect (McCarthy and Abdou 1991, Molokov 1993). Such effect is expected to exist in the HCLL breeding blanket design and can alter considerably the channel flow. In order to take into account such fluid-solid-fluid interaction, wall can be modelled with some conservative assumptions at the interface (see section 5.2.5). Such multi-channel effect was studied by Mistrangelo and Bühler (2009) using the CFX code.

However, if no multi-channel effect or other fluid-solid interactions are expected to exist, an alternative to fully simulate the solid is the thin wall boundary condition from Walker (1981). Such boundary condition is widely used despite the fact that some problems at corner regions have been found (Temperley and Todd 1971, Walker 1981 and Tabeling 1982). A comparison of both strategies using OpenFOAM code is carried out by Mistrangelo (2010).

4.1.2 Wall functions

Electrically conducting fluids under the influence of a high magnetic field tend to develop a flat core velocity profile where boundary layers play an important role. Indeed, Hartmann boundary layers have a characteristic thickness $\sim a/Ha^{-1}$ and are responsible for the Joule and viscous dissipation. In contrast, side boundary layers have a characteristic thickness $\sim a/Ha^{-1/2}$ and, under certain conditions, they can carry the main part of the flow by means of jets parallel to the wall. Thus, mesh refinements in such boundary layers at high Ha is a quite expensive requirement.

In order to avoid such meshing, some wall functions for Hartmann boundary layers have been proposed. The most commonly used wall function was proposed by Walker (1981) and assumes a linear Hartmann boundary layer. It results in a modified version of the thin wall boundary condition. More complex wall functions that allow mass transfer across the boundary layers are the one from Hunt and Ludford (1968) and the one from Pothérat *et al.* (2002). These latter approaches are specially interesting for Bödewadt-Hartmann pumping cases (Davidson and Pothérat 2002).

4.1.3 MHD Turbulence

It is well known that flow regime moves from laminar to turbulent as Reynolds number (Re) increases. Turbulence has multiple definitions, but basically, it is typically related

with highly random, unsteady and three-dimensional fluid motion. However, in MHD flows, turbulence can be found in quasi two-dimensional (Q2D) flows. Whether the flow is Q2D or fully 3D depends on the ratio Re/Ha and on the wall electrical conductivity ratio (C_w). Typically, for perfectly insulated walls where $C_w = 0$, the critical (Re/Ha) ratio is $(Re/Ha)_{cr} = 300$ as stated by Smolentsev and Moreau (2007). Thus, for higher Reynolds, the flow is fully 3D and turbulent. Below the limit, the flow is laminar or Q2D turbulent. Flow in breeding blankets is expected to be below such limit.

Q2D turbulence is caused by eddy elongation along magnetic field lines. Thus, all three dimensional effects are confined in the thin Hartmann layers at the walls perpendicular to the magnetic field, where almost all Ohmic and viscous forces occur. For a detailed explanation, see Davidson (2001).

As in pure hydrodynamics, turbulence can be numerically studied by means of direct numerical simulations (DNS) or by the use of turbulence models. Such models can be classified as LES and RANS models. Few models have been developed related with high Ha and low Rm numbers. LES models have been applied to study homogeneous turbulence (with no wall effect); a recent review can be found in Knaepen and Moreau (2008). Among RANS models, several zero-equation models with anisotropic definition of the turbulent viscosity have been developed in order to asses Q2D turbulence, such as those from Smolentsev and Moreau (2006) for 2D MHD with internal shear layers, and from Cuevas *et al.* (1997) for 3D MHD (section 5.3); but zero-equation models, due to their nature, do not reproduce the internal turbulence structure. A more advanced one-equation model based on an extra turbulent kinetic energy equation is exposed by Smolentsev and Moreau (2007) for the 2D set of equations. Two-equation models for MHD turbulence are unknown to the author; however, some DNS simulations have been carried out by Smolentsev and Moreau (2006) in order to analyse the internal turbulence structure of the flow in a simplified channel. DNS simulations for the entire module are not affordable nowadays, and further research should be done in order to obtain more reliable Q2D turbulence models for blanket simulation.

It is worth mentioning that, following suggestions from Rodi (1993), MHD turbulence models should account for buoyancy effects as a function of the Richardson number, Ri, which is a ratio of the buoyant forces with the inertial forces, and can be expressed as $Ri = GrRe^{-2}$. However, no such model, applied to MHD turbulence, has been found by the author.

4.2 Review of buoyant MHD convection research

Buoyant MHD convection is a critical issue for the correct understanding of liquid metal flows under breeding blanket conditions. The eutectic PbLi in current BB designs is exposed to high Grashof numbers, typically in the range of $10^9 - 10^{12}$. In absence of a magnetic field, this Gr number would indicate that transitional flow and some instabilities could appear. However, when a transverse magnetic field is present, the core flow is dramatically damped and, depending on wall electric properties, jets can appear near the walls. This core damping has a re-laminarisation effect on the flow, increasing the critical Gr number.

Modelling magnetoconvective flow in the blanket is a complex issue and all efforts done in this direction so far imply some flow or geometry simplifications. In general, flow is assumed to be inductionless, the Boussinesq hypothesis is applied, and no Joule generation nor viscous dissipation is considered. Hereafter, main landmarks are exposed with special focus on the assumed flow conditions, being such conditions perfectly defined by dimensionless numbers (see section 3.3 for a detailed explanation of their meaning). Also, particular emphasis has been done related with volumetrically heated flows, as is the typical scenario in breeding blanket channels.

In Ozoe and Okada (1989) the effect of the magnetic field orientation on the natural convection was numerically analysed for three-dimensional cubical enclosures. Later, the same authors carried out the corresponding experimental study (Okada and Ozoe 1992).

Garandet *et al.* (1992) made an analytical study of a two-dimensional cavity with vertical magnetic field (parallel to gravity), considering both thermally insulated and conducting Hartmann walls, and a fixed horizontal temperature gradient. In both cases, a one-dimensional velocity profile in the core, linear at high Ha numbers, and the classical exponential profile in the Hartmann layer were obtained.

A high Ha number asymptotic analysis was made by Alboussière *et al.* (1996) considering the flow to be inertialess. Although the analysis considers the driving force to be independent of the fluid velocity, which is not valid for buoyancy flows, the study shows the relevance of the nature of electric symmetry along magnetic field lines on the magnitude of the velocity. Later, Bühler (1998) made an asymptotic analysis specifically for buoyant magnetohydrodynamic flows assuming that the flow remains laminar and the walls are electrically thin. The Peclet number ($Pe = PrGrHa^{-2}$) was considered sufficiently low to neglect inertia effects on energy balance. Moreover, the assumed high Interaction parameter (or Stuart number $N = Ha^2/Re$) allowed to consider the flow to be inertialess. In the study, high-velocity jets were observed for the first time along per-

fectly conducting side walls (parallel to the magnetic field). In this asymptotic analysis, and considering an imposed heat flux, the influence on the symmetry was highlighted. Bühler (1998) also studied the case of uniform volumetric heating, where Hartmann walls were adiabatic and heat was removed through side walls, which were considered at the same temperature. It was shown that, despite a uniform temperature along magnetic field lines exist, the flow may deviate considerably from two-dimensionality.

In di Piazza and Ciofalo (2002a) a differentially heated cavity with transverse magnetic field was studied with a steady 3D algorithm implemented in a CFD code. The fluid was considered to be lead lithium and Ha was in the range 10^2-10^3, wall conductivity ratio varied between 0 and ∞. Results show the existence of a complex three-dimensional flow with secondary motions. The suppression of convective motion as Ha or C_w increase was observed. The same authors studied numerically a volumetrically heated cubic enclosure with the same algorithm in di Piazza and Ciofalo (2002b). The fluid was considered to be lead-lithium and the study covered a range of Grashof numbers from 10^7 to 10^9, whereas Ha was between 10^2-10^3 and different wall conductivities were assumed. With the obtained high Peclet number and low Interaction parameter, it was necessary to take into account convective heat transfer and inertia effects on the momentum balance. In all studied cases, the magnetic damping was sufficient to stabilise the flow, despite the fact that secondary motions were still present. It was demonstrated that the critical Grashof number increases with Ha.

Following results by Bühler (1998), the existence of the high velocity jets at the side boundary layers was deeply investigated by Molokov and Bühler (2003), where it was stated that the amount of fluid carried by these jets at the side boundary layer is proportional to the electric potential gradient between the layer and the core. Under some temperature distributions, the electric current lines are tangential to all walls and thus the induced jets are reduced drastically.

Kharicha *et al.* (2004) studied numerically the transient buoyant convection of a lead-lithium filled cavity with non-uniform heat source. Since $0 < Pe \leq 1.07$, the convective term in momentum equation was neglected. In the case of a horizontal cavity, flow conditions were such ($Ha = 1 \cdot 10^4$–$2 \cdot 10^4$, $Gr \sim 5 \cdot 10^9$ and electrically conducting walls) that the magnetic damping was sufficient to stabilise the flow, and only a unique recirculation cell located at the hottest part of the cavity was obtained. Pressure driven buoyant duct flows were also studied where buoyant convection was found to be strong enough to generate some vortical patterns. In the same range of Ha and Gr but considering a high velocity pressure-driven flow as applied to the DCLL blanket, Vetcha *et al.* (2009) made a stability analysis with a 2.5D code based on a pseudo-spectral method. Due to the high Re, Q2D turbulence was assumed. Results indicate that, under DCLL

blanket conditions, all disturbances associated with Q2D turbulent buoyant flows in the front ducts will likely be damped by the strong toroidal magnetic field.

Thus, the presence of vortical structures is associated with a moderate electromagnetic damping, a moderate pressure-driven flow and a high buoyant force. In this direction, a non-inertialess flow with $0 \leq Ha \leq 10^4$, $Gr = 4 \cdot 10^7$ and electrically insulated walls was studied experimentally and numerically by Authié *et al.* (2003). The experimental setup consisted of a vertical enclosure with horizontal magnetic field, either perpendicular or parallel to the imposed temperature gradient. At $Ha \leq 800$ the fluid presented unsteady vortices aligned with the magnetic field lines, whose dimensions were about the channel width. The transient evolution of experimental Nusselt was analysed and compared with the numerical one considering laminar flow and quite coarse meshes.

Recently, several summaries of thermofluid MHD critical issues related to breeding blankets have been published: see for instance Reimann *et al.* (1995) for the self-cooled proposal, Reimann *et al.* (2006) for HCLL blanket design, and Smolentsev *et al.* (2008) for the US DCLL design. A recent summary on MHD thermofluid critical issues in blankets can be found in Smolentsev *et al.* (2010).

Part II

Development

This part is the core of the present dissertation as it covers all the studied strategies for MHD simulation under nuclear fusion conditions.

Nuclear fusion conditions, as applied to breeding blankets, include high magnetic field, high temperature gradient and thermal load, and, last but not least, tritium and helium breeding and transport. Other effects would include thermal and electromagnetic stresses on structures and corrosion.

This dissertation is focused on MHD and thermal effects, whereas tritium transport, when needed, is simplified to a transport of a passive scalar, with no helium interaction. Also, the thermal load is considered as known (but not necessarily constant in space or time), hence, no neutronic analysis is carried out. Despite such simplifications, the flow is quite complex and several modelling strategies can be considered. In this section, some MHD modelling strategies are first exposed and, afterwards, the chosen thermal MHD coupling described.

The proposed modelling strategies have been implemented in the OpenFOAM toolbox. Such tool has been chosen for several reasons: (1) leading developers have a long experience on CFD modelling so that the quality of the code can be assumed, (2) it is widely used and, hence, validated for a wide variety of cases, (3) it is open source, what means that the code is totally transparent and allows the introduction of code improvements and new developments, (4) it is currently being improved by a vast community, mainly supported by the official group SGI (http://www.openfoam.com/), but also by one of the original developers under Wikki Ltd. (http://www.wikki.co.uk/), and (5) feedback from leading developers can easily be obtained from the forum web site (http://www.cfd-online.com/Forums/openfoam/).

OpenFOAM (Field Operation And Manipulation) CFD Toolbox is a free, open source CFD software package. The code is an object oriented numerical simulation toolkit for continuum mechanics, written in C++. The toolkit implements operator-based implicit and explicit second and fourth-order Finite Volume discretisation in three dimensional space and on curved surface. More insight on code structure can be found in the official manuals and in Jasak (1996).

Details on code implementation and validation steps are exposed all along Chapters 5 and 6.

This part is to be understood as linked with Chapter 3, where the physical phenomena, the considered hypotheses or flow assumptions, and the resulting governing equations were exposed.

5 MHD modelling strategies

There are several approaches for modelling pure MHD. Here, only the three of them applied in the framework of this thesis are exposed. The section is split in three parts. In the first part the full set of equations 3.5 is considered, including implementation strategies and validation cases. In the second part, the reduced set of equations 3.7, corresponding to the low Magnetic Reynolds approximation, is studied. This part also includes an stability analysis, a wall function implementation, and the fluid-solid coupling strategy, along with validation cases. In the last part of this section, the 2D system of equations is introduced. This 2D approach, not mentioned in Chapter 3, is a result of CPU requirements for the application case presented in Chapter 8.

The different modelling approaches and validation steps are presented according to the chronological order in which they have been applied. Moreover, as these approaches were implemented and used in different stages of the development of the present thesis, there is some lack of uniformity in the presentation of the results (error estimation, analyses, etc.).

5.1 B-formulation

The B-formulation is based on the full set of equations 3.5 and, hence, it considers the bi-directional coupling between velocity and the magnetic field. The critical point is to enforce the solenoidal nature of the magnetic field ($\nabla \cdot \mathbf{B} = 0$). Although the initial magnetic field satisfies this constraint, multi-dimensional simulations do not guarantee it along time evolution. If $\nabla \cdot \mathbf{B} = 0$ is not guaranteed, the solution may incorporate

errors and, even worse, may become unstable. There are several strategies to deal with this problem (Tóth 1998):

1. Increase of spatial resolution. This is the simplest technique and consists of increasing the mesh resolution (i.e. reducing the grid size) until the magnetic field divergence becomes small enough for the solution to converge. This works only for stable schemes.

2. Non-conservative formulation. This technique consists of including in the momentum (3.5b) and magnetic field (3.5c) equations new non-conservative source terms. Such terms, proportional to $\nabla \cdot \mathbf{B}$, appear when equation 3.2a is not accounted for in the development of the final set of equations. These source terms should remain zero all along the simulation. As found by Powell (1994), the main advantage is that, if a 8-wave Riemann solver is used, the system remains stable. The error associated with $\nabla \cdot \mathbf{B}$ persists, but is small.

3. Vector potential formulation. The final set of equations can be rewritten in terms of the vector potential $\mathbf{A}$ ($\mathbf{B} = \nabla \times \mathbf{A}$); thus, the divergence free constrain is always satisfied. The disadvantage of this approach is that the order of spatial derivatives increases by one, which reduces the order of accuracy. With this formulation the equations are not in a conservative form, become complicated in 3D, and the boundary conditions on the vector potential may not be physically intuitive.

4. Constrained transport formulation. The original constrained transport method by Evans and Hawley (1988) offers a simple and efficient solution by using staggered grids for finite difference schemes. The magnetic field components are represented on the cell interfaces, whereas density, momentum and energy in the cell centres. In order to adapt this method to finite volume schemes, Tóth (2000) proposed a central differencing method.

5. Projection scheme. This method was proposed by Brackbill and Barnes (1980) as a correction to the magnetic field after the time step is completed, by some arbitrary numerical scheme. The name comes from the idea that the predicted magnetic field obtained at a time step can be projected to a divergence-free (new) magnetic field for the same time step.

Although high spatial resolution is needed in the process of assessment of numerical errors, it is of great interest that the developed code does not require fine meshes to be conservative; thus, the first method is not of interest. In OpenFOAM, all main variables are defined at cell centres so that, the constrained transport formulation is

not applicable. Therefore, if $\mathbf{B}$ is to be the main variable and the already implemented OpenFOAM solvers are to be used (for simplicity), the Projection method proposed by Brackbill and Barnes (1980) is the most adequate. Indeed, the Projection method is the one implemented in the official OpenFOAM version. This method is based on the decomposition of a vector field into the sum of a curl and a gradient:

$$\mathbf{B}^* = \nabla \times \mathbf{A} \; + \; \nabla\psi \tag{5.1}$$

where $\mathbf{B}^*$ is the predicted magnetic field, $\mathbf{A}$ is the vector potential and ψ is a scalar function. Taking the divergence of both sides, a Poisson equation for ψ is obtained:

$$\nabla^2\psi = \nabla \cdot \mathbf{B}^* \tag{5.2}$$

Thus, the predicted magnetic field needs to be corrected by:

$$\mathbf{B} = \mathbf{B}^* \; - \; \nabla\psi \tag{5.3}$$

To ensure that the obtained $\mathbf{B}$ is solenoidal, the Laplace operator in the ψ Poisson equation 5.2 must be evaluated in two steps, that is, as a divergence of the gradient ($\nabla^2\psi = \nabla \cdot (\nabla\psi)$). Thus, the divergence operator used in the Laplace operator must be the same as the one used for calculating $(\nabla \cdot \mathbf{B}^*)$ in 5.2 and, the gradient operator used in the Laplace operator must be equal to the one used for calculating $(\nabla\psi)$ in 5.3. Note that the correction on the magnetic field (equation 5.3) does not affect the current density $\mathbf{j} = \nabla \times \mathbf{B} = \nabla \times \mathbf{B}^*$.

The method implies an extra Poisson equation, but it can be efficiently solved with either direct or iterative solvers. It is also important to apply the boundary conditions to the corrected magnetic field and to choose good boundary conditions for the Poisson equation.

Next, the algorithm used to implement the B-formulation to OpenFOAM is described.

5.1.1 Algorithm 1: B-PISO

First of all, let's define a general transport equation for $\mathbf{v}$ as: $\mathbf{A_v}(\mathbf{v})\ \mathbf{v} = \mathbf{b_v}(\mathbf{v})$. Defining D and G as the divergence and gradient discrete operators respectively, the set of governing equations 3.5 can be written in discrete form for each grid node yielding:

$$D(\mathbf{v}) \; = \; 0 \tag{5.4a}$$

$$\underbrace{\frac{\partial \mathbf{v}}{\partial t} \; + \; D(\phi_v \mathbf{v}) \; - \; D(\nu G(\mathbf{v})) - D\left(\frac{\phi_B}{\rho \; \mu_m}\mathbf{B}\right) + G\left(\frac{\mathbf{B}^2}{2\rho \; \mu_m}\right)}_{\mathbf{A_v}(\mathbf{v}) \; \mathbf{v}} = \underbrace{- \, G\left(p/\rho\right)}_{\mathbf{b_v}(\mathbf{v})} \tag{5.4b}$$

$$\underbrace{\frac{\partial \mathbf{B}}{\partial t} \; + \; D(\phi_v \mathbf{B}) \; - \; D(\phi_B \mathbf{v}) - D\left(\frac{1}{\eta} G(\mathbf{B})\right)}_{\mathbf{A_B}(\mathbf{B}) \; \mathbf{B}} = \; 0 \tag{5.4c}$$

$$D(B) \; = \; 0 \tag{5.4d}$$

where, according to OpenFOAM notation, $\mathbf{S}_f$ is the face surface, $\phi_v = (\mathbf{v}_f \cdot \mathbf{S}_f)$, $\phi_B = (\mathbf{B}_f \cdot \mathbf{S}_f)$ and the subscript f indicates the interpolated value at control volume's face. Matrix $\mathbf{A_v}(\mathbf{v})$ can be split in diagonal terms $\mathbf{a_v}(\mathbf{v})$ and off-diagonal terms. A new matrix can be now defined as $\mathbf{H_v}(\mathbf{v}) = -(\mathbf{A_v}(\mathbf{v}) \; \mathbf{v} \; - \; \mathbf{a_v}(\mathbf{v}) \; \mathbf{v})$. Following this procedure, a new matrix $\mathbf{H_B}(\mathbf{B})$ is obtained for the magnetic field $\mathbf{B}$.

Continuity and momentum coupling is solved following the pressure-based PISO-like algorithm developed by Weller *et al.* (1998). Thus, the algorithm presented in this section is hereafter called $B - PISO$ algorithm. In pressure-based algorithms, continuity equation is manipulated by means of momentum equation to obtain a pressure equation. Here, momentum equation is used as a pre-conditioner for the velocity in order to improve the accuracy of the Laplacian solver for the pressure equation. Once the new pressure is obtained, the velocity is corrected. Very schematically, and using the above mentioned matrix notation, the MHD algorithm used for the full set of equations is listed in Algorithm 1. As can be seen, the Picard linearisation method has been used as well as the Jacobi pre-conditioner. This algorithm was already available in the official OpenFOAM version, except for the magnetic field correction step, that was implemented according to the Projection Method from Brackbill and Barnes (1980).

Another improvement with respect to the original algorithm has been the splitting of the magnetic field in $\mathbf{B_o}$, the externally applied magnetic filed, and b, the induced one. This allows the user to impose a fixed external magnetic field (that do not need to be constant in time and/or in space), which is the common practise in fusion technology applications. Thus, new boundary conditions can be used (equations 5.5 and 5.6, being $\mathbf{n}$ the surface normal unit vector), where the user needs to define the initial map for $\mathbf{Bo}$ and $\mathbf{b}$, and the $\mathbf{B}$ map is created as the sum of both, with $\mathbf{Bo}$-type boundary conditions.

$$\mathbf{B} = \mathbf{Bo} \qquad \text{electrically insulated wall} \tag{5.5}$$

$$\frac{\partial \mathbf{B}}{\partial \mathbf{n}} = 0 \qquad \text{perfectly conducting wall} \tag{5.6}$$

Algorithm 1 (B-PISO)

1. Initial map for $\mathbf{v}$*,* p*,* $\mathbf{B_o}$*,* $\mathbf{b}$ *and* ψ*. Evaluate* $\phi_v = (\mathbf{v}_f \& \mathbf{S}_f)$ *and* $\phi_B = (\mathbf{B}_f \& \mathbf{S}_f)$

2. Prepare momentum discrete coefficients (eq. 5.4b):

$$\mathbf{A_v}(\mathbf{v})\ \mathbf{v} \ \rightarrow\ \mathrm{fvm}::\mathrm{ddt}(\mathbf{v}) + \mathrm{fvm}::\mathrm{div}(\phi_v, \mathbf{v}) - \mathrm{fvm}::\mathrm{laplacian}(\nu, \mathbf{v}) - \mathrm{fvc}::\mathrm{div}(\phi_B, \mathbf{B}/(\rho\ \mu_m)) + \mathrm{fvc}::\mathrm{grad}(magSqr(\mathbf{B})/(2\rho\ \mu_m))$$

$$\mathbf{a_v}(\mathbf{v}) \ \rightarrow\ \mathrm{diag}(\mathbf{A_v}(\mathbf{v})) \qquad \mathbf{H_v}(\mathbf{v}) \ \rightarrow\ -(\mathbf{A_v}(\mathbf{v})\ \mathbf{v} - \mathbf{a_v}(\mathbf{v})\ \mathbf{v})$$

Solve momentum equation $\mathbf{A_v}(\mathbf{v})\ \mathbf{v} = -\mathrm{fvc}::\mathrm{grad}(p)/\rho$ *to get* $\mathbf{v}^*$

3. PISO loop, with a fixed number of iterations.

Velocity pre-conditioner: $\mathbf{v}' = \left(\frac{\mathbf{H_v}(\mathbf{v}^*)}{\mathbf{a_v}(\mathbf{v}^*)}\right)$, $\phi'_v = (\mathbf{v}'_f \& \mathbf{S}_f)$

Solve pressure equation (pEqn): $\mathrm{fvm}::\mathrm{laplacian}(\frac{1}{\mathbf{a_v}(\mathbf{v}')\ \rho}, p) = \mathrm{fvc}::\mathrm{div}(\phi'_v)$

Correct ϕ'_v *by means of the implicit terms* $\phi_v = (\phi_v)' - \mathrm{pEqn.flux}$

Solve continuity equation for error estimation: $\mathrm{fvc}::\mathrm{div}(\phi_v)$

Correct $\mathbf{v}'$ *and update boundary conditions* $\mathbf{v} = \mathbf{v}' - \frac{1}{\mathbf{a_v}(\mathbf{v}')\ \rho} * \mathrm{fvc}::\mathrm{grad}(p)$

4. Magnetic loop, with a fixed number of iterations.

Prepare magnetic field discrete coefficients (eq. 5.4c):

$$\mathbf{A_B}(\mathbf{B})\ \mathbf{B} \ \rightarrow\ \mathrm{fvm}::\mathrm{ddt}(\mathbf{B}) + \mathrm{fvm}::\mathrm{div}(\phi_v, \mathbf{B}) - \mathrm{fvc}::\mathrm{div}(\phi_B, \mathbf{v}) - \mathrm{fvm}::\mathrm{laplacian}(\tfrac{1}{\eta}, \mathbf{B})$$

$$\mathbf{a_B}(\mathbf{B}) \ \rightarrow\ \mathrm{diag}(\mathbf{A_B}(\mathbf{B}))\ \textit{and}\ \mathbf{H_B}(\mathbf{B}) = -(\mathbf{A_B}(\mathbf{B})\ \mathbf{B} - \mathbf{a_B}(\mathbf{B})\ \mathbf{B})$$

Solve magnetic field equation $\mathbf{A_B}(\mathbf{B})\ \mathbf{B} = 0$ *to get* $\mathbf{B}^*$

Solve ψ *equation (*ψ*Eqn):* $\mathrm{fvm}::\mathrm{laplacian}(\frac{1}{\mathbf{a_B}(\mathbf{B}*)}, \psi) = \mathrm{fvc}::\mathrm{div}(\phi'_B)$

Correct ϕ'_B *by means of the implicit terms* $\phi_B = (\phi_B)' - \psi\mathrm{Eqn.flux}$

Solve conservation of $\mathbf{B}$ *equation for error estimation:* $\mathrm{fvc}::\mathrm{div}(\phi_B)$

Correct $\mathbf{B}$ *and update boundary conditions* $\mathbf{B} = \mathbf{B} - \frac{1}{\mathbf{a_B}(\mathbf{B})} * \mathrm{fvc}::\mathrm{grad}(\psi)$

5. Next time step.

Determine the time step.

Return to step 2.

Note: OpenFOAM's notation has been used

Validation: Hartmann, Shercliff and Hunt cases

Three basic validation cases have been studied: Hartmann flow (Hartmann 1937), Shercliff case (Shercliff 1953) and Hunt's case (Hunt 1965). In all the simulations carried out in this section, time step has been fixed fulfilling the CFD constrain $\mathcal{C}$ (Courant *et al.* 1967) and the magnetic damping time $\tau = \frac{\rho}{\sigma_m B^2}$ constrain from Davidson (2001):

$$\mathcal{C} \leq 1\ (0.5 \text{ for 2D cases}) \qquad \text{and} \qquad \Delta t < \tau$$

All validation cases reach a steady state. Numerically, it has been considered that the steady state is reached when the variation in all variables (compared with values at previous time step) is less than 10^{-6}.

The equations have been solved by the (Bi-)Conjugate Gradient with incomplete-Cholesky pre-conditioner. In all the simulated cases, solver precision has been set to 10^{-8} for vectorial fields, whereas 10^{-9} has been set for scalar fields. Inner iterations through the PISO loop have been set to 3.

Hartmann flow

Hartman's flow is the basic 2D MHD case for code validation; it is found between two infinite parallel walls with a transverse constant magnetic field (in y direction). The imposed inlet flow is parallel to this walls (x direction) and has a parabolic profile. Walls are electrically insulated. The system is sketched in figure 5.1.

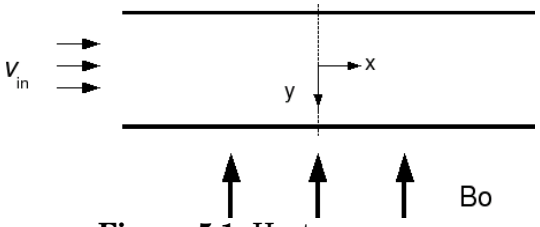

Figure 5.1: Hartmann case

The analytical solution is:

$$v = v_0 \frac{cosh(Ha) - cosh(Ha\ y/a)}{cosh(Ha) - sinh(Ha)/Ha}$$

For the simulation, a 2D mesh has been defined in the x-y plane; hence, the Hartmann boundary layers are included in the domain and need to be solved. Wall distance is $2a = 2$ m and the length is five times this distance. The initial mesh (mesh 1) has been defined with 100×40 nodes uniformly distributed.

The non-slip velocity boundary condition has been imposed at walls and a fixed uniform velocity of $v_{in} = v_o = 1$ m/s has been imposed at the inlet. At the outlet, developed velocity boundary conditions have been assumed. Fluid properties are such that, under the above mentioned flow conditions, $Re = 2$.

The Hartmann channel has been simulated for $Ha \in [0, 20]$. In figure 5.2 the velocity profile at the middle length of the channel is represented for each Ha number at steady state. It can be seen how, as Ha increases, maximum velocity is damped and, at the same time, Hartmann boundary layers develop. These Hartmann layers have a thickness of the order of ($a\ Ha^{-1}$), being a the half of the channel width.

In order to evaluate the mesh consistency of the algorithm, several meshes have

been used for $Ha = 20$, the resulting error is exposed in table 5.1, where the error has been evaluated according to equation 5.7, being v_{theory} the analytical velocity obtained from equation 5.7 and v the numerical solution. It can be seen that the error reduces drastically with the mesh density. In fact, in order to obtain $\epsilon < 1$, four nodes have been required at Hartmann boundary layer.

$$\epsilon = max\left(\frac{|v - v_{theory}|}{v_{theory}}\right) \cdot 100 \tag{5.7}$$

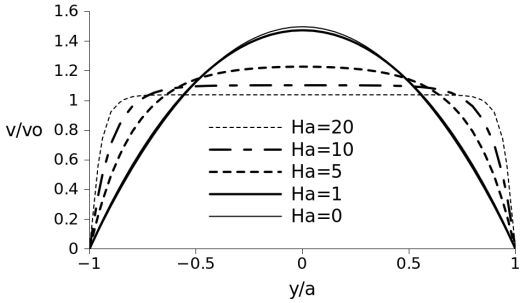

Figure 5.2: M-shaped profiles for different Ha

mesh	nodes	ϵ %
1	100 x 40	19.45
2	200 x 80	2.69
3	400 x 160	0.97

Table 5.1: Velocity error in Hartmann's case, as a function of the mesh for Ha=20. B-PISO algorithm.

Shercliff's case

In Shercliff (1953), the steady motion of an electrically conducting, viscous fluid along rectangular channels in the presence of an imposed magnetic field is analysed. The applied magnetic field is perpendicular to a pair of walls and all four walls are non-conducting ($C_w = 0$). To obtain the analytical solution, Shercliff presents the case where conditions are streamwise invariant (in the z-direction), excluding the pressure, what fits with developed flow conditions. For a case set up as that shown in figure 5.3 and a fixed pressure gradient, the analytical solution has been found and exposed in several works. Here, the corrected solution given by Ni *et al.* 2007 is shown, which is a reformulation for high Hartmann numbers of the solution presented by Hunt (1965) when all walls are perfectly insulated. The solution is:

$$v_z = \nu^{-1} V \left(-\frac{\partial p}{\partial z}\right) a^2 \tag{5.8}$$

$$V = \sum_{k=0}^{\infty} \frac{2(-1)^k cos(\alpha_k \xi)}{l\alpha_k^3} (1 - V_2 - V_3) \tag{5.9}$$

$$V_2 = \frac{\left(d_B\, r_{2k} + \frac{1-exp(-2r_{2k})}{1+exp(-2r_{2k})}\right) \frac{exp(-r_{1k}(1-\eta))+exp(-r_{1k}(1+\eta))}{2}}{\frac{1+exp(-2r_{1k})}{2} d_B N_k + \frac{1+exp(-2(r_{1k}+r_{2k}))}{1+exp(-2r_{2k})}} \tag{5.10}$$

$$V_3 = \frac{\left(d_B\, r_{1k} + \frac{1-exp(-2r_{1k})}{1+exp(-2r_{1k})}\right) \frac{exp(-r_{2k}(1-\eta))+exp(-r_{2k}(1+\eta))}{2}}{\frac{1+exp(-2r_{2k})}{2} d_B N_k + \frac{1+exp(-2(r_{1k}+r_{2k}))}{1+exp(-2r_{1k})}} \tag{5.11}$$

where the dimensionless coordinate along magnetic field lines is $\eta = x/a$ and the one perpendicular to it is $\xi = y/a$. $l = b/a$ is the aspect ratio, and $d_B = C_w = \sigma_w \delta_w/(\sigma a)$ is the Hartmann wall conductivity ratio, which, for Shercliff's case equals zero. Also:

$$\begin{aligned} N_k &= \left(Ha^2 + 4\alpha_k^2\right)^{1/2} \\ r_{1k}, r_{2k} &= \frac{1}{2}\left(\pm Ha + \left(Ha^2 + 4\alpha_k^2\right)^{1/2}\right) \\ \alpha_k &= \left(k + \frac{1}{2}\right)\frac{\pi}{l} \end{aligned}$$

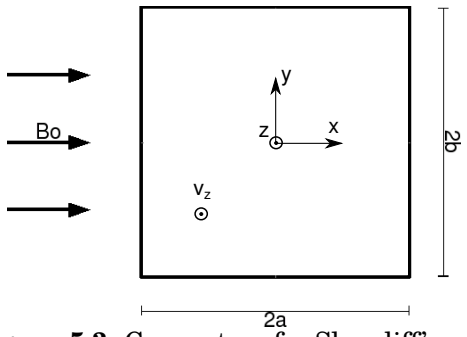

Figure 5.3: Case set up for Shercliff's case

Periodic boundary conditions have been implemented where a mean velocity is fixed by the user and the code evaluates the corresponding pressure drop. This strategy reduces drastically the number of points along channel axis and, hence, the computational time. Thus, a 3D mesh with only three nodes along z-axis is used.

In figure 5.4, the velocity and the induced magnetic field in z-direction have been plotted for $Ha = 1000$. At such a high Ha, the core velocity is flat and boundary layers very thin, specially Hartmann boundary layers.

The simulation results for different Ha and meshes have been tabulated in table 5.2. All meshes except the third one in table 5.2 (80×30 nodes for $Ha = 1000$) are defined so as to include four nodes at Hartmann boundary layer. The mesh concentration (conc. in table 5.2) refers to the ratio between the largest volume and the smallest one. The eighth and ninth columns of this table correspond to the velocity errors with respect to the analytical solution along one axis, i.e. ϵ_x represents the error along x axis. Since such errors are obtained at some fixed nodes not corresponding to real ones (as a post-process in OpenFOAM), the solution has been interpolated. Hence, the exposed errors also include interpolation errors that should decrease with mesh refinement. It can be

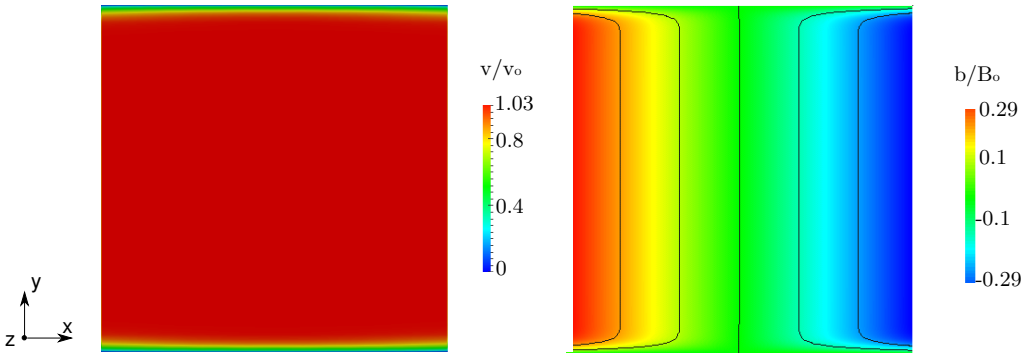

Figure 5.4: Results for Shercliff's case at $Ha = 10^3$ and $Re = 10$. Axial velocity profile (left), and axial induced magnetic field (right), B-PISO algorithm.

seen that, provided the Hartmann boundary layers are correctly modelled, the velocity error is kept below 2 %. When different meshes are used ($Ha = 10^3$), the error decreases drastically with mesh refinement.

Ha	Re	τ	mesh	conc.	$Ha^{-1/2}$	Ha^{-1}	ϵ_y %	ϵ_x %	δ_s/a	δ_{Ha}/a
100	9	0.100	40 x 40	10	0.1	0.01	1.6	0.6	0.4	0.07
300	10	0.035	80 x 40	100	0.058	0.003	0.9	0.1	0.2	0.01
1000	10	0.003	80 x 30	200	0.032	0.001	3.6	0.05	0.08	0.005
1000	10	0.003	160 x 60	200	0.032	0.001	0.5	0.01	0.08	0.005

Table 5.2: Main results for the Schercliff's case with B-PISO algorithm.

The resulting thickness of each boundary layer (δ_s and δ_{Ha}) is obtained approximately from results and can be compared with the theoretical values also exposed in table 5.2 ($Ha^{-1/2}$ and Ha^{-1}, respectively). It can be seen that, despite the low accuracy of the measured boundary layer thickness, the order of magnitude coincides with the theoretical one.

A detailed comparison of the simulated velocity profile at side boundary layers, compared with the analytical solution, is exposed in figure 5.5. Good accuracy can be observed.

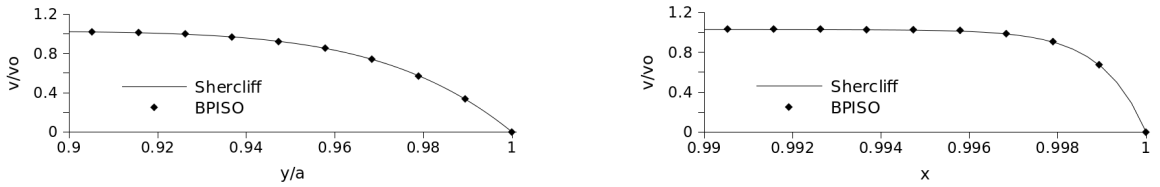

(a) (b)

Figure 5.5: Side layer (a) and Hartmann layer (b) axial velocity profiles for $Ha = 10^3$ and $Re = 10$. Comparison between numerical results and analytical solution for Shercliff's case, with B-PISO algorithm.

Hunt's case

In Hunt (1965) different wall conductivities were studied for a rectangular duct similar to that exposed in previous section. In case II of that article, Hartmann walls are conducting (with wall conductivity ratio from 0 to ∞) whereas side walls are perfectly insulated. The geometry and dimensions are the same as those for Shercliff's case. The particular case of perfectly conducting Hartmann walls, which is commonly called Hunt's case, is of great interest since it reproduces the so called M-shaped velocity profile with a flat core velocity and jets at side boundary layers (see section 3.4.1 for a detailed explanation). At high enough Ha, a reverse flow appears between the jet and the core flow; thus, Hunt's case provides an excellent set-up for code validation with a complex velocity profile.

As in the previous case, walls are non-slip and periodic boundary conditions are considered along the channel axis. The analytical resolution is the same as for Shercliff's case but with $d_B = C_{w,Ha} = \infty$. From numerical velocity profiles at different Ha, exposed in figure 5.6, it can be observed the dependency of the M-shaped profile with Hartmann. When jets appear at the side wall ($Ha \geq 100$), the core velocity is much smaller compared to the Shercliff's solution at the same Ha number, in fact, it takes values around $v/v_o = 10^{-2}$. In these cases, the difference between the theoretical solution and the simulated one is of the order of machine error and, hence, the relative velocity error is very difficult to reduce by mesh refinement (ϵ_y error in table 5.3). Therefore, to get an order of magnitude of the quality of the solution, the mean flow error (ϵ_v) has been calculated. To obtain this error, the pressure gradient computed by the code is used to calculate the theoretical mean velocity from the Hunt's solution (equation 5.8). The ϵ_v error, also called mean flow error, is the relative error between the computed mean mass flow and the theoretical one. In table 5.3 these results are listed for different Ha and meshes. It can be seen that the mean flow error is small enough to consider that accurate results are obtained. Note that the magnetic Reynolds number is kept always below 1. Some cases have been simulated with $Rm = 300$ and some conver-

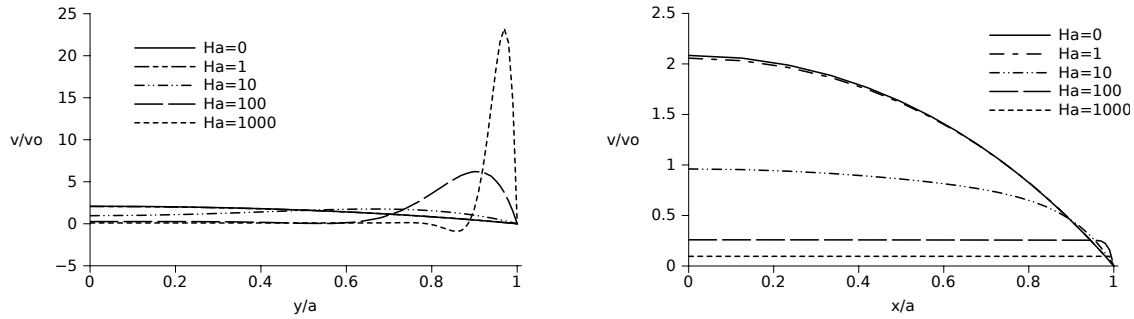

(a) (b)

Figure 5.6: Side layer (a) and Hartmann layer (b) axial velocity profiles for Hunt's case at different Ha and $Re = 10$, B-PISO algorithm.

Ha	Re	Rm	N	τ	mesh	conc.	ϵ_x %	ϵ_y %	ϵ_v %
0	10	0.01	0	∞	40 x 40	10 x 10	2.80	2.80	0.3
1	10	0.01	0.1	10^4	40 x 40	10 x 10	2.77	2.74	0.3
10	10	0.01	10	10^2	40 x 40	10 x 10	2.21	2.23	0.2
100	10	0.01	10^3	1	40 x 40	10 x 10	1.95	4449.23	0.6
1000	10	0.01	10^5	10^{-2}	40 x 40	10 x 10	21.09	332.68	4.2
1000	10	0.01	10^5	10^{-2}	60 x 60	200 x 100	0.17	255.91	1.6
1000	10	0.01	10^5	10^{-2}	60 x 80	200 x 200	0.48	198.26	1.6
1000	10	0.01	10^5	10^{-2}	60 x 120	200 x 200	0.21	78.22	1.5
1000	10	0.01	10^5	10^{-2}	80 x 140	100 x 400	0.22	72.65	1.5

Table 5.3: Main results for the Hunt's case with B-PISO algorithm.

gence problems have been experimented due to the bidirectional coupling between the velocity and the magnetic field.

5.2 ϕ-formulation

As mentioned in section 3.2.2, the final set of equations 3.7 obtained when the inductionless approximation is considered requires less computational time than the full set of equations solved by B-PISO algorithm. The main drawback is the need for an accurate electric current estimator that ensures current conservation. Here, the conservative strategy from Ni *et al.* (2007) is chosen.

In this section, two different algorithms are introduced (ϕ-FSPM and ϕ-PISO), being the unique difference between them the pressure-velocity coupling strategy.

5.2.1 Algorithm 2: ϕ-FSPM

The pressure.based algorithm proposed by Ni *et al.* (2007) follows a Four Step Projection Method. Thus, exactly the same algorithm has been implemented in OpenFOAM, resulting in Algorithm 2, hereafter called ϕ-FSPM. In this algorithm, the pressure gradient term in the momentum equation is neglected and the Lorentz force term in the same equation is explicit, for the velocity predictor estimation step. Then, the pressure equation is solved and the predicted velocity can be corrected. Afterwards, the electric potential equation is solved. Finally, the electric current and the Lorentz force are evaluated.

In order to conserve the electric current charge, Ni *et al.* (2007) proposed three alternatives. From those, the one applied here is the proposal based on a conservative formula of the Lorentz force. It first requires a consistent scheme for calculation of the current flux on cell faces. This step has been implemented following equation 5.13, where j_n stands for the cell surface orthogonal component of the current density flux, the subscript f indicates the interpolated value at control volume's face, $\mathbf{S}_f$ is the face surface of the control volume, and ∇_{sn} is a surface normal gradient that already includes non-orthogonal mesh corrections. Once j_n is obtained, the Lorentz force can be evaluated at cell centres following equation 5.14, where Ω_c is the cell volume and $\mathbf{C}$ is the cell centre.

$$\chi = (\sigma_f(\mathbf{v}_f \times \mathbf{B_o}_f)) \cdot S_f \tag{5.12}$$

$$j_n = -\sigma_f(\nabla_{sn}\phi) \cdot |\mathbf{S}_f| + \chi \tag{5.13}$$

$$\mathbf{j} \times \mathbf{B_o} = -\frac{1}{\Omega_c}\sum_f (j_n \cdot (\mathbf{B_o} \times \mathbf{C})_f) - \mathbf{C} \times \frac{1}{\Omega_c}\sum_f \left(j_n \cdot \mathbf{B_o}_f\right) \tag{5.14}$$

Returning to the original set of equations 3.7, and following the same strategy than for the B-PISO algorithm in section 5.1.1, the equations can be written in discrete form for each grid node, yielding:

$$D(\mathbf{v}) = 0 \tag{5.15a}$$

$$\underbrace{\frac{\partial \mathbf{v}}{\partial t} + D(\phi_v \mathbf{v}) - D(\nu G(\mathbf{v})) - (\mathbf{j} \times \mathbf{B_o})/\rho}_{\mathbf{A_v}(\mathbf{v})\ \mathbf{v}} = \underbrace{-G(p/\rho)}_{\mathbf{b_v}(\mathbf{v})} \tag{5.15b}$$

$$D(\sigma G(\phi)) = D(\sigma(\mathbf{v} \times \mathbf{B_o})) \tag{5.15c}$$

$$\mathbf{j} = \sigma(-G(\phi) + \mathbf{v} \times \mathbf{B_o}) \tag{5.15d}$$

where, D and G are the divergence and gradient discrete operators, respectively, and,

according to OpenFOAM notation, $\phi_v = (\mathbf{v}_f \cdot \mathbf{S}_f)$ is the face volumetric flux. As before, matrix $\mathbf{A_v}(\mathbf{v})$ can be split in diagonal terms $\mathbf{a_v}(\mathbf{v})$ and off-diagonal terms. A new matrix can be now defined as $\mathbf{H_v}(\mathbf{v}) = -(\mathbf{A_v}(\mathbf{v})\ \mathbf{v}\ -\ \mathbf{a_v}(\mathbf{v})\ \mathbf{v})$.

With the conservative constraints from Ni *et al.* (2007) (equations 5.13 and 5.14) and the above mentioned notation, Algorithm 2 is obtained.

Algorithm 2 (ϕ-FSPM)

1. Initial map for $\mathbf{v}$*,* p *and* ϕ*. Evaluate* ϕ_v *and Lorentz force.*

2. FSPM loop with a fixed number of iterations

2.1 Prepare momentum discrete coefficients (eq. 5.15b)

$\mathbf{A_v}(\mathbf{v})\ \mathbf{v}\ \rightarrow\ \mathrm{fvm::ddt}(\mathbf{v}) + \mathrm{fvm::div}(\phi_v, \mathbf{v}) - \mathrm{fvm::laplacian}(\nu, \mathbf{v}) - \frac{(\mathbf{j}\times\mathbf{B_o})}{\rho}$

$\mathbf{a_v}(\mathbf{v})\ \rightarrow\ \mathrm{diag}(\mathbf{A_v}(\mathbf{v}))$ $\qquad$ $\mathbf{H_v}(\mathbf{v})\ \rightarrow\ -(\mathbf{A_v}(\mathbf{v})\ \mathbf{v} - \mathbf{a_v}(\mathbf{v})\ \mathbf{v})$

Solve momentum equation $\quad \mathbf{A_v}(\mathbf{v})\ \mathbf{v} = 0 \quad$ *to get* $\mathbf{v}'$

Evaluate $\quad \phi'_f = \mathbf{v}'_f\ \&\mathbf{S}_f$

2.2. Solve pressure equation (pEqn): $\mathrm{fvm::laplacian}(\frac{1}{\mathbf{a_v}(\mathbf{v}')\ \rho}, p) = \mathrm{fvc::div}(\phi'_v)$

Correct ϕ'_v *by means of the implicit terms* $\quad \phi_v = \phi'_v - \mathrm{pEqn.flux}$

Solve continuity equation for error estimation: $\quad \mathrm{fvc::div}(\phi_v)$

Correct $\mathbf{v}'$ *and update boundary conditions* $\quad \mathbf{v} = \mathbf{v}'\ -\ \frac{1}{\mathbf{a_v}(\mathbf{v}')\ \rho} * \mathrm{fvc::grad}(p)$

2.3. Magnetic coupling:

Evaluate the magnetic flux term $\quad \chi = (\sigma_f * (\mathbf{v}_f \times \mathbf{B_o}_f))\&\mathbf{S}_f$

Solve electric potential equation: $\quad \mathrm{fvm::laplacian}(\sigma, \phi) = \mathrm{fvc::div}(\chi)$

Evaluate j_n *(eq. 5.13)*

Evaluate the Lorentz force (eq. 5.14)

Solve conservation of j_n *for error estimation:* $\quad \mathrm{fvc::div}(j_n)$

3. Next time step.

Determine the time step.

Return to step 2.

Note: OpenFOAM's notation has been used

When the electric potential is the main electromagnetic variable, the corresponding boundary conditions are:

$$\begin{array}{lll} \frac{\partial\phi}{\partial\mathbf{n}} = 0 & \text{electrically insulated wall} & (j_n = 0) \\ \phi = 0 & \text{perfectly conducting wall} & \left(\dfrac{\partial j_n}{\partial\mathbf{n}} = 0\right) \end{array}$$

where $\mathbf{n}$ stands for the surface normal unit vector.

Validation: Shercliff and Hunt cases

As suggested by Ni *et al.* (2007), the crank-Nicholson scheme is used; hence, the method is second order in time. The Central-Difference discretisation in space has been chosen. The equations have been solved by the (Bi-)Conjugate Gradient with incomplete-Cholesky pre-conditioner. Two different validation cases have been studied: (1) Shercliff's case, and (2) Hunt's case, both explained in section 5.1.1. Finally, a comparison with the B-PISO algorithm performance at coarse meshes is carried out.

In all simulated cases, solver precision has been set to 10^{-8} for velocity and 10^{-9} for pressure and electric potential. Inner iterations through the FSPM loop have been set to 3. And the steady state has been defined to have relative error between successive time steps below 10^{-7}.

Shercliff's case

Shercliff's case has been studied for $Ha = 100$ and $Re = 10$ ($N = 10^3$) in a rectangular channel (figure 5.3). Taking advantage of the developed flow profile, a 3D mesh with periodic inlet/outlet boundary conditions, based on a fixed mass flow rate and the corresponding pressure drop evaluation, is used; therefore, with only three nodes in the channel axis direction the flow is perfectly reproduced. Walls are defined as non-conducting imposing $\nabla_n \phi = 0$. Different meshes have been considered, as defined in table 5.4. The coarsest mesh, mesh 0, has already 7 nodes in Hartmann boundary layer; hence, all the meshes are fine enough to accurately capture the flow profile, as can be observed in figure 5.7.

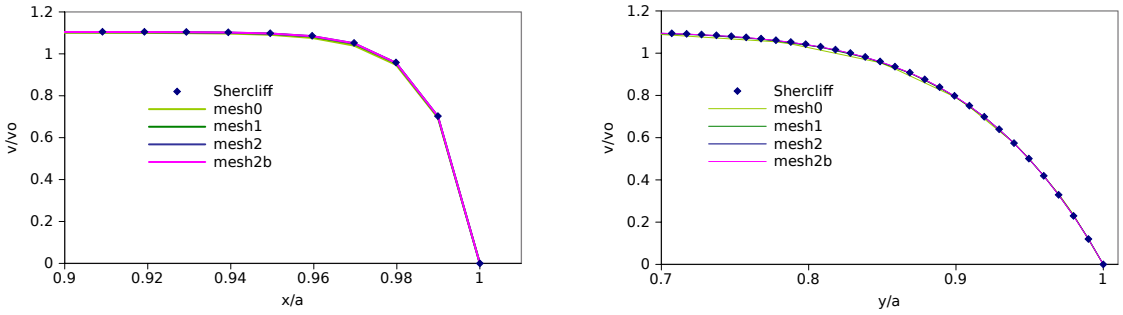

(a) (b)

Figure 5.7: Hartmann layer (a) and Side layer (b) axial velocity profiles for Shercliff's case at $Ha = 100$ and $Re = 10$, ϕ-FSPM algorithm.

Being v_o the mean flow velocity and Ω the studied domain, and the subscript th

indicating the theoretical value (according to equation 5.9), the errors exposed in table 5.4 can be defined as:

$$\begin{aligned} \epsilon_p &= 100 \cdot \frac{|\nabla p - \nabla p_{th}|}{\nabla p_{th}} \quad \% \\ \epsilon_v &= 100 \cdot mean\left(\frac{|v - v_{th}|}{v_o}\right) \quad \% \\ L_2(\Omega) &= \left(\int_\Omega \left(\frac{|v - v_{th}|}{v_o}\right)^2 dV\right)^2 \end{aligned}$$

$\nabla \cdot j_{ac}$ accounts for the accumulative electric current divergence, all along the simulation. Thus, results exposed in table 5.4 indicate that: (1) the electric current is not perfectly conserved at each time step in coarse meshes, despite the fact that the overall electric current is conserved all along the simulation (low $\nabla \cdot j_{ac}$ values), (2) mesh refinement reduces the non-conservation of electric currents, (3) for an accurate estimation of the pressure gradient (with an error below 1 %), more than 7 nodes at the Hartmann boundary layer are required, (4) the mean velocity error is very small, even at coarse meshes, and (5) the error decreases very fast with mesh refining at coarse meshes but not at fine ones. Finally, it can be said that the ϕ-FSPM algorithm has a good behaviour for Shercliff's case, with accurate results in reasonable meshes.

mesh	nodes	$\nabla \cdot j$	$\nabla \cdot j_{ac}$	ϵ_p %	ϵ_v %	$L_2(\Omega)$
0	40×20	$1.70 \cdot 10^{-5}$	$2 \cdot 10^{-19}$	1.83	0.36	$7.8 \cdot 10^{-3}$
1	80×40	$4.56 \cdot 10^{-6}$	$2 \cdot 10^{-20}$	0.57	0.15	$3.3 \cdot 10^{-3}$
2	160×80	$1.19 \cdot 10^{-6}$	$-3 \cdot 10^{-19}$	0.22	0.11	$2.2 \cdot 10^{-3}$
2a	160×160	$5.48 \cdot 10^{-7}$	$2 \cdot 10^{-9}$	0.20	0.10	$2.0 \cdot 10^{-3}$

Table 5.4: Simulation errors for Shercliff's case ($Ha = 100$, $Re = 10$) with ϕ-FSPM algorithm.

Hunt's case

Hunt's case has been studied for $Ha = 10^3$ and $Re = 700$ ($N = 1.43 \cdot 10^3$) in a rectangular channel (figure 5.3). Compared to Shercliff's validation test, the Hartmann number is substantially higher and, as a result, boundary layers are much thinner. As before, a 3D mesh with periodic inlet/outlet boundary conditions, based on a fixed mass flow rate and the corresponding pressure drop evaluation, is used. Side walls are defined to

be non-conducting ($\nabla_n \phi = 0$) whereas, at Hartmann walls, the boundary condition imposes $\phi = 0$. The studied meshes are defined in table 5.5. Compared with the simulated cases for Shercliff's case, these meshes are very coarse; for instance, mesh 3 includes only 4 nodes in Hartmann boundary layer. This results in very inaccurate flow profiles for mesh 0, as can be seen in figure 5.8. Such errors are quickly reduced with mesh

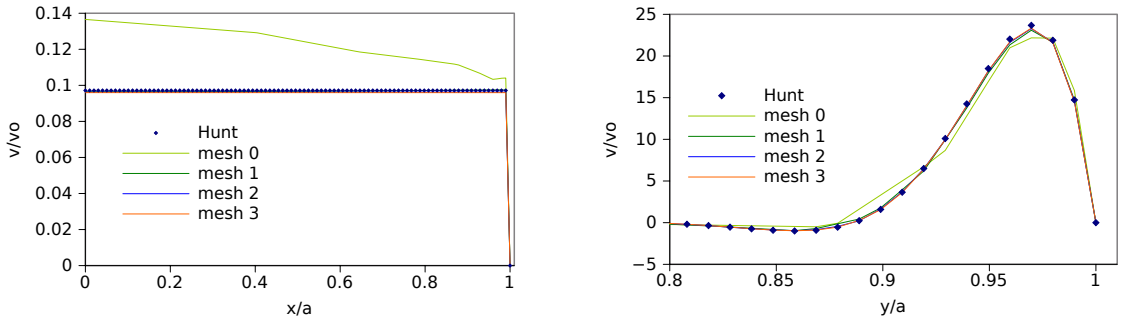

(a) (b)

Figure 5.8: Hartmann layer (a) and Side layer (b) axial velocity profiles for Hunt's case at $Ha = 10^3$ and $Re = 700$, ϕ-FSPM algorithm.

refinement, as shown in table 5.5. Here, the same error definition as in the previous validation has been used. From the velocity profile along side boundary layer, it can be stated that two critical points exist: (a) the peak of the jet, and (b) the recirculation zone. In order to quantify the accuracy in the peak zone, ϵ_{peak} has been defined, which corresponds to the relative velocity error just at the peak of the side boundary layer jet. As before, the error is reduced drastically in mesh 1. It can be stated that the algorithm provides accurate results also for Hunt's case, even at very coarse meshes. This is an interesting result since, for the simulation of the entire blanket, due to computational resources limitations, the simulated mesh might not be as fine as desired.

mesh	nodes	$\nabla \cdot j$	$\nabla \cdot j_{ac}$	ϵ_{peak} %	ϵ_v %	$L_2(\Omega)$
0	20×20	$4.14e-5$	$2.3e-9$	6.34	20.89	1.04
1	40×40	$7.79e-6$	$1.0e-9$	2.47	4.30	0.20
2	80×80	$1.75e-6$	$2.6e-9$	1.63	1.51	0.08
3	160×160	$3.01e-7$	$1.7e-10$	1.41	1.39	0.09

Table 5.5: Simulation errors for Hunt's case ($Ha = 10^3$, $Re = 700$) with ϕ-FSPM algorithm.

Comparison with B-PISO algorithm

Comparing ϵ_v results for Hunt's case at $Ha = 10^3$ in tables 5.3 and 5.5, with mesh 40×40 it can be predicted that both algorithms behave very similar. Assuming that the low magnetic Reynolds approximation is valid, and provided that the first order Euler temporal scheme is used, main difference between both algorithms is that B-PISO algorithm provides a better pressure-velocity coupling, based on PISO strategy.

Considering the first order temporal discretisation and the Central Difference spatial discretisation for both algorithms, a comparison of their behaviour for Shercliff's and Hunt's cases has been done. The chosen time step criterion follows the constraint in equation 5.19, according to the 1D monotone stability analysis described in section 5.2.2. In all cases, the (Bi-)Conjugate Gradient solver with the incomplete-Cholesky pre-conditioner has been used.

Shercliff's case

In table 5.6 the chosen meshes and simulation results for Shercliff's case with $Ha = 10^2$, $Re = 10$, $N = 10^3$ and $a = b$ are shown. In the table, N_{Ha} and N_{side} stand for the number of nodes on Hartmann and side boundary layers, respectively. It can be seen that ϕ-FSPM algorithm presents a better behaviour at very coarse meshes whereas B-PISO has a better accuracy improvement with mesh refinement. With very fine meshes, both results present almost the same error.

mesh	concentration	nodes	N_{Ha}	N_{side}	B-PISO ϵ_v %	ϕ-FSPM ϵ_v %
0	uniform	20×20	0.1	1	91.53	13.10
1	uniform	40×40	0.2	2	16.84	8.21
2	uniform	80×80	0.4	4	2.91	4.04
3	uniform	160×160	0.8	8	0.77	1.45
A	wall conc.	184×140	4	15	0.15	0.11

Table 5.6: Error comparison between B-PISO and ϕ-FSPM algorithms for Shercliff's case ($Ha = 10^2$, $Re = 10$).

In figure 5.9 the oscillating behaviour of B-PISO algorithm at very coarse meshes, linked with its needs of artificial numerical diffusion for such coarse meshes, is made explicit. Thus, it can be stated that B-PISO algorithm behaves as a high order scheme. In a detailed analysis of the results, where the diffusion term is compared with the

Lorentz force term in the momentum equation, it has been observed that at coarse meshes, both terms are not balanced. Thus, al alternative method for evaluating mesh quality could be based on the analysis of the balance between diffusion and Lorentz terms.

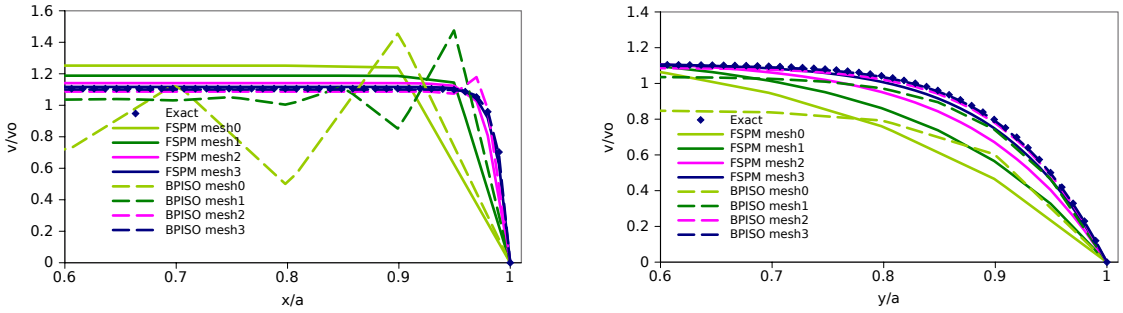

(a) (b)

Figure 5.9: Hartmann layer (a) and Side layer (b) axial velocity profiles for Shercliff's case at $Ha = 10^2$ and $Re = 10$, comparison for different meshes and both B-PISO and ϕ-FSPM algorithms.

Hunt's case

In table 5.7 the chosen meshes and simulation results for Hunt's case with $Ha = 10^3$, $Re = 10$, $N = 10^3$ and $a = b$ are shown. Like in Shercliff's case, the error is substantially lower for the ϕ-FSPM algorithm at coarse meshes. Also, according to figure 5.10, oscillations appear at very coarse meshes for B-PISO algorithm.

mesh	concentration	nodes	N_{Ha}	N_{side}	B-PISO, ϵ_v %	ϕ-FSPM, ϵ_v %
2	uniform	80×80	0.08	2.5	30.08	17.26
3	uniform	160×160	0.16	5.1	7.67	5.21
A	wall conc.	240×336	4	7.9	–	1.70

Table 5.7: Error comparison between B-PISO and ϕ-FSPM algorithms for Hunt's case ($Ha = 10^3$, $Re = 10$).

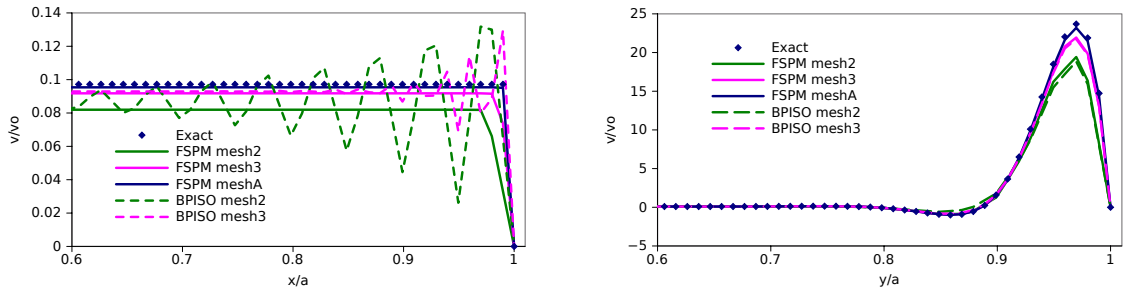

(a) (b)

Figure 5.10: Hartmann layer (a) and Side layer (b) axial velocity profiles for Hunt's case at $Ha = 10^3$ and $Re = 10$. Comparison for different meshes and both B-PISO and ϕ-FSPM algorithms.

Conclusions

To conclude, ϕ-FSPM algorithm has better time requirements (lower CPU costs) for each iteration and has better convergence with very fine meshes. In contrast, B-PISO algorithm needs less inner iterations and, thus, finds the steady state faster, but behaves as a high order scheme, hence, presents oscillations near a discontinuity.

Thus, a combination of both algorithms is desired. Such combination is exposed in section 5.2.5.

5.2.2 Stability Analysis 1: Monotone scheme

According to Patankar (1980), the most simple stability analysis of a numerical scheme applied to a given transport equation is based on imposing that all coefficients in the discrete equation have the same sign.

The 1D linearised momentum equation 3.7b, applying the Central Difference scheme in space and the first order Euler (explicit) in time, can be expressed as:

$$\frac{\partial \mathbf{v}}{\partial t} + (\mathbf{v}\cdot\nabla)\mathbf{v} = -\frac{\nabla p}{\rho} + \nu\nabla^2\mathbf{v} + \frac{\mathbf{j}\times\mathbf{B_o}}{\rho}$$
$$a_i v_i = a_i^0 v_i + a_{i+1}^0 v_{i+1} + a_{i-1}^0 v_{i-1} + b_i$$

where, given a control volume of a one-dimensional mesh, the central node corresponds to subscript i whereas the east and west nodes to subscripts $(i+1)$ and $(i-1)$ respectively. Superscript '0' stands for previous time step. The explicit Lorentz force term has been simplified to vB_o^2 according to Leboucher (1999), what implies that the main flow direction is perpendicular to the externally applied magnetic field. For a fixed time step

Δt and a uniform mesh spaced as Δx, the coefficients are:

$$\begin{aligned} a_i &= 1 \\ a_i^0 &= 1 - \frac{\sigma B_o^2 \Delta t}{\rho} - \frac{2\nu\Delta t}{(\Delta x)^2} \\ a_{i+1}^0 &= -\frac{v_o \Delta t}{2\Delta x} + \frac{\nu \Delta t}{(\Delta x)^2} \\ a_{i-1}^0 &= \frac{v_o \Delta t}{2\Delta x} + \frac{\nu \Delta t}{(\Delta x)^2} \end{aligned}$$

Thus, if all the coefficients are to have the same sign, two constrains for stability are obtained:

$$\begin{aligned} \mathcal{L} + \mathcal{D} &\leq 1 \\ \mathcal{C}/\mathcal{D} &\leq 1 \end{aligned}$$

where $\mathcal{C}$, $\mathcal{D}$ and $\mathcal{L}$ are defined in 5.17. Note that the second constrain is typical (Patankar 1980) for Central Difference scheme and corresponds to a grid Peclet number lower than 2. Note also that $\mathcal{L} = N\mathcal{C}$, where N is the interaction parameter.

$$\mathcal{C} = \frac{v_o \Delta t}{\Delta x} \tag{5.17a}$$

$$\mathcal{D} = \frac{2\nu\Delta t}{(\Delta x)^2} \tag{5.17b}$$

$$\mathcal{L} = \frac{\sigma B_o^2 \Delta t}{\rho} = N\mathcal{C} \tag{5.17c}$$

Combining both mentioned constrains would yield to:

$$\mathcal{C} + \mathcal{L} \leq \mathcal{L} + \mathcal{D} \leq 1 \tag{5.18}$$

This double constrain has been simplified to equation 5.19, which is the constrain implemented in the ϕ-FSPM algorithm and tested hereafter. It has to be mentioned that, since the temporal scheme is not explicit but implicit except for the Lorentz force term, this constrain is useful in terms of accuracy but is not needed in terms of stability. In cases where the diffusion is not relevant (laminar cases), $\mathcal{D}$ can be neglected from equation 5.19.

$$\mathcal{C} + \mathcal{L} + \mathcal{D} \leq 1 \tag{5.19}$$

Sensitivity analysis on time step criterion

Considering Hunt's case at $Ha = 10^3$ and $Re = 700$, and assuming laminar flow, a sensitivity analysis on time step criterion is performed. Since the final flow is two-dimensional, results obtained by the monotone stability analysis should be modified accordingly. In pure hydrodynamical flows, it is widely accepted that the 1D constrain $\mathcal{C} \leq 1$ should be reduced to $\mathcal{C} \leq 0.5$ for 2D flows and $\mathcal{C} \leq 0.2$ for 3D flows (these values are suitable for uniform meshes). The same effect is expected to be found for the MHD case.

For pure hydrodynamic cases, the diffusive contribution to the accuracy constrain ($\mathcal{D}$) is often neglected. Following such strategy, several ($\mathcal{C}+\mathcal{L}$) values have been studied and compared with a simulation that fulfils the theoretical 2D constrain ($\mathcal{C} + \mathcal{L} + \mathcal{D} \leq 0.5$).

To carry out such analysis, a fully 3D mesh is required with a fixed velocity at the inlet, otherwise the periodic inlet/outlet boundary condition could alter the transient behaviour of the flow. The channel dimensions are $2a \times 2a \times L$, where $L = 10a$. A fixed 3D mesh of $60 \times 40 \times 50$ nodes (x-y-z) has been used, with a high concentration towards Hartmann walls (of factor 100), a low concentration towards side walls (factor 10) and uniform along channel axis. The results with this mesh, according to parameters shown in table 5.5, are expected to be accurate since Hartmann layers are meshed into 12 nodes. For the transient analysis, an initial map corresponding to developed hydrodynamic flow with a fixed mass flux at the inlet is imposed. The total pressure at the outlet has been fixed.

In table 5.8 results for different time steps are shown. In the table, τ_{steady} stands for the total time required to reach the steady state (defined as a maximum relative variation of the velocity of 10^{-7}). The electric current is conserved in all the cases and the L_2 norm error along each axis is minimised for $\mathcal{C} + \mathcal{L} = 0.2$ (which is a typical value for 3D cases), what indicates the three-dimensional nature of the flow due to the entrance effect, despite the length of the channel. The velocity profiles, exposed

$\mathcal{C}+\mathcal{L}$	Δt (s)	τ_{steady} (s)	$\nabla \cdot j$	$\nabla \cdot j_{ac}$	$L_2(x)$	$L_2(y)$
0.2	0.4	531.176	$3.5e-5$	$3e-9$	0.19	0.40
0.5	1	530.714	$7.6e-5$	$3e-9$	0.34	0.82
1	2	531.429	$1.4e-4$	$4e-9$	0.54	1.50
2	3.33	541.667	$1.6e-4$	$4e-9$	0.60	1.71

Table 5.8: Transient behaviour of ϕ-FSPM algorithm, for Hunt's case ($Ha = 10^3$, $Re = 700$).

in figure 5.11, make explicit the above mentioned minimisation of the L_2 norm errors when $\mathcal{C} + \mathcal{L} = 0.2$. This figure also features the results for the case where the full constrain including the diffusion term (equation 5.18 extrapolated to a 2D case) is taken into account, which implies an even smaller time step. It can be seen that, with the latter time step, both the numerical and analytical solutions match. Therefore, the diffusive contribution to the accuracy constrain should not be omitted.

In figure 5.12(a), the temporal evolution of the error is plotted, showing the good convergence of the algorithm and the inaccuracy of the results when $\mathcal{C} + \mathcal{L} = 2$. This is a relevant result since it indicates that, although stability is guaranteed, the time step criterion can alter substantially the accuracy of the numerical result. In figure 5.12(b) it can be seen that a relatively large number of inner iterations (20) is required at the first stage of the transient simulation whereas at an advanced time only 2-3 inner iterations are needed to converge.

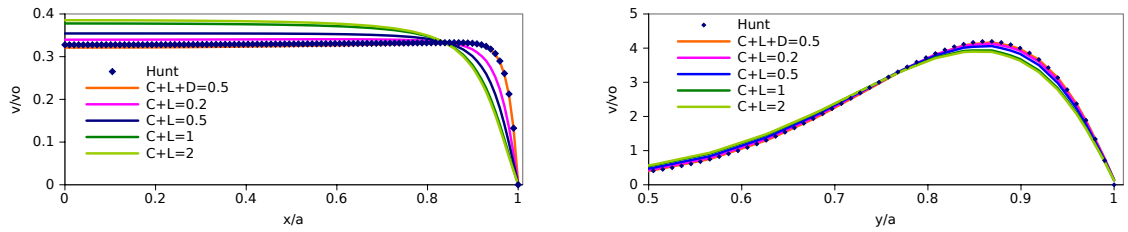

(a) (b)

Figure 5.11: Hartmann layer (a) and side layer (b) axial velocity profiles for Hunt's case at $Ha = 10^3$ for different time step criterion, ϕ-FSPM algorithm.

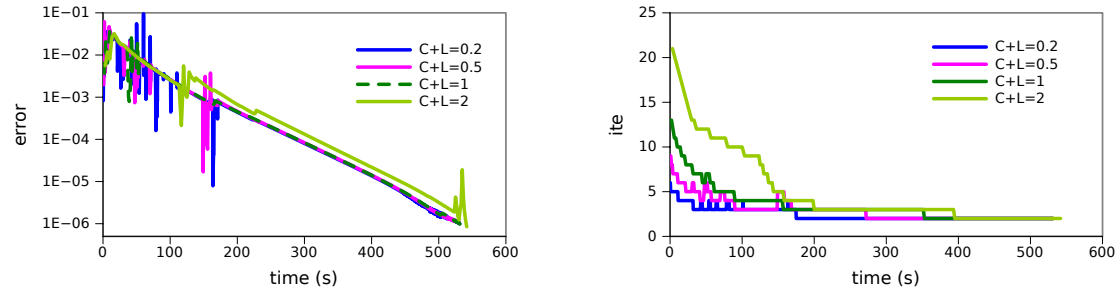

(a) (b)

Figure 5.12: Error evolution with time (a) and inner iteration evolution with time (b) for Hunt's case at $Ha = 10^3$ for different time step criterion ($\mathcal{C} + \mathcal{L}$), ϕ-FSPM algorithm.

It is worth mentioning that the inaccuracy of results is strongly affected by non-uniformity of the mesh. Indeed, for a uniform mesh, when the time step constrain is met in one control volume, it is met in the entire domain. This is not the case of non-uniform meshes, where the most restrictive cell (usually the smallest one) is the one that fixes the time step; with that time step, numerical diffusion in all other cells is expected to exist. If a uniform time step is used over the entire domain (as is the present case), the diffusion problem cannot be avoided.

5.2.3 Stability Analysis 2: von Neumann analysis

A von Neumann stability analysis of a linearised momentum equation can be easily performed in order to obtain an order of magnitude of the time step required by the algorithm in a more accurate manner than with the monotonic scheme exposed in section 5.2.2. Such analysis, hereafter exposed, has been performed with Maple software.

The von Neumann stability analysis, described in many books, e.g. Leveque (2002) and Hoffman (2001), consists on finding the so called amplification factor A for the Fourier Transformation of the momentum equation (equation 5.20, where U, k, Δx and Δt are the discrete velocity, the wave number, the mesh size and the time step, respectively) and calculating the required constraints in order to fulfil $|A| \leq 1$, which is a sufficient condition for stability.

$$U^{n+1}(k) = A(k, \Delta x, \Delta t) U^n(k) \tag{5.20}$$

Regarding to ϕ-formulation algorithms (ϕ-FSPM in section 5.2.1 and ϕ-PISO in section 5.2.5), the aim is analysing the stability of the momentum equation where all terms except the Lorentz force term are treated implicitly and the Central Difference scheme is used for both advection and diffusion terms. In a first approach, and in order to decouple momentum from continuity and temperature equations, pressure gradient and buoyancy terms are omitted from momentum equation. Moreover, the system is considered 1D and the grid uniform. Under this discretisation, the discrete momentum equation is:

$$U_i^{n+1} - U_i^n + \frac{\mathcal{C}}{2}\left(U_{i+1}^{n+1} - {}_{i-1}^{n+1}\right) = \frac{\mathcal{D}}{2}\left(U_{i+1}^{n+1} - 2U_i^{n+1} + U_{i-1}^{n+1}\right) - \mathcal{L}U_i^n \tag{5.21}$$

where $\mathcal{C}$, $\mathcal{D}$ and $\mathcal{L}$ are $\frac{v\ \Delta t}{\Delta x}$, $\frac{2\nu\ \Delta t}{\Delta x^2}$ and $\frac{\sigma\ B_0^2\ \Delta t}{\rho}$ respectively (defined in equations 5.17). Subscript indicates the grid position whereas superscript indicates the time step.

The obtained amplification factor is:

$$A = \frac{(2-2\mathcal{L})\,(2-2\mathcal{D}cos(k\Delta x)+2\mathcal{D})}{(2-2\mathcal{D}cos(k\Delta x)+2\mathcal{D})^2+4\mathcal{C}^2sin(k\Delta x)^2} - i\,\frac{2\,(2-2\mathcal{L})\,\mathcal{C}sin(k\Delta x)}{(2-2\mathcal{D}cos(k\Delta x)+2\mathcal{D})^2+4\mathcal{C}^2sin(k\Delta x)^2}$$

Since $(|A|)^2 \leq 1$ is a condition for stability, for the sake of simplicity $(|A|)^2$ is evaluated, yielding:

$$(|A|)^2 = \frac{(\mathcal{L}-1)^2}{1+\mathcal{D}^2cos(k\Delta x)^2-2\mathcal{D}cos(k\Delta x)-2\mathcal{D}^2cos(k\Delta x)+2\mathcal{D}+\mathcal{D}^2+\mathcal{C}^2-\mathcal{C}^2cos(k\Delta x)^2}$$

It can be easily seen that for $k\Delta x = 0$ the constrain $\mathcal{L} \leq 2$ is already obtained, but with the special case $\mathcal{L} = 1 \;\rightarrow\; A = 0$. The same analysis for other $k\Delta x$ factors does not provide any extra information because the obtained constrains are always fulfilled.

When looking for maxima or minima of $(|A|)^2$, three different solutions for $k\Delta x$ are obtained. The first solution is the already mentioned $k\Delta x = 0$ and the other two solutions:

$$arctan\left(\pm\,\frac{\left(-\mathcal{D}^2-2\mathcal{D}^2\mathcal{C}^2+\mathcal{C}^4-2\mathcal{D}^3\right)^{1/2}}{-\mathcal{D}^2+\mathcal{C}^2}\;,\;\frac{-\mathcal{D}^2-\mathcal{D}}{-\mathcal{D}^2+\mathcal{C}^2}\right)$$

If $(|A|)^2$ is evaluated for these latter solutions, the stability condition results in:

$$\frac{\left(\mathcal{C}^2-\mathcal{D}^2\right)(\mathcal{L}-1)^2}{\mathcal{C}^2\,(2\mathcal{D}+\mathcal{C}^2+1)} < 1$$

Hence, it can be stated that the 1D linear momentum equation discretised by an implicit scheme except for the Lorentz force term, and using the Central Difference scheme (equation 5.21) is stable provided that $\mathcal{L} \leq 2$ (with the exception of $\mathcal{L} = 1$), is never perfectly accurate and implies a phase error of:

$$\phi = arctan\left(\frac{\Im(A)}{\Re(A)}\right) = arctan\left(\frac{\mathcal{C}sin(k\Delta x)}{-1+(cos(k\Delta x)-1)\,\mathcal{D}}\right)$$

The above mentioned result can be also observed in figure 5.13, where the locus of the amplification factor, as a function of $\mathcal{L}$, $\mathcal{C}$ and $\mathcal{D}$ numbers is represented. It can be proved that even with high values of $\mathcal{C}$ and $\mathcal{D}$, the solution is still stable provided $\mathcal{L} \leq 2$ (with the exception of $\mathcal{L} = 1$, which gives $A = 0$).

When no magnetic field is applied, the classical convection-diffusion equation is obtained and the scheme becomes unconditionally stable, as was also stated in Hoffman (2001).

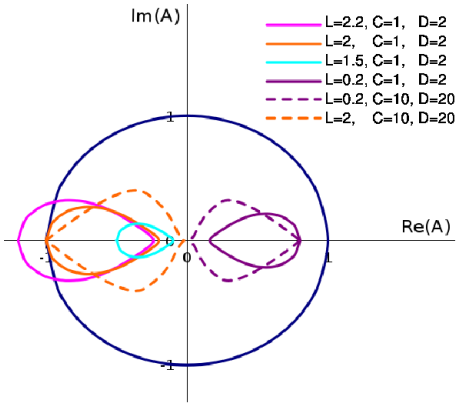

Figure 5.13: Locus of the amplification factor A

5.2.4 Wall function

The efficiency of Direct Numerical Simulations (DNS) of MHD duct flows under intense magnetic fields mainly depends on how the flow inside the very thin Hartmann layers is addressed. In order to avoid computing the flow inside these layers, specific boundary conditions at the interface between the bulk flow and the Hartmann layers relying on analytical functions (wall functions) can be used. The implementation of such wall functions in OpenFOAM in the framework of the present thesis was deemed necessary, regarding the CPU time limitations of the thermal-hydraulics group at the UPC. To this aim, a short stay at Coventry University, with Alban Pothérat and Vincent Dousset as hosts, was carried out. The wall function implementation could be efficiently carried out because both groups (at Coventry University and at UPC) were already developing MHD tools in OpenFOAM.

Wall functions rely on Taylor expansions of the flow quantities with respect to the flow parameters Ha and N. The wall function implemented in the short stay was the one proposed by Walker (1981). This wall function neglects terms of order $(1/Ha)$. In this approximation, the normal velocity at the interface between the Hartmann layers and the bulk flow is neglected because this velocity is of order $1/Ha$. So, no fluid exchange is allowed at this interface. This wall function will be referred to as *linear wall function*.

The linear wall function has been implemented as described in Leboucher (1999) and Muck *et al.* (2000). It basically consists of a Neumann-type boundary condition of the form represented in equation 5.22 which has to be solved implicitly. Hence, for each time step a new internal loop has to be built where the electric potential and its boundary condition have to be solved. The slip boundary condition is used for velocity.

$$\nabla_n \phi \;=\; -(aC_w + \delta_{Ha})\, \nabla^2_{\perp} \phi \tag{5.22}$$

The l.h.s. in equation (5.22) is the Neumann-type (fixed gradient) boundary condition that has to equal the r.h.s. obtained from the results of solving the electric potential equation (3.7c). The subscript n represents the wall normal direction whereas $\perp$ includes both wall parallel directions in a 3D frame. So, if $n = x$ then $\nabla^2_\perp \phi = \frac{\partial \phi^2}{\partial y\, \partial y} + \frac{\partial \phi^2}{\partial z\, \partial z}$. The coefficient $(aC_w + \delta_{Ha})$ is the sum of the wall conductivity ratio ($C_w = (\sigma_w\ \delta_w)/(\sigma a)$) and the boundary layer thickness ($\delta_{Ha} = a/Ha$), where a is half of the dimension parallel to the magnetic field.

Hence, once the linear wall function has been implemented, the new algorithm is already able to deal with walls with finite and nonzero conductivity, which is a very useful code improvement in order to be able to simulate more real cases. However, some problems have been observed by the author at high C_w in corner regions that make such wall function unsuitable for its use as a solid wall emulator. Recently, Mistrangelo (2010) has proposed a new solid emulator with OpenFOAM code by solving a 2D ϕ equation for the wall surface and coupling it with the 3D ϕ equation at the fluid region.

Validation: Shercliff's case

The implemented linear wall function has been validated with Shercliff's case (Shercliff 1953) already described in section 5.1.1. The case set up is represented in figure 5.3 and the analytical solution is obtained from equation 5.9. In this case $b = 2a$.

First, a mesh influence analysis has been carried out for $Ha = 50$ and imposing a pressure gradient of $d(p/\rho)/dz$=1.6 Pa/m in equation 5.8, what corresponds to $Re = 46.3$ and $N = 54$. The Hartmann boundary layer depth has been set to $\delta_{Ha} = a/Ha$. Four different meshes have been studied, as listed in table 5.9. The finest one corresponds to a DNS mesh and, thus, has been used without wall function. Meshes 0, 1 and 2 are coarser meshes that need wall functions. In fact, mesh 2 equals the DNS mesh except at Hartmann boundary layers.

In table 5.9, N_{side} corresponds to the number of nodes in side boundary layers (of depth $a/Ha^{1/2}$), ϵ_m stands for the relative mass flux error, and ϵ_x and ϵ_y are the relative velocity errors along x or y axis, respectively. Velocity profiles of the simulated cases are shown in figure 5.14. Note that ϵ_m is evaluated here instead of the pressure gradient error (as was done in previous validation cases); this is because the periodic boundary condition used here is defined so that a pressure gradient is imposed instead of an inlet mean velocity. The boundary condition, consequently, evaluates the mass flux.

Obviously, the relative velocity error along x axis (along magnetic field lines) is substantially larger when the wall function is used, since Hartmann boundary layers are not simulated. However, both ϵ_m and ϵ_y are lower when the linear wall function is used with mesh 2. Moreover, the computational time (CPU time in table 5.9) is drastically

mesh	nodes	N_{side}	ϵ_m %	ϵ_y%	ϵ_x%	CPU time
Full DNS	26×80	30	0.67	1.19	3.27	3h 53'
2	16×80	30	0.41	0.55	57.86	2h 12'
1	16×52	20	0.30	1.28	57.86	42'
0	8×40	15	0.51	4.77	57.86	5'

Table 5.9: Simulation results of ϕ-FSPM algorithm with linear Wall Function for Shercliff's case ($Ha = 50$, $N = 54$).

reduced, as the reduction in mesh nodes is predominant over the extra time required for the boundary condition inner iterations. It can be stated that, for a fixed Ha and N, the mesh can be coarsened without any substantial loss of accuracy and with a great improvement on the CPU time. Indeed, comparing DNS mesh with mesh 0, the mesh has been coarsened by a factor of 0.15 but the reduction on the mass flow accuracy has been 0.24 % whereas the time reduction has been more than 98 %, what means a reduction time from almost 4 hours to 5 minutes. These are very promising results.

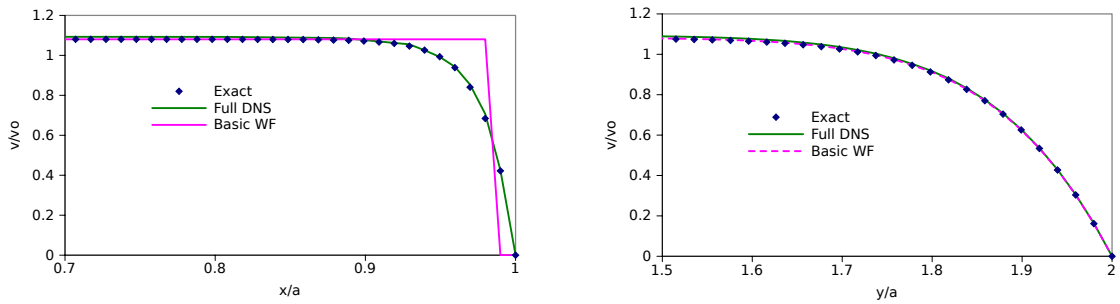

(a) (b)

Figure 5.14: Hartmann layer (a) and side layer (b) axial velocity profiles for Shercliff's case at $Ha = 50$ and $Re = 46.3$, with and without Wall Function (WF), ϕ-FSPM algorithm.

A second study has been carried out with the aim of defining the optimal Hartmann boundary layer depth. To this aim, the same case has been repeated with mesh 1 but with double δ_{Ha}. From results in table 5.10 and figure 5.15, it can be stated that, despite a slight reduction in CPU time for $\delta_{Ha} = 2a/Ha$, simulating the Hartmann boundary layer as having a depth of $\delta_{Ha} = a/Ha$ yields more accurate results.

A third study has consisted on analysing the Ha range of applicability of the linear wall function. Keeping constant the pressure gradient, Hartmann number has been

mesh	δ_{Ha}	ϵ_m %	ϵ_y%	ϵ_x%	CPU time
1	a/Ha	0.30	1.28	57.86	42'
1	$2a/Ha$	4.22	2.00	12.79	39'

Table 5.10: Influence of δ_{Ha} on wall function performance with ϕ-FSPM algorithm ($Ha = 50$, $N = 54$).

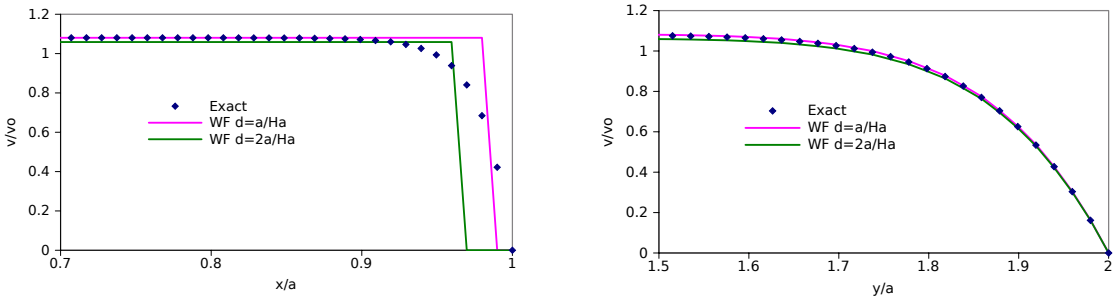

(a) (b)

Figure 5.15: Hartmann layer (a) and side layer (b) axial velocity profiles for Shercliff's case at $Ha = 50$ and $Re = 46.3$, with Wall Function (WF) and different Hartmann boundary layer depths, ϕ-FSPM algorithm.

modified. Some results have been exposed in table 5.11. The case with $Ha = 50$ is the same is in the previous studies, whereas in cases with higher Hartmann numbers the inlet velocity profile has been obtained from the exact solution for the above mentioned pressure drop.

Ha	Re	N	mesh	nodes	N_{side}	ϵ_m %	ϵ_y%	ϵ_x%	CPU time
50	46.3	$5 \cdot 10$	2	16×80	30	0.41	0.55	57.86	2h 12'
100	23.7	$4.2 \cdot 10^2$	2	16×80	30	0.25	0.75	56.63	1h 48'
500	4.9	$5.1 \cdot 10^4$	3	20×70	20	0.10	0.57	0.64	9h 46'
1000	2.5	$4.0 \cdot 10^5$	3	20×70	20	0.44	0.68	0.03	17h 59'

Table 5.11: Influence of Ha on wall function performance with the ϕ-FSPM algorithm (for a fixed dp/dz).

The behaviour of the linear wall function improves as Ha increases since this wall function is obtained under the assumption of both high Ha and high N. At $Ha < 50$, the wall function has been proved to work until the limit of $Ha = 35$, but at low Ha the convergence of the boundary condition inner loop is difficult and, hence, the wall function needs to be relaxed.

5.2.5 Algorithm 3: ϕ-PISO

This third algorithm arises from the requirements of algorithm improvement exposed in the comparison study between B-PISO and ϕ-FSPM algorithms in section 5.2.1. But an even stronger reason for the development of this third algorithm are the problems observed when simulating channels with all walls perfectly conducting. Under such cases, strange flow behaviour was observed where unphysical unsteady inverse velocity jets where obtained. In front of such relevant problem, and analysing the comparison study mentioned above, this third algorithm was developed.

The algorithm follows basically the ϕ-FSPM magnetic field treatment, but pressure-velocity coupling follows a PISO-type algorithm (similar to B-PISO algorithm). The basic structure of the algorithm is exposed in Algorithm 3. Also, it accounts for the linear wall function exposed in section 5.2.4 and fluid-solid coupling, as explained below.

Fluid-solid coupling

Solid coupling implementation has a dual goal. On one hand it provides an interesting alternative to the thin-wall condition, avoiding the corner region problems mentioned in section 5.2.4. On the other hand, it is essential for accurate thermofluid MHD simulation.

To implement fluid-solid coupling in OpenFOAM, and according to the latest OpenFOAM releases 1.6-ext and 1.7.1, two different strategies may be followed. A first strategy implies coupling both domains (fluid and solid) by means of internal boundary conditions. An example of this strategy can be found in the *chtMultiRegionFoam* algorithm in the official OpenFOAM-1.7.1 version. The main drawback is the need of an iterative process between both liquid and solid domains if a converged transient simulation is needed. The second strategy, hereafter called *grid coupling strategy*, consists on directly coupling both meshes (fluid and solid) and solving a unique matricial system. Since different transport equations are required at each domain, the matricial system is built from the corresponding two transport equations, each one attributed to one sub-domain. Such strategy can be found in the *ConjugateHeatFoam* algorithm, available in the extended OpenFOAM-1.6-ext release from Wikki Ltd. Obviously, in order to couple both transport equations, the main variable must be conserved at the interface. For electromagnetic coupling, both the electric potential and the electric current are conserved at the interface, hence, this second strategy is perfectly suitable in the present study. The disadvantage of the grid coupling strategy lays on the need of dealing with larger mesh domains at solver level; however, this disadvantage is com-

Algorithm 3 (ϕ-PISO)

1. Initial map for $\mathbf{v}$, p *and* ϕ.
Evaluate $\phi_v = \rho * (\mathbf{v}_f \cdot \mathbf{S}_f)$ *and Lorentz force.*

2. Prepare momentum discrete coefficients (eq. 5.15b) for FLUID DOMAIN:
$\mathbf{A_v}(\mathbf{v})\ \mathbf{v} \ \rightarrow\ \mathrm{fvm}::\mathrm{ddt}(\rho,\mathbf{v}) + \mathrm{fvm}::\mathrm{div}(\phi_v,\mathbf{v}) - \mathrm{fvm}::\mathrm{laplacian}(\nu\rho,\mathbf{v}) - (\mathbf{j}\times\mathbf{B_o})$
$\mathbf{a_v}(\mathbf{v})\ \rightarrow\ \mathrm{diag}(\mathbf{A_v}(\mathbf{v}))$ $\quad$ $\mathbf{H_v}(\mathbf{v})\ \rightarrow\ -(\mathbf{A_v}(\mathbf{v})\ \mathbf{v} - \mathbf{a_v}(\mathbf{v})\ \mathbf{v})$
Solve momentum equation $\quad \mathbf{A_v}(\mathbf{v})\ \mathbf{v} = -\mathrm{fvc}::\mathrm{grad}(p) \quad$ *to get* $\mathbf{v}^*$

3. PISO loop, with a fixed number of iterations, in LIQUID DOMAIN.
Velocity pre-conditioner: $\quad \mathbf{v}' = \left(\frac{\mathbf{H_v}(\mathbf{v}^*)}{\mathbf{a_v}(\mathbf{v}^*)}\right), \quad \phi_v' = \rho * (\mathbf{v}'_f \& \mathbf{S}_f)$
Solve pressure equation (pEqn): $\quad \mathrm{fvm}::\mathrm{laplacian}(\frac{\rho}{\mathbf{a_v}(\mathbf{v}')}, p) = \mathrm{fvc}::\mathrm{div}(\phi_v')$
Correct ϕ_v' *by means of the implicit terms* $\quad \phi_v = (\phi_v)' - \mathrm{pEqn.flux}$
Solve continuity equation for error estimation: $\quad \mathrm{fvc}::\mathrm{div}(\phi_v)$
Correct $\mathbf{v}'$ *and update boundary conditions* $\quad \mathbf{v} = \mathbf{v}' \ - \ \frac{1}{\mathbf{a_v}(\mathbf{v}')} * \mathrm{fvc}::\mathrm{grad}(p)$

4. Magnetic coupling with COUPLED DOMAINS:
Evaluate the magnetic flux term in LIQUID DOMAIN $\quad \chi = (\sigma_f * (\mathbf{v}_f \times \mathbf{B_o}_f)) \& \mathbf{S}_f$
Solve electric potential equation ON COUPLED DOMAINS:
FLUID DOMAIN: $\quad \mathrm{fvc}::\mathrm{div}(\chi) - \mathrm{fvm}::\mathrm{laplacian}(\sigma,\phi) = 0$
SOLID DOMAIN: $\quad -\mathrm{fvm}::\mathrm{laplacian}(\sigma_{solid},\phi_{solid}) = 0$
Evaluate j_n *in LIQUID and SOLID DOMAINS (eq. 5.13)*
Evaluate the Lorentz force in LIQUID DOMAIN (eq. 5.14)
Solve conservation of j_n *for error estimation in LIQUID DOMAIN:* $\quad \mathrm{fvc}::\mathrm{div}(j_n)$

5. Next time step.
Determine the time step.
Return to step 2.

Note: OpenFOAM's notation has been used

pensated by the fact that no inner iterations at the interface are required. In the frame of the present PhD thesis, the grid coupling strategy has been implemented.

Thus, very schematically, the hydrodynamic PISO algorithm is solved for the fluid domain, obtaining both the velocity and the pressure field maps. Then, both domains are coupled and the electric potential equation is solved (without velocity term in the solid domain; see Algorithm 3). With the obtained electric potential, the electric current and the Lorentz force term can be evaluated and the iterative loop closed.

Validation: fringing magnetic field

Basic validation steps for Shercliff's and Hunt's case have yielded the same results as with the ϕ-FSPM algorithm, since they consist of basically the same equations but a different pressure-velocity coupling. However, ϕ-PISO algorithm does not present any problem when all walls are perfectly conducting.

An interesting validation case that includes fluid-solid coupling and 3D effects is the fringing magnetic field case from Sterl (1990). It consists on a rectangular duct with constant cross-section and thin walls where liquid metal flows, as sketched in figure 5.16. A non-uniform magnetic field, varying in the streamwise direction according to equation 5.23, is present. The behaviour of such flow would correspond to the flow at an inlet of the magnet, where the magnetic field is low. Sterl's results are obtained numerically and no experimental data exists. However, for flow outgoing the magnet (from the high magnetic field region to the non-magnetic field region) some experiments can be found for both circular and rectangular ducts in Reed *et al.* (1987). Here, the study carried out by Sterl (1990) has been chosen since it deals with lower Hartmann and Reynolds numbers.

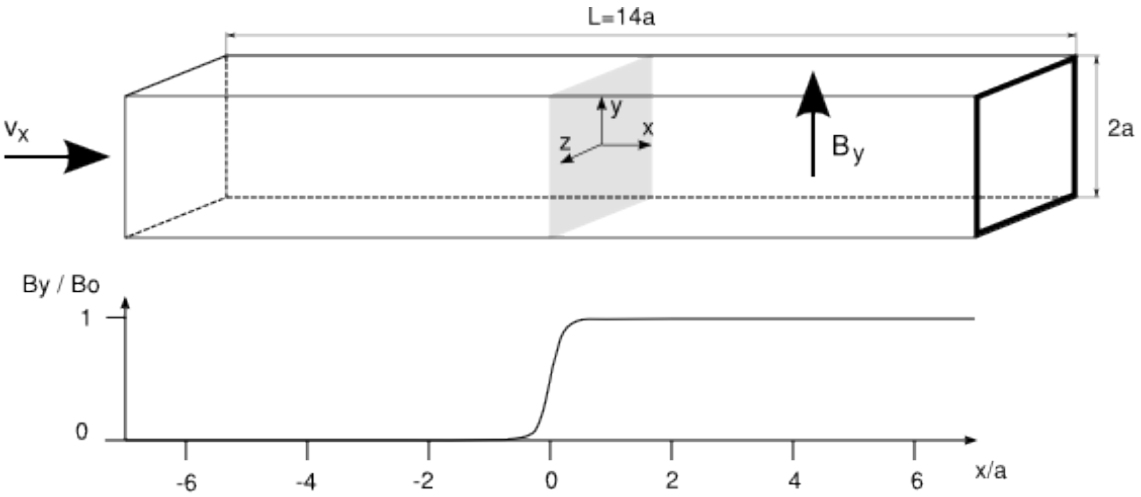

Figure 5.16: Sketch of the channel with fringing magnetic field.

$$B_y(x) = \frac{B_o}{1 + exp(-x/x_o)} \tag{5.23}$$

The chosen magnetic field shape (equation 5.23) only has one component of the magnetic field vector different from zero to save computational time. The gradient of the magnetic field profile is fixed by the x_o magnitude. If x_o is positive, the magnetic field

rises from zero to B_o, whereas negative x_o values represent a magnetic field decrease from B_o to zero. For the studied case, $x_o = 0.15$ has been used, obtaining the magnetic field profile shown in figure 5.16.

A correct magnetic field would be divergence and curl-free. However, the imposed magnetic field (equation 5.23) does not fulfil the curl-free condition. A comparison between equation 5.23 and a curl-free but non divergence-free version of it was performed by Sterl (1990). Results justified the use of equation 5.23 with reasonably small differences, including a small reduction of the pressure drop and of the amount of fluid driven into the side layers. Such results are in accordance with arguments given by Talmage and Walker (1987).

The simulated case corresponds to $Ha = 50$, $Re = 2.5$ ($N = 10^3$), $C_w = 0.1$ ($\sigma_{wall}/\sigma = 2.5$) and $x_o = 0.15$. Several structured non-uniform meshes have been studied and are listed in table 5.12, where N_{side}, N_{Ha}, N_{wall} and N_{centre} stand for nodes in side boundary layers (of depth $3a/Ha^{0.5}$), nodes in Hartmann boundary layers (of depth $2a/Ha$), nodes across the wall and nodes in the central part of the channel in x direction (of width $4a$), respectively. Such boundary layers' depth have been chosen from previous results, as those exposed in table 5.2. It can be seen that: (1) mesh 0 is a very coarse mesh with only two nodes in the Hartmann boundary layer, (2) mesh 1 has been strongly refined along main flow direction (x axis) and across side and Hartmann boundary layers, (3) in mesh 2 such refinement in boundary layers is reinforced as well as across the solid walls, (4) mesh 3 is based on mesh 2 but with a more uniform mesh, and (5) mesh 4 is a very fine mesh, considered here as the reference one for error estimation.

mesh	N_{side}	N_{Ha}	N_{wall}	N_{centre}	N_{total}
0	9	2	3	30	59600
1	21	5	3	120	561280
2	28	8	5	120	860800
3	28	8	5	120	1610240
4	36	12	10	120	2444800

Table 5.12: Description of several meshes used to simulate the fringing magnetic field case from Sterl (1990), with ϕ-PISO algorithm.

Velocity profiles just after the magnetic field step are shown for three different meshes in figure 5.17. It can be seen that velocity is captured with good accuracy even

with mesh 1. Some characteristic errors are exposed in table 5.13, where ϵ_v stands for the relative velocity error along z axis at $x/a = 0.13$ and ϵ_ϕ stands for the relative electric potential error along x axis at side boundary layer ($z/a = 1$). All errors are calculated considering results obtained with mesh 4 as the reference ones. As expected, mesh errors are considerably reduced with mesh refinement and results obtained with mesh 3 can be considered accurate enough. By comparing results from meshes 2 and 3 it can be stated that mesh uniformity is required in order to accurately capture the jet.

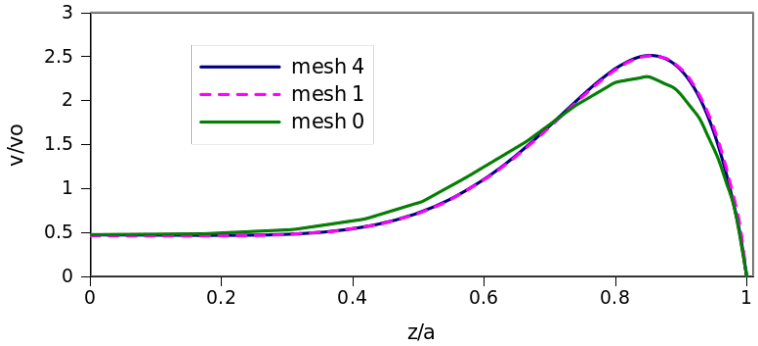

Figure 5.17: Velocity profiles for the fringing magnetic field case at $x/a = 0.13$, for different meshes.

mesh	$max\,(\epsilon_v)$	$avg\,(\epsilon_v)$	$max\,(\epsilon_\phi)$	$avg\,(\epsilon_\phi)$
0	$1.83 \cdot 10^{1}$	$8.97 \cdot 10^{0}$	4.25	0.44
1	$2.41 \cdot 10^{0}$	$8.56 \cdot 10^{-1}$	0.09	0.02
2	$1.45 \cdot 10^{0}$	$4.80 \cdot 10^{-1}$	0.38	0.14
3	$9.21 \cdot 10^{-1}$	$4.97 \cdot 10^{-1}$	0.29	0.05

Table 5.13: Relative errors obtained with the simulated meshes, considering results obtained with mesh 4 as the reference ones. Fringing magnetic field case from Sterl (1990), with ϕ-PISO algorithm.

In order to provide an overview of the flow in the fringing magnetic field case, velocity profiles at different duct cross-sections are shown in figure 5.18. The transition from purely hydrodynamic flow to the M-shaped MHD flow can be clearly observed. Whereas

Hartmann boundary layers, once formed, remain without changes, side boundary layers experience large changes along the x axis. In fact, the M-shaped profile is maximised at $x = 0$.

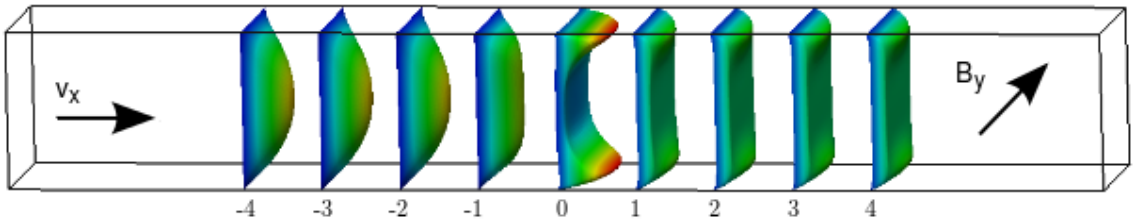

Figure 5.18: Velocity profiles at different cross sections for the fringing magnetic field case.

Before giving a qualitative reasoning of such profiles, it is required that the characteristic parameters be plotted. Those parameters are: (1) the dimensionless magnetic field (normalised by B_o), (2) the dimensionless pressure on the centreline, $p(x, 0, 0)$ (adimensionalised by $\rho v^2 N$), (3)the dimensionless pressure at the sidewall, $p(x, 0, 1)$, (4) the dimensionless streamwise pressure gradient, $-\partial_x p(x, 0, 0)$, and (5) the dimensionless transverse potential difference, $\Delta\phi(x) = |\phi(x, 1, 0) - \phi(x, 0, 1)|$ (adimensionalised by avB_o). All these parameters obtained with the simulation and mesh 3 are compared with the numerical results from Sterl (1990) in figure 5.19. A good agreement can be seen for all parameters and differences are only observed for the electric potential at the developed MHD flow region. As stated by Mistrangelo (2006), such differences can be caused by the high numerical resolution used in our simulations.

The change in the flow profile shape along the channel can be easily explained with the help of figure 5.19 and the electric potential field map in figure 5.20. In the developed MHD region, the electric current path remains almost in the $y - z$ plane due to the y electric potential gradient. However, at the central part of the channel where a magnetic field gradient exists, a streamwise electric potential gradient is formed and currents travel along x axis closing their path for current conservation, as the electric current streamlines in figure 5.20 show. Such electric current paths generate strong Lorentz forces just after the B inflection point that oppose the flow and, just at the centre, a spanwise (transverse) Lorentz force appears that pushes the fluid towards the centre (sketched in figure 5.20). The effect of this force is compensated by the pressure gradient, as can be seen in figure 5.19. As a result, the main part of the flow travels through narrow side jets and the M-shaped profile is enhanced. As the flow moves forward, the unique component of the Lorentz force is the streamwise component which

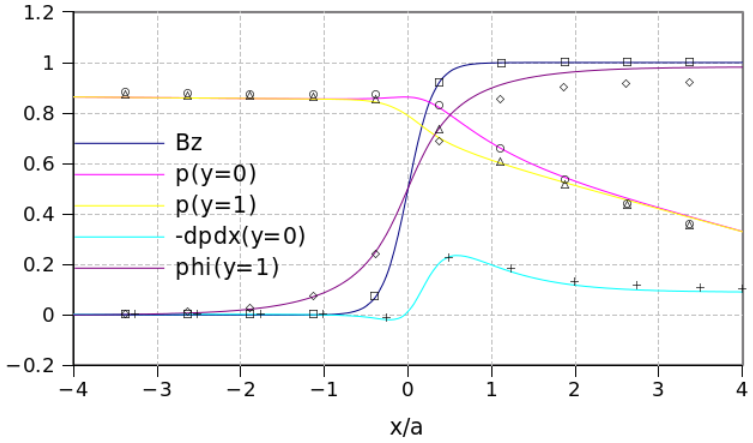

Figure 5.19: Comparison between simulated results using mesh 3 and results from Sterl (1990)

magnitude is smaller than at the centre of the channel, thus, the M-shaped profile is less abrupt and the MHD flow becomes fully developed.

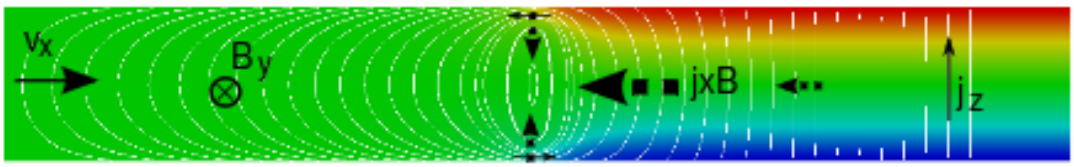

Figure 5.20: Electric potential distribution and electric current stream lines for the fringing magnetic field case. Lorentz force directions are sketched.

The above mentioned x component of the electric current is plotted in figure 5.21 just at the central cross-section and along the $z+$ axis. It can be seen that, in the fluid domain ($0 < z/a < 1$), a negative electric current exists close to the side wall. As the wall has a higher electrical conductivity than the fluid (2.5 times higher, in this case), electric currents in the wall ($z/a > 1$) are considerably higher.

5.3 A 2D approach

At large interaction parameters, viscous effects are restricted to thin boundary layers and an inviscid core region exists (figure 3.2). It has been shown that the core velocity and the electric potential do not vary along magnetic field lines at leading order of

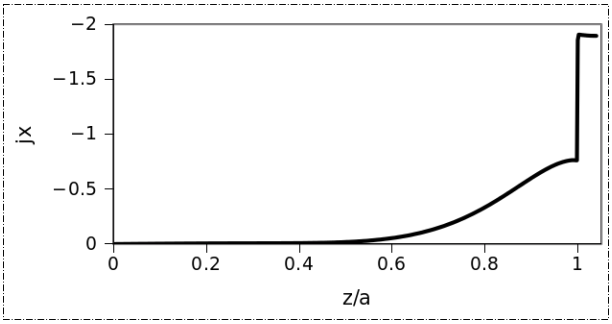

Figure 5.21: Streamwise electric current component (dimensionless) along the $z+$ axis for the fringing magnetic field case, including fluid and solid domains.

approximation (Müller and Bühler 2001).

The same behaviour is observed when turbulence is present. Indeed, at high Reynolds, very low magnetic Reynolds, and high interaction parameter, the energy-containing eddies are rapidly stretched in the magnetic field direction. Thus, Quasi-two-dimensional (Q2D) turbulence appears. Across planes perpendicular to the magnetic field, energy is transferred by means of electromagnetic and viscous forces, being the latter relatively smaller as Reynolds increases. Such electromagnetic and viscous forces act as damping forces in the Hartmann layers.

When the flow can be assumed 2D, the three-dimensional MHD equations 3.7 can be integrated along magnetic field lines according to Sommeria and Moreau (1982). When all walls are perfectly insulating, such integration yields:

$$\nabla \cdot \mathbf{v}_\perp \;=\; 0 \tag{5.24a}$$

$$\frac{\partial \mathbf{v}_\perp}{\partial t} \;+\; (\mathbf{v}_\perp \cdot \nabla)\mathbf{v}_\perp \;=\; -\frac{1}{\rho}\nabla p_d + \nu \nabla^2 \mathbf{v}_\perp \;+\; \frac{\mathbf{v}_\perp}{\tau} \tag{5.24b}$$

where $\mathbf{v}_\perp$ is the velocity vector perpendicular to magnetic field lines and τ is the Hartmann braking time $\tau = Ha^{-1}a^2/\nu$. For conducting Hartmann walls, with a finite wall conductivity ratio C_w, the Hartmann braking time can be evaluated as (Müller and Bühler 2001, Smolentsev *et al.* 2008):

$$\tau = Ha^{-1}\frac{a^2}{\nu}\left(\frac{1}{1 + C_w Ha/(1+C_w)}\right) \tag{5.25}$$

A more recent 2D approach based on the vorticity equation can be found in Müller and Bühler (2001), which yields:

$$\nabla_\perp \cdot ((1+C_w)\nabla_\perp \phi) = \; \omega \tag{5.26a}$$

$$\frac{\partial \omega}{\partial t} \; + \; \left((\nabla \psi) \times (\nabla \omega)\right)_{\parallel} \; = \; \frac{1}{Re} \nabla_{\perp}^{2} \omega \; - \; \frac{a}{\tau Re \nu} \omega \; - \; \frac{N}{1 + C_w} \nabla_{\perp} C_w \cdot \nabla_{\perp} \phi \tag{5.26b}$$

$$\nabla_{\perp}^{2} \psi \; = \; -\omega \tag{5.26c}$$

where ω is the vorticity component aligned with the magnetic field and ψ is the stream function. In equation 5.26b, the term including τ represents the decay of vorticity whereas the last term accounts for vorticity production due to variation of wall conductivity. Such term is not considered in the most classical approach from Sommeria and Moreau (1982), as shown in equation 5.24b.

The 2D approach, when applicable, is a very useful MHD modelling strategy in terms of reduced CPU time.

Next, the algorithm used to implement the 2D set of equations 5.24 to OpenFOAM is described.

5.3.1 Algorithm 4: SM82

The algorithm follows basically the OpenFOAM's original PISO algorithm but includes an extra term corresponding to magnetic damping, according to equation 5.24b. Such term involves the Hartmann braking time τ, which is provided by the user. The basic structure of the algorithm is exposed in Algorithm 4. It also accounts for fluid-solid coupling, as explained in section 5.2.5.

Following the same strategy than for previous algorithms (see, for instance, section 5.1.1), the set of equations 5.24 can be written in discrete form for each grid node, yielding:

$$D(\mathbf{v}_{\perp} \; = \; 0 \tag{5.27a}$$

$$\underbrace{\frac{\partial \boldsymbol{\rho} \, \mathbf{v}_{\perp}}{\partial t} \; + \; D(\phi_v \mathbf{v}_{\perp}) \; - \; D(\nu \, \rho \, G(\mathbf{v}_{\perp})) \; + \; \frac{\rho \, \mathbf{v}_{\perp}}{\tau}}_{\mathbf{A_v}(\mathbf{v}_{\perp}) \; \mathbf{v}_{\perp}} = \underbrace{- \, G(p)}_{\mathbf{b_v}(\mathbf{v}_{\perp})} \tag{5.27b}$$

where, D and G are the divergence and gradient discrete operators, respectively. According to OpenFOAM notation, $\phi_v \; = \; \rho \left(\mathbf{v}_{\perp f} \cdot \mathbf{S}_f \right)$ is the face mass flux and the subscript f indicates the interpolated value at control volume's face. As before, matrix $\mathbf{A_v}(\mathbf{v}_{\perp})$ can be split in diagonal terms $\mathbf{a_v}(\mathbf{v}_{\perp})$ and off-diagonal terms. A new matrix can be now defined as $\mathbf{H_v}(\mathbf{v}_{\perp}) = -(\mathbf{A_v}(\mathbf{v}_{\perp}) \; \mathbf{v}_{\perp} \; - \; \mathbf{a_v}(\mathbf{v}_{\perp}) \; \mathbf{v}_{\perp})$. With this notation, the hereafter called SM82 algorithm is exposed in Algorithm 4.

Algorithm 4 (SM82)

1. Initial map for $\mathbf{v}_\perp$ *and* p*. Evaluate* ϕ_v*.*

2. Prepare momentum discrete coefficients (eq. 5.27b):

$\mathbf{A_v}(\mathbf{v})\ \mathbf{v} \ \rightarrow\ \mathrm{fvm}::\mathrm{ddt}(\rho,\mathbf{v}_\perp) + \mathrm{fvm}::\mathrm{div}(\phi_v,\mathbf{v}_\perp) - \mathrm{fvm}::\mathrm{laplacian}(\nu\rho,\mathbf{v}_\perp) + \frac{\rho\ \mathbf{v}_\perp}{\tau}$

$\mathbf{a_v}(\mathbf{v}) \ \rightarrow\ \mathrm{diag}(\mathbf{A_v}(\mathbf{v}))$ $\qquad$ $\mathbf{H_v}(\mathbf{v}_\perp) \ \rightarrow\ -(\mathbf{A_v}(\mathbf{v}_\perp)\ \mathbf{v}_\perp - \mathbf{a_v}(\mathbf{v}_\perp)\ \mathbf{v}_\perp)$

Solve momentum equation $\quad \mathbf{A_v}(\mathbf{v}_\perp)\ \mathbf{v}_\perp = -\mathrm{fvc}::\mathrm{grad}(p) \quad$ *to get* ${\mathbf{v}_\perp}^*$

3. PISO loop, with a fixed number of iterations.

Velocity pre-conditioner: $\quad {\mathbf{v}_\perp}' = \left(\frac{\mathbf{H_v}({\mathbf{v}_\perp}^*)}{\mathbf{a_v}({\mathbf{v}_\perp}^*)}\right), \quad \phi_v' = \rho * ({\mathbf{v}_\perp}_f' \& \mathbf{S}_f)$

Solve pressure equation (pEqn): $\quad \mathrm{fvc}::\mathrm{div}(\phi_v') - \mathrm{fvm}::\mathrm{laplacian}(\frac{\rho}{\mathbf{a_v}({\mathbf{v}_\perp}')}, p) = 0$

Correct ϕ_v' *by means of the implicit terms* $\quad \phi_v = (\phi_v)' + \mathrm{pEqn.flux}$

Solve continuity equation for error estimation: $\quad \mathrm{fvc}::\mathrm{div}(\phi_v)$

Correct ${\mathbf{v}_\perp}'$ *and update boundary conditions* $\quad \mathbf{v}_\perp = {\mathbf{v}_\perp}' - \frac{1}{\mathbf{a_v}({\mathbf{v}_\perp}')} * \mathrm{fvc}::\mathrm{grad}(p)$

4. Next time step.

Determine the time step.

Return to step 2.

Note: OpenFOAM's notation has been used

Validation: Shercliff's case

Shercliff's case has been studied for $Ha = 300$ and $Re = 10$ ($N = 9 \cdot 10^3$) in a rectangular channel (figure 5.3). The same case has been studied using either ϕ-PISO and SM82 algorithms. When the ϕ-PISO algorithm has been used, the mesh is 3D and periodic inlet/outlet boundary conditions, based on a fixed mass flow rate, are imposed; therefore, with only three nodes in channel axis direction the flow is perfectly reproduced. The same boundary condition has been used for the 2D mesh used with the SM82 algorithm.

Different meshes have been considered, as defined in table 5.14. Note that, when the SM82 algorithm has been used, only one node in the direction of the magnetic field has been considered. The coarsest 3D mesh, mesh 0, has already 6 nodes in the Hartmann boundary layer; hence, all meshes are fine enough to accurately capture the core velocity, as can be seen in figure 5.22.

A first order temporal scheme and the Central-Difference discretisation in space have been chosen. The (Bi-)Conjugate Gradient solver with incomplete-Cholesky preconditioner has been used. In all simulated cases, solver precision has been fixed to 10^{-8} for velocity and 10^{-9} for pressure (and electric potential for the ϕ-PISO algorithm). The steady state has been defined to have relative variation between successive time steps below 10^{-7} for all variables.

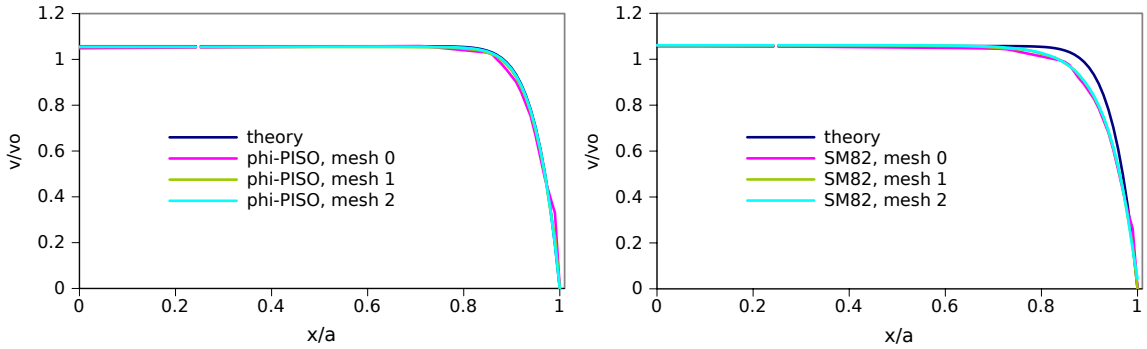

(a) (b)

Figure 5.22: Side layer axial velocity profiles for Shercliff's case at $Ha = 300$ and $Re = 10$ using mesh 1. ϕ-PISO (a) and SM82 (b) algorithm comparison.

Being v_o the mean flow velocity and v_c the velocity at the centre of the channel, and indicating the subscript th the theoretical value (according to equation 5.9), the errors exposed in table 5.14 can be defined as:

$$\begin{aligned} \epsilon_p &= 100 \cdot \frac{|\nabla p - \nabla p_{th}|}{\nabla p_{th}} \quad \% \\ \epsilon_v &= 100 \cdot average\left(\frac{|v - v_{th}|}{v_o}\right) \quad \% \\ \epsilon_{vc} &= 100 \cdot \left(\frac{|v_c - v_{th,c}|}{v_o}\right) \quad \% \end{aligned}$$

These errors are evaluated along y axis (perpendicular to the applied magnetic field). Thus, results exposed in table 5.14, together with velocity profiles in figure 5.22, indicate that: (1) velocity profile in side boundary layer is not accurately obtained with the SM82 algorithm (2) the SM82 algorithm has a substantially reduced pressure gradient error, specially at coarse meshes, (3) whereas the ϕ-FSPM algorithm presents good consistency (error is reduced as mesh refinement is increased), SM82 does not. Thus, it can be stated that the SM82 algorithm presents very good behaviour at coarse meshes but, with fine meshes, the overall (average) precision might decrease.

Due to the above mentioned SM82 behaviour, SM82 algorithm has only been used in those cases where a 3D mesh is not affordable due to CPU limits, as is the case studied in Chapter 8.

Turbulence model

The flow studied in Chapter 8 presents Q2D turbulence; hence, the SM82 algorithm needs to account for a Q2D turbulence model. The chosen RANS model to be imple-

		ϕ-FSPM			SM82		
mesh	nodes ($N_y \times N_z$)	ϵ_p %	ϵ_v %	$\epsilon_v c$ %	ϵ_p %	ϵ_v %	$\epsilon_v c$ %
0	14×20	3.20	0.82	0.87	0.17	1.92	0.15
1	28×40	1.12	0.43	0.28	0.33	0.82	0.34
2	56×80	0.43	0.25	0.22	0.36	0.82	0.38

Table 5.14: Simulation errors for Shercliff's case ($Ha = 300$, $Re = 10$) with ϕ-PISO and SM82 algorithms.

mented has been the zero-equation model from Smolentsev and Moreau (2006). In this model, focused on Q2D turbulence caused by shear layers, the turbulent (eddy) viscosity perpendicular to the magnetic field lines $\nu_{t,\perp}$ is obtained considering an elementary shear layer of thickness δ and a momentum equation for the core velocity in accordance with Sommeria and Moreau (1982), yielding:

$$\nu_{t,\perp} = 0.25\delta^2/\tau \tag{5.28}$$

where τ is the Hartmann braking time. The thickness of the shear layer can be estimated following the work of Messadek and Moreau (2002) (equation 5.29), where experimental measurements of a circular tank filled with mercury and under a vertical magnetic field and radial horizontal electric currents were analysed. Despite the singularity of the experimental setup, Smolentsev and Moreau 2006 pointed out that the obtained thickness correlation can be applied if Q2D turbulence exist. This correlation is:

$$\delta \sim 2a \left(\frac{Ha}{Re} \right)^{-1/2} \tag{5.29}$$

Moreover, following the numerical simulation strategy exposed in Smolentsev and Moreau (2006), a wall-damping factor is introduced in order to correct the eddy-viscosity in the regions near the walls. Such wall-damping factor varies exponentially from zero to one within the boundary layer. This results in a non-uniform effective viscosity ($\nu_{eff} = \nu + \nu_{t,\perp}$) so that a second term in the momentum equation must be introduced, as exposed in equation 5.30.

$$\frac{\partial \mathbf{v}_\perp}{\partial t} \; + \; (\mathbf{v}_\perp \cdot \nabla)\mathbf{v}_\perp \; = \; -\frac{1}{\rho}\nabla p_d + \; \nabla \cdot (\nu_{eff} \nabla \mathbf{v}_\perp) \; + \; (\nabla \mathbf{v}_\perp)\,(\nabla \nu_{eff}) \; + \; \frac{\mathbf{v}_\perp}{\tau} \tag{5.30}$$

In the algorithm, both viscous terms are implemented as:

$$\begin{aligned}
\nabla \cdot (\nu_{eff} \nabla \mathbf{v}) \quad &+ \quad (\nabla \mathbf{v}) \, (\nabla \nu_{eff}) \; = \\
&= \quad \frac{1}{3} \nu_{eff} \nabla \left(\nabla \cdot \mathbf{v} \right) \; + \; \nabla \cdot (\nu_{eff} \nabla \mathbf{v}) \; - \; \frac{2}{3} \left(\nabla \nu_{eff} \right) (\nabla \cdot \mathbf{v}) \; + \; (\nabla \mathbf{v}) \, (\nabla \nu_{eff}) \\
&= \quad -\frac{2}{3} \nabla \left(\nu_{eff} \nabla \cdot \mathbf{v} \right) \; + \; \nabla \cdot \left(\nu_{eff} \left((\nabla \mathbf{v}) + (\nabla \mathbf{v})^T \right) \right) \\
&= \quad \nabla \cdot (\nu_{eff} \nabla \mathbf{v}) \; + \; \nabla \cdot \left(\nu_{eff} \left((\nabla \mathbf{v})^T - \frac{2}{3} \; trace \left((\nabla \mathbf{v})^T \right) \right) \right) \\
&= \quad \nabla \cdot (\nu_{eff} \nabla \mathbf{v}) \; + \; \nabla \cdot \left(\nu_{eff} \; dev2 \left((\nabla \mathbf{v})^T \right) \right)
\end{aligned} \tag{5.31}$$

where *trace* and *dev2* are OpenFOAM objects defined in the official version. The above mentioned procedure for non uniform viscosities is already used in some OpenFOAM applications.

6 Thermal MHD coupling

In this section the coupling of MHD flows with thermal transport is explained. Such phenomenon has multiple names, including thermofluid MHD (Smolentsev *et al.* 2010), magnetoconvection (Müller *et al.* 1999) or buoyant MHD (di Piazza and Bühler 1999), among others. Here, the most simple but global name 'thermal MHD' has been used. The fluid motion is affected by temperature gradients but it is not necessarily driven only by natural convection, as the 'buoyant MHD' label seems to indicate. Indeed, the flow can be driven by an external force (a pressure gradient, for instance) but due to the existence of a thermal load, buoyant convection exists as well. Therefore, the fluid motion becomes even more complex than in pure MHD flows and some thermal instabilities are to be expected.

In order to carry out such coupling, following the development exposed in section 3.3, a new scalar equation corresponding to the temperature field (equation 3.11) together with a modified momentum equation according to the Boussinesq hypothesis and the corresponding buoyant term (equation 3.13) are to be considered. The final set of dimensionless governing equations is exposed in equations 3.17.

Next, the algorithm used to implement the the thermal coupling to OpenFOAM is described and validated.

6.1 Algorithm 5: ϕT-PISO

The implemented algorithm follows the same structure than the ϕ-PISO algorithm (section 5.2.5) and includes the energy equation, or temperature equation, sequentially.

As done in section 5.1.1, a general transport equation is defined for $\mathbf{v}$ as: $\mathbf{A_v}(\mathbf{v})\ \mathbf{v} = \mathbf{b_v}(\mathbf{v})$. Defining D and G as the divergence and gradient discrete operators respectively, the set of governing equations 3.17 can be written in discrete form for each grid node yielding:

$$D(\mathbf{v}) \ = \ 0 \tag{6.1a}$$

$$\underbrace{\frac{\partial \rho_o\ \mathbf{v}}{\partial t} \ + \ D(\phi_v \mathbf{v}) \ - \ D(\nu\ \rho_o\ G(\mathbf{v})) \ - \ (\mathbf{j} \times \mathbf{B_o}) + \ \beta_o\ \rho_o\ (T - T_o)\, \mathbf{g}}_{\mathbf{A_v}(\mathbf{v})\ \mathbf{v}} = \underbrace{-\ G(p_d)}_{\mathbf{b_v}(\mathbf{v})} \tag{6.1b}$$

$$D(\sigma G(\phi)) \ = \ D(\sigma(\mathbf{v} \times \mathbf{B_o})) \tag{6.1c}$$

$$\mathbf{j} \ = \ \sigma(-G(\phi) \ + \ \mathbf{v} \times \mathbf{B_o}) \tag{6.1d}$$

$$\frac{\partial \rho_o\ T}{\partial t} \ + \ D(\phi_v T) \ - \ D(\alpha\ \rho\ G(T)) \ - \ S_{thermal}/C_p \ = \ 0 \tag{6.1e}$$

where, according to OpenFOAM notation, $\phi_v \ = \ \rho_o\,(\mathbf{v}_f \cdot \mathbf{S}_f)$ is the face mass flux and the subscript f indicates the interpolated value at control volume's face. Matrix $\mathbf{A_v}(\mathbf{v})$ can be split in diagonal terms $\mathbf{a_v}(\mathbf{v})$ and off-diagonal terms. A new matrix can be now defined as $\mathbf{H_v}(\mathbf{v}) = -(\mathbf{A_v}(\mathbf{v})\ \mathbf{v} \ - \ \mathbf{a_v}(\mathbf{v})\ \mathbf{v})$.

As mentioned in section 5.2.1, the electric current conservative scheme based on a conservative formula of the Lorentz force proposed by Ni *et al.* (2007) is considered. It first requires a consistent scheme to calculate the current flux on cell faces. This step has been implemented following equation 6.3, where j_n stands for the cell surface orthogonal component of the current density flux, $\mathbf{S}_f$ is the face surface of the control volume, and ∇_{sn} is a surface normal gradient that already includes non-orthogonal mesh corrections. Once j_n is obtained, the Lorentz force can be evaluated at cell centres following equation 6.4, where Ω_c is the cell volume and $\mathbf{C}$ are the cell centre coordinates.

$$\chi \ = \ (\sigma_f(\mathbf{v}_f \times \mathbf{B_o}_f)) \cdot S_f \tag{6.2}$$

$$j_n \ = \ -\sigma_f(\nabla_{sn}\phi) \cdot |\mathbf{S}_f| + \chi \tag{6.3}$$

$$\mathbf{j} \times \mathbf{B_o} \ = \ -\frac{1}{\Omega_c} \sum_f (j_n \cdot (\mathbf{B_o} \times \mathbf{C})_f) - \mathbf{C} \times \frac{1}{\Omega_c} \sum_f \left(j_n \cdot \mathbf{B_o}_f\right) \tag{6.4}$$

Continuity and momentum coupling is solved following the pressure-based PISO-like algorithm defined by Weller *et al.* (1998). Thus, this algorithm is hereafter called

ϕT-PISO algorithm. In pressure-based algorithms, a pressure equation is obtained from the continuity equation together with the momentum equation. Here, the momentum equation is used as a pre-conditioner for the velocity in order to improve the accuracy of the Laplacian solver for the pressure equation. Once the new pressure is obtained, the velocity is corrected. Very schematically, and using the above mentioned matrix notation, the thermal MHD algorithm used for the full set of equations is exposed in Algorithm 5. The Picard linearisation method has been used as well as the Jacobi pre-conditioner.

The implemented algorithm also accounts for the linear wall function presented in section 5.2.4.

The same thermal coupling methodology (including fluid-solid thermal coupling) has been applied to the SM82 algorithm (section 5.3.1).

6.2 Validation for steady flows

A fully developed flow in a horizontal square section of a differentially heated long vertical enclosure, in the presence of a strong horizontal magnetic field, has been analysed following the study from Tagawa *et al.* (2002). In that study, all walls were perfectly insulated and temperature profile was imposed to be linear. The authors obtained analytical results for the central velocity gradient under two different flow configurations: (1) perpendicular temperature gradient with respect to magnetic field, which is called the perpendicular case, represented in figure 6.1 and (2) the corresponding parallel case. Both solutions are given in equation 6.5, where W and X are the dimensionless velocity and coordinate in the direction of the temperature gradient, respectively normalised with L and ν/L. The characteristic dimension L, also used in the Ha and Gr numbers, corresponds to the dimension of the cavity square section ($2a$).

$$\frac{dW}{dX}_{\perp} = \frac{-Gr}{2\ Ha} \qquad \frac{dW}{dX}_{\parallel} = \frac{-Gr}{Ha^2} \tag{6.5}$$

Tagawa *et al.* (2002) numerically reproduced flows at $Gr = 10^4$ and $Ha = (\ 0,\ 100,\ 500,\ 2000\ )$, and compared the obtained results with the analytical solution in equation 6.5. A non-uniform mesh was proposed, with 32×32 nodes in the horizontal plane (fully developed flow), 8 nodes at side boundary layers and 1 node at Hartmann boundary layers. A mesh sensitivity analysis was carried out by increasing the number of nodes in the Hartmann boundary layer whereas keeping the total mesh size.

In the present validation, the same cases as in Tagawa *et al.* (2002) have been reproduced and the errors with respect to the analytical solution quantified and presented

Algorithm 5 (ϕT-PISO)

1. Initial map for $\mathbf{v}$*,* p_d*,* ϕ *and* T*.*
Evaluate $\phi_v = \rho_o * (\mathbf{v}_f \cdot \mathbf{S}_f)$ *and Lorentz force.*

2. Prepare momentum discrete coefficients (eq. 6.1b):
$\mathbf{A_v}(\mathbf{v})\ \mathbf{v} \ \rightarrow\ \mathrm{fvm}::\mathrm{ddt}(\rho,\mathbf{v}) + \mathrm{fvm}::\mathrm{div}(\phi_v,\mathbf{v}) - \mathrm{fvm}::\mathrm{laplacian}(\nu\rho,\mathbf{v})$
$-(\mathbf{j}\times\mathbf{B_o}) + \beta_o\rho_o\,(T-T_o)\,\mathbf{g}$
$\mathbf{a_v}(\mathbf{v}) \ \rightarrow\ \mathrm{diag}(\mathbf{A_v}(\mathbf{v}))$ $\qquad$ $\mathbf{H_v}(\mathbf{v}) \ \rightarrow\ -(\mathbf{A_v}(\mathbf{v})\ \mathbf{v} - \mathbf{a_v}(\mathbf{v})\ \mathbf{v})$
Solve momentum equation $\quad \mathbf{A_v}(\mathbf{v})\ \mathbf{v} = -\mathrm{fvc}::\mathrm{grad}(p_d)$ $\quad$ *to get* $\mathbf{v}^*$

3. PISO loop, with a fixed number of iterations.
Solve temperature equation (equation 6.1e):
$\mathrm{fvm}::\mathrm{ddt}(\rho,T) + \mathrm{fvm}::\mathrm{div}(\phi_v,T) - \mathrm{fvm}::\mathrm{laplacian}(\alpha,T)$
$= \mathrm{fvm}::\mathrm{Sp}(S_{thermal}/(C_pT),T)$
Velocity pre-conditioner: $\quad \mathbf{v}' = \left(\frac{\mathbf{H_v}(\mathbf{v}^*)}{\mathbf{a_v}(\mathbf{v}^*)}\right), \quad \phi_v' = \rho * (\mathbf{v}_f'\&\mathbf{S}_f)$
Solve pressure equation (pdEqn): $\quad \mathrm{fvm}::\mathrm{laplacian}(\frac{\rho}{\mathbf{a_v}(\mathbf{v}')}, p_d) = \mathrm{fvc}::\mathrm{div}(\phi_v')$
Correct ϕ_v' *by means of the implicit terms* $\quad \phi_v = (\phi_v)' - \mathrm{pdEqn.flux}$
Solve continuity equation for error estimation: $\quad \mathrm{fvc}::\mathrm{div}(\phi_v)$
Correct $\mathbf{v}'$ *and update boundary conditions* $\quad \mathbf{v} = \mathbf{v}' - \frac{1}{\mathbf{a_v}(\mathbf{v}')} * \mathrm{fvc}::\mathrm{grad}(pd)$

4. Magnetic coupling:
Evaluate the magnetic flux term $\quad \chi = (\sigma_f * (\mathbf{v}_f \times \mathbf{B_o}_f))\&\mathbf{S}_f$
Solve electric potential equation: $\quad \mathrm{fvc}::\mathrm{div}(\chi) - \mathrm{fvm}::\mathrm{laplacian}(\sigma,\phi) = 0$
Evaluate j_n *(eq. 6.3)*
Evaluate the Lorentz force (eq. 6.4)
Solve conservation of j_n *for error estimation:* $\quad \mathrm{fvc}::\mathrm{div}(j_n)$

5. Next time step.
Determine the time step.
Return to step 2.

Note: OpenFOAM's notation has been used

in table 6.1. It can be observed that the obtained numerical results are in very good agreement with results from Tagawa *et al.* (2002). It has to be mentioned that if, instead of locating just one node on the Hartmann boundary layer ($N_{Ha} = 1$), two nodes are considered with the same mesh size, the accuracy is increased by about one order of magnitude.

Velocity field and electric potential field with electric current stream lines are shown in figure 6.2 for the perpendicular case and in figure 6.3 for the parallel one, both for $Ha = 100$. In figures, Φ is the dimensionless electric potential, normalised with $\phi/\nu B$.

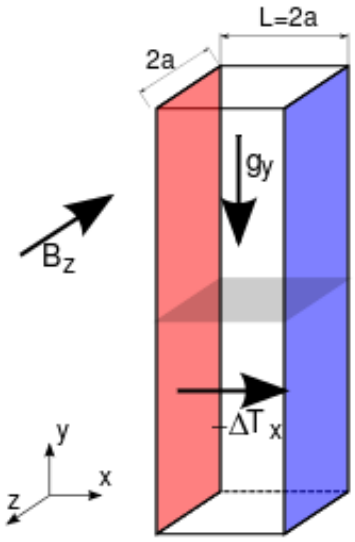

Figure 6.1: Sketch of the case setup for the perpendicular case of Tagawa *et al.* (2002).

condition				analytical	results		
case	Ha	nodes	N_{Ha}	dW/dX	W	dW/dX	error %
perpendicular	0	32×32	1	–	73.02	355.5	–
	100	32×32	1	50.00	17.61	55.25	10.48
		32×64	2		16.86	51.41	2.81
		32×96	3		16.71	50.65	1.28
		32×128	4		16.66	50.38	0.74
	500	32×32	1	10.00	4.51	11.28	12.78
		32×64	2		4.22	10.32	3.18
		32×96	3		4.17	10.15	1.44
		32×128	4		4.15	10.09	0.88
	2000	32×32	1	2.50	1.24	2.80	12.17
parallel	100	32×32	1	1.00	3.04	0.99	1.12
	500	32×32	1	0.04	0.69	0.04	0.06

Table 6.1: Numerical results for a developed buoyant flow with a strong magnetic field. Comparison against analytical solution from Tagawa *et al.* (2002).

Concerning the perpendicular case, buoyancy velocity profiles induce an electric current according to Ohm's law which, in the core, travels from the centre to both side boundary layers (following negative potential gradient). Since currents need to close their path inside the fluid domain for conservation, the **j** streamlines show the four regions observed in figure 6.2(b). The induced currents generate a Lorentz force that opposes the flow, reducing the magnitude of the buoyant convection. In figure 6.2(a) the

typical linear velocity gradient at the core of the cavity is observed; such gradient is reduced as Ha increases. When the thermal gradient is aligned with the magnetic field (parallel case), the induced electric currents travel from one side boundary layer to the other and close their path in a unique structure, as shown in figure 6.3(b). This circulation produces a damping Lorentz force at the core whereas at side boundary layers the Lorentz force vanishes. Thus, the flow is forced to circulate through the four thin side boundary layer jets of figure 6.3.

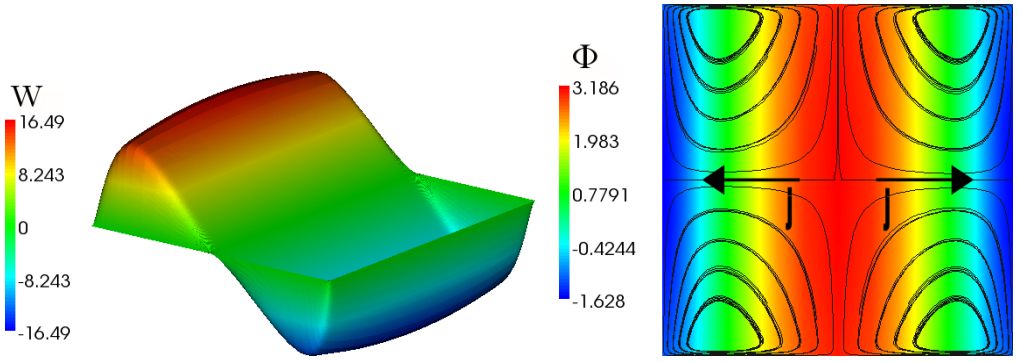

(a) Velocity field

(b) Electric potential and electric current stream lines

Figure 6.2: Results for a fully developed flow with insulated walls for $Gr = 10^4$, $Ha = 100$ and temperature gradient perpendicular to the magnetic field.

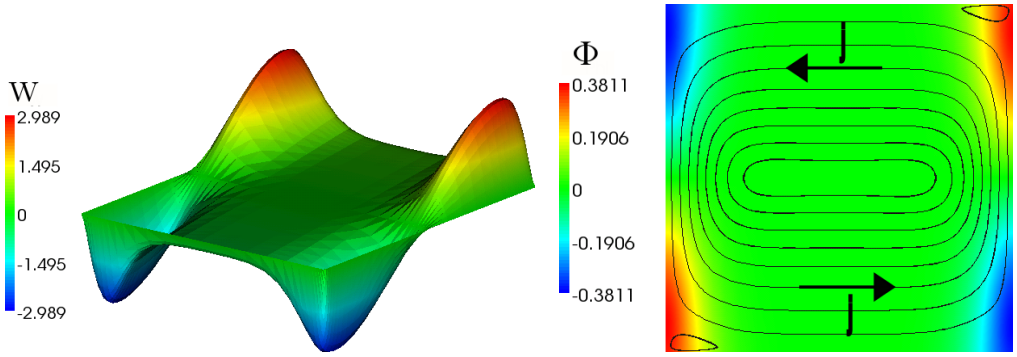

(a) Velocity field

(b) Electric potential and electric current stream lines

Figure 6.3: Results for a fully developed flow with insulated walls for $Gr = 10^4$, $Ha = 100$ and temperature gradient parallel to the magnetic field.

6.3 Validation for unsteady flows

In other to simulate a real 3D case, the same cavity is closed with top and bottom walls being the total height $7.5\ L$. Following indications from Authié *et al.* (2003), the case with $Gr = 4 \cdot 10^6$ has been simulated for Ha 100 and 500. In this case, the temperature profile is not imposed and the temperature gradient is always perpendicular to the magnetic field direction. Results for velocity, electric potential and temperature are shown in figures 6.4 and 6.5. As obtained in Authié *et al.* (2003), a steady solution is obtained for Ha 500 with similar flow profiles as in the fully developed case, except for the top and bottom walls. A unique velocity vortex is generated and temperature profile is almost linear. The obtained mean Nusselt number is 1.56. When Ha is reduced to 100, three unsteady vortices appear (figure 6.5(a)) and the temperature field is no more linear; in this case the magnetic field is not strong enough to suppress thermal instabilities. In this case, a mean Nusselt number of 2.85 ± 0.2 is obtained. Both Nusselt numbers are consistent with the experiments from Okada and Ozoe (1992). The obtained results for $Ha = 100$ do not follow the numerical solution given in equation 6.5 since the flow is fully 3D.

In order to simulate a flow setup within the range of the experimental results, Authié *et al.* (2003) studied the time evolution of the Nusselt number at $Gr = 4 \cdot 10^7$, where the flow is expected to be more complicated and oscillatory. Here, some of the studied cases are reproduced using the 3D algorithm ϕT-PISO coupled with the linear wall function presented in section 5.2.4. Some results are represented in figure 6.6, where $\tau = L^2/\nu$ is the dimensionless time. In order to compare these results with the ones of Authié *et al.* (2003), it has to be kept in mind that, since flow properties are different in both studies (although Pr is the same), τ scales different.

In figure 6.6(b), results for $Ha = 200$ obtained with the mesh proposed by Authié *et al.* (2003), labelled as 'coarse mesh', are compared with results obtained with a finer mesh. The coarse mesh size in the horizontal cross section ($x \times z$) is (32×32), whereas the fine mesh is (40×32), hence the fine mesh has a better resolution along the temperature gradient direction. From results in figure 6.6, it can be stated that the flow is unstable and that mesh influence is relevant, what makes the obtained Nusselt number non accurate. Such mesh size influence on Nusselt number is consistent with the discrepancies between numerical and experimental Nusselt values reported by Authié *et al.* (2003).

In order to understand the nature of the observed flow fluctuations, the dimensionless numbers are evaluated following the analysis presented in section 3.3.2 (where the characteristic dimension was a instead of L). Characteristic dimensionless numbers are

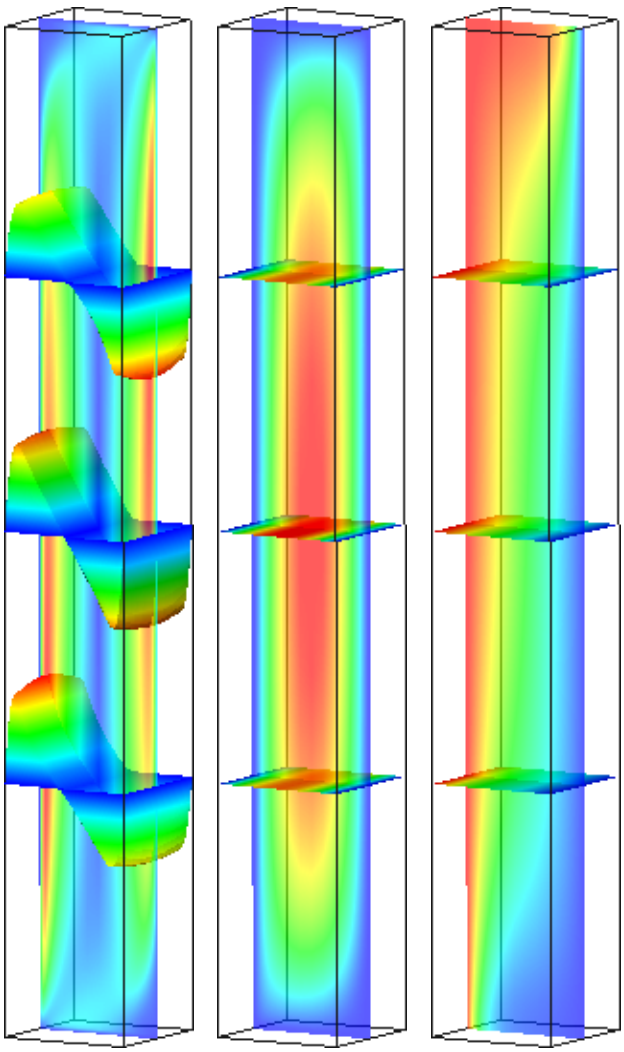

(a) v (b) ϕ (c) T

Figure 6.4: Results for a cavity of height $7.5L$ with perpendicular temperature gradient, $Gr = 4 \cdot 10^6$ and $Ha = 500$.

listed in table 6.2. It can be observed that: (1) the equivalent Reynolds number (Re') is quite high at low Ha numbers, (2) the ratio Re'/Ha_a indicates that at $Ha = 0$ the flow is turbulent with a 3D flow pattern and for $Ha \geq 100$ the flow presents Q2D turbulence or remains laminar, (3) due to the high Peclet numbers, inertia effects cannot be neglected in the energy balance, and (4) the high equivalent interaction parameter indicates that inertia effects can be neglected from the momentum balance at $Ha \geq 300$. As a result, with such dimensionless analysis and the observed results, it can be stated that the hydrodynamic flow is 3D turbulent, and at low to moderate Hartmann number Q2D turbulence develops. In order to precisely capture the associated flow oscillations, a very fine mesh is required.

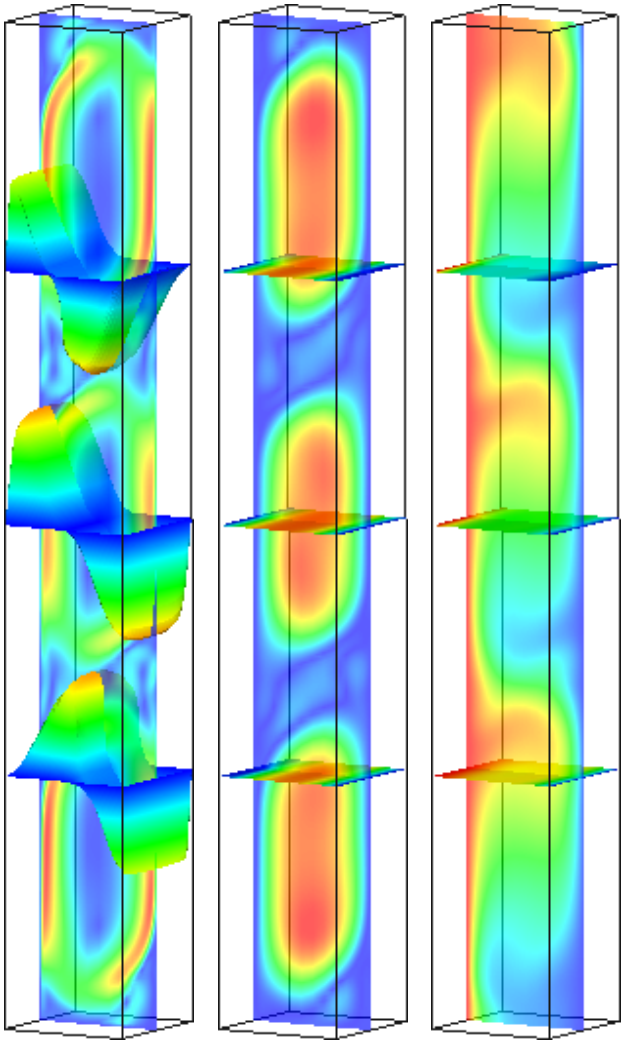

(a) v (b) ϕ (c) T

Figure 6.5: Results for a cavity of height $7.5L$ with perpendicular temperature gradient, $Gr = 4 \cdot 10^6$ and $Ha = 100$.

In order to determine at what Hartmann the flow remains laminar but becomes unstable (for instance, periodic), Fourier transformations in space and time of the numerical results are required. A first attempt towards such analysis is carried out in Chapter 9, where flow conditions are simplified and a mesh fine enough is used (and justified).

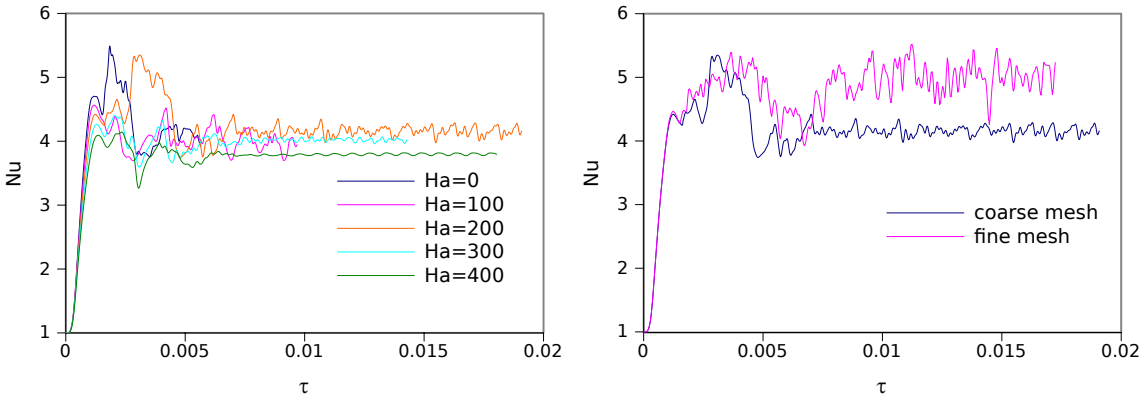

(a) (b)

Figure 6.6: Nusselt analysis for a cavity of height $7.5L$ with perpendicular temperature gradient, $Gr = 4 \cdot 10^7$, (a) Hartmann influence evaluated with a coarse mesh (the same mesh used by Authié *et al.* (2003) and (b) mesh influence on the $Ha = 200$ case.

Ha_L	0	100	200	300	400
$u_{o,MHD} = \frac{\nu}{a}\frac{Gr_a}{Ha_a^2}$	∞	0.08	0.02	0.009	0.005
$Re' = \frac{Gr_a}{Ha_a^2}$	∞	2000	500	222	125
Re'/Ha_a	∞	40	5	1.5	0.6
$Pe = \frac{Pr\,Gr_a}{Ha_a^2}$	∞	50	12.5	5.6	3.1
$Ly^2 = N' = \frac{Ha_a^4}{Gr_a}$	∞	1.2	20	101	320

Table 6.2: Dimensionless numbers analysis for a cavity of height $7.5L$ with perpendicular temperature gradient, $Gr_L = 4 \cdot 10^7$.

6.4 Algorithm 6: ϕT-PISO_FSI

For fluid-solid thermal coupling, the grid coupling strategy for the electromagnetic coupling explained in section 5.2.5 has been applied. Thus, both energy equations for fluid and solid domains are coupled in a unique matricial system of equations.

Following the strategy proposed in the extended OpenFOAM version (OpenFOAM-1.6-ext, from Wikki Ltd.) under the name *conjugateHeatFoam*, the energy (temperature) equations for both solid and fluid domains correspond to equations 6.6 (where $\phi_v = (\mathbf{v}_f \cdot \mathbf{S}_f)$), which are written in a non-conservative form (the argument inside the derivatives in the left hand side is (T) instead of $(\rho C_p T)$). However, an energy balance all over the domain using numerical values obtained with this strategy results in some inaccuracies. Only when $\rho C_p = 1$ and the mesh size at both sides of the interface is the same, the balance matches. The problem has been solved implementing the conservative form of the energy equation (equations 6.7, being $\phi_v = \rho_o (\mathbf{v}_f \cdot \mathbf{S}_f)$), where

the argument inside the derivatives in the l.h.s. is $(\rho_o C_p T)$. Theoretically, both sets of equations should provide the same solution; however, due to the discretisation strategy, the differences can become relevant.

$$\frac{\partial T}{\partial t} + D(\phi_v T) - D(\alpha G(T)) - S_{thermal}/(\rho_o C_p) = 0 \tag{6.6a}$$

$$\frac{\partial T_{solid}}{\partial t} - D(\alpha_{solid} G(T_{solid})) - S_{thermal,solid}/(\rho_{o,solid} C_{p,solid}) = 0 \tag{6.6b}$$

$$\frac{\partial(\rho_o C_p T)}{\partial t} + D(C_p\ \phi_v T) - D(kG(T)) - \rho_o\ C_p\ S_{thermal} = 0 \tag{6.7a}$$

$$\frac{\partial(\rho_{o,solid} C_{p,solid} T_{solid})}{\partial t} - D(k_{solid} G(T_{solid})) - \rho_{o,solid}\ C_{p,solid}\ S_{thermal,solid} = 0 \tag{6.7b}$$

The thermally and electromagnetically coupled algorithm where the conservative set of equations are used, hereafter called ϕT-PISO_FSI, is shown in Algorithm 6.

The consequences of dealing with one or other algorithm are shown in the application case 3, in Chapter 9, where the flow is buoyant predominant and unsteady and, hence, the discrepancies between solutions obtained by both algorithms are large.

Algorithm 6 (ϕT-PISO_FSI)

1. Initial map for $\mathbf{v}$, p_d, T *and* ϕ.

Evaluate $\phi_v = \rho_o * (\mathbf{v}_f \cdot \mathbf{S}_f)$ *and Lorentz force.*

2. Prepare momentum discrete coefficients (eq. 5.15b) for FLUID DOMAIN:

$\mathbf{A_v}(\mathbf{v})\ \mathbf{v} \ \rightarrow\ \mathrm{fvm::ddt}(\rho_o, \mathbf{v}) + \mathrm{fvm::div}(\phi_v, \mathbf{v}) - \mathrm{fvm::laplacian}(\nu\rho_o, \mathbf{v})$
$-(\mathbf{j} \times \mathbf{B_o}) + \beta_o \rho_o (T - T_o)\,\mathbf{g}$

$\mathbf{a_v}(\mathbf{v}) \ \rightarrow\ \mathrm{diag}(\mathbf{A_v}(\mathbf{v}))$ $\qquad$ $\mathbf{H_v}(\mathbf{v}) \ \rightarrow\ -(\mathbf{A_v}(\mathbf{v})\ \mathbf{v} - \mathbf{a_v}(\mathbf{v})\ \mathbf{v})$

Solve momentum equation $\mathbf{A_v}(\mathbf{v})\ \mathbf{v} = -\mathrm{fvc::grad}(p_d)$ *to get* $\mathbf{v}^*$

3. PISO loop, with a fixed number of iterations, in LIQUID DOMAIN.

Velocity pre-conditioner: $\mathbf{v}' = \left(\frac{\mathbf{H_v}(\mathbf{v}^*)}{\mathbf{a_v}(\mathbf{v}^*)}\right)$, $\quad \phi'_v = \rho_o * (\mathbf{v}'_f \& \mathbf{S}_f)$

Solve pressure equation (pdEqn): $\mathrm{fvm::laplacian}(\frac{\rho_o}{\mathbf{a_v}(\mathbf{v}')}, p_d) = \mathrm{fvc::div}(\phi'_v)$

Correct ϕ'_v *by means of the implicit terms* $\phi_v = (\phi_v)' - \mathrm{pdEqn.flux}$

Solve continuity equation for error estimation: $\mathrm{fvc::div}(\phi_v)$

Correct $\mathbf{v}'$ *and update boundary conditions* $\mathbf{v} = \mathbf{v}' - \frac{1}{\mathbf{a_v}(\mathbf{v}')} * \mathrm{fvc::grad}(p_d)$

4. Thermal coupling with COUPLED DOMAINS:

Solve temperature equation ON COUPLED DOMAINS:

FLUID DOMAIN: $\mathrm{fvm::ddt}(\rho_o\ C_p, T) + \mathrm{fvm::div}(\phi_v\ C_p, T)$
$-\mathrm{fvm::laplacian}(k, T) = \rho_o\ C_p\ S_{thermal}$

SOLID DOMAIN: $\mathrm{fvm::ddt}(\rho_{o,solid}\ C_{p,solid}, T_{solid})$
$-\mathrm{fvm::laplacian}(k_{solid}, T_{solid}) = \rho_{o,solid}\ C_{p,solid}\ S_{thermal,solid}$

5. Magnetic coupling with COUPLED DOMAINS:

Evaluate the magnetic flux term in LIQUID DOMAIN $\chi = (\sigma_f * (\mathbf{v}_f \times \mathbf{B_o}_f))\& \mathbf{S}_f$

Solve electric potential equation ON COUPLED DOMAINS:

FLUID DOMAIN: $\mathrm{fvc::div}(\chi) - \mathrm{fvm::laplacian}(\sigma, \phi) = 0$

SOLID DOMAIN: $-\mathrm{fvm::laplacian}(\sigma_{solid}, \phi_{solid}) = 0$

Evaluate j_n *in LIQUID and SOLID DOMAINS (eq. 5.13)*

Evaluate the Lorentz force in LIQUID DOMAIN (eq. 5.14)

Solve conservation of j_n *for error estimation in LIQUID DOMAIN:* $\mathrm{fvc::div}(j_n)$

6. Next time step.

Determine the time step.

Return to step 2.

Note: OpenFOAM's notation has been used

Part III

Applications

7 U-bend in the HCLL blanket

7.1 Motivation

In this first application case, the integrated effect of volumetric heating and magnetic field on tritium transport is being addressed, as applied to EU HCLL-TBM. In the EU HCLL-TBM the eutectic Pb-15.7Li flows radially at low velocities (see section 2.3.1 for a detailed description of the blanket), and, due to the high thermal load, buoyant structures might appear. Tritium, generated in and transported by liquid metal, may eventually permeate through channel walls. Moreover, some tritium trapping zones may exist, as flow vortical structures or helium bubbles. The accurate prediction of tritium inventories and permeation fluxes is of crucial interest for safety reasons.

Some efforts towards such tritium prediction have been already carried out by tritium system codes, as the one by Gastaldi *et al.* (2008) for HCLL DEMO. Such codes are proposed on the basis of steady state flow process diagrams. A more detailed tritium model was implemented in TMAP7 1D tritium transport tool by Moreno and Sedano (2009). Future improvements of such system codes are expected to include, in a modular way, computational refinements at component channel level. In this direction, it is necessary to include fluid interaction effects. However, very few authors deal with thermal MHD coupling and tritium analysis at the same time. For example, Gabriel *et al.* (2007) apply the CEA code *cas3m*, a finite element based CFD tool, to study two simplified HCLL radial channels, coupled by means of internal boundary conditions.

The study is 2.5D and assumes steady state. Tritium is transported considering it as a passive scalar. The main conclusion is that natural convection in HCLL is not relevant for tritium permeation, increasing by less than 10 % the permeation rate.

The study carried out in the frame of the present application case analyses the buoyant flow in a simplified HCLL blanket similar to that studied by Gabriel *et al.* (2007), but considering the influence of the U-bend that joints both radial channels near the First Wall. Indeed, a simplified 3D configuration, corresponding to one inlet and one outlet channels (both between one stiffening plate and two adjacent cooling plates) and the 180 degree bend, is analysed. For more details on the complete HCLL geometry for ITER reactor see, e.g., Rampal and Aiello (2006). Geometry and dimensions of the simulated channel are sketched in figure 7.1.

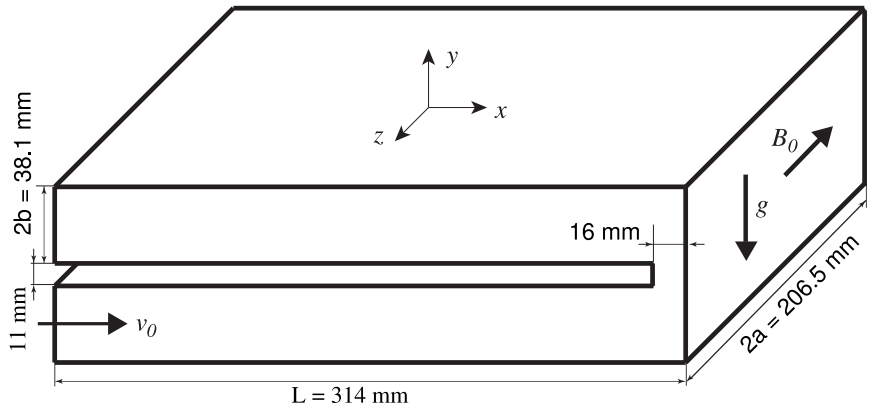

Figure 7.1: Geometry and dimensions for the simplified channel

The study includes first a case set-up description. Modelling strategies are then summarised (section 7.2). In section 7.3, results of the study are given considering both electrically insulated and perfectly conducting walls. This section includes an analysis of the effect of channel boundary conditions (inlet/outlet) on tritium transport, and a sensitivity analysis of tritium permeation fluxes to diffusivity and solubility parameters. A final discussion is included in section 7.4.

7.1.1 Flow parameters and case set-up

The fluid is the eutectic Pb-15.7Li. Properties are taken from the Pb-15.7Li database (Mas de les Valls *et al.* 2008) obtaining a Prandtl number of $1.51 \cdot 10^{-3}$ at 723.15 K. In

this study, a magnetic field of 0.7 T perpendicular to the flow (z axis in figure 7.1, which represents the toroidal direction in the fusion reactor) is considered.

Setting boundary conditions is a main concern. Real boundary conditions would imply to simulate the whole blanket, even the manifolds and connecting pipes; any partial analysis of the real geometry includes non realistic boundary conditions. For the simplified system depicted in figure 7.1, velocity is assumed to be known and uniform at the inlet, walls are non-slip and a free outlet with fixed pressure is imposed. Temperature is uniformly fixed at inlet and walls at 723.15 K. The incoming flow at the inlet contains no tritium and, at the outlet, tritium leaves the domain only by advection since tritium concentration gradient is set to zero. Wall boundary conditions follow equation 7.3.

Source terms (heat deposition and tritium generation) in equations 3.11 and 7.1 decrease with r, the distance from the first wall along the radial direction (x axis in figure 7.1). For the present study they are somewhat arbitrarily chosen to be:

$$\begin{aligned} S_{thermal} &= 5.37 \cdot 10^7 \; exp(-88.91 \; r) \; + \; 5.15 \cdot 10^6 \; exp(-8.069 \; r) \quad \text{W/m}^3 \\ S_{tritium} &= 6.64 \cdot 10^{-7} \; r^{(-1.2473)} \quad \text{mol/m}^3\text{s} \end{aligned}$$

which are of the order of magnitude of the values found in ITER-TBM.

Under HCLL-ITER specifications, liquid metal flows at a low velocity, between 0.1–1 mm/s, which corresponds, according to dimensions in figure 7.1, to Reynolds number of 48–480 at the inlet ($Re_{D_{in}}$). The Hartmann number is $Ha_a = 1740$ and the interaction parameter or Stuart number is $N_a = 3935$. Here, subscripts indicate the chosen characteristic dimension. For Grashof number evaluation, the temperature gradient is calculated from the integration of the heat deposition in a single inlet/outlet channel obtaining $\Delta T_L = S_{thermal} L/k = 2.51$ and $Gr_L = 5.2 \cdot 10^9$. For tritium transport, the Schmidt number is $Sc = 134$.

When thermal MHD coupling is studied, as in the present case, and following the normalisation from Bühler (1998) (and explained in detail in section 3.3.2), the equivalent Re number is $Gr_a/Ha_a^2 = 61.2$ and the corresponding interaction parameter is $Ha_a^4/Gr_a = 5 \cdot 10^4$. Peclet number is $Pe = Gr \; Pr \; Ha^{-2} = 0.9$ which is not very small, so convective heat transfer has to be considered. Since $Gr_a/Ha^{5/2} = 41$, inertia effects cannot be omitted.

The above mentioned scenario, with high Ha and Gr numbers, indicates that mesh refinement is a key issue, specially at boundary layers and in the U-bend. However, an optimal mesh in terms of mesh induced errors is not affordable for computational limitations. Hence, relatively coarse meshes are to be used and mesh errors quantified. In the following analyses, three different meshes have been defined as a function of

the number of nodes in Hartmann boundary layers (of width a/Ha) and side boundary layers (of width $a/Ha^{1/2}$). The finest mesh is called *mesh 2* and is the one considered *a priori* as reasonably adequate for MHD simulations, as it has 4 nodes in each Hartmann boundary layer, 10 nodes in each side boundary layer, and 777600 nodes for the whole system. The coarsest mesh, called *mesh0*, has only 2 nodes in the Hartmann boundary layers and 5 in the side ones, with 92784 nodes. *Mesh 1* is an intermediate mesh between *mesh 0* and *mesh 2* with 291168 nodes in total.

A mesh quality analysis can be done comparing the obtained numerical pressure drop along the U-bend (Δp_d).

7.2 Modelling strategies

Related to thermal MHD coupling, two different algorithms have been used. For electrically insulated walls, the ϕ-FSPM algorithm described in section 5.2.1 is coupled with heat transport equation following the same procedure explained in section 6.1. However, for perfectly conducting walls, due to ϕ-FSPM algorithm limitations, the ϕT-PISO algorithm described in section 6.1 is used. Some results concerning to the perfectly insulating walls have been repeated with the more accurate ϕT-PISO algorithm with almost the same results.

The application of Boussinesq hypothesis is justified since density variation is less than 0.1 % for the range of temperatures expected in the HCLL. However, further analyses in order to evaluate the effects of this assumption are needed.

Time marching is accomplished differently for the FSPM algorithm than for the PISO one. In the case of the FSPM algorithm, an internal loop for each time step is implemented in order to permit real transient simulations. However, the code can also be run in a pseudo-transient mode by simply reducing the number of internal loop iterations (in this study this number is 2). When PISO algorithm is considered, since the error is drastically reduced with only 2 iterations, there is no need of using the pseudo-transient mode.

In the Breeding Blanket, tritium breeds at the same time as helium; hence, a detailed tritium transport model needs to account for 1) the possible helium bubble nucleation and its coalescence, 2) effect of bubbles on liquid metal transport, 3) surface tritium transport including tritium recombination at bubble surface and wall interaction, and 4) other effects as Soret effect, for example. Thus, the physical phenomena are complex and require dealing with two phase flows and material property uncertainties, among others. In this direction, an attempt on tritium/helium transport in HCLL has been carried out by Batet *et al.* (2011) and Fradera *et al.* (2011). In the

present work it is assumed that tritium does not alter liquid metal properties nor flow behaviour and the presence of helium bubbles has been omitted. Thus, a passive scalar transport equation (equation 7.1) is sufficient to model tritium transport and has been sequentially implemented. In equation 7.1, C_T stands for tritium concentration, D_T for the tritium diffusion coefficient, and $S_{tritium}$ for the tritium generation.

$$\frac{\partial C_T}{\partial t} + (\mathbf{v} \cdot \nabla) C_T = \nabla \cdot (D_T \nabla C_T) + S_{tritium} \tag{7.1}$$

The terms in equation 7.1 can be non-uniform in space and non-constant in time. In fact, it typically follows an exponential correlation with the distance to the First Wall, as mentioned in previous section.

Despite the walls are not modelled in the present study, they can be indirectly considered in tritium analysis by means of the wall boundary condition. In this case, with equal tritium partial pressure in the liquid metal (LM) and the structural material (SM), Sievert's law can be used to find a relationship of both tritium concentrations at fluid-solid interface (equation 7.2). By imposing equal tritium fluxes at both sides of the interface, tritium concentration gradient can be obtained from equation 7.3, where $C_{T,LMi}$ and $C_{T,SMi}$ are tritium concentration at the fluid/solid interface for the liquid metal and the structural material (Eurofer) respectively, k_s is Sievert's coefficient and d the wall width. In order to obtain equation 7.3, it has been considered that tritium concentration at outer solid wall is zero. This clearly is an oversimplification of reality and implies that both: 1) recombination is instantaneous at the outer solid wall, and 2) concentration in cooling helium channels is zero as well.

$$\frac{C_{T,LMi}}{k_{s,LM}} = \frac{C_{T,SMi}}{k_{s,SM}} \tag{7.2}$$

$$D_{T,LM} \left(\frac{\partial C_{T,LM}}{\partial x} \right)_i = D_{T,SM} \left(\frac{\partial C_{T,SM}}{\partial x} \right)_i \simeq - \frac{D_{T,SM} k_{s,SM}}{k_{s,LM}} \frac{C_{T,LMi}}{d} \tag{7.3}$$

7.2.1 Numerical aspects

Simulations are carried out with a (Bi-)Conjugate Gradient solver. In all the equations, the Central Difference scheme has been used for the spatial discretisation whereas temporal discretisation is first order accurate. Steady state criterion is fixed with a relative error of 10^{-6} for each field map. For full transient simulations, convergence criterion at each time step is set to 0.5 10^{-6}.

Since all terms in momentum equation are solved implicitly except the Lorentz force term, this latter term is the critical one for stability purposes. As justified in section

5.2.3, the time step criteria has been chosen from a 1D stability analysis obtaining the constraint ($\mathcal{L} \leq 2.0;\ \mathcal{L} \neq 1$), according to equation 7.4.

$$\mathcal{L} = \frac{\sigma\ B_0^2\ \Delta t}{\rho} \tag{7.4}$$

It is well known that for a 3D case, the time constrain must be reduced. In OpenFOAM, and for pure 3D hydrodynamic cases where the Courant number $\mathcal{C}$ has to be fulfilled, it is suggested to use always $\mathcal{C} \leq 0.2$ instead of the 1D constrain $\mathcal{C} \leq 1$. In the present study, following the previous suggestion, $\mathcal{L} \leq 0.2$ has been imposed and it has been proved to be sufficient for a stable and accurate simulation.

When in the following, a pseudo-transient simulation is done with the FSPM algorithm, two internal iterations are carried out. However, since time restrictions are met, results are still accurate, as will be proved in section 7.3. In fact, for the transient simulations, usually a high number of iterations is only needed for the first time steps and, afterwards, 2–3 iterations are sufficient.

7.3 Results

The basic analysis is split in three parts: (1) pure hydrodynamics, (2) MHD, and (3) heat transfer MHD. Afterwards, two different analysis in order to understand the obtained results are carried out including (i) the effect of channel boundary conditions (inlet/outlet) on tritium transport, and (ii) a sensitivity analysis of tritium permeation fluxes to diffusivity and solubility parameters.

7.3.1 Pure hydrodynamics

In the pure hydrodynamic analysis neither a magnetic field nor temperature gradients exist in the system. The hydrodynamic analysis not only is essential for a better understanding of the phenomena that appear in more complex flow situations, but it also provides the correct scenario for the initial ITER phases (without plasma) and for some real transients.

The system has been simulated for different Reynolds numbers using *mesh 2* (defined in section 7.1.1) without time step inner convergence (pseudo-transient simulation), although the time step accuracy criterion given in section 7.2.1 (i.e., $\mathcal{L} \leq 0.2$) is met. Reynolds numbers are chosen to cover the range of typical HCLL-ITER values.

Figure 7.2 illustrates how higher Reynolds numbers correspond to larger jet velocities at the U-bend. Considering that only one of the several sub-channels of a HCLL-

$Re_{D_{in}}$	flow	mesh	Δp_d (Pa)
48	steady	0	$1.47 \cdot 10^{-3}$
		1	$1.57 \cdot 10^{-3}$
		2	$1.61 \cdot 10^{-3}$
480	unsteady	0	$5.69 \cdot 10^{-2}$

Table 7.1: Summary of simulation results for the pure hydrodynamic case

like breeder unit is simulated, it seems better to use the Reynolds number at the gap (so is, using the gap hydraulic diameter instead of the channel's) to characterise the oscillating behaviour, given the fact that the flow at the gap would be several times larger for the same $Re_{D_{in}}$ in a simulation of the whole unit. For $Re_{gap} \gtrsim 395$ the flow becomes unstable because shear instability appears (Drazin 2002); oscillations propagate through the outlet channel.

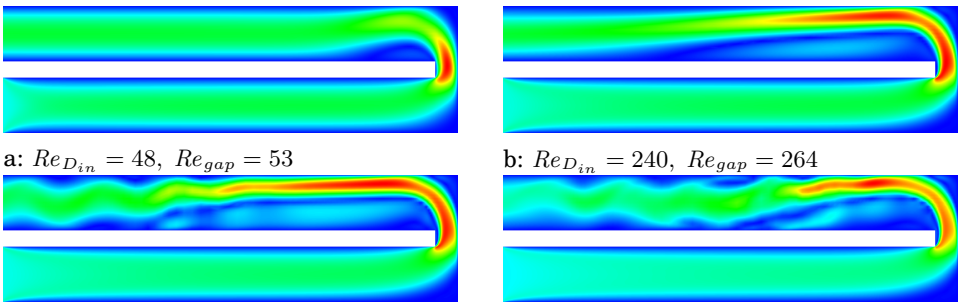

a: $Re_{D_{in}} = 48,\ Re_{gap} = 53$ b: $Re_{D_{in}} = 240,\ Re_{gap} = 264$

c: $Re_{D_{in}} = 360,\ Re_{gap} = 395$ d: $Re_{D_{in}} = 480,\ Re_{gap} = 527$

Figure 7.2: Velocity maps as a function of Reynolds number. Flow starts being unstable at about $Re_{D_{gap}}$ of 395.

Oscillations in HCLL have not been reported before. This result is of crucial interest because oscillations could affect the structure of the module.

Mesh influence on pressure drop is analysed for $Re_{D_{in}} = 48$ (corresponding to case *a* of figure 7.2) using the three meshes mentioned in section 7.1.1. Although the calculated pressure drop (table 7.1) slightly depends on the mesh refinement, values are quite similar.

All the above mentioned results have been obtained by means of pseudo-transient simulations in the FSPM, defined in section 7.2, which is only correct if a steady solution is known to exist. In case of instabilities, oscillations or turbulence, full transient simulation (converged at each time step) is required. Both pseudo-transient and full

transient simulations have been compared for the channel at $Re_{D_{in}} = 480$ (case *d* of figure 7.2) and *mesh 0*. A phase space map for both simulations is shown in figure 7.3(a). The phase space map is obtained defining the critical point p_{critic}, corresponding to the middle length of the outlet channel, where the oscillations are more severe. Time evolution of the magnitude of velocity is shown in figure 7.3(b). Both the periodic nature of the solution and the order of magnitude of velocity obtained in the two cases are very similar, but the period of the oscillation is not. Thus, for a detailed quantification of the period of the oscillation and hence, the vibrations that the flow induces in the structure, a full transient simulation would be required.

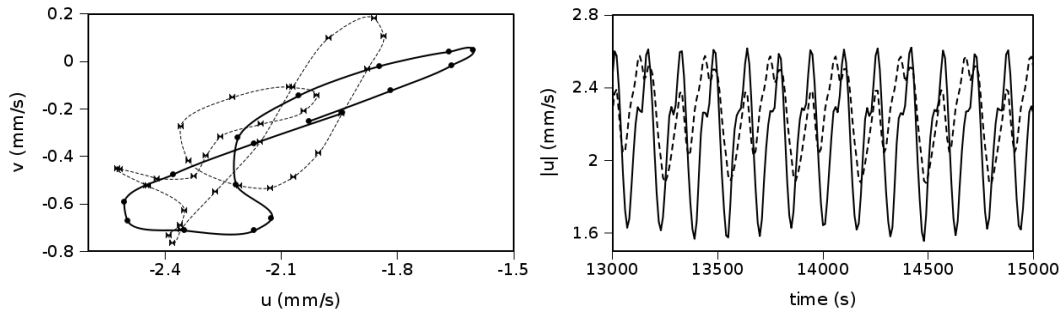

(a) (b)

Figure 7.3: (a) phase space map and (b) temporal evolution at p_{critic} point for the pure hydrodynamic case with $Re_{D_{in}} = 480$ and *mesh 0*. Comparison of full transient simulations (solid line) and pseudo-transient simulations (dotted line).

7.3.2 MHD

Since walls in HCLL blanket have a finite conductivity C_w, a realistic MHD simulation of the U-channel would imply to electrically couple the walls with the fluid. This coupling could be achieved either by modelling the solid and numerically coupling both domains, or by applying the thin wall boundary condition from Müller and Bühler (2001), which is, theoretically, only valid for fully developed flows. Since fluid-solid coupling is required not only for the MHD simulation but also for the thermal and tritium analysis, the simulation of solid wall coupling is of utmost interest. It is beyond the scope of the present study such coupling analysis and, as a first approximation of the influence of magnetoconvection on tritium transport, two idealised electric boundary conditions are considered at walls: 1) a perfect insulated wall $C_w = 0$ and b) a perfect conducting wall $C_w = \infty$. Both cases are analysed separately.

Perfectly insulated walls

At $Ha_a = 1740$ and considering perfectly insulated walls, simulation results show how the Lorentz force is able to stabilise the oscillating flow obtained at $Re_{D_{in}} = 480$, as shown in figure 7.4(a). The stabilised flow is 2D except in Hartmann boundary layers.

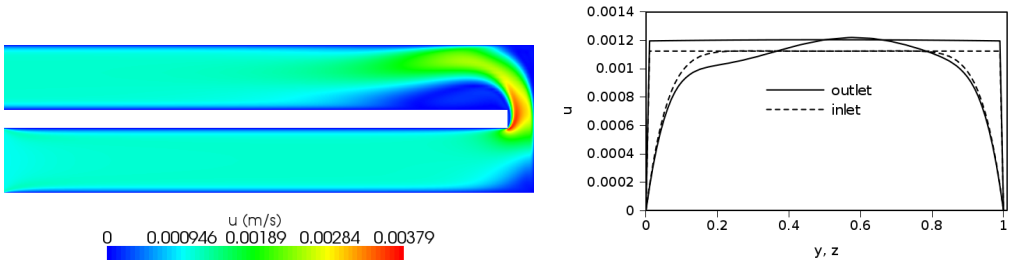

(a) Velocity field

(b) Velocity profiles

Figure 7.4: Velocity field and profiles for $Re_{D_{in}} = 480$ and $Ha_a = 1740$, with $C_w = 0$. Velocity profiles are taken at the central x plane.

In figure 7.4(b) velocity profiles in the centre of the inlet and outlet channels are shown. As expected, the inlet channel has a symmetric flow profile and can be considered as almost fully developed flow. However, flow in the outlet channel cannot be considered as fully developed because of the stagnation zone appearing just after the U-bend.

Electric potential field for $Re_{D_{in}} = 480$ is shown in figure 7.5 for the central plane perpendicular to the magnetic field, nevertheless, the electric potential is constant along magnetic field lines. As expected, isolines for electric potential follow velocity streamlines. It is more interesting to observe the electric current stream lines, shown in the same figure. It is obvious that the entrance effect is quite important, the flow needing almost half of the inlet channel to become fully developed (a fixed homogeneous inlet velocity has been imposed). At the bend, the jet and the reattachment zone provoke a quite complicated electric current path that is not developed until almost the end of the outlet channel.

Pressure drop for all MHD simulations is shown in table 7.2. As expected, MHD effects increases pressure drop. When comparing Δp_d obtained for the three meshes (at $Re_{D_{in}}$ 480), it can be seen that *mesh 1* is required to obtain an accurate simulation.

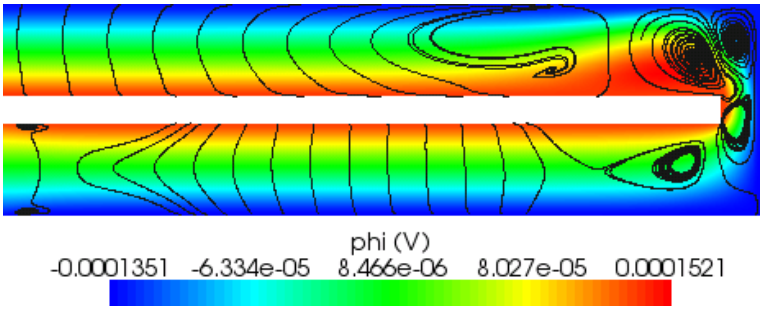

Figure 7.5: Electric potential field and electric current streamlines for $Re_{D_{in}} = 480$ and $Ha_a = 1740$, with $C_w = 0$.

Perfectly conducting walls

When perfectly conducting walls are considered, the M-shaped profile is recovered except for the bend, as shown in figure 7.6(b). At the bend, the jet is reduced in size but involves a higher velocity (figure 7.6(a)). However, the magnetic field is strong enough to obtain not only a stable solution but also a developed flow profile at the outlet channel.

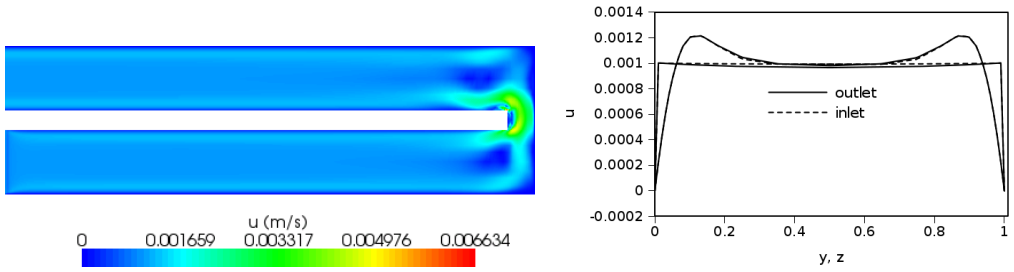

(a) Velocity field

(b) Velocity profiles

Figure 7.6: Velocity field and profiles for $Re_{D_{in}} = 480$ and $Ha_a = 1740$, with $C_w = \infty$. Velocity profiles are taken at the central x plane.

Electric potential field for $Re_{D_{in}} = 480$ is shown in figure 7.8 for the central plane perpendicular to the magnetic field. In order to capture the electric potential gradients at the bend, the chosen legend does not allow to see the electric potential gradient in the inlet and outlet channel, which is qualitatively similar to the one shown in figure 7.5 for insulated walls. In contrast of what occurs when $c_w = 0$, in the perfectly conducting walls case the electromagnetic coupling is strong enough to reduce substantially the entrance effect and to minimise the zone affected by the U-bend; thus, the electric

current streamlines look quite regular all along the system, except for the bend itself. At the bend, strong electric potential gradients appear related to each of the vortices shown in figure 7.7 for more clarity. If walls conductivity is to be considered finite, higher velocity jets are expected at the inlet and outlet channels and, thus, an even more complicated flow profile at the U-bend.

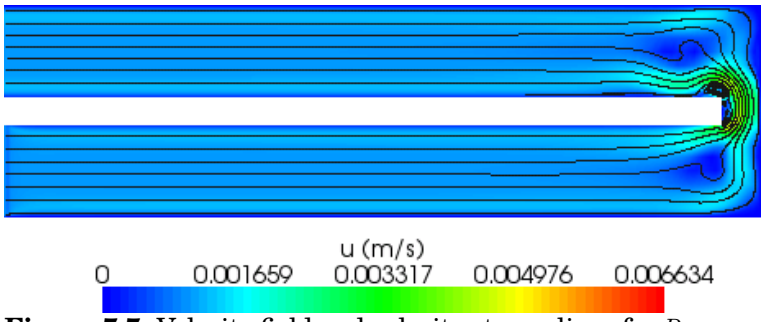

Figure 7.7: Velocity field and velocity streamlines for $Re_{D_{in}} = 480$ and $Ha_a = 1740$, with $C_w = \infty$.

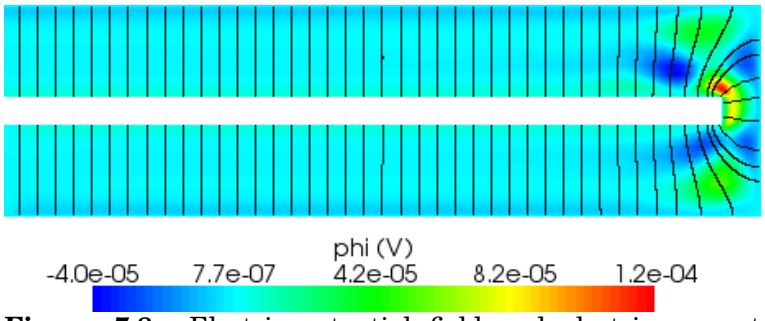

Figure 7.8: Electric potential field and electric current streamlines for $Re_{D_{in}} = 480$ and $Ha_a = 1740$, with $C_w = \infty$.

As expected, according to table 7.2, pressure drop is substantially increased when conducting walls are considered. When a mesh quality analysis is performed with perfectly conducting walls, it can be stated that *mesh0* is fine enough to provide good Δp_d precision. Thus, under the studied flow conditions, perfectly conducting walls need less mesh refinement than insulating walls.

C_w	$Re_{D_{in}}$	flow	mesh	Δp_d (Pa)
0	48	steady	0	$1.60 \cdot 10^{-2}$
	480	steady	0	$1.85 \cdot 10^{-1}$
			1	$1.90 \cdot 10^{-1}$
			2	$1.91 \cdot 10^{-1}$
∞	48	steady	0	$2.50 \cdot 10^{1}$
	480	steady	0	$2.49 \cdot 10^{2}$
			1	$2.48 \cdot 10^{2}$

Table 7.2: Summary of simulation results for the MHD study

7.3.3 Heat transfer MHD

In this section, the complete coupled case with $Gr_L = 5.21 \cdot 10^9$ has been analysed. Mainly, all simulations are carried out with *mesh 0* due to simulation run time limitations. Indeed, if τ_{CPU} represents the CPU time in seconds needed to simulate 1 physical second, and the case has been run in parallel with openMPI and using 3 cores (Intel Core2 2.5MHz), for $Re_{D_{in}} = 480$ and $C_w = 0$, τ_{CPU} is 184 and 1500 for *mesh 0* and *1* respectively. Also, for $Re_{D_{in}} = 480$ and $C_w = \infty$, the simulation time is reduced to $\tau_{CPU} = 133$ and 580 for *mesh 0*and *mesh 1* respectively. If the mean residence time (without considering vortices) in the whole system is about 800 s, then, the minimum simulation time is 1.7, 13.9, 1.2 and 5.4 days respectively. If an unsteady solution exists, the required simulation time is increased substantially. Simulations with a finer mesh (*mesh 2*) can take a couple of months.

As shown in the following, unstable flows are often found. Thus, full transient simulations are always done, either for FSPM and PISO algorithms. As stated in section 7.2, the FSPM has been used for cases where $C_w = 0$ whereas PISO algorithm, due to its better coupling, is used for $C_w = \infty$ cases. PISO algorithm reaches exactly the same solution for $C_w = 0$ than FSPM.

Perfectly insulated walls

The complete coupled case with $Gr_L = 5.21 \cdot 10^9$ has been analysed for *mesh0* and velocity and temperature field maps are shown in figure 7.9. For both Reynolds numbers 48 and 480, vortices appear in the solution at the inlet, due to Rayleigh-Bénard instability, the bend and the outlet, as shown in figures 7.9(a) and 7.9(c). The inlet vortex is indirectly imposed by the inlet temperature boundary condition; in fact, in real blankets the lead lithium is already heated when it enters the blanket and thus, such vortex is not expected to exist. The most relevant aspect is that, for both Reynolds numbers, the

same maximum velocity is obtained in vortices located at the bend despite the fact that the difference in the flow rate is of one order of magnitude. At the same time, when comparing this peak velocity with the one obtained in the pure MHD case (7.4(a)), it can be stated that the value obtained in the MHD thermofluid simulation is not a direct consequence of the channel narrowing. All this indicates the natural convection predominance in the flow.

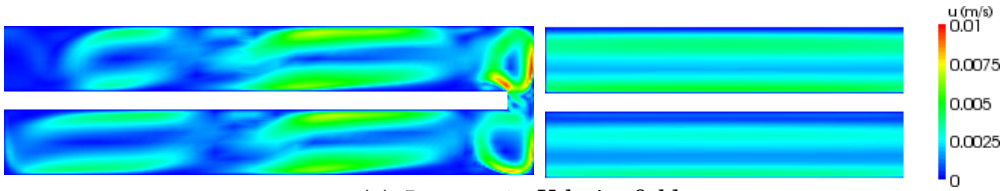

(a) $Re_{D_{in}} = 48$, Velocity field

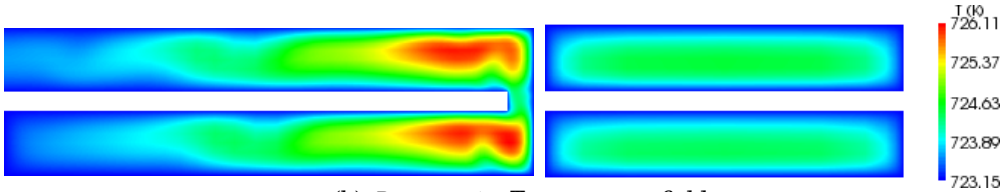

(b) $Re_{D_{in}} = 48$, Temperature field

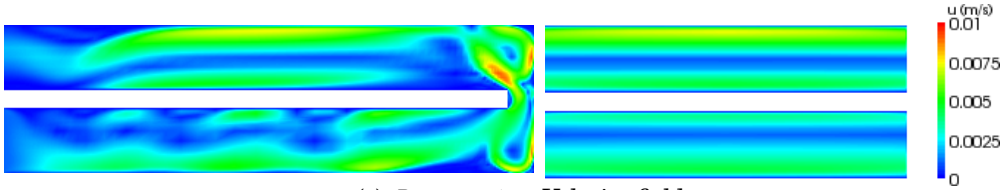

(c) $Re_{D_{in}} = 480$, Velocity field

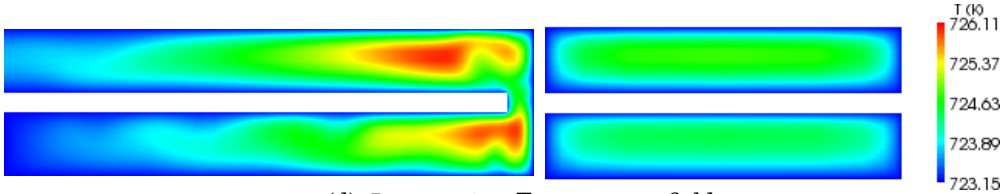

(d) $Re_{D_{in}} = 480$, Temperature field

Figure 7.9: Velocity and temperature fields with $Ha_a = 1740$ and $Gr_L = 5.21 \cdot 10^9$, with $C_w = 0$. Middle plane for z axis on the left and middle plane for x axis on the right. Results obtained with *mesh 0* and Boussinesq hypothesis.

In figures 7.9(b) and 7.9(d) it can be observed how the temperature field experiences two hot spots before and after the bend, with similar temperatures in both cases. However, due to fixed wall temperature boundary condition, the U-bend itself is at a lower temperature. The temperature field is clearly 3D whereas vortices are stretched in z

axis, along magnetic field lines. For the sake of clarity, the stream lines are sketched for the case with $Re_{D_{in}} = 48$ in figure 7.10.

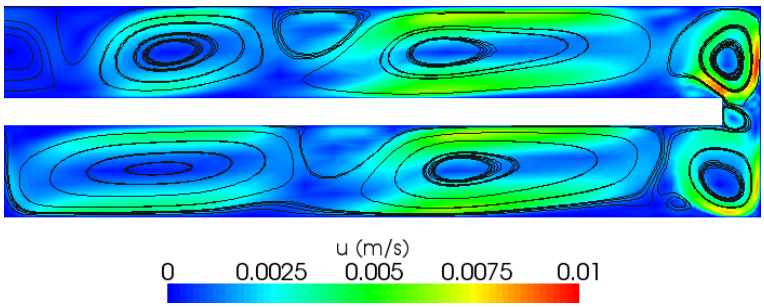

Figure 7.10: Streamlines for $Re_{D_{in}} = 48$, $Ha_a = 1740$ and $Gr_L = 5.21 \cdot 10^9$, with $C_w = 0$.

Despite the similarity in the buoyancy force and the natural convection phenomenon, the case with $Re_{D_{in}} = 480$ is steady whereas the case with $Re_{D_{in}} = 48$ is periodic. Flow oscillation is mainly located at the U-bend, as shown by the phase space map in figure 7.11. The period of such oscillation is around 27 s and only alters the temperature field by 0.2 degree.

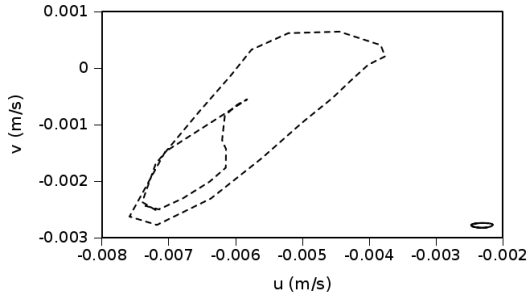

Figure 7.11: Phase space map for $Re_{D_{in}} = 48$, $Ha_a = 1740$ and $Gr_L = 5.21 \cdot 10^9$, with $C_w = 0$. Solid line (bottom right corner) represents a point at the centre of the outlet channel and dotted line represents a point at the bend.

For $Re_{D_{in}} = 480$ the simulation has also been carried out for *mesh1* in order to analyse mesh quality. Results show (figure 7.12) that a substantially different velocity field is obtained with a finer mesh, despite buoyant predominance of the flow still exists and

the same maximum velocity at vortices is obtained (see figure 7.9(c) for comparison). This discrepancy is evident when comparing pressure drop (Δp_d) in table 7.3. Therefore, finer meshes would be necessary to accurately determine flow profiles.

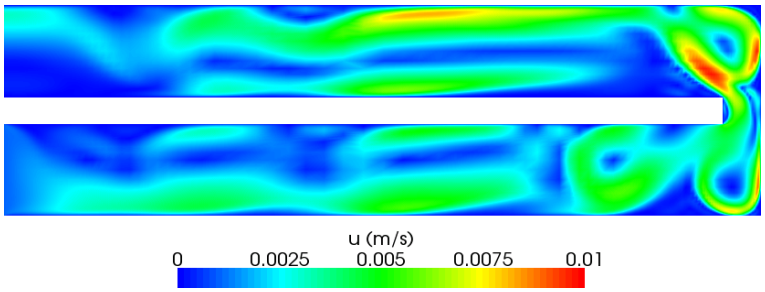

Figure 7.12: Velocity field for $Re_{D_{in}} = 480$, $Ha_a = 1740$ and $Gr_L = 5.21 \cdot 10^9$, with $C_w = 0$ and *mesh1*.

The pressure drop for both Reynolds numbers is of the same order of magnitude (see table 7.3). This indicates again that buoyancy dominates flow convection. Comparing these pressure drops with the ones obtained for purely MHD cases, it can be stated that buoyancy increases substantially Δp_d, specially at low Reynolds numbers.

Electric potential isocontours for $Re_{D_{in}} = 48$ are plotted in figure 7.13. ϕ isocontours take the form of elongated structures which coincide with velocity vortices. Indeed, from the simplified set of equations from Bühler (1998), it is already shown that the Laplacian of the electric potential equals the vorticity component in the magnetic field direction.

It is worth mentioning that a fixed wall temperature is not realistic, but provides a first overview on the main phenomena. In a fluid-coupling simulation, such temperature gradients perpendicular to walls would not appear and vortices might be damped. But then, if the complete blanket were to be simulated, the observed flow perturbations due to buoyancy could be increased. Therefore, more sophisticated simulations are needed to fully determine the nature of the flow in a real HCLL blanket.

Perfectly conducting walls

When perfectly conducting walls are considered, the same maximum velocity, located at the bend (figures 7.14(a) and 7.14(c)), is observed for both Reynolds numbers, as in case $C_w = 0$. Despite this fact seems to indicate the predominance of the natural convection in the flow, velocity streamlines make evident the complex flow (at low velocities) obtained for Reynolds 48, whereas for Reynolds 480 the flow is fully developed every-

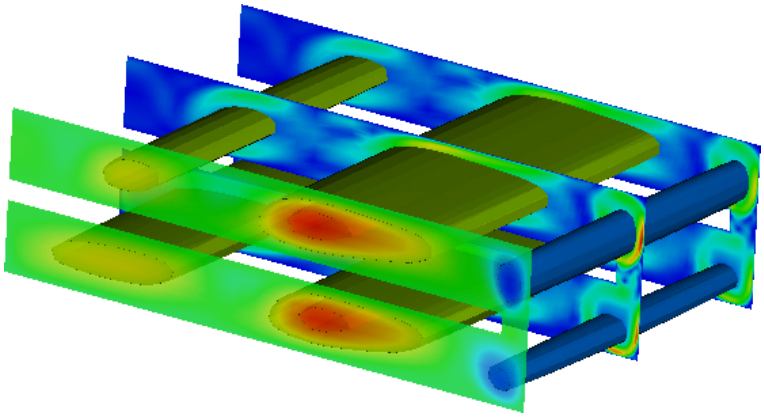

Figure 7.13: Electric potential isocontours for $Re_{D_{in}} = 48$, $Ha_a = 1740$ and $Gr_L = 5.21 \cdot 10^9$, with $C_w = 0$. The front plane shows the electric potential field whereas the central and the back planes show the velocity field.

where except at the bend itself. For both Reynolds the solution is unstable but flow oscillations are mainly located at the bend. At $Re_{D_{in}} = 48$, the period of such oscillation is around 200 s and only alters the temperature field by 0.1 degree, while at $Re_{D_{in}} = 480$ the oscillations are minimum (less than 0.01 degrees) with a low period (around 0.15 s). It has to be mentioned that the inlet vortex is damped for Reynolds 48 whereas it is suppressed for Reynolds 480. Temperature fields from figures 7.14(b) and 7.14(d) are quite similar to those for perfectly insulated walls.

Electric potential isocontours for $Re_{D_{in}} = 48$ are plotted in figure 7.15. As commented previously, peak values of ϕ are located at the velocity vortices, the sign of ϕ indicating the direction of the rotation. The electric current stream lines are similar to those obtained for the $C_w = 0$ MHD case in 7.8.

For $Re_{D_{in}} = 480$ the simulation has also been carried out for *mesh1* in order to analyse mesh quality. However, the obtained results are very similar to the ones obtained for *mesh 0*, as demonstrated by the resulting pressure drop in table 7.3. Therefore, accurate results are already obtained with *mesh 0*.

In contrast of what was obtained for $c_w = 0$, pressure drop is quantitatively different (one order of magnitude) for each Reynolds number. Such difference indicates the predominance of electromagnetic pressure drop.

7.3.4 Influence of boundary conditions on tritium permeation

Bred tritium travels along the channel, its inventory being affected by permeation through walls. Evaluation of tritium inventory and tritium permeation ratio (hereafter called TPR) is needed for, among other, safety reasons.

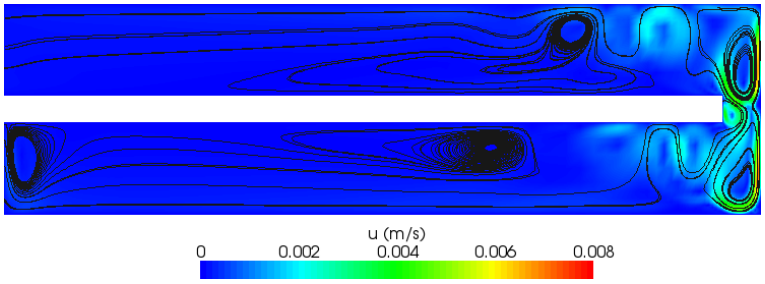

(a) $Re_{D_{in}} = 48$, Velocity field

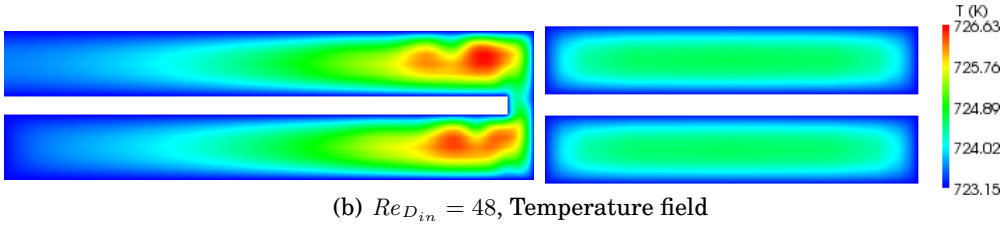

(b) $Re_{D_{in}} = 48$, Temperature field

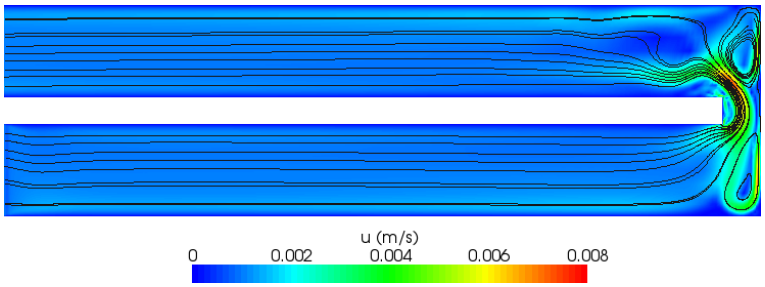

(c) $Re_{D_{in}} = 480$, Velocity field

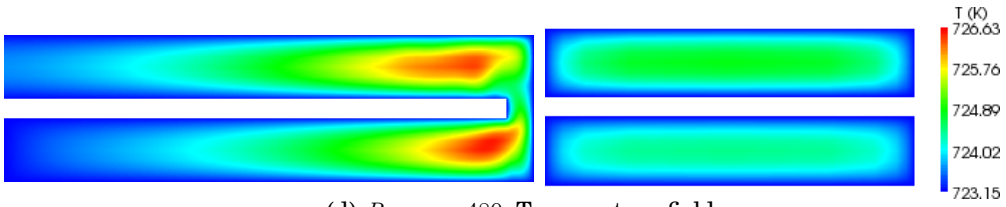

(d) $Re_{D_{in}} = 480$, Temperature field

Figure 7.14: Velocity and temperature fields with $Ha_a = 1740$ and $Gr_L = 5.21 \cdot 10^9$, with $C_w = \infty$. Middle plane for z axis on the left and middle plane for x axis on the right. Results obtained with *mesh 0* and Boussinesq hypothesis.

As mentioned in section 7.2, tritium transport can be simplified considering tritium as a passive scalar. Of course, a more realistic approach taking into account helium and its effects on tritium transport if helium bubbles are present, would provide different TPR and tritium inventories than those obtained here. However, present results can be seen as a preliminary TPR analysis with the aim of providing the influence on TPR under different flow (and numerical) situations.

In the case study sketched in figure 7.1 three critical boundary conditions need to be

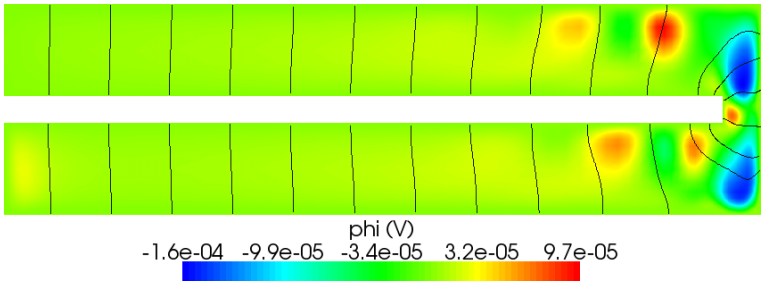

Figure 7.15: Electric potential field and electric current streamlines for $Re_{D_{in}} = 48$, $Ha_a = 1740$ and $Gr_L = 5.21 \cdot 10^9$, with $C_w = \infty$.

C_w	$Re_{D_{in}}$	flow	mesh	Δp_d (Pa)
0	48	unsteady	0	0.66
	480	unsteady	0	0.62
			1	0.55
∞	48	unsteady	0	23.9
	480	unsteady	0	247.9
			1	247.1

Table 7.3: Summary of simulation results for the MHD thermofluid study

defined: at the inlet, wall and outlet.

Concerning to wall boundary condition, equation 7.3 has been used with a tritium diffusion coefficient in lead lithium of 10^{-9} m^2/s, which is of the same order of magnitude as the expected one (Mas de les Valls *et al.* 2008). Tritium solubility coefficient in lead lithium is somewhat arbitrarily chosen to be $2.9 \cdot 10^{-3}$ mol/m^{3}Pa$^{0.5}$, which is in the middle of the range (two orders of magnitude) of the proposed values. A sensitivity analysis for these values is shown in section 7.3.5. For the structural material coefficients, a diffusivity of $1.12 \cdot 10^{-8}$ m^2/s and a solubility coefficient of $1.825 \cdot 10^{-2}$ mol/m^{3}Pa$^{0.5}$ have been considered according to Esteban *et al.* (2007).

In the present study, a zero tritium concentration is imposed at inlet, which would correspond to an idealised Tritium Extraction System (TES). At the outlet, since vortices may be present, a zero gradient boundary condition is fixed for the outcoming flow, whereas a zero concentration is fixed for the incoming flow. In the following, the outlet boundary condition is analysed in more detail.

Tritium concentration fields for perfectly insulating walls are shown in figure 7.16. At both Reynolds numbers, high concentration is obtained at vortices and at the outlet. Vortices are expected to transport a high tritium concentration due to the stagnant velocities and high residence time, so that it is reasonable to obtain a high tritium concen-

tration in vortices. What is not so straightforward is to identify the reason for the high concentration obtained at the outlet, specially for $Re_{D_{in}} = 48$, as can be seen in figure 7.17 (note that tritium concentration at the outlet more than doubles the concentration at the middle plane of the outlet channel). This unphysical result is a combination of the presence of vortices crossing the outlet section and the outlet tritium boundary condition.

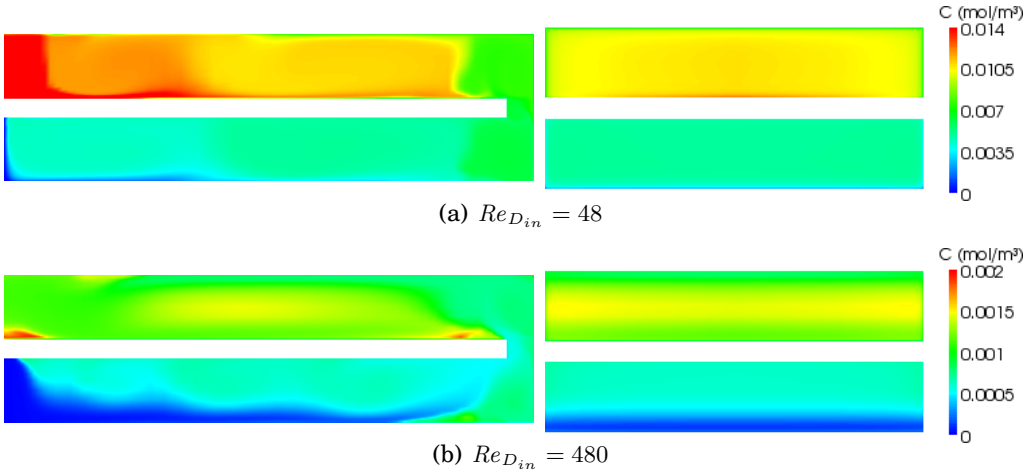

(a) $Re_{D_{in}} = 48$

(b) $Re_{D_{in}} = 480$

Figure 7.16: Passive scalar concentration fields for $D_T = 10^{-9}$ m/s and $k_s = 2.9 \cdot 10^{-3}\ mol/m^3 Pa^{0.5}$, with $Ha_a = 1740$, $Gr_L = 5.21 \cdot 10^9$ and $C_w = 0$. Middle plane for *z* axis on the left and middle plane for *x* axis on the right. Results obtained with *mesh 0* and Boussinesq hypothesis.

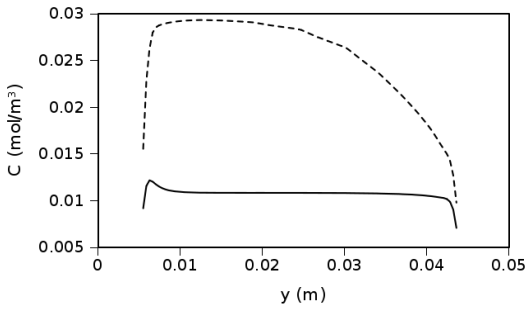

Figure 7.17: Passive scalar concentration profiles for $D_T = 10^{-9}$ m/s and $k_s = 2.9 \cdot 10^{-3}\ mol/m^3 Pa^{0.5}$, with $Re_{D_{in}} = 48$, $Ha_a = 1740$, $Gr_L = 5.21 \cdot 10^9$ and $C_w = 0$. Profiles are obtained on *y* axis at the centre of the outlet channel (solid line) and at the outlet (dotted line).

Parameter	$0L$	$0.25L$	$0.50L$	$0.75L$
TPR %	20.7	18.8	17.9	17.7
J_{Ha} %	9.8	12.9	13.1	12.9
$C_{T,mean}$ (mol/m^3)	$8.0 \cdot 10^{-3}$	$5.0 \cdot 10^{-3}$	$3.6 \cdot 10^{-3}$	$2.1 \cdot 10^{-3}$

Table 7.4: Cut-off position effect on tritium permeation analysis for $Re_{D_{in}} = 48$, $Ha_a = 1740$, $Gr_L = 5.21 \cdot 10^9$ and $C_w = 0$, using *mesh 0*. The diffusion coefficient is $D_T = 10^{-9}$ m^2/s and the Sievert's constant $k_s = 2.9 \cdot 10^{-3}$ mol/m^{3}Pa$^{0.5}$.

In order to obtain a TPR which does not depend on the outlet boundary condition, a different set up has been studied based on limiting the region where the tritium source exists, avoiding tritium generation near the inlet/outlet of the U-channel. Therefore, four different cut-off positions have been defined: at $0L$, $0.25L$, $0.5L$ and $0.75L$, where L is the channel length (figure 7.1). All cases have been simulated using the wall boundary condition based on Sievert's law and with $Re_{D_{in}} = 48$. In table 7.4 results are listed. Three parameters are compared: 1) TPR, 2) $C_{T,mean}$ which is the mean tritium concentration and is representative of the tritium residence time, and 3) J_{Ha}, which is the percentage of permeation through the Hartmann walls and indicates 3D effects (Notice that the Hartmann walls surface is 15 % of the total wall surface).

As expected, average tritium concentration ($C_{T,mean}$) decreases as the cut-off position increases. Permeation is substantially reduced for $0.25L$ case and, later for $0.50L$ case, whereas $0.75L$ case experiences little TPR reduction. The first reduction is caused by the independence between core solution and outlet boundary condition, which is exactly the aim of this study. However, the second TPR reduction can be explained by the fact that tritium source term is neglected at the central stagnant region between two main vortices (figure 7.10). Stagnant zones imply, if any tritium is generated there, high tritium concentrations (and residence times) and, thus, high permeation fluxes if such stagnant zone is close to the wall. Therefore, the most realistic TPR value is the one obtained from $0.25L$ case.

From results in table 7.4, it can be stated that if a 2.5D simulation were to be carried out by omitting Hartmann walls, the error on TPR would be around 10 % ($J_{Ha} \sim 10$).

7.3.5 Sensitivity analysis on tritium physical data

A large span of data regarding tritium transport parameters (D_T, k_s) exists in literature. Therefore, a sensitivity analysis on this parameters is of crucial interest. Here, the analysis is carried out considering both insulating and perfectly conducting walls. In order to avoid the influence of the outlet boundary condition, tritium source term close to the outlet is neglected (case $0.25L$ from previous section). Among the available

data (see Mas de les Valls *et al.* (2008) for a summary of it), two extreme values of D_T and k_s have been chosen. Values for diffusion coefficient are chosen from Terai *et al.* (1992) (DT, $2.41 \cdot 10^{-9}$ m^2/s) and Reiter (1991) (DR, $1.41 \cdot 10^{-9}$ m^2/s). Sievert's constant has been chosen from Aiello *et al.* (2006) (SA, $2.56 \cdot 10^{-2}$ mol/m^{3}Pa$^{0.5}$) and Reiter (1991) (SR, $1.01 \cdot 10^{-3}$ mol/m^{3}Pa$^{0.5}$). All correlations are evaluated at 700 K and parameters are considered constant with temperature.

From comparing results (table 7.5) for $Re_{D_{in}} = 48$ and $C_w = 0$, the huge difference on TPR as a function of the chosen D and k_s values becomes obvious. In fact, it can be stated that: 1) main uncertainties come from k_s value and larger k_s implies lower TPR, and 2) D_T value uncertainty is not so critical and its relationship with TPR is not straightforward due to the complex vortical flow. Facing such differences on TPR as a function of (mainly) k_s, tritium transport analysis only make sense in terms of design optimisation, but not for an accurate TPR estimator.

By comparing results for different Reynolds numbers, it can be observed that larger Reynolds numbers reduce tritium concentration and limit TPR, as had been stated by Reimann *et al.* (2006).

From results in table 7.5 the mesh quality can also been analysed. Indeed, for Reynolds 480, two different meshes have been used (*mesh 0* and *mesh 1*). The obtained results indicate that perfectly conducting walls, and under the studied flow conditions, requires less mesh resolution than insulating walls.

The most important result from this sensitivity analysis is, probably, the fact that almost the same TPR is obtained for both C_w values. This phenomena can be explained by the fact that high velocities are present near walls for both $C_w = 0$ and $C_w = \infty$. Indeed, for perfectly insulating walls, big vortical structures appear due to thermal instabilities, whereas when perfectly conducting walls are considered, side boundary jets exist.

7.4 Discussion

In the present work, modelling of integrated effect of volumetric heating and magnetic field on tritium transport in HCLL blanket-type channels is studied. To this aim, a 3D MHD algorithm based on an electric potential formulation, together with temperature coupling using Boussinesq hypothesis, has been used.

The HCLL blanket-type channel that has been studied corresponds to an inlet and outlet lead lithium channel between two cooling plates and the stiffening plates. It includes the gap that connect both channels at the first wall. Hence, the simulated channel can be defined as a U-bend where the fluid travels perpendicular to the (toroidal)

$Re_{D_{in}}$, C_w, mesh	case	TPR %	J_{Ha} %	$C_{T,mean}$ (mol/m^3)
48, 0, *mesh0*	DT-SA	3.4	18.1	$5.8 \cdot 10^{-3}$
	DT-SR	33.2	10.0	$4.2 \cdot 10^{-3}$
	DR-SR	29.8	9.8	$4.4 \cdot 10^{-3}$
	DR-SA	3.5	18.2	$5.8 \cdot 10^{-3}$
480, 0, *mesh0*	DT-SA	0.4	15.3	$6.7 \cdot 10^{-4}$
	DT-SR	5.6	12.3	$6.3 \cdot 10^{-4}$
480, 0, *mesh1*	DT-SA	0.4	14.9	$6.3 \cdot 10^{-4}$
	DT-SR	5.2	11.8	$5.9 \cdot 10^{-4}$
48, ∞, *mesh0*	DT-SA	3.5	17.9	$5.6 \cdot 10^{-3}$
	DT-SR	25.8	17.1	$4.4 \cdot 10^{-3}$
480, ∞, *mesh0*	DT-SA	0.4	11.6	$5.1 \cdot 10^{-4}$
	DT-SR	4.7	12.6	$4.9 \cdot 10^{-4}$
480, ∞, *mesh1*	DT-SA	0.4	11.2	$5.2 \cdot 10^{-4}$
	DT-SR	4.8	12.1	$4.9 \cdot 10^{-4}$
	DR-SR	4.2	12.0	$4.9 \cdot 10^{-4}$
	DR-SA	0.5	10.6	$5.2 \cdot 10^{-4}$

Table 7.5: Tritium permeation analysis for $Ha_a = 1740$ and $Gr_L = 5.21 \cdot 10^9$, for different diffusivities and Sievert's constants.

magnetic field. The thermofluid MHD flow in such a channel is complex and, in order to give a major insight in the phenomenon, different scenarios have been studied including: 1) pure hydrodynamics with Reynolds 48 and 480, 2) MHD with Hartmann number 1740 and 3) MHD thermofluid coupling with Grashof $5.21 \cdot 10^9$.

A jet is produced at the narrowing of the channel in the U-bend for pure hydrodynamic simulations. When this jet reaches the wall, it can experience shear stress instabilities that travel all along the outlet channel. Flow shear instabilities have been found for $Re_{gap} \gtrsim 395$. Considering that only one out of four sub-channels of the breeder unit have been simulated, the actual critical Reynolds might be slightly different.

For the MHD simulation, two different electric boundary conditions have been considered: insulating walls and perfectly conducting walls. When insulating walls are considered, the magnetic field is able to suppress the formation of the jet at low Reynolds numbers, and the flow becomes stable among the studied Reynolds. For perfectly conducting walls, the flow is also stable but the M-shaped profile is obtained all along the channels except at the bend. Mesh requirements are lower for perfectly conducting walls than for insulated walls, since no jet reaches the wall. The effect of a fixed homogeneous inlet velocity is evident for the insulated walls case as a large entrance zone is found. However, when perfectly conducting walls are considered, the flow is fully-developed almost everywhere except at the bend itself. Further study is needed

in this direction mainly by increasing the Hartmann number to real ITER conditions and by electrically coupling the fluid and the structural material, which would provide larger jets at side boundary layers.

The considered thermal source, which is of the same order of magnitude as the expected in ITER reactor, is sufficient to induce natural convection in the studied channels, with independence of the Reynolds number and electric wall boundary condition. Such natural convection can become unstable with periodic velocity oscillations at the U-bend. However, thermal induced oscillations are not significant. When insulating walls are considered, vortices appear all over the channel due to inverse thermal gradients between fluid and fixed wall temperature. In contrast, for perfectly conducting walls, such vortices are mainly found at the bend, specially at high Reynolds numbers. It is worth mentioning that a fixed wall temperature is not realistic, but provides a first overview on the main phenomena. In a fluid-coupling simulation, high temperature gradients perpendicular to walls would not appear and vortices might be damped. Also, with a higher Hartman number, the ratio $Gr/Ha^{5/2}$ would be substantially lower and inertia effects could be neglected, which was observed by Vetcha *et al.* (2009) for the DCLL blanket design. However, if the complete blanket were to be simulated, the observed flow perturbations due to buoyancy could be increased. To sum up, more sophisticated simulations are needed to fully determine the nature of the flow in a real HCLL blanket.

A tritium transport analysis has been performed on the obtained MHD thermofluid simulations. A detailed analysis on the effect of inlet/outlet boundary condition has been done. Moreover, a sensitivity analysis to diffusivity and solubility is carried out. As expected, the large uncertainties on tritium physical data (specially Sievert's coefficient) produce large variations on the obtained permeation ratio, varying about one order of magnitude. Another expected result is that, at higher Reynolds number, tritium permeation is reduced. What was not expected is that, under the studied flow conditions, permeation ratio is independent on wall electric conductivity. This is explained by the existence of velocity jets either in insulated walls and perfectly conducting walls. In the first case, the jets correspond to the M-shaped profile. In the second case, jets are part of vortical structures caused by thermal instabilities. Therefore, it is urgent to analyse the flow behaviour considering fluid-solid coupling.

To sum up, further studies considering fluid-solid coupling, a higher Hartman number and a more detailed geometry of the blanket are needed. However, for an accurate tritium permeation ratio prediction, it is urgent to develop new and precise measurements of tritium transport data, specially of solubility.

8 2D analysis of the TECNO_FUS blanket concept

8.1 Motivation

In the frame of the Spanish Breeding Blanket Technology Programme TECNO_FUS, that started on 2008, the dual-coolant liquid metal blanket for DEMO specifications is considered for design refinements. The proposed new blanket concept is hereafter called TECNO_FUS blanket. It can be considered as a transition option towards a self-cooled concept, which implies higher theoretical thermal efficiency. Design is relatively simple (thus robust) exploiting the excellent thermal and breeding properties of the alloy Pb-15.7Li and the satisfactory non-structural functions of SiC inserts under irradiation (to be developed and tested). At the present status of the study (Juanas and Fernández 2009), liquid-metal channels are conceived as vertical insulated banana-shape (poloidal) channels where main refinements include: a) optimised channel geometry and b) improvements on flow channel inserts.

This application case intends to yield firsts simulation results concerning liquid metal flow profiles and thermal behaviour. Such (preliminary) analysis can provide useful data not only to understand the flow in TECNO_FUS channels but also to optimise the design.

In this chapter, an explanation of the TECNO_FUS proposal is given (section 8.1.1) along with a brief overview of flow characterisation and model (section 8.1.2). Previous overviews of phenomena related to liquid metal blanket designs, and available

strategies to model them, have been presented for several designs or proposals, including Reimann *et al.* (1995) for the Self-cooled blanket, Reimann *et al.* (2006) for the HCLL, and Smolentsev *et al.* (2008) for the US DCLL. All them focus on critical blanket issues such as MHD pressure drop, electrical insulation, three dimensional flows, multi-channel effect, buoyancy-driven flows, etc. A recent summary on MHD thermofluid critical issues in blankets can be found in Smolentsev *et al.* (2010). Following such studies, in section 8.1.2, the expected MHD flow in TECNO_FUS blanket is characterised and, accordingly, some modelling strategies are proposed.

The applied modelling strategies used in the present study are described in section 8.2, whereas results can be found in section 8.3. The modelling study focuses on optimisation of thermal performance of the TECNO_FUS blanket, which means a maximised LM temperature increment (between inlet and outlet) while keeping the Eurofer temperature below its limits (about 550ºC) and minimising the thermal stresses across the FCI. Final discussion of the study can be found in section 8.4.

8.1.1 Definition of the proposed TECNO_FUS blanket concept

According to Juanas and Fernández 2009, the reactor is split in 12 segments, each one consisting of two inboard and three outboard blanket modules, the latter shown in figure 8.1. Initially, each module consists of four banana-shaped (poloidal) channels, two in the front and two in the back, connected at the bottom of the module. Liquid metal (Pb-15.7Li) flows from the inlet manifold at the top, down through the front channels and returns through the back channels up to the outlet manifold. The blanket poloidal length L is 9193 mm, so it covers almost all the poloidal dimension of the reactor. Each channel has a radial depth $2b$ of 355 mm and a toroidal width $2a$ of 610 mm. More details of the geometry are given in figure 8.1.

The present status of the design considers, with 3450 MW of fusion power, a neutron wall loading for the blanket of 2.1 MW/m^2. The amplification factor, defined as the effective thermal deposition (deposited and generated power) divided by the original thermal deposition, is estimated to be 1.16. The thermal load for the TECNO_FUS geometry has been obtained from a 2D-axisymmetric neutronic assessment using a simplified, onion layer-like, isometric model from Catalán *et al.* (2010). At the current status of the study, no poloidal distribution is considered. From results in Catalán *et al.* (2010), the thermal load can be expressed following an exponential curve (equation 8.1), where r stands for the distance to the First Wall.

$$S_{thermal} = 12\mathbf{exp}(-4.8r) + 40\mathbf{exp}(-20r) \qquad \mathrm{MW/m^3} \tag{8.1}$$

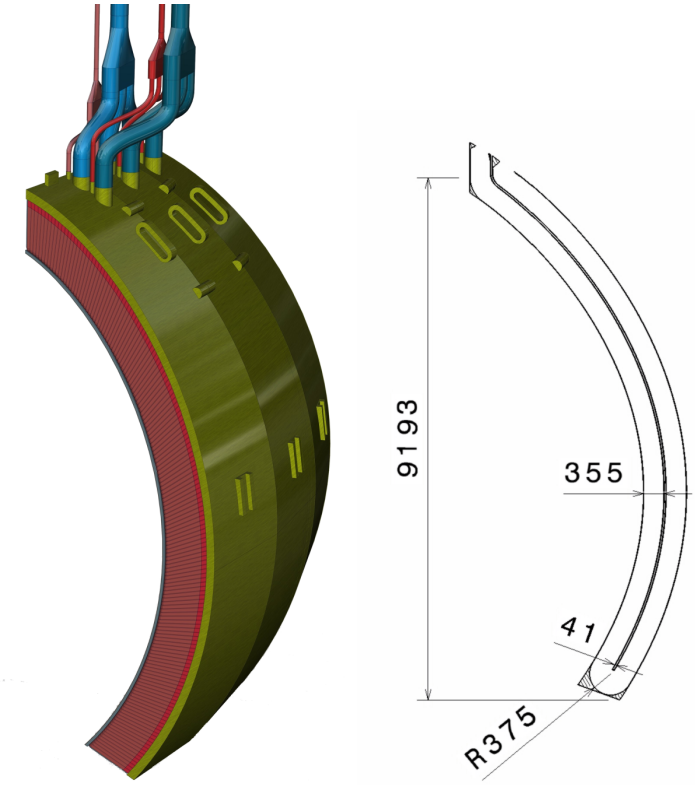

Figure 8.1: Three outboard blanket modules forming a segment (left) and module dimensions in mm (right) for the present TECNO_FUS proposal from Juanas and Fernandez (2009)

Improvements on the above mentioned neutronic load and channel geometry are currently being carried out, however, minor changes are expected on MHD thermofluid properties.

As liquid metal (LM) flows, it experiences a huge thermal load caused both by thermal deposition from plasma's reaction and by neutron reactions in PbLi. At the same time, the large magnetic field, responsible for plasma confinement, interacts with the flow velocity inducing electric currents and, thus, generating the Lorentz force that opposes the flow. All of this results in a considerable increase of fluid temperature at the inlet channel only diminished by helium cooling channels at the walls. Preliminary TECNO_FUS blanket characterisation considers a helium average temperature of 400 ^{o}C and an inlet LM temperature of 450 ^{o}C. A LM temperature gradient of 300 ^{o}C would be desirable to permit efficient heat extraction through a super-critical CO_2 heat exchanger. Thus, the flow rate should be high enough to avoid excessive thermal stresses on the structure but, at the same time, able to provide a high LM outlet temperature. MHD pressure drop is not an aspect of major concern due to the presence of flow channel inserts (FCIs). Indeed, the present TECNO_FUS blanket concept con-

siders the FCIs to be directly in contact with the steel so that no pressure equalisation openings are needed. Thus, a reasonable reduction of the MHD pressure drop can be achieved with relatively low values of the FCI electrical conductivity.

8.1.2 Flow characterisation and model

Considering a toroidal magnetic field of 7 T, the Hartmann number for the previously defined TECNO_FUS blanket is $Ha_a = 51390$. Velocity specifications lay in the range of $0.1 - 1.0$ m/s, which corresponds to a Reynolds number at the inlet of $Re_{D_{in}} = 3.3 \cdot 10^5 - 10^6$. Therefore, parameter $R = Re_a/Ha_a = 4.4 - 44.2$ for TECNO_FUS concept lays in the range of US DCLL and self-cooled blanket designs. For the estimation of the Grashof number (Gr), a characteristic temperature scale has been defined as $\Delta T = \bar{S}_{thermal}\, b^2/\lambda$, which is associated with the average radial thermal load $\bar{S}_{thermal}$ and the liquid metal conductivity λ. For the TECNO_FUS blanket, $Gr_b = 2.8 \cdot 10^9$ is obtained, which is in accordance with the dual-coolant concept (Smolentsev *et al.* 2010). All dimensionless numbers have been calculated using the PbLi database from Mas de les Valls *et al.* (2008).

Under the above mentioned flow conditions, and considering the large poloidal length of each banana-shaped channel, the flow could be modelled using the two-dimensional set of equations from Sommeria and Moreau (1982) (SM82) which include an extra diffusive term in the momentum equation due to the contribution of Hartmann boundary layers. Such system of equations has already been commented in section 5.3. Main differences between 3D and 2D models rely on boundary layers at side walls. The obtained 2D boundary layers might differ from Shercliff boundary layers (in real 3D flows) because of the different origin of each one, as pointed out by Pothérat (2007). Therefore, 2D results, while of great value, should be contrasted with detailed 3D simulations.

In contrast, for specific complex flow zones, such as the 180^o turn at the bottom of the module where the four channels merge, or the inlet and outlet manifolds, a three-dimensional numerical code must be applied in order to accurately capture the main flow parameters, such as the pressure drop and the local Nusselt number. Indeed, manifolds and complex geometries are responsible for the major part of the total pressure drop and it can not be reduced significantly using insulating FCI, acting uniquely as thermal insulators. The required 3D MHD code could consider the inductionless approximation, but special emphasis should be placed on conserving electric currents (see for example Ni *et al.* 2007). Such 3D algorithm could be improved with the Hartmann wall function from Bühler (1994) (see section 5.2.4), or more sophisticated ones from Hunt and Ludford (1968) and Pothérat *et al.* (2002).

Under the above mentioned $Re_{D_{in}}$, MHD turbulence is expected to exist. Following the Ha_a–Re_a diagram in Smolentsev and Moreau (2007), the liquid metal flow in the TECNO_FUS proposal would correspond to the Q2D region. This implies that all three dimensional effects are confined in the thin Hartmann layers at the walls perpendicular to the magnetic field, where almost all Ohmic and viscous forces occur. The existing turbulence models have been described in section 4.1.3.

Electrical coupling between the LM channel and walls could give rise to the multi-channel effect (McCarthy and Abdou 1991, Molokov 1993). However, since FCIs electric conductivity is very low, and provided that the thickness of the FCIs is sufficient, the multi-channel effect would be minimised. Anyway, the velocity jets that would appear in the side boundary layers, caused by non-zero wall conductance ratio, could experience flow instabilities and, hence, fluctuations. Such fluctuations are not expected to alter the core flow profile, as stated in Cuevas *et al.* (1997).

According to results in sections 7 and 9, thermal effects are expected to be 3D. Indeed, in HCLL-type LM channels, such effects might represent up to 10 % of the total thermal losses. Therefore, despite using the SM82 set of equations for the MHD modelling, the temperature field should be solved by a 3D solver.

When comparing the characteristic velocity at which buoyancy forces balance Lorentz forces ($v_{o,MHD} = (Gr/Ha^2)(\nu/a) \sim 10^{-7}$ m/s), with the mean flow velocity ($0.1 - 1.0$ m/s), it is evident that buoyancy, despite the high Gr number, is not expected to play a relevant role on velocity profiles, even in the downward channel, where flow inertia and buoyancy oppose each other. Such effect is confirmed by the Archimedes Number (Gr/Re^2), which is below unity. In this direction, the Boussinesq hypothesis could be applied to couple both the heat transport and MHD equations. However, the applicability of this hypothesis under the high temperature gradient present in the LM channels should be verified. Moreover, thermal coupling between LM, FCI, structural material and helium cooling channels would provide a more accurate modelling of the thermal process. This, at the same time, could alter the flow profile.

8.2 Modelling strategies

The chosen algorithm to be applied in this second application case is the 2D MHD algorithm SM82, described in section 5.3.1, coupled with heat transport as explained in sections 6.1 and 6.4. Such algorithm has been chosen due to its reduced CPU costs. Indeed, since the poloidal flow in the TECNO_FUS blanket is to be modelled, with special focus on heat extraction and efficiencies, the 3D mesh required for the large poloidal length of each banana-shaped channel would be unaffordable with the available CPU

resources in our group.

Turbulence has been modelled following the 0-equation RANS MHD model from Smolentsev and Moreau (2006) (see section 5.3.1). As suggested by the authors, for an estimation of the turbulent thermal diffusivity, a turbulent Prandtl number of 1.1 has been considered. No extra correction has been introduced for thermal effects.

Since accurate steady state solutions are to be found, time marching is accomplished by two iterations for each time step and without velocity pre-conditioner (momentum equation is not explicitly solved). Simulations are carried out with a (Bi)-Conjugate Gradient solver. In all the equations, the Central Difference scheme has been used for the spatial discretisation whereas temporal discretisation is first order accurate. Steady state criterion is fixed with a relative error of 10^{-7} for each field map.

A special Robin type boundary condition has been applied in the external walls (in contact with the fluid domain), following equation 8.2, where U_{eq} stands for the overall heat transfer coefficient, $T_{b.c.}$ and T_{He} stand for the boundary and helium temperatures and n represents the surface normal vector. Equation 8.2 represents a 1D steady state thermal balance between the liquid metal interface (with subscript $b.c.$, as for boundary condition), and the helium cooling channels. Indeed, the heat flux that leaves the LM domain (by a thermal diffusive process following Fourier's law) equals the total heat extracted by helium.

$$U_{eq}\left(T_{b.c.} - T_{He}\right) \;=\; k\left(\frac{\partial T}{\partial n}\right)_{b.c.} \tag{8.2}$$

The overall heat transfer coefficient might include several thermal resistances as the thermal convection associate resistance in the cooling fluid (helium), and the thermal diffusive resistance of both the FCI and the structural material (Eurofer, EU). The final expression is shown in equation 8.3, where δ stands for the wall thickness.

$$U_{eq} \;=\; \frac{1}{h_{He}^{-1} \;+\; \frac{\delta_{FCI}}{k_{FCI}} \;+\; \frac{\delta_{EU}}{k_{EU}}} \tag{8.3}$$

The above mentioned temperature boundary condition is a fixed gradient based boundary condition. Thus, at each iteration, $(dT/dn)_{b.c.}$ is evaluated according to equation 8.2, where $T_{b.c.}$ corresponds to the previous iteration value. The user needs to specify both T_{He} and U_{eq} values.

As can be observed, the balance used in equation 8.2 corresponds to an idealised 1D flat wall balance, where no thermal generation exists in the solid domain. In fact, thermal loads would also exist in solid walls, but they are not considered in the present preliminary study. Moreover, the 1D idealisation might only be valid for small enough Biot numbers, which is not exactly the present case. In order to account for 2D heat

transfer, the fluid domain should be coupled with the solid domains (FCI and EU) following the coupling strategy described in section 5.2.5. A study in this direction has been carried out and discussed in section 8.3.2.

8.3 Results

This section is split into two different studies.

In the first study, a sensitivity analysis of Eurofer surface temperature to inlet velocity is carried out. As a required step, an analysis of mesh induced error is done in order to define an adequate mesh for further studies. Then, for different LM inlet velocities, the critical design parameters are evaluated and discussed, including: (a) LM temperature gain along the blanket ΔT_{LM}, (b) maximum Eurofer temperature $T_{max,EU}$, that must be kept below 550 ºC, and (c) thermal stresses across FCI layer ΔT_{FCI}.

The second study consists of a sensitivity analysis of FCI thermal conductivity. Such analysis includes a comparison between the coupled domain configuration, considering LM, FCI and Eurofer domains, and the single domain configuration corresponding to the LM domain with a Robin type thermal boundary condition at walls, following equation 8.2.

8.3.1 Sensitivity analysis of mass flow rate

TECNO_FUS blanket velocity specifications lay in the range of $0.1 - 1.0$ m/s. The exact value is to be defined as a function of several analyses including thermal efficiency, tritium extraction, thermal loads in the structural materials and FCI, and MHD pressure drop, among others. The present study is a preliminary analysis where an adequate flow rate is proposed in terms of maximum liquid metal temperature increment and Eurofer temperature below material limitations. In this direction, a sensitivity analysis of inlet velocity has been carried out.

Simulations are conducted considering electrically insulated walls due to the presence of FCIs. A non-slip boundary condition has been considered at walls, despite recent studies from Smolentsev (2009) indicate that interfacial slip will exist. A poloidal distribution of the thermal load (equation 8.1) with a poloidal factor of 1.2 has been considered, whereas keeping constant the average value of $S_{thermal}$ for the entire blanket. The poloidal factor represents poloidal non-uniformities of the thermal deposition due to plasma's shape; indeed, in the equatorial region of the blanket, the thermal load is expected to be larger than in the top and bottom zones. The resulting thermal load field map is shown in figure 8.2 left.

A fixed and uniform inlet temperature of 723.15 K has been assumed, which is a simplification of the real case but provides a reasonable initial map without preventing from a correct evaluation of the liquid metal temperature increment between inlet and outlet (ΔT_{LM}). The Robin type thermal boundary condition at walls shown in equation 8.2 has been implemented considering a constant helium temperature of 673.15 K and an overall (helium/Eurofer/FCI, equation 8.3) heat transfer coefficient of 3000 W/m^2 K; such value corresponds to the limiting case of infinite thermal convection coefficient for helium and hence, exclusively depends on wall thickness. Here, a FCI layer of 2 mm depth and thermal conductivity $k_{FCI} = 15$ W/m·K (Shinavski 2008) and an Eurofer layer of 6 mm depth and thermal conductivity $k_{EU} = 30$ W/m·K are considered. An infinite value of the helium thermal convection coefficient has been chosen due to the lack of accurate values under TECNO_FUS cooling channels conditions. The overall heat transfer coefficient may vary considerably for different FCI depths and thermal properties, which is studied in next section.

The obtained velocity field map does not differ substantially from the isothermal MHD case (without thermal load and with zero gradient thermal boundary conditions) for all studied inlet velocities, and only experience a soft tilt due to buoyancy. This behaviour, so different from that obtained in the DCLL design (Smolentsev *et al.* 2008), is due to the relevance of inertia in front of buoyancy. In figure 8.2, both relative velocity and temperature fields are shown for an inlet velocity of 0.4 m/s ($Re_a \sim 9 \cdot 10^5$). A unique stagnation zone is observed corresponding to the internal wall of the 180^o bend at the bottom of the blanket. Due to the high Lorentz force, no jet is formed after the abrupt bend. Due to the large thermal load present in the downcoming channel, and due to the accumulated enthalpy, the LM temperature increases as the flow reaches the bottom of the blanket. At the outcoming channel, the thermal load is substantially reduced and the cooling wall effect reduces the LM temperature. At the internal part of the bend, since the fluid velocity is lower, the temperature is maximum. Thus, the maximum Eurofer temperature is also expected at this region of the blanket.

Mean Nusselt number as a function of inlet velocity is shown in figure 8.3. For Nusselt number evaluation, the temperature differences between the inlet and helium channels is considered, together with the characteristic length a, following equation 8.4. In order to measure the discretisation error, three different non-structured meshes have been used; their number of nodes are, from coarse to fine, $6.6 \cdot 10^4$, $1.4 \cdot 10^5$ and $3.3 \cdot 10^5$, and hereafter they are referred as meshes 0, 1 and 2 respectively. Mesh 2 has four nodes in side boundary layers. For all meshes the velocity profiles are very similar, except in side boundary layers. Accordingly, it can be stated that calculated Nusselt number is strongly mesh-dependent. However, as shown in figure 8.3, for this

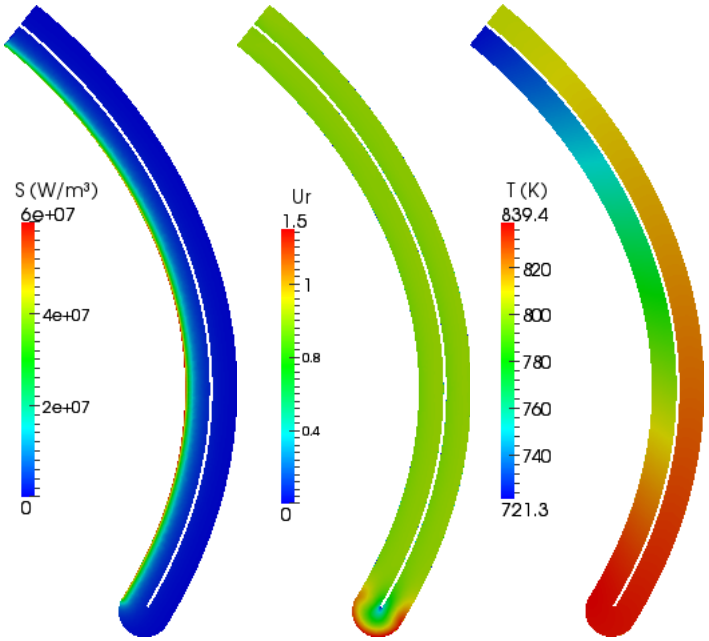

Figure 8.2: From left to right: thermal load, relative velocity field and temperature field for an inlet velocity of 0.4 m/s and mesh 2

preliminary analysis, sufficient accuracy is achieved with mesh 1.

$$Nu = \frac{(dT/dn)_{b.c.}}{(T_{inlet} - T_{He})/a} \tag{8.4}$$

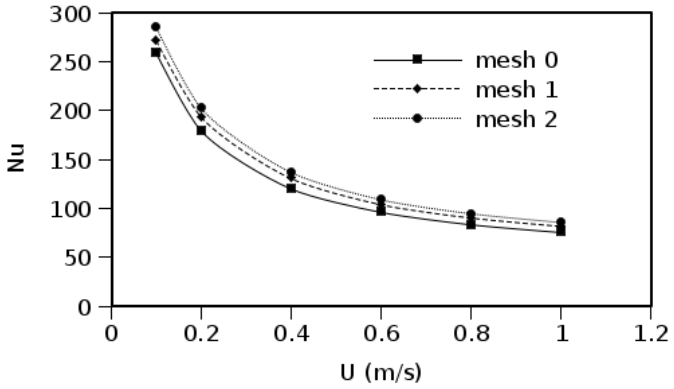

Figure 8.3: Nusselt number as a function of the inlet velocity

With the wall temperature and wall temperature gradient obtained from simulations, Eurofer surface temperature can be extrapolated applying Fourier law in the wall normal direction, for a given FCI depth and thermal conductivity, following equation 8.5. For material limitations, such temperature should be kept below 550^o C. An evolution of Eurofer surface temperature as a function of the inlet velocity is shown in figure 8.4. From these results, it can be stated that a minimum velocity of about 0.3 m/s is required under the considered thermal load and boundary conditions.

$$T_{max,EU} = max\left(T_{b.c.} - abs\left(\frac{(dT/dn)_{b.c.}\, k\delta_{FCI}}{k_{FCI}}\right)\right) \tag{8.5}$$

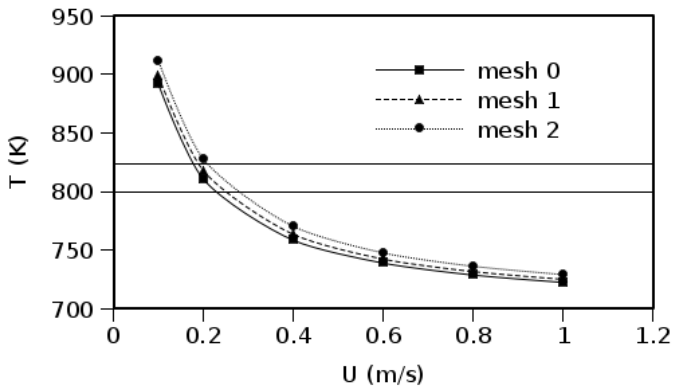

Figure 8.4: Extrapolated temperature at Eurofer surface as a function of the inlet velocity

For a better comprehension of the general thermal phenomena, several temperatures are given in figure 8.5. T_{mean} corresponds to the average LM temperature, while T_{max} is its maximum value. It can be observed that, as expected, mean flow temperature decreases with increasing mass flux. This, at the same time implies a lower ΔT_{LM}, evaluated as the difference between the mean outlet temperature T_{out} and the inlet temperature. $T_{max,wall}$ corresponds to the maximum LM temperature at walls. Comparing $T_{max,wall}$ with $T_{max,EU}$, the thermal insulation properties of the FCI become evident.

The temperature difference across the FCI, can be obtained following equation 8.6. Such temperature difference is shown in figure 8.6 together with ΔT_{LM} and the total

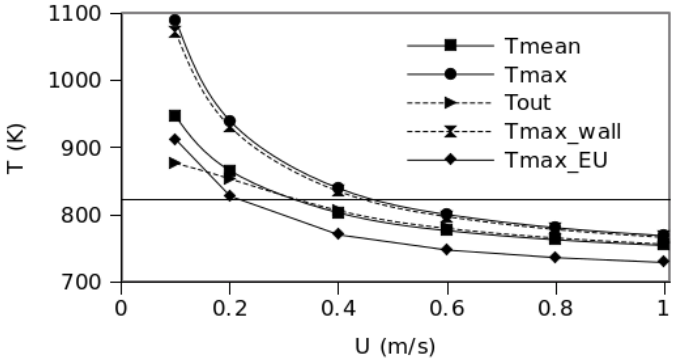

Figure 8.5: Different temperatures obtained and/or extrapolated from simulation results as a function of the inlet velocity, mesh 1

thermal power flux extracted by the fluid, $(q/A)_{LM}$, calculated following equation 8.7.

$$\Delta T_{FCI} = max\left(abs\left(\frac{(dT/dn)_{b.c.}\, k\delta_{FCI}}{k_{FCI}}\right)\right) \tag{8.6}$$

$$(q/A)_{LM} = \rho c_p v_{in} \Delta T_{LM} \tag{8.7}$$

In terms of ΔT_{LM}, ΔT_{FCI} and $T_{max,EU}$, the optimum inlet velocity would be of about 0.2 m/s, but in order to improve ΔT_{LM} and reduce ΔT_{FCI} and $T_{max,EU}$, an optimisation on FCI depth and thermal properties should be carried out (see next section). Moreover, according to figure 8.6, a fourth design parameter should be included: the total thermal power flux extracted by the fluid $(q/A)_{LM}$. It can be stated that, under the above mentioned flow conditions and with this preliminary evaluation, a higher inlet velocity would improve the total extracted heat.

8.3.2 Sensitivity analysis of FCI thermal properties

As mentioned above, the previous results correspond to a FCI thermal conductivity of 15 W/m·K FCI from Shinavski (2008) and an FCI thickness of 2 mm. According to Smolentsev *et al.* (2006), the thermal conductivity of SiC FCI can lay between 1-20 W/m·K, depending on the fabrication technique. The chosen FCI and its depth can alter considerably the thermal behaviour of the blanket.

In the present study, an assessment through sensitivity and parametric analyses of the required FCI thermal conductivity is performed. The case set up is the same as in the previous study. The chosen inlet velocity is 0.2 m/s since it has been previously found to be optimal in terms of $T_{max,EU}$, maximum ΔT_{LM}, minimum ΔT_{FCI} and maximum q_{LM}.

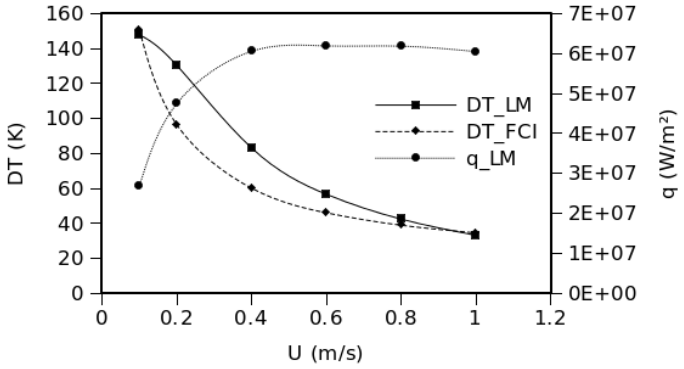

Figure 8.6: Temperature differences for the liquid metal and FCI, together with total heat extracted by the LM as a function of the inlet velocity, mesh 1

k_{FCI}	0	1	2	5	10	15	20
U_{eq}	0	454	833	1667	2500	3000	3333

Table 8.1: Several FCI thermal conductivity, and corresponding overall heat transfer coefficient, considered in the present study

Following the same procedure for thermal boundary condition evaluation, an infinity thermal convection coefficient for helium is considered, Eurofer layer is estimated to be 6 mm depth and with a thermal conductivity of 29.5 W/m·K, and a 2 mm depth FCI layer is considered. Varying k_{FCI}, the equivalent overall heat transfer coefficient can be estimated according to equation 8.3. In practise, using the boundary condition in equation 8.2, what really defines the influence of FCI is the ratio $(k/\delta)_{FCI}$. Thus, the present study can be understood as a sensitivity and parametric analysis of the required $(k/\delta)_{FCI}$ ratio. The simulated cases are summarised in table 8.1. In all cases, and according to previous results, the so called *mesh 1* has been used.

As expected, Nusselt number increases with U_{eq}, so is, with FCI thermal conductivity (figure 8.7). Ideally, for the present design, in between of the DCLL and the Self-cooled concepts, the Nusselt number should be as low as possible in order to obtain a maximum ΔT_{LM}.

In figure 8.8, some characteristic temperatures are shown. As previously, T_{LM} is the average LM temperature and $T_{max,EU}$ is the maximum extrapolated temperature at Eurofer applying Fourier's law, for a given FCI depth and thermal conductivity, as expressed in equation 8.5. $T_{mean,FCI}$ has been extrapolated following equation 8.8. It can be observed that, whereas average LM temperature decreases with U_{eq}, maximum

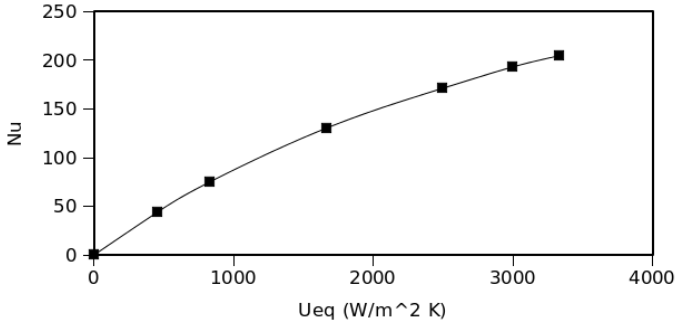

Figure 8.7: Nusselt number as a function of U_{eq}.

temperature at Eurofer increases. Ideally, if FCI were a perfect thermal conductor, Eurofer and LM temperatures would become equal at the interface. It can be seen that FCI mean temperature is almost constant along U_{eq} simulated values.

$$T_{mean,FCI} \sim \left(T_{max,wall} - \frac{\Delta T_{FCI}}{2} \right) \tag{8.8}$$

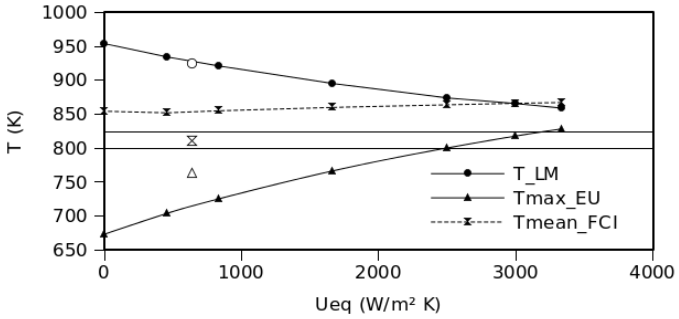

Figure 8.8: Characteristic temperatures as a function of U_{eq}.

Analysing the maximum Eurofer temperature behaviour with U_{eq}, it can be stated that a maximum FCI thermal conductivity of 10 W/m·K should be guaranteed for a 2 mm FCI thickness ($U_{eq} \leq 2500$ W/m^2·K) and under the studied flow conditions.

Concerning LM temperature increment along the blanket (figure 8.9), at 0.2 m/s and under the above mentioned flow conditions, an increase of 300 ^{o}C would only be possible for perfectly insulating FCI. A more realistic temperature gain of $\sim$250 ^{o}C would be

desirable. However, ΔT_{FCI} can become a serious problem in terms of thermal stresses, as, for FCI thermal conductivity of 1–2 W/m·K ($U_{eq} \leq 833$ W/m^2·K), $\Delta T_{FCI} \sim 270$ ^{o}C, which can be considered too high. An alternative would be to increase the FCI depth δ_{FCI} while keeping the ratio k_{FCI}/δ_{FCI}.

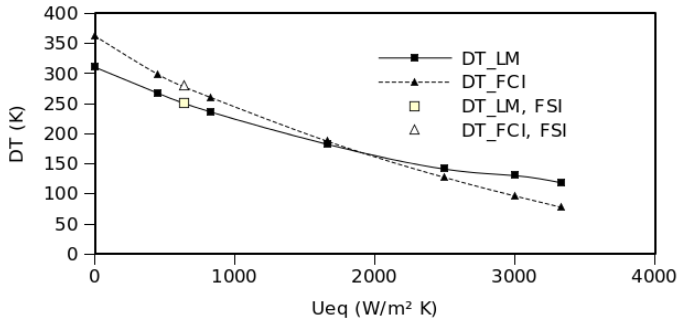

Figure 8.9: Temperature differences for the liquid metal and FCI as a function of U_{eq}.

Finally, in figure 8.10, the thermal losses through walls q_{wall} and the LM power gain q_{LM}, evaluated according to equations 8.9 and 8.10 respectively, are plotted in percentage using the total heat generated in the blanket (equation 8.1). In the equations, S, ρ, c_p and v stand for control volume surface area, LM density, LM heat capacity and LM velocity, respectively. It must be reminded that such values are obtained for a 2D simulation, neglecting the thermal contribution of Hartmann walls. Considering the obtained results, and for TECNO_FUS blanket specifications, a FCI thermal conductivity of 1–2 W/m·K would be recommended.

$$(q/A)_{wall} = \int_{wall} \left(kS \left(\frac{dT}{dn} \right) \right) \tag{8.9}$$

$$(q/A)_{LM} = \int_{inlet}^{outlet} \left(\rho c_p v T + kS \left(\frac{dT}{dn} \right) \right) \tag{8.10}$$

Previous results have been compared with a simulation where both FCI and Eurofer layers have been also modelled and thermally coupled to the LM. For such simulation, the FCI mesh has $3.9 \cdot 10^5$ nodes whereas Eurofer is meshed into $2.8 \cdot 10^5$ nodes. The LM mesh is the same as in previous simulations, with $1.4 \cdot 10^5$ nodes. Such refined solid meshes have been required because of their small thickness (2 mm and 6 mm, respec-

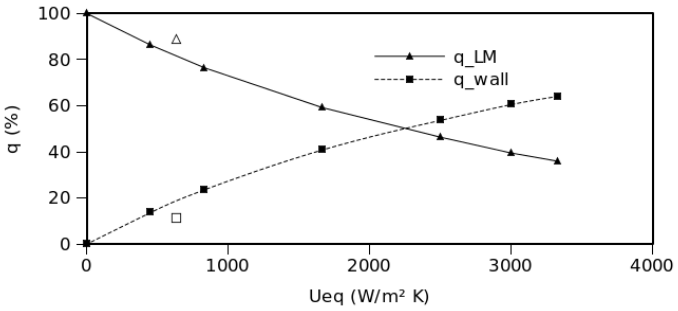

Figure 8.10: Thermal fluxes ratio as a function of U_{eq}.

tively). The thermal conductivity of FCI has been chosen to be, according to previous results and following suggestions by Yu *et al.* (2010), 1.8 W/m·K. The helium thermal convection coefficient has been chosen to be 4000 W/m^2·K, according to Smolentsev *et al.* (2006). This results in an equivalent overall heat transport coefficient of about $U_{eq} = 639$ W/m^2·K. Results are shown in previous figures (8.7-8.10) with blank markers and the label 'FSI', which stands for Fluid-Solid Interface.

From the results, it can be stated that the overall phenomenon is well captured with a unique liquid domain and a thermal boundary condition according to equation 8.2. Indeed, both ΔT_{LM} and ΔT_{FCI} are accurately predicted, as well as the thermal losses ratio. However, $T_{max,EU}$ and $T_{mean,FCI}$ appear to not accurately follow te extrapolated values. Such deviations might be caused by 2D phenomena not modelled in the above mentioned expressions.

In figure 8.11, the temperature field map of the internal U-bend region in the studied TECNO_FUS blanket is shown. The three domains (LM, FCI and Eurofer) can be clearly distinguished as well as the used non-uniform mesh. From the temperature field map it becomes evident the thermal insulator nature of the FCI.

In all simulated cases, approximately the 18 % of the total wall losses occur through the first wall, about 34 % through the external wall, and about 47 % across the internal wall. Hence, in order to further improve the design, helium cooling channels design should consider such differences.

8.4 Discussion

In this second application case of the present PhD dissertation, MHD issues of the flow inside banana-shaped channels of the proposed TECNO_FUS DEMO concept have been qualified. Among the most relevant issues, MHD turbulence modelling is, probably, the most relevant aspect since flow profile is strongly dependent on it. The lack of

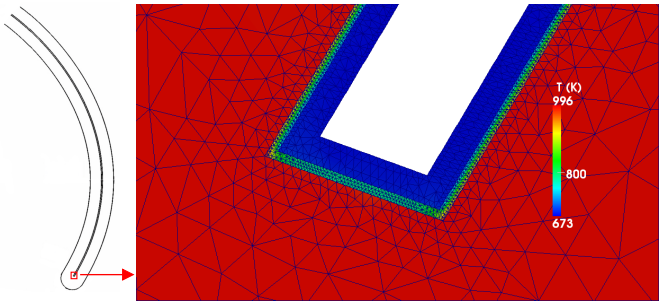

Figure 8.11: Temperature map and mesh definition for the fluid-solid coupled case.

an accurate MHD turbulence model is commented, specially when buoyancy effects have to be considered. Other critical aspects include electrical and thermal coupling, Hartmann wall functions and three-dimensional flows are expected to appear at the inlet/outlet manifolds as well as at the bottom of the blanket.

Preliminary results for a 2D toroidal plane of the TECNO_FUS blanket are presented, together with a sensitivity analysis of Eurofer surface temperature to inlet velocity. The obtained velocity profile does not present any vortex except at the internal wall of the bend. Hence, MHD turbulence effects are strong enough to compensate buoyancy. The analysis has allowed to know in detail the nature of the flow and mesh requirements. Likewise, it has made evident the need for further optimisation in the definition of FCI, both in thickness and thermal conductivity.

In this direction, a second sensitivity analysis of FCI thermal conductivity has been carried out. The chosen design parameters include the LM temperature gain ΔT_{LM}, the maximum Eurofer temperature $T_{max,EU}$ (that must be kept below 550 ºC), the thermal stresses across FCI layer ΔT_{FCI} and the thermal LM gain q_{LM}.

The coupled domain configuration, considering LM, FCI and Eurofer domains, has been compared with a single domain configuration corresponding to the LM domain with a Robin type thermal boundary condition at walls, following equation 8.2. From the obtained results, it can be stated that the overall phenomena is well captured with a unique liquid domain. Indeed, both ΔT_{LM} and ΔT_{FCI} are accurately predicted, however, $T_{max,EU}$ evaluation requires more refinement. The use of a single domain is very interesting in terms of reduced CPU time.

Results indicate that, on the base of optimised ΔT_{LM} criteria, considering 6 mm of Eurofer and 2 mm of FCI, an inlet LM velocity of 0.2 m/s or lower and a thermal conductivity of about 1–2 W/m·K would be recommended. In order to avoid high temperature differences across the FCI layer, FCI thickness should be increased keeping

the $(k/\delta)_{FCI}$ ratio. In contrast, for a maximised q_{LM}, and under the above mentioned design specifications, higher velocities would be preferable, which would also imply a reduced ΔT_{FCI}. However, this second thermal strategy would result in a lower LM temperature increment, which is not desirable for efficiency reasons.

For an accurate assessment of the cooling system requirements, heat losses at both side and Hartmann walls should be predicted. Such analysis could be carried out by 2D simulations of a fully-developed flow across a radial-toroidal plane.

9 Influence of wall thermal modelling on MHD buoyancy

9.1 Motivation

Lead lithium flowing inside breeding blanket channels in a fusion reactor is subject to a Hartmann number of the order of 10^4 and a Grashof number of about $10^9 - 10^{12}$. Hence, the resulting electromagnetic force tends to stabilise the core flow, whereas buoyancy is strong enough to oppose such effect. As pointed out in section 3.4.2, in the DCLL design buoyancy can be of the same order of magnitude as the electromagnetic force, while in the HCLL design buoyancy is expected to be dominant. As a result, the liquid metal flow in liquid metal breeding blankets can present vortical patterns. Indeed, according to previous studies exposed in section 4.2 (Bühler 1998, di Piazza and Ciofalo 2002a, Kharicha *et al.* 2004, Vetcha *et al.* 2009 and Authié *et al.* 2003), the presence of vortical structures is associated with a moderate electromagnetic damping, a moderate pressure-driven flow and a dominant buoyant force. Even if the magnetic damping is strong enough to stabilise the flow, secondary motions can still be present (di Piazza and Ciofalo 2002a). Moreover, although temperature along magnetic field lines is uniform, the flow may deviate considerably from two-dimensionality (Bühler 1998). Further research is required in order to understand such secondary motions and 3D flows in breeding blanket liquid metal channels.

With the focus on the HCLL blanket, and motivated by results previously obtained (Chapter 7), the pressure-driven flow in a horizontal channel, subject to a horizontal

magnetic field perpendicular to one pair of walls and under a uniform thermal load, is studied. A sketch of the case set up is shown in figure 9.1. Under the studied flow conditions ($Ha = 3000$ and $Gr = 2.6 \cdot 10^{11}$), the magnetic field is not able to completely suppress the vortices. However, despite its unstable nature, flow is expected to remain laminar. With the aim of analysing the influence of the wall boundary condition on flow vortical structures, different scenarios are considered for the helium cooling of the walls: (1) fixed wall inner surface temperature, (2) overall heat transfer coefficient between LM and helium cooling channels, and (3) fluid-solid coupling (LM/Eurofer) with the external solid wall being cooled by helium (see section 9.2 for a detailed explanation). Therefore, in cases (2) and (3) average wall temperature is expected to be different for upper and lower walls, what implies that the fluid is not only subject to a thermal load but also to a thermal gradient between walls.

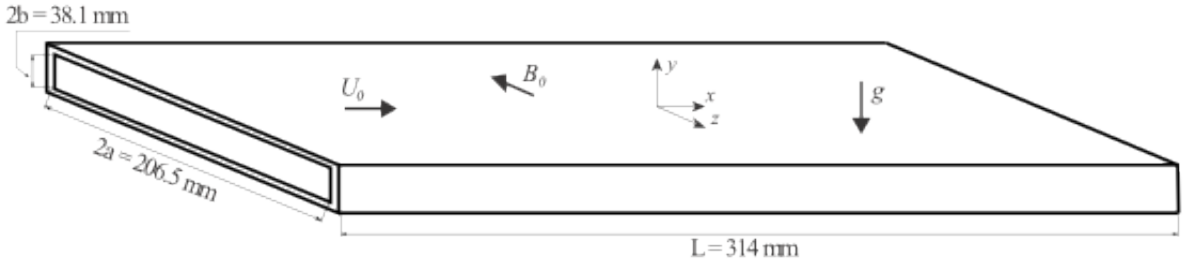

Figure 9.1: Sketch of the channel geometry

In this third application case, the unstable nature of the resulting flow within the channel sketched in figure 9.1 is studied, as well as its influence on relevant thermal parameters, including Nusselt number and power losses. First, the flow is characterised by its dimensionless numbers and a theoretical prediction of flow nature is carried out. Then, results of the numerical study are exposed and discussed.

9.1.1 Flow characterisation

According to the boundary conditions explained in section 9.2, the pressure-driven flow in the channel sketched in figure 9.1 has a Reynolds number $Re_a = 770$, based on the channel half width dimension a. A Hartmann number $Ha_a = 3000$ has been considered since it implies a very strong magnetic damping while allowing the use of a relatively coarse mesh. The chosen uniform thermal source term ($S_{thermal}$) corresponds to the average thermal load expected in the HCLL blanket (Gabriel *et al.* 2007). Thus, $Gr_a = 2.6 \cdot 10^{11}$, where the characteristic temperature gradient is evaluated according to $\Delta T = S_{thermal} a^2 / k$, being k the thermal conductivity of the fluid. All fluid properties have

been calculated using the PbLi database (Mas de les Valls *et al.* 2008).

Following the Ha–Re diagram by Smolentsev and Moreau (2007), the flow is expected to be laminar, however, since buoyancy is relevant, if not dominant, a better characterisation of the flow is required. According to the dimensionless equations 3.17-3.17e (section 3.3.2), the characteristic dimensionless numbers are: (1) $Gr_a Ha_a^{-2}$ which plays the role of the Reynolds number and equals $2.9{\cdot}10^4$, (2) $Ha_a^4 Gr_a^{-1}$ which is an equivalent Interaction parameter and equals $3.0{\cdot}10^2$, and (3) $Pe = PrGrHa^{-2}$, which equals $4.5{\cdot}10^2$. The interaction parameter, despite being high, is not sufficient to neglect inertia terms in the momentum equation. Peclet number is greater than unity, which means that inertia cannot be neglected from energy balance. Thus, the flow corresponds to the unsteady inertial flow zone in the stability diagram from Molokov (1997). Whether the flow is laminar (and unsteady) or experiences Q2D turbulence cannot be predicted *a priori*. However, considering results exposed in Chapter 7, in the present study it has been assumed that $Ha_a = 3000$ is high enough to keep Gr_a below its critical limit.

In a recent study by Gelfgat and Molokov (2011), the stability of Q2D flow in a laterally heated 3D box with a strong magnetic field normal to main circulation is analysed. As a result of such study, the critical Grashof number for oscillatory instability of steady flows to appear is obtained, for several Grashof numbers and aspect ratios. The flow is quite different that the one studied here as, instead of the inlet and outlet boundary conditions, two isothermal hot and cold walls are imposed. Moreover, no thermal load is assumed and two different configurations for the horizontal walls are considered: thermally insulated or perfectly heat conducting walls. Despite such differences, the vortical flow pattern reproduced in that work is also expected to exist in the present studied configuration, what might indicate that the conclusions obtained in that work could be applied to the present one. In the work from Gelfgat and Molokov (2011), Prandtl number has the same value as in the present case, walls are also electrically insulating and aspect ratios from 4 to 10 are considered (here, the aspect ratio is 8.24). From their results, taking into account the present configuration, the critical Grashof number would lay between $1.9{\cdot}10^9$–$6.5{\cdot}10^9$. Therefore, it could be predicted beforehand that oscillatory flows are expected in the present configuration.

9.2 Modelling strategies

For this application case, different algorithms are required depending on how the wall is simulated. Indeed, for case (1), with a fixed wall temperature, and case (2), where an overall heat transfer coefficient is calculated, the 3D algorithm ϕT-PISO (section 6.1) with a unique domain, corresponding to liquid metal, is used. However, for case

(3), with fluid-solid coupling, the ϕT-PISO_FSI algorithm has been used (section 6.4). Differences obtained in case (3) both with conservative and non-conservative energy equations are shown and justified in section 9.3.

In all cases, fully 3D simulations are carried out in order to accurately predict the flow nature, including secondary 3D effects.

The pressure-driven flow sketched in figure 9.1 is considered to have a mean velocity of 1 mm/s, typical of HCLL blanket. Inlet boundary condition for the channel is a critical aspect, since it can alter considerably the flow nature. Available information on the design is not sufficient to determine the velocity profile at the blanket channels' inlet. It is assumed that inlet flow is well mixed and, as a result, temperatures are almost homogeneous and no big vortical structures exist at the channel entrance. As a first approximation, an inlet velocity profile corresponding to the fully developed MHD flow is imposed together with a constant inlet temperature of 723.15 K. Outlet is simulated with a free boundary condition.

The non-slip velocity boundary condition is imposed at walls, and three different thermal boundary conditions at walls are analysed. In case (1), the inner wall temperature is equal to the LM inlet temperature. This case corresponds to the most simple configuration, studied in application case 1, in Chapter 7. In case (2), following the same procedure as in Chapter 8, a thermal convection boundary condition is imposed following equation 9.1, where U_{eq} stands for the overall heat transfer coefficient, $T_{b.c.}$ stands for the LM boundary temperature; T_{He} stands for the helium boundary temperature; and n is the surface normal vector. Equation 9.1 represents a 1D steady state thermal balance between the liquid metal interface (with subscript $b.c.$, as for boundary condition), and the helium cooling channels. Indeed, the heat flux that leaves the LM domain (by a thermal diffusive process following Fourier's law) equals the total heat extracted by helium. Here, $T_{He} = 675.15$ K and $U_{eq} = 3336$ W/m^2 K; such value corresponds, according to equation 9.2, to 3 mm of Eurofer (Mergia and Boukos 2008) and a helium thermal convection coefficient of 5500 W/m^2 K (following numerical results from Aiello *et al.* 2009). In case (3), LM (PbLI) and structural material (Eurofer) are thermally coupled and the thermal boundary condition, of a convective type, is placed at the external wall surface ($U_{eq} = h_{He}$).

$$U_{eq}\left(T_{b.c.} - T_{He}\right) \;=\; k\left(\frac{\partial T}{\partial n}\right)_{b.c.} \tag{9.1}$$

$$U_{eq} \;=\; \frac{1}{h_{He}^{-1} + \frac{\delta_{EU}}{k_{EU}}} \tag{9.2}$$

The balance used in equation 9.1 corresponds to an idealised 1D flat wall balance, where no thermal generation exists in the solid domain. In fact, thermal loads would

also exist in solid walls, but they are not taken into account in the present study. Moreover, the 1D idealisation would only be valid for small enough Biot numbers, which is not exactly the present case. Thus, comparing results obtained with wall simulation strategies (2) and (3) would provide valuable information on whether such simplification can be applied or it introduces unacceptable inaccuracies in the results.

In the present study, and as a first step, the idealised case of electrically fully insulated walls is analysed. Two reasons support this simplification. First, it makes fluid-solid thermal coupling effects explicit; since walls do not allow electric currents to travel outside the fluid domain, all three cases would be equivalent. Second, it increases the dominance of buoyancy; indeed, it is expected that using real Eurofer electric conductivity, magnetic field damping will increase along with the stability of the flow (di Piazza and Ciofalo 2002b, Gabriel *et al.* 2007 and results presented in Chapter 7).

For unsteady flow analysis, a transient simulation is required. Thus, the initial field map plays an important role. With the idea of providing an initial map field as realistic as possible, the initial v, p and ϕ maps are obtained from fully developed MHD simulations. In terms of temperature, it is expected that the temperature map be very similar to the one obtained for purely diffusive thermal conditions, except in strongly vortical zones. Therefore, the initial temperature map has been chosen to be the corresponding to purely diffusive thermal conditions (Pe=0) with a thermal source term of $5.45 \cdot 10^6$ W/m^3, which, as explained in section 9.1.1, is the average value expected for HCLL blanket design (Gabriel *et al.* 2007) and yields $Gr_a = 2.6 \cdot 10^{11}$. No thermal source term is considered in the solid domain.

The time step for an accurate transient 3D simulation is chosen so as the constrain $\mathcal{L} \leq 0.2$ is fulfilled. Such value has been taken from an adaptation to a 3D simulation of the 1D stability analysis presented in section 5.2.3. In some periods of the transient calculation, the time step has been reduced in order to capture all fluid instabilities.

In order to y reproduce the flow pattern, a mesh with $2.1 \cdot 10^5$ nodes has been used for the liquid domain, with 4 nodes in the Hartmann boundary layer of depth $2a/Ha$, and 15 in the side one of depth $2a/Ha^{0.5}$. Walls are assumed to be made of 3 mm of Eurofer. For the solid domain simulation, a solid mesh with $9.4 \cdot 10^4$ nodes has been considered, which has 7 nodes in the normal fluid-solid interface direction. Results of a mesh quality analysis are shown in section 9.3.2.

A first order Euler Implicit in time and second order Central Difference in space numerical discretisations has been applied, except for the convective terms ($D(\phi_v v)$ in the momentum equation 6.1b and $D(\phi_v T)$ in temperature equation 6.1e). In such terms, the OpenFOAM scheme *Gauss limitedLinearV 1* has been used, which corresponds to a

total variation diminishing scheme (TVD, Jasak 1996).

Simulations are carried out with preconditioned (bi)-conjugate gradient. The Diagonal incomplete-Cholesky pre-conditioner is used for solving scalar transport equations (T, p and ϕ), whereas the incomplete-LU pre-conditioner is used for solving momentum equation. The solver tolerance is set to 10^{-8} for velocity and 10^{-9} for the scalar variables.

9.3 Results

The present application case can be split into several sub-studies, including:

- A purely diffusive thermal condition analysis, carried out by totally decoupling temperature from momentum (Pe=0, section 9.3.1). Such study has been useful to evaluate numerical results both from ϕT-PISO and ϕT-PISO_FSI algorithms. It has also provided the initial temperature maps for transient simulations.
- A mesh quality analysis carried out with a reference and an extremely fine meshes, by means of FFT studies (section 9.3.2).
- The thermal wall treatment analysis (section 9.3.3), in order to evaluate the possible differences found on results obtained using the three proposed wall treatments.
- An analysis of the critical Grashof number for flow oscillations to appear (section 9.3.4).
- Periodic (cyclic) boundary conditions analysis in order to evaluate the effect of the inlet/outlet boundary condition (section 9.3.5).

Results are finally discussed in section 9.4.

9.3.1 Velocity-temperature decoupled case: 2D thermal effects

The differences that might appear due to the three different ways in which thermal effects in the wall are modelled (1: fixed wall temperature, 2: overall heat transfer coefficient and 3: fluid-solid coupling with helium thermal convection coefficient) may be explained by analysing the three cases with the temperature field decoupled from the momentum balance. This situation can be easily reproduced, by solving the temperature equation with no convective term and without solving neither continuity (pressure) nor momentum equations.

Temperature field maps for such simulation are shown in figure 9.2 for a central plane perpendicular to the magnetic field, and in figure 9.3 for a central spanwise plane. It is obvious that cases (2) and (3) are very similar, whereas the average temperature is considerably higher for the case (1). Hence, in case (1), walls do not extract enough heat to reproduce the physical flow conditions. In figure 9.3 the 3D nature of the temperature field is made explicit.

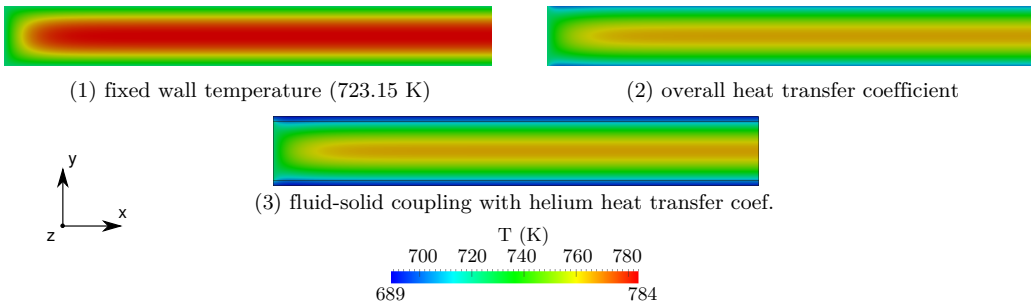

Figure 9.2: Decoupled temperature map fields for the three cases in a central plane perpendicular to the magnetic field lines

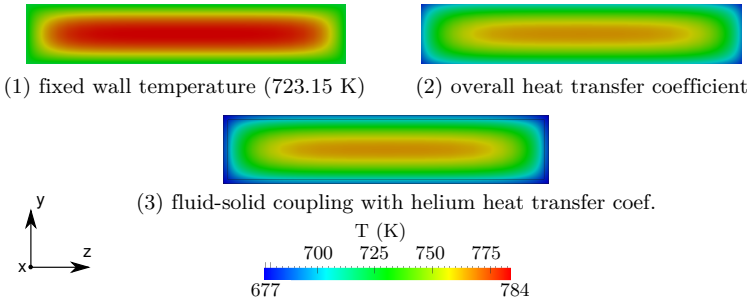

Figure 9.3: Decoupled temperature map fields for the three cases in a central spanwise plane.

The above mentioned qualitative differences can be quantified in terms of average and maximum temperatures and heat fluxes, as listed in table 9.1. The liquid metal average temperature T_{avg} and the inlet/outlet temperature difference ΔT_{LM}, together with average wall temperatures (T_{side} and T_{Ha}) are shown in table 9.1. Second row values for cases (2) and (3) in the table correspond to the average temperature at the

case	q_{LM} %	q_{side} %	q_{Ha} %	T_{avg} K	T_{side} K	T_{Ha} K	ΔT_{LM} K
(1) fixed temp.	3.0	43.6	4.9	758.00	723.15	723.15	36.18
(2) overall U_{eq}	0.2	44.6	5.3	736.43	700.89	690.92	14.08
					689.97	683.95	
(3) FSI	0.0	44.6	5.3	736.31	700.71	690.21	13.93
					689.51	682.56	

Table 9.1: Simulation results for the non-buoyant simulations

external walls in contact with helium; such temperature is just at the external solid boundary in case (3), whereas, in case (2) it is extrapolated according to equation 9.3, where $T_{b.c.}$ is the temperature at the LM boundary, $(dT/dn)_{b.c.}$ is the normal temperature gradient at the boundary, and δ_{EU} and k_{EU} are the Eurofer wall thickness and thermal conductivity respectively. Equation 9.3 is obtained from a 1D steady balance between the pure diffusive thermal flux (following Fourier's law) in the fluid boundary side and in the solid boundary side.

$$T_{extrapolated,\ wall} = average\left(T_{b.c.} - abs\left(\frac{(dT/dn)_{b.c.}\, k_{LM}\ \delta_{EU}}{k_{EU}}\right)\right) \tag{9.3}$$

Apart from the expected temperature differences between case (1) and the other two cases, it is worth noting the ability to capture the 3D temperature field by case (2). Indeed, the extrapolated wall temperature values obtained in case (2) are almost equal to the values computed in the simulation of case (3).

Heat fluxes include heat loses across the walls (q_{side} and q_{Ha} respectively) and liquid metal gain (q_{LM}). They are shown in table 9.1 in percentage with respect to the total thermal load. Since the system is symmetric in *y* and *z* axis, thermal flux across the upper and lower side walls is identical, and the same occurs for the top and bottom Hartmann walls. The values shown in table 9.1 correspond to only one of the walls. It can be seen that, in all cases, the heat extracted through the side walls is about one order of magnitude higher than the one extracted by Hartmann walls. The main difference relies on the liquid metal thermal gain, which is substantially larger in case (1).

The difference between the average LM temperature and the average side wall temperature can be used as a rude indicator of the buoyancy force. The value of this difference is about 35 K regardless of the strategy applied for the wall. Thus, it appears that buoyancy has the same relevance in all three cases.

case	q_{LM} %	q_{side} %	q_{Ha} %	T_{avg} K	T_{side} K	T_{Ha} K	ΔT_{LM} K
(3) FSI, C	0.0	44.6	5.3	736.31	700.71	690.21	13.93
					689.51	682.56	
(3) FSI, NC	6.1	41.7	5.3	765.86	731.27	711.38	49.71
					708.00	694.58	

Table 9.2: Simulation results comparison between the conservative formulation and the non-conservative one

Conservative versus non-conservative fluid-solid coupling

Case (3) has been simulated with the ϕT-PISO_FSI algorithm, which implements the conservative form of the energy equation (section 6.4). However, as mentioned in Chapter 6, the first thermal MHD algorithm implemented in the frame of the present PhD dissertation was the ϕT-PISO algorithm, based on the non-conservative form of energy equation. In this latest case, the temperature is the energy variable; hence, the energy equation is divided by density and heat capacity, obtaining a temperature equation (equation 3.11). In order to thermally couple fluid and walls, two temperature equations are implemented, following the *conjugateHeatFoam* solver strategy from extended OpenFOAM distribution (OpenFOAM-1.6-ext, from Wikki Ltd.), one for the fluid domain and the other for the solid domain.

Case (3) was simulated at first with such non-conservative algorithm. However, when an energy balance was performed on the obtained results, the non-conservative nature of the algorithm become evident. Only when the studied fluid and solid were defined to have $\rho C_p = 1$, with equal grid sizes at both sides of the interface, then results were conservative. As a result, the conservative form of the energy equation (equations 6.7) was implemented, obtaining the expected results, i.e. similar to those obtained with case (2), as shown in table 9.1. Differences between results obtained in both algorithms are shown in table 9.2, where NC and C stand for non-conservative and conservative, respectively.

To sum up, it can be stated that with the non-conservative algorithm (NC) the unbalance between fluid and solid domain is produced by $(\rho C_p)/(\rho C_p)_{solid}$ ratio and grid size difference. If inertia dominates the flow, thermal inaccuracies do not alter the flow profile. However, for a strongly buoyant flow, which often it becomes unstable, the non-conservative algorithm cannot be applied.

9.3.2 Mesh requirements

In order to evaluate mesh quality, it is necessary to repeat at least one simulation with a very fine mesh and to evaluate the differences in the obtained simulation results. Here, case (1) considering full thermal MHD coupling (i.e. coupling energy and momentum balances) has been simulated with the mesh defined in section 9.2, called *mesh 0*, and with a very fine mesh called *mesh 1*.

Mesh 1 has $2.16 \cdot 10^6$ nodes, with 8 nodes in each Hartmann boundary layer of depth $2a/Ha$, and 30 in each side boundary layer of depth $2a/Ha^{0.5}$. Thus, while boundary layer precision has been doubled, the overall number of nodes has been increased by one order of magnitude, what implies that the mesh is much more dense and uniform and, thus, all vortical structures are better captured.

As exposed and discussed in section 9.3.3, the flow is unstable and complex. Thus, the comparison between results obtained with different meshes is not straightforward. Assuming the oscillatory nature of the flow, it seems appropriate to compare an average velocity map for each mesh, obtained from several instantaneous maps, in order to avoid numerical noise. Due to the high CPU requirements for simulations with *mesh 1*, and in order to avoid the first part of the transient simulation where the initial field map influence is maximal, the map obtained in case (1) –fixed wall temperature– after 346 s with *mesh 0*, has been used as the initial map for *mesh 1*. From time 346 s to 351.6 s, simulations with both meshes have been carried out. During the simulations, 20 field maps have been printed for each case, which have been used for mesh quality comparison.

The time consumed in such a short simulation (from 346 s to 351.6 s) is 4 hours for *mesh 0*, whereas *mesh 1* has needed 93 hours [1]. Thus, it is out of the research group present CPU capacities to simulate a long transient phenomenon with *mesh 1*.

Before showing the results of the FFT analysis using the above mentioned 20 field maps, results obtained with both meshes at 350 s are qualitatively compared (figures 9.4-9.6). It can be seen that some small vortices that are detected with *mesh 1*, are damped with *mesh 0*. However, main vortical structures are well captured by the coarse mesh as well. The presence of vortices is also visible on the temperature and electric potential field maps. From results, it can be stated that the characteristic dimension of vortical structures is the channel height, and that the flow appears to remain laminar.

However, for an accurate estimation of the quality of *mesh 0*, the (spatial) 2D Fast Fourier Transformation analysis, in a plane perpendicular to magnetic field lines, has been performed. Such plane has been chosen as representative of the whole domain,

[1] Such simulations have been carried out in parallel mode using 32 processors Intel(R) Xeon(TM) CPU 3.00GHz, from RDLab cluster

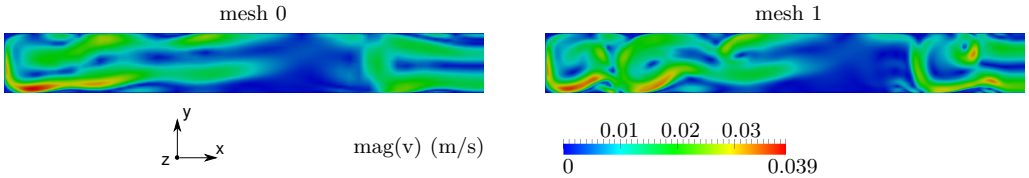

Figure 9.4: Magnitude of the velocity field for the two meshes at 350 s in case (1).

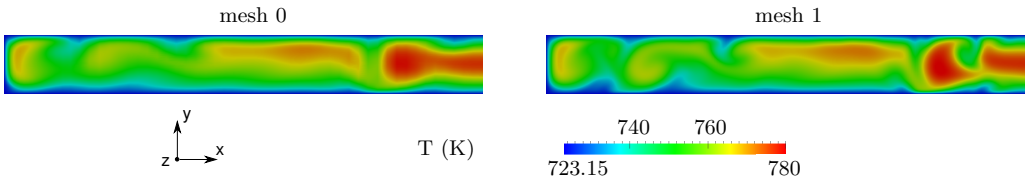

Figure 9.5: Temperature field for the two meshes at 350 s in case (1).

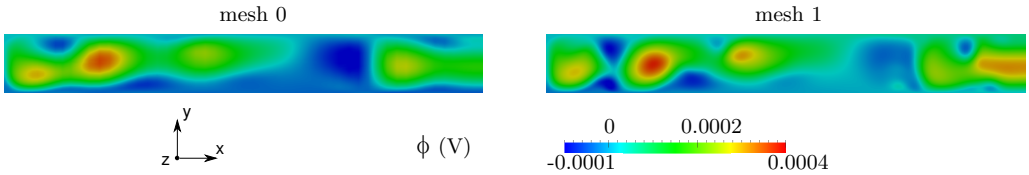

Figure 9.6: Electric potential field for the two meshes at 350 s in case (1).

since velocity is almost uniform along magnetic field lines, except at Hartmann boundary layers. Therefore, a 3D analysis would provide no extra information regarding stability. The variable to be analysed is the magnitude of the velocity field, which provides information on vortex velocity.

Once the 20 field maps have been obtained for each mesh, the first step has been to interpolate the values into a uniform mesh of $128 \times 128 \times 32$ nodes. The number of nodes of such mesh is a power of two in each direction, which is required for the FFT post-process (Brigham 1988) carried out by means of QtOctave software. The size of this uniform mesh has been selected so that cell volume size is equivalent to the average cell volume size in *mesh 1*. It is worth mentioning that the interpolation (from each mesh to the uniform FFT mesh) introduces numerical noise to the solution, however, such interpolation cannot be avoided.

With the interpolated velocity maps, the FFT is performed at each time step and an average FFT is carried out using all 20 available maps for each mesh. In figure 9.7 the results for each mesh are shown, where axes correspond to spatial frequency domain (units: 1/m) and the magnitude is the average FFT (see table 9.3 for FFT peak values). The differences between different mesh results become evident. Indeed, the

mesh 0			*mesh 1*		
FFT	freq. x (1/m)	freq. y (1/m)	FFT	freq. x (1/m)	freq. y (1/m)
-10.142178	0.000000	0.000000	-10.245506	0.000000	0.000000
-7.246165	0.000000	-26.242862	-7.421329	0.000000	26.242862
-7.246165	0.000000	26.242862	-7.421329	0.000000	-26.242862
-6.701677	6.369414	-26.242862	-6.636632	6.369414	-26.242862
-6.701677	-6.369414	26.242862	-6.636632	-6.369414	26.242862
-5.678351	-6.369414	0.000000	-5.549106	-6.369414	-26.242862
-5.678351	6.369414	0.000000	-5.549106	6.369414	26.242862
-5.569888	-6.369414	-26.242862	-5.533302	0.000000	-52.485724
-5.569888	6.369414	26.242862	-5.533302	0.000000	52.485724
-5.456719	0.000000	-78.728586	-5.422255	0.000000	-78.728586
-5.456719	0.000000	78.728586	-5.422255	0.000000	78.728586
-5.272528	6.369414	-104.971448	-5.320377	-6.369414	0.000000
-5.272528	-6.369414	104.971448	-5.320377	6.369414	0.000000
-4.988556	6.369414	-52.485724	-5.030290	0.000000	-104.971448
-4.988556	-6.369414	52.485724	-5.030290	0.000000	104.971448

Table 9.3: FFT major peaks for both meshes

core frequency span is larger for *mesh 1*, but such enlargement corresponds to low FFT values. This means that smaller structures are captured with the fine mesh. However, same peak locations and with almost the same FFT magnitude are obtained by both meshes, as detailed in table 9.3. To conclude, and according to the exposed results, *mesh 0* is fine enough to provide accurate information on the flow nature and the principal vortical structures.

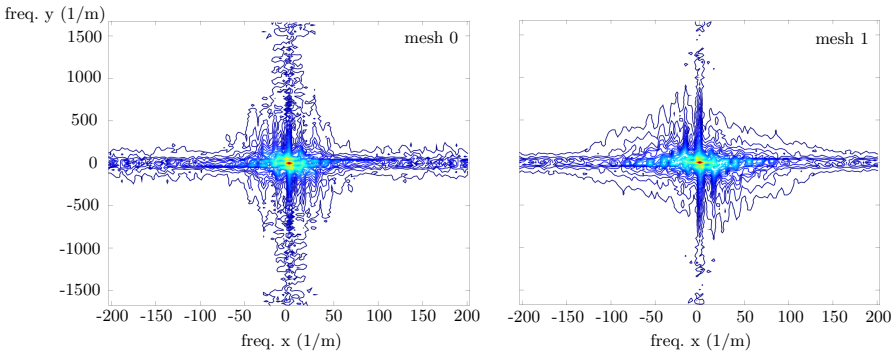

Figure 9.7: Spatial 2D FFT of the magnitude of the velocity in a x-y plane (perpendicular to the magnetic field), for *mesh 0* and *mesh 1*.

With the support of these results, all the simulations presented in the following sections have been carried out with *mesh 0*.

9.3.3 Influence of thermal boundary condition

For the three studied thermal boundary conditions, with $Re_a = 770$, $Ha_a = 3000$ and $Gr_a = 2.6 \cdot 10^{11}$, the flow is unstable. Thus, it appears that buoyancy is predominant. In figure 9.8 velocity, temperature and electric potential maps after 40 seconds from initial condition are shown for case (2). Although at 40 s the flow is still evolving, the effects of the initial conditions have been already damped and the complex flow pattern, with several vortical structures, can already be observed. Such vortices are elongated along magnetic field lines; however, the velocity field is slightly 3D and (not shown in the figure) temperature field is clearly 3D.

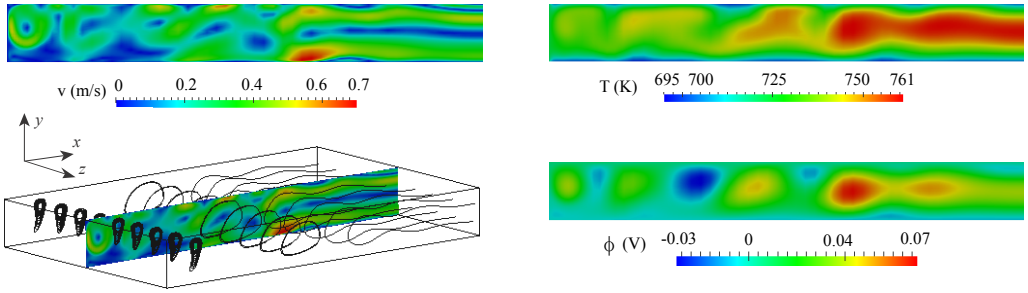

Figure 9.8: Velocity, temperature and electric potential results for case (2) (overall thermal convection coefficient of 3336 W/m^{2}K) at 40 s after the initial time. At the bottom left of the figure, velocity streamlines are plotted together with the velocity map at the central plane. It can be seen that velocity field is not fully 2D.

For the three studied cases, vortices with a characteristic length of approximately the channel height are observed. Also, as the simulation time increases, inlet vortices become more stable and independent of the rest of vortical structures, which travel along the channel length. Therefore, it can be concluded that neither the thermal strategy applied for the walls nor the inlet boundary condition are the unique cause for vortices to exist. Indeed, the effective cause for vortices to exist is the deposited thermal load together with the presence of cooling walls.

Transient evolution of the average LM temperature (figure 9.9(a)) is quite similar for cases (2) and (3), what indicates that the thermal boundary condition (equation 9.1) provides sufficient information to capture the overall buoyancy phenomenon. The temporal fluctuations experienced by the average temperature are not relevant, being always less than 5 ^{o}K. However, the average outlet velocity largely fluctuates for all three cases (figure 9.9(b)). This fluctuation is explained by the presence of travelling

vortices and the hot spot that exists in its core (see figure 9.8). Hence, when the bulk of a vortex crosses the outlet boundary condition, the average outlet temperature is expected to increase substantially, recovering lower temperature values when the vortex has totally crossed the outlet boundary condition.

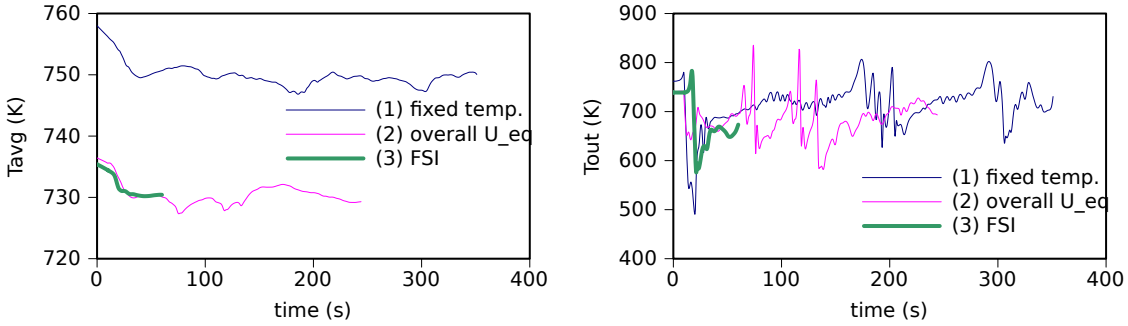

(a) (b)

Figure 9.9: Transient evolution of average LM temperature (a) and average outlet temperature (b) for the three cases.

For Nusselt number estimation, the initial temperature field map, corresponding to a thermally decoupled case ($Pe = 0$), is used as the reference value, following equation 9.4. Thus, Nusselt number provides with information on the non purely diffusive nature of the flow. Indeed, if the flow would remain stable and, thus, stratified, Nusselt number would remain very close to unity. Results for the transient evolution of the average Nusselt number at the upper (y+) side wall (figure 9.10(a)) indicate that, for all three strategies of wall boundary condition, heat transfer is enhanced duo to buoyancy effects. In fact, the heat transfer increase can be grossly estimated to be about 20% ($Nu \sim 1.2$). The oscillations of the average Nusselt number indicate, once more, the unstable nature of the flow.

$$Nu = average\left(\frac{(dT/dn)_{b.c.}}{(dT/dn)_{b.c.,Pe=0}}\right) \tag{9.4}$$

Temporal evolution of the average Nusselt number for case (2) is plotted in figure 9.10(b) for the four walls. It can be seen that heat transfer is only enhanced at the upper side wall. This result is explained from the temperature field map in figure 9.8. Indeed, hot spots are mainly located at the upper half of the channel and, hence, since helium temperature and heat transfer coefficient are assumed equal in all walls, temperature difference across the wall is higher for the upper side wall.

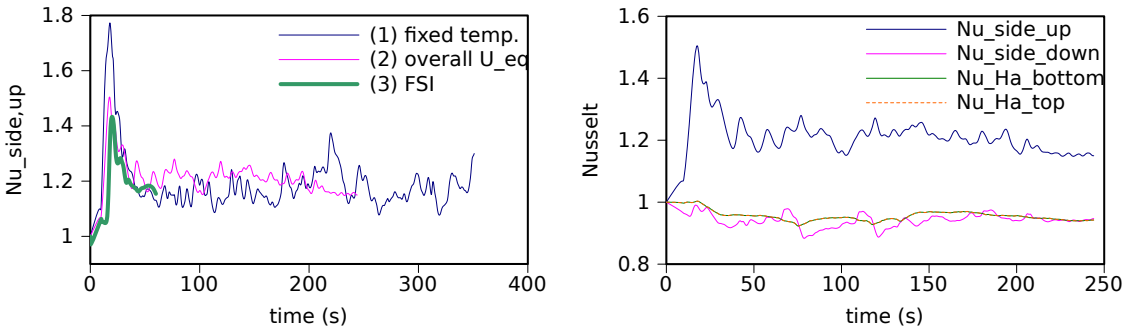

(a) (b)

Figure 9.10: Transient evolution of average Nusselt number (a) at the upper side wall for the three cases, (b) in all four walls for case (2).

case	T_{avg}	T_{out}	$T_{side,up}$	$T_{side,down}$	T_{Ha}	$Nu_{side,up}$	$N_{vortices}$	$\|\phi\|_{avg}$	$\|v\|_{max}$
1	749.5	687.6	723.2	723.2	723.2	1.20	18	$1.9 \cdot 10^{-2}$	1.04
2	730.4	661.3	706.6	698.9	690.3	1.21	16	$2.2 \cdot 10^{-2}$	0.72
3	730.3	664.9	705.5	698.5	689.5	1.18	18	$2.3 \cdot 10^{-2}$	0.89

Table 9.4: Comparison for the three cases at 40 s from the initial time. Temperatures are in K whereas ϕ and v are dimensionless

Since both average Nusselt numbers in Hartmann walls are equal, it can be stated that, despite 3D thermal effects are observed, the temperature field is, as expected, symmetric along magnetic field lines.

In table 9.4 some characteristic temperatures and Nusselt numbers are compared for the three cases at maps corresponding to 40 s. Once more, cases (2) and (3) yields almost the same results. For all three cases, it can be observed that the upper (y+) side wall is considerably hotter than the other walls, being both Hartmann walls at the same temperature.

When calculating the heat fluxes for case (2) (figure 9.11), it can be stated that heat is mainly removed by side walls, being the heat removed by each Hartmann wall about 5% of the total gain. Similar transient evolution of the heat fluxes is obtained for cases (1) and (3).

A surprising result in figure 9.11 is that, despite large oscillations due to the unstable flow nature, the LM is mainly cooled all along the channel (what was not the case for $Pe = 0$ simulations). This, of course, is an unrealistic result probably caused by boundary conditions. Indeed, a fixed inlet temperature (probably too high) and a zero gradient outlet temperature, together with the presence of vortical structures, are not representative of the real problem. To that it must be added the fact that the He cooling

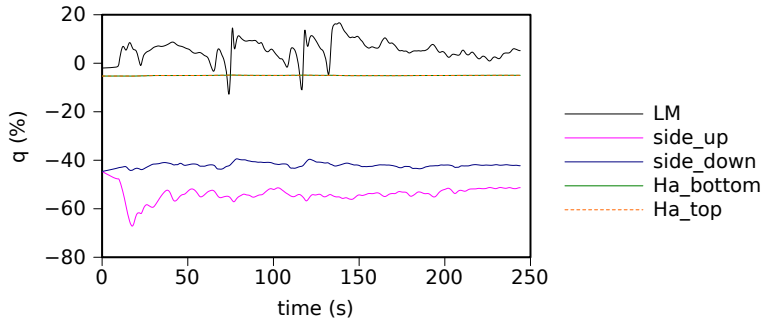

Figure 9.11: Transient evolution of heat fluxes for case (2). Results are shown in % with respect the total thermal load.

channels are assumed at constant temperature. It has to be mentioned that this effect is not observed in case (1). To further analyse this issue, the same flow set up but with periodic boundary conditions is studied and discussed in section 9.3.5.

In order to quantify the number and magnitude of the existing vortices, the measurement of the vorticity is not suitable since vorticity is maximum not only at the centre of the vortices but also at walls. Therefore, local maxima/minima of electric potential are used as vortex indicators. Such type of analysis has not been found in the literature by the author but, according to figure 9.8, it seems a proper method for vortex detection. The analysis consists of first extracting ϕ data for the central plane perpendicular to the applied magnetic field, and then finding electric potential maxima/minima by going into each cell and comparing ϕ values with its neighbours. Results of the analysis are shown in table 9.4, where the total number of vortices, $N_{vortices}$, the average among the obtained $N_{vortices}$ of the peak ϕ magnitude within them and the maximum dimensionless velocity all over the domain (as an indicator of the buoyancy predominance in the flow) are shown. From the results it can be stated that the three cases present the same complex flow pattern and no relevant differences are obtained.

9.3.4 Instabilities evolution with Gr

According to what was mentioned in section 9.1.1 related to the work of Gelfgat and Molokov (2011), the expected critical Grashof number for oscillatory instability of steady flows applied to the present configuration would lay between $1.9{\cdot}10^9$–$6.5{\cdot}10^9$. Indeed, under the present flow conditions ($Gr_a = 2.6{\cdot}10^{11}$), the flow has proved to be unstable. In this section, the effect of the Grashof number in the results is studied. To this aim, case (1) (fixed wall temperature) is simulated for different thermal loads according to the law $(\alpha \times S_{thermal})$, where α is a scale factor that takes values between 0.01 and 1. The underlying idea is to decrease the Grashof number to the point it reach the expected

α	Gr	$Re' = Gr/Ha^2$	$v_{o,MHD}$	$N' = Ha^4/Gr$
1	$2.6{\cdot}10^{11}$	$2.9{\cdot}10^{4}$	$3.8{\cdot}10^{-2}$	$3.0{\cdot}10^{2}$
0.6	$1.6{\cdot}10^{11}$	$1.8{\cdot}10^{4}$	$2.3{\cdot}10^{-2}$	$5.1{\cdot}10^{2}$
0.1	$2.6{\cdot}10^{10}$	$2.9{\cdot}10^{3}$	$3.8{\cdot}10^{-3}$	$3.0{\cdot}10^{3}$
0.05	$1.3{\cdot}10^{10}$	$1.5{\cdot}10^{3}$	$1.9{\cdot}10^{-3}$	$6.1{\cdot}10^{3}$
0.01	$2.6{\cdot}10^{9}$	$2.9{\cdot}10^{2}$	$3.8{\cdot}10^{-4}$	$3.0{\cdot}10^{4}$

Table 9.5: Simulations varying the total thermal load, case (1).

critical value. The studied cases are listed in table 9.5. As explained in section 3.3.2, $Re' = Gr/Ha^2$ plays the role of the Reynolds number, $v_{o,MHD}$ is the velocity required for the electromagnetic forces to balance with buoyant forces, and $N' = Ha^4/Gr$ plays the role of the Interaction parameter. Values of $v_{o,MHD}$, when compared with the mean flow velocity of 1 mm/s, provide an idea whether the Hartmann number is high enough to suppress buoyant effects or not. According to $v_{o,MHD}$ and results from Gelfgat and Molokov (2011), the case with $\alpha = 0.01$ is expected to remain stable whereas the other studied cases ($\alpha \geq 0.05$) might present some oscillations or periodicities.

From the transient evolution of the average LM temperature (figure 9.12(a)) it could seem that flow oscillations do not appear until $\alpha > 0.1$. However, in an evaluation of the upper side wall average Nusselt (figure 9.12(b)) oscillations do appear at lower α values. In fact, the only calculation in which flow remains stable corresponds to the value of $\alpha = 0.01$. This result coincides perfectly with what has been extrapolated from Gelfgat and Molokov (2011) results and from $v_{o,MHD}$ analysis.

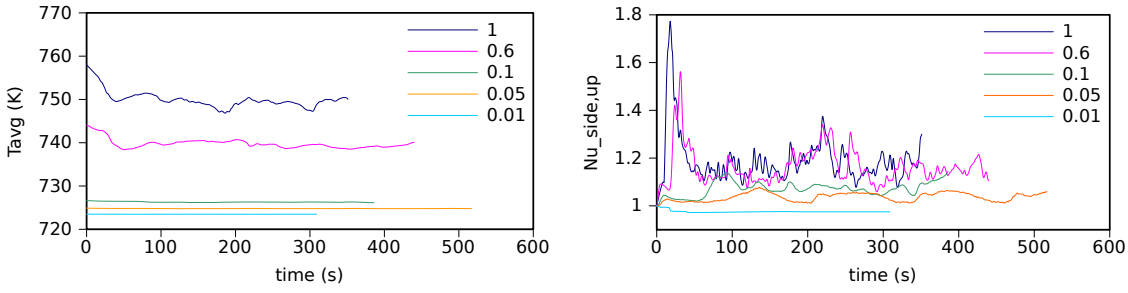

(a) (b)

Figure 9.12: Transient evolution of average LM temperature (a) and Nusselt number at the upper side wall (b) for several α values, being α the scaling coefficient of $S_{thermal}$.

Periodicity of results cannot be predicted and, in this direction, larger simulation

time would be required. Theoretically, periodic flow is expected to exists at low α values, whereas higher α are expected to induce chaotic flows.

For a better analysis, some characteristic parameters as a function of α are plotted in figure 9.13. These values are obtained by time averaging the transient results (skipping the initial 40 s), and the corresponding standard deviation is shown in error bars. As expected, LM average temperature increases with α, but the same effect cannot be observed on the LM outlet temperature. Heat transfer is enhanced with α, as can be seen in the increase of the average Nusselt number; however, such increase is less pronounced at high Gr numbers. The same effect can also be observed on heat fluxes through the upper and lower side walls.

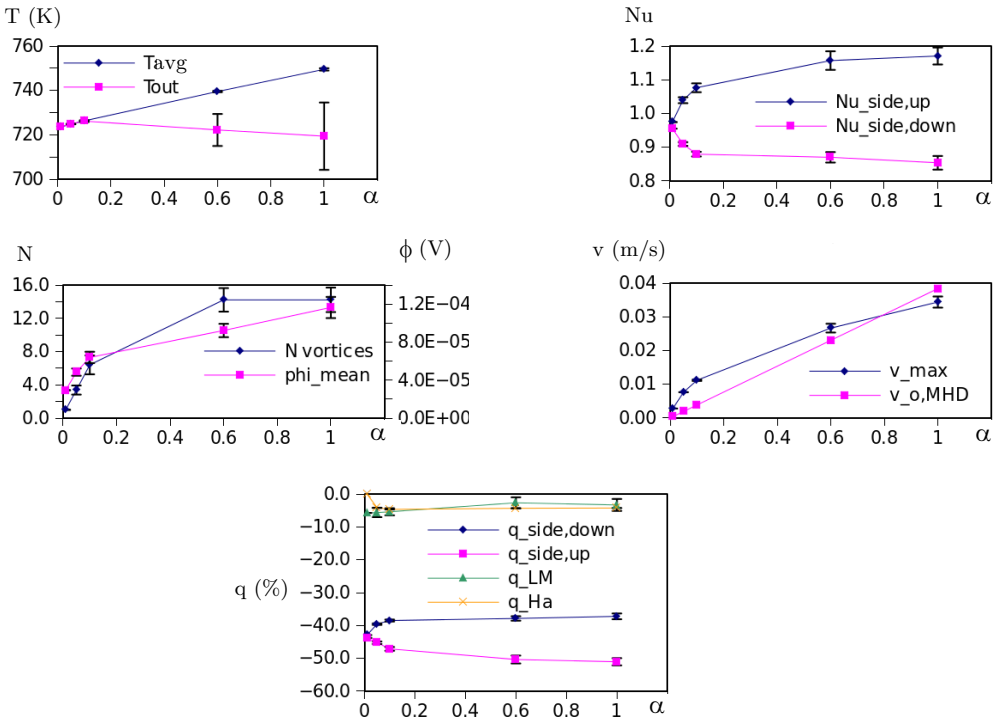

Figure 9.13: Characteristic parameters as a function of α values, being α the scaling coefficient of $S_{thermal}$.

It can be seen in the heat fluxes plot that for $\alpha \geq 0.1$, the thermal flux ratio extracted by each wall remains, more or less, the same regardless of the Gr. Approximately, about 48 % is extracted by the upper side wall, whereas the lower one extracts about 38 % of

the total thermal gain. Both Hartmann walls extract the same flux ratio, about 5 %, which is more or less what is gained by the LM. The magnitude of the obtained heat fluxes is better understood when compared to the wall surface ratio, which for each side wall represents 38 % of the total boundary surface, whereas for each Hartmann wall only represents 7 %. When results are compared to the ones obtained for a purely diffusive case (table 9.1) it can be stated that, for the buoyant flow, heat extraction is enhanced in the upper side wall and reduced in the lower side wall and in both Hartmann walls.

In order to quantify the number and magnitude of the existing vortices, local maxima/minima of electric potential are considered as indicators of core vortices, as explained in the previous section. Concerning average values of the number of vortices, $N_{vortices}$, it can be seen that for $\alpha = 0.01$ only one vortex exists, which corresponds to the one induced by the inlet boundary condition (figure 9.14). As α increases, the number of vortices also increase, until $\alpha \simeq 0.6$; above this point the average number of vortices remains constant with α. Despite such constant $N_{vortices}$ value, the rotational velocity of the existing vortices increases with α, as can be seen by the average ϕ value and the maximum velocity.

When the maximum velocity is compared to the characteristic one ($v_{o,MHD}$, which balances buoyancy and Lorentz forces), three flow regions are distinguished. In the first one, corresponding to $(\alpha \leq 0.01)$, flows are stable due to inertia dominance ($v_{inlet} > v_{o,MHD}$). The second region corresponds to $0.01 \leq \alpha \leq 0.85$, where $v_{max} > v_{o,MHD}$. Finally, in the third region$v_{max} < v_{o,MHD}$. From the observed results, it can be stated that the second region is where heat transfer is specially enhanced, whereas in the third region both the Nusselt number and the number of vortices remain constant with α.

9.3.5 Periodic flow boundary conditions

In order to avoid the forcing of the inlet vortex (figures 9.8 and 9.14), periodic (cyclic) flow boundary conditions can be applied. Such conditions are introduced in the code by means of a zero gradient outlet boundary conditions for all variables (velocity, pressure, electric potential and temperature); the obtained outlet values are then imposed at inlet. Of course, this strategy can be done because a structured mesh is being used. Since periodic boundary condition has to be also used for pressure, a forced pressure gradient is imposed in the momentum equation so that the specified mean velocity value is fulfilled. Therefore, the solved pressure equation of the ϕT-PISO algorithm only serves for continuity reasons.

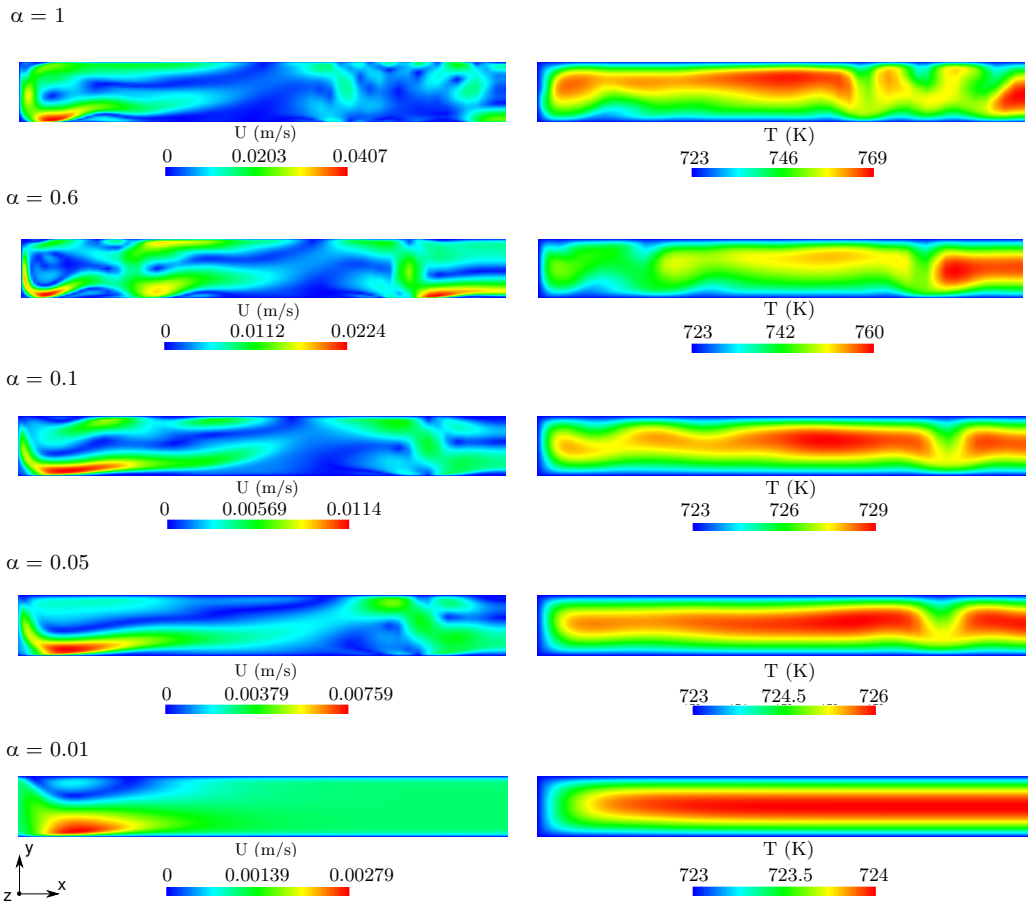

Figure 9.14: Velocity and temperature field maps for different α values, being α the scaling coefficient of $S_{thermal}$.

Results obtained for the case (2) at 40 s from the initial time (figure 9.15) show the unstable nature of the flow even when periodic boundary conditions are applied. When the obtained results are compared with the ones obtained with a simulation where a fixed temperature and velocity are fixed at the inlet (figure 9.8), it can be stated that velocity is lower using periodic boundary conditions and the number of vortical structures is reduced. However, the characteristic length of such vortices is the same in both simulations.

Transient average temperature and Nusselt numbers, obtained from simulation results with both fixed and periodic boundary conditions, are compared in figure 9.16 with two different approaches to the wall boundary condition, cases (1) and (2). It can be stated that the flow has the same behaviour in both cases. However, when comparing the number of vortical structures, it can be seen that with the periodic boundary condition the number of vortical structures is substantially lower.

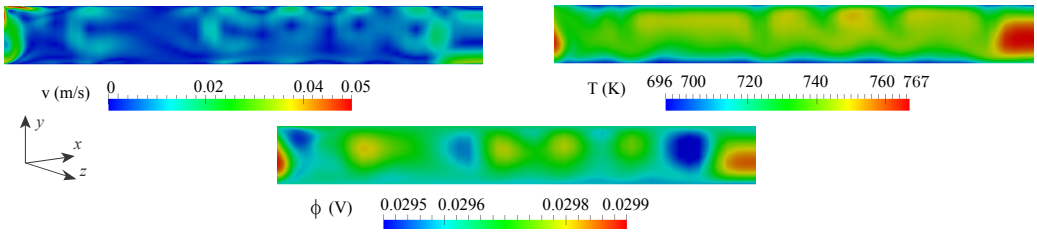

Figure 9.15: Velocity, temperature and electric potential field maps for case (2) with periodic boundary conditions at 40 s from the initial time.

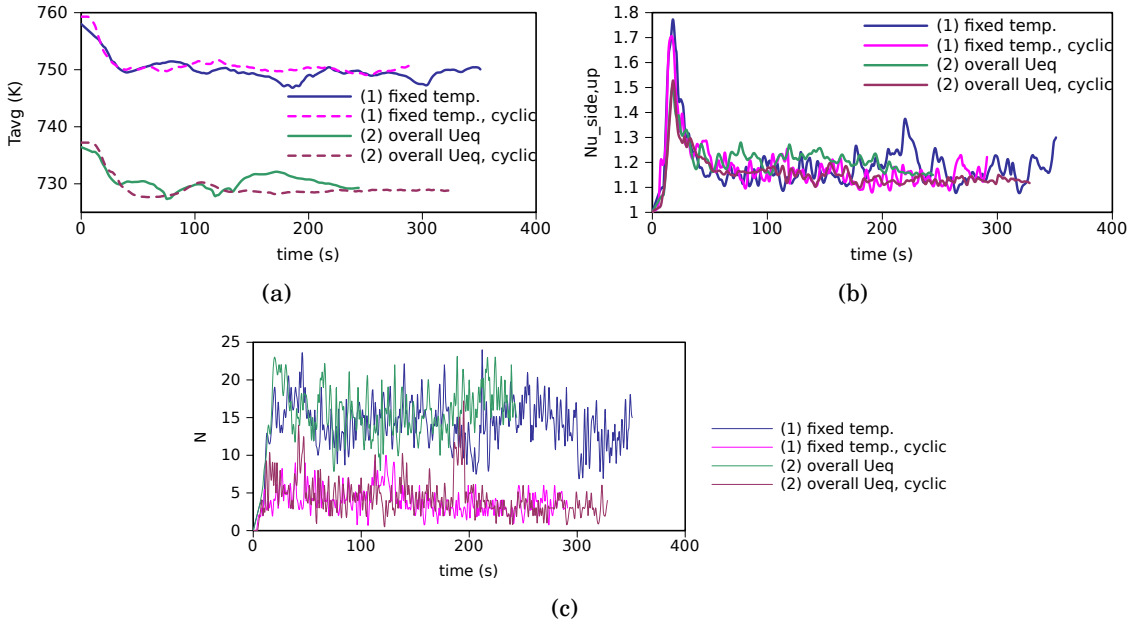

Figure 9.16: Transient evolution of average LM temperature (a), average Nusselt number at the upper side wall (b), and number of vortices (c) for periodic and non-periodic flow set-ups, with cases (1) and (2).

When some characteristic temperatures and heat fluxes are compared for case (2) (table 9.6), the similarity between both (fixed and periodic boundary conditions) results becomes evident.

Results obtained in cases (2) and (3) with cyclic boundary conditions are compared in figures 9.17(a) and 9.17(b). It can be seen that, although the average temperature is quite similar, some differences exist specially regarding the number of vortical structures. Indeed, when the fluid-solid thermal coupling (case (3)) is considered, the number of vortices is substantially reduced. Therefore, the damping effect of heat transport along the structure (in the streamwise direction) is relevant for flow stability studies.

case (2)	T_{avg}	$T_{side,up}$	$T_{side,down}$	T_{Ha}	T_{out}
fixed	730.0 ± 1.2	706.5 ± 0.9	699.2 ± 0.5	690.1 ± 0.2	683.4 ± 37.5
cyclic	728.2 ± 0.4	705.7 ± 0.6	699.2 ± 0.2	689.0 ± 0.1	672.3 ± 21.5

case (2)	q_{LM} %	$q_{side,up}$ %	$q_{side,down}$ %	q_{Ha} %
fixed	5.6 ± 4.4	-53.7 ± 1.4	-41.9 ± 0.9	-5.0 ± 0.1
cyclic	4.1 ± 1.7	-52.4 ± 0.9	-41.9 ± 0.3	-4.7 ± 0.0

Table 9.6: Characteristic temperatures anf heat flux ratios for case (2), with fixed and periodic (cyclic) boundary conditions.

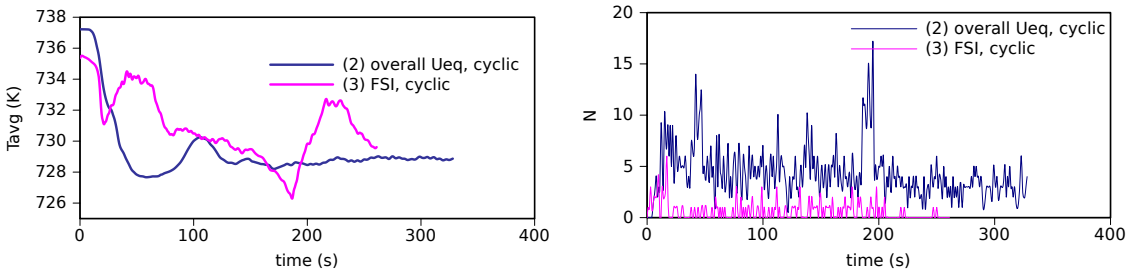

(a) (b)

Figure 9.17: Transient evolution of average LM temperature (a) and number of vortices (b) for periodic (cyclic) flow set-ups with cases (2) and (3).

Since the oscillatory nature of the flow and heat fluxes do not vary substantially when comparing results with fixed and periodic boundary condition, it might be concluded that the vortex at the inlet (induced by the fixed boundary condition) does not alter substantially the flow. However, the influence of the inlet vortex can be stronger for lower thermal loads, where buoyancy is not so dominant. Therefore, the simulations were repeated for smaller α values (the thermal load scaling factor). Results of the analysis are shown in figure 9.18. A long time simulation is needed for oscillations to appear at $\alpha = 0.05$, while no oscillation is observed for $\alpha = 0.01$. The obtained oscillating nature of the flow matches perfectly with the obtained with fixed inlet boundary conditions.

9.4 Discussion

In this third application case, a summary of the research carried out related to unsteady buoyant MHD flows caused by internal heating, at high Ha and Gr numbers, has been assessed. The most critical aspect lies on whether the flow is unstable and laminar or Q2D turbulent. In this direction, the characterisation by means of dimensionless

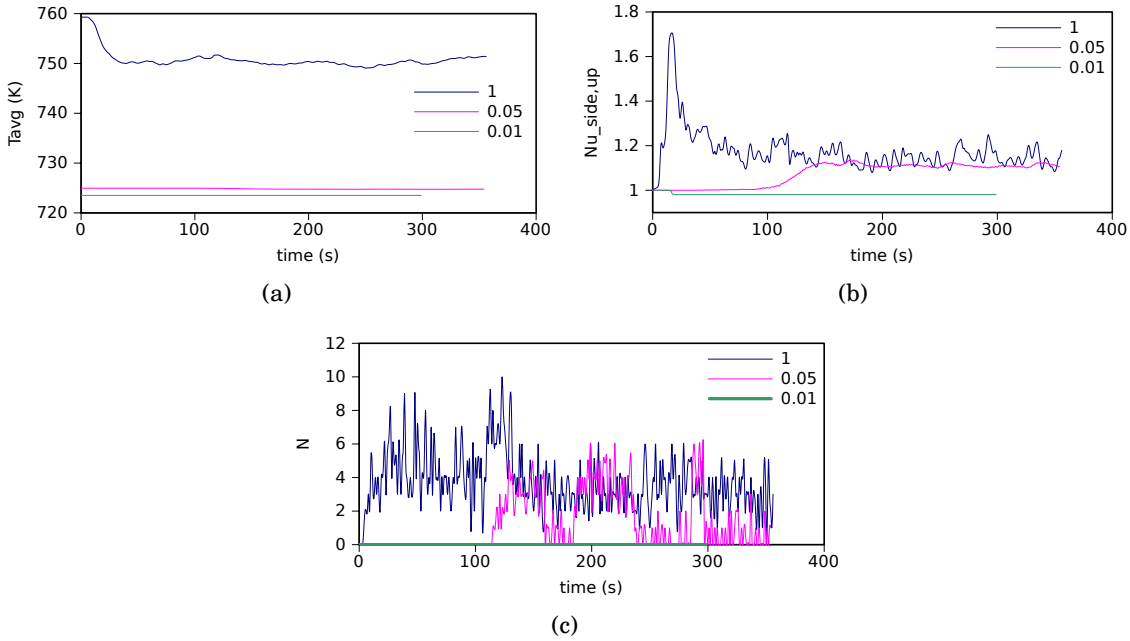

Figure 9.18: Transient evolution of average LM temperature (a), average Nusselt number at the upper side wall (b), and number of vortices (c) for several α values and periodic flow conditions in case (1), being α the scaling coefficient of $S_{thermal}$.

numbers is of crucial interest and the use of a fine enough mesh that captures all flow structures is essential.

Under the assumed flow conditions ($Re_a = 770$, $Ha_a = 3000$ and $Gr_a = 2.6 \cdot 10^{11}$) a mesh study based on FFT analysis has been performed. Results indicate that the basic mesh used for the present study is fine enough to capture all flow information.

The velocity-temperature decoupled case ($Pe = 0$) has been studied and results with conservative and non-conservative energy equations have been compared. The need of a conservative formulation is made explicit.

The critical Grashof number above which flow oscillations appear is found to lay in the range $Gr_{a,cr} = 2.6 \cdot 10^9 - 1.3 \cdot 10^{10}$, which matches well with the values extrapolated from Gelfgat and Molokov (2011).

Three modelling strategies for the thermal transfer at the wall have been applied in order to determine the nature of the vortical structures found in previous work (Chapter 7). The three options are (1) fixed wall temperature, as in Chapter 7, (2) overall heat transfer coefficient, and (3) fluid-solid coupling. Moreover, two inlet/outlet boundary conditions are analysed: (a) fixed inlet velocity and temperature, and (b) periodic flow conditions. It has been shown that complex vortical structures appear in all cases and that they are not uniquely caused by the inlet flow temperature nor by the wall

boundary condition.

A vortices detection method based on identifying local maxima/minima of the electric potential has been built. From such analysis, it has been possible to quantify the decrease of vortical structures due to the introduction of periodic instead of fixed boundary conditions. However, the remaining vortices have the same characteristic length as those that appear with the fixed inlet velocity and temperature boundary condition. Such characteristic length is the channel height.

Fluid-solid thermal coupling is required for an accurate prediction of the flow nature, in terms of number of vortical structures. However, average temperatures and heat fluxes are accurately predicted with the use of an overall heat transfer coefficient.

For the three studied wall conditions, the thermal flux extracted by each wall is independent of the inlet/outlet boundary condition or Grashof number. Approximately, about 48 % of the thermal load is extracted by the upper side wall, whereas the lower one extracts about 38 %. Both Hartmann walls extract the same flux ratio, about 5 %, which is more or less what is gained by the LM. When these values are compared to the heat fluxes in a purely diffusive case ($Pe = 0$) it can be stated that heat extraction is enhanced by buoyancy in the upper side wall, whereas it is reduced in the lower side wall and in both Hartmann walls.

It is worth mentioning that finite electric conductivity at solid region should also be addressed for a full comprehension of the phenomena occurring in the EU HCLL blanket channels.

Part IV

Final Remarks

10 Conclusions on MHD modelling

The first step for MHD modelling is to define the main electromagnetic variable, which can be (1) the induced magnetic field, (2) the electric potential, or (3) the electric current. If the flow presents high magnetic Reynolds number (as in astrophysics), the induced magnetic field formulation must be considered. Otherwise, the decision should be chosen in terms of restrictions on CPU time and code properties. Indeed, the induced magnetic field formulation (B-formulation) requires solving the three components of the induced magnetic field transport equation, fulfilling the solenoidal nature of $\mathbf{B}$ and calculating electric currents for Lorentz force estimation. The electric potential formulation (ϕ-formulation) substitutes a ϕ Laplacian equation for the $\mathbf{B}$ transport equation and the $\mathbf{B}$ divergence free equation. The electric current formulation (j-formulation) replaces such Laplacian equation with the three components of a $\mathbf{j}$ equation. Therefore, the ϕ-formulation is expected to require less CPU time for each algorithm iteration. However, if electric current conservation is not fulfilled, the algorithm would have a worst convergence leading to a higher number of iterations per time step, which would reduce the advantage of a ϕ-formulation.

At the present stage of the study, the author suggests to follow the ϕ-formulation strategy based on the conservative formula of the Lorentz force from Ni *et al.* (2007). However, the author has no experience with the j-formulation from Smolentsev *et al.* (2010), which could be a promising MHD modelling strategy.

The performance of the implemented MHD modelling strategy strongly depends on the hydrodynamic part of the algorithm. For a pressure-based Navier-Stokes implementation, several pressure-velocity coupling strategies exist. Among them, a projection method and a PISO-like algorithm have been studied in the frame of the present PhD thesis. Of course, the selection of the strategy depends on the CFD tool to be used. From the obtained results, the second-order PISO-like algorithm implemented in OpenFOAM (Weller *et al.* 1998) has proved to be robust it requires less inner iterations, which reduces substantially the CPU time.

A key aspect for CPU time reduction is the implementation of a Hartmann wall function, which avoids meshing the Hartmann boundary layer (of order Ha^{-1}). In this direction, the linear wall function from Leboucher (1999) has been successfully implemented yielding satisfactory results. However, since such wall function does not allow a net flux crossing the boundary layer, it is not suitable for cases with vortical structures, where 3D secondary flows are expected (as in application cases 1 and 3, in Chapters 7 and 9). Therefore, advanced wall functions, as the one proposed by Pothérat *et al.* (2002), should be implemented.

The electromagnetic coupling of the walls is crucial in order to study real flows. Indeed, when finite electrical wall conductivity is considered for MHD simulations, the M-shaped profile is retrieved and the electromagnetic damping increased with respect to the electrically insulated case. Such coupling can be implemented by means of the thin wall boundary condition (Müller and Bühler 2001), which in fact is an expansion of the linear wall function mentioned above. However, when the implemented wall function is used as the thin wall boundary condition, it presents some problems in corner regions. A possible alternative is to follow the suggestions from Mistrangelo (2010), where a 2D ϕ equation is solved on the system surface and coupled with the 3D (Laplacian) ϕ equation.

When the thermal coupling of the walls is also required, fluid-solid domains coupling is essential. In this direction, the implemented algorithm has accounted for fluid-solid coupling following OpenFOAM's strategy in *ConjugateHeatFoam*, available in the extended OpenFOAM-1.6-ext release from Wikki Ltd.

The influence of the time step on the simulation results is often underestimated. In fact, time step is not only crucial for stability purposes, but also for the accuracy of the results. In this direction, special emphasis has been placed on the estimation of the required time step criterion, either by means of a more conservative monotone scheme (Patankar 1980) or by 1D linear stability von Neumann analysis. However, such analysis, apart from being a simplification of the real one (by means of linearisation and 1D reduction), is specific for each spatial and temporal numerical scheme. Hence, such analysis should be carried out for each discretisation strategy.

In some simulations where the flow is expected to be Q2D, it seems more appropriate to use a specific MHD modelling strategy for 2D flows, as the one proposed by Sommeria and Moreau (1982) (SM82), which has also been implemented in OpenFOAM. Such modelling neglects possible 3D flows expected to occur in vortical flow patterns and, hence, the use of the SM82 algorithm has to be restricted to very simple flows. An advanced configuration for such modelling strategy is described by Müller and Bühler (2001), and its study and implementation in OpenFOAM should be carried out by the

author in a near future.

Last but not least, MHD turbulence is a crucial issue to consider for dual-coolant breeding blankets and most of the engineering MHD flows. Under strong magnetic fields, MHD turbulence becomes Q2D, but the lack of Q2D MHD turbulence models makes its simulation unaffordable. In the present study, the 0-equation RANS model from Smolentsev and Moreau (2006) has been implemented; however, further studies should be conducted before accurately predict LM flow in dual-coolant BB channels.

11 Conclusions on thermal MHD modelling

Thermal modelling of fluids is a classical field of study. The first decision to make, when modelling thermal transport within a fluid, is whether to consider that the fluid density varies substantially with temperature or not. In the present study, the fluid is PbLi, whose density dependence on temperature is relatively mild. Indeed, PbLi thermal expansion coefficient is one order of magnitude lower than typical values for gases, and half the value for liquid water. Thus, the Boussinesq hypothesis is perfectly applicable on the Navier-Stokes equations.

When electromagnetic effects are to be considered, no special issues with respect to MHD modelling appear. In fact, the unique B-energy coupling would be the Joule effect, which is neglected in the present study. Such simplification, despite being widely accepted, should be further analysed in future studies.

In terms of algorithm structure, the energy equation can be simply introduced sequentially in a fractional step algorithm, or as an extra equation inside PISO loop, in a PISO-like algorithm.

To implement fluid-solid coupling in OpenFOAM, according to the latest OpenFOAM releases 1.6-ext and 1.7.1, two different strategies could be followed. A first strategy would imply to couple both domains (fluid and solid) by means of internal boundary conditions. An example of this strategy can be found in the *chtMultiRegionFoam* algorithm in the official OpenFOAM-1.7.1 version. The main drawback is the need of an iterative process between both liquid and solid domains if a converged transient simulation is needed. The second strategy, called grid coupling strategy, would be coupling directly both meshes (fluid and solid) and solving a unique matricial system. Since different transport equations are required at each domain, the matricial system would be built from the corresponding two transport equations, each one attributed to one subdomain. Such strategy can be found in the *ConjugateHeatFoam* algorithm, available in the extended OpenFOAM-1.6-ext release from Wikki Ltd. Obviously, in order to couple both transport equations, the main variable must be conserved at the interface. For

electromagnetic coupling, both the electric potential and the electric current are conserved at the interface, whereas for thermal coupling, temperature must be equal at each side of the interface. Hence, the second strategy is perfectly suitable in the present study. The disadvantage of the grid coupling strategy lays on the need of dealing with larger mesh domains at solver level; however, this disadvantage is compensated by the fact that no inner iterations at the interface are required. In the frame of the present PhD thesis, the grid coupling strategy has been implemented.

Special attention has to be placed in order to couple correctly liquid-solid domains. Indeed, if the mesh is strongly non-uniform and fluid properties are very different across the boundary layer, some non-conservative effects might be present. In this direction, special emphasis has been placed so as to keep the conservative form of the energy equation in both domains.

It is worth mentioning the influence that inlet/outlet boundary conditions might have on the flow profile, specially for strongly buoyant flows. For academic or idealised cases, such influence can be avoided by the use of periodic (cyclic) boundary conditions. However, for a physically realistic flow set up, the domain of study should be enlarged until achieve known temperature (and velocity) boundary conditions, which is often too demanding.

12 Conclusions on breeding blanket studies

For an ideal simulation of any liquid metal breeding blanket, the studied domain should start/end outside the magnetic field region, far upflow from the inlet and downflow from the outlet manifolds, so that inlet/outlet boundary conditions could be more accurately defined. Both the externally applied magnetic field and the thermal load should vary in space and time according to each breeding blanket design. The code should be able to manage different scales including liquid metal domain, solid structures (Eurofer, FCI, etc.) and helium cooling channels. Thermal effects should be coupled to MHD effects, and fluid-solid thermal and electrical coupling considered. A 3D mesh would be required, refined at Hartmann and side boundary layers, which is by itself a very restrictive condition at typical breeding blanket Hartmann numbers. The used algorithm should be fully 3D and transient. Mechanical stresses and deformations of solid structures caused by temperature differences or electromagnetic forces should also be simulated. Finally, tritium and helium bred in the liquid metal should be considered, not only because tritium inventories and permeation fluxes are relevant for blanket design (for tritium self-sufficiency of the fusion reactor and for safety reasons), but also because tritium and helium might alter liquid metal electrical and thermal properties and, hence, LM flow profiles.

Obviously, such simulations are not affordable nowadays. All we can do is to simplify the system, assume some hypotheses and model only those issues that have greater interest. Once the results are obtained, a deep analysis of the solution is required, together with an estimation of the effect that those issues not considered or the relaxation of assumptions imposed would have on the results.

In the frame of the present PhD dissertation, main issues of interest are MHD and

thermal effects. The system has always been simplified by restricting the analysis to liquid metal channels, avoiding manifolds, expansions and helium cooling channels. The developed tool, however, can be applied to all type of geometries. Some hypotheses assumed in all simulations, such as the Boussinesq hypothesis, or the low magnetic Reynolds approximations (both assumptions are widely accepted). Moreover, due to CPU computational resources limitation, mesh size has always been a critical aspect. As a result, the obtained *know-how* related to liquid metal flows in breeding blanket modules can only be partial and subject to the influence of aspects not taken into account (i.e. presence of helium bubbles).

The implemented tool has been applied to understand the flow in two different breeding blankets: the EU HCLL and the TECNO_FUS blanket concept.

12.1 HCLL breeding blanket channels

In order to study the liquid metal flow in HCLL channels, 3D thermal-MHD simulations have been carried out. Special attention has been given to buoyancy effects and flow oscillations. In the study, although both the Reynolds and the Grashof numbers are kept within the same range as the expected ones, the considered Hartmann number is about one order of magnitude lower than the expected one, which provides with a substantially reduced electromagnetic damping.

In terms of liquid metal modelling in the HCLL blanket, fluid-solid MHD coupling determines, together with the Hartmann number, the magnitude of the electromagnetic damping. Therefore, the numerical tool must include electromagnetic fluid-solid coupling. However, results have shown that, if the only output parameters needed from the simulation are averaged values of temperatures, Nusselt and heat fluxes, fluid-solid thermal coupling can be avoided, being replaced by the use of a thermal boundary condition based on an estimation of the overall heat transfer coefficient (from tne LM to the He cooling channels). To this aim, an accurate estimator of the heat transfer coefficient helium-Eurofer is required. Nevertheless, in order to detect buoyancy induced vortices, fluid-solid thermal coupling is required in the simulation.

In terms of the flow nature in the HCLL blanket LM channels, it can be summarised that:

- A jet is produced at the narrowing of the channel in the U-bend for a pure hydrodynamic scenario. When this jet reaches the wall, it can experience shear stress instabilities that travel all along the outlet channel. Such jet is damped by electromagnetic forces.

- It has been proved that the temperature field is always 3D.
- The thermal flux extracted by each wall is independent of the Grashof number. Approximately, about 48 % of the thermal load is extracted by the upper side wall, whereas the lower one extracts about 38 %. Both Hartmann walls extract the same power, about 5 %, which is more or less the thermal power carried away by the LM.
- It can be anticipated that, when a realistic electromagnetic damping is simulated using appropriate values for the Ha and the electric conductivity ratio, the flow in the core of the channel remains 2D except in the Hartmann boundary layers, and vortical structures are only expected to exist near the gap close to the first wall.
- If vortical structures exist along the channel, their characteristic length is expected to be the channel height.
- If vortical structures exist, the existence of 3D secondary motions is probable. Their effect on the main flow and on relevant design parameters (e.g. tritium permeation ratio) should be analysed.

For an accurate prediction of the tritium permeation ratio (TPR), it is urgent to develop new and precise measurements of tritium transport properties, specially solubility. In the present study, a preliminary tritium analysis has been addressed considering tritium a passive scalar and neglecting helium influence on the flow (He is a by-product of the breeding reaction with lithium). Results show similar TPR values for electrically conducting and insulating walls (because LM velocities near the side walls are similar in both cases, due to either M-shape profile or vortical structures). Moreover, since Hartmann walls represent about 15 % of the total wall surface, their influence on the overall TPR is not negligible, reaching values of about 10 % of the total permeate tritium flux.

12.2 TECNO_FUS blanket concept

The TECNO_FUS blanket is a dual-coolant type concept, with high LM velocities. Therefore, inertia is predominant in front of buoyancy. Correspondingly, the flow in the core of the banana-shaped (toroidal) channels is expected to be 2D, except at Hartmann boundary layers, with no vortical structures. Thus, the 2D MHD model from Sommeria and Moreau (1982) can be used coupled with 2D thermal effects.

Among the issues which are relevant for the simulation, MHD turbulence modelling is, probably, the most prominent aspect since flow profile is strongly dependent on it.

However, there is a lack of accurate Q2D MHD turbulence models, specially when buoyancy effects have to be considered.

The thermal performance of the blanket can be defined by means of the LM temperature gain (which should be of order $\sim 300^o$C), the maximum temperature of the structural material (Eurofer, that must be kept below 550^oC), the thermal stress across the FCI, and the LM thermal gain (which depends on the temperature gain but also on the LM flow rate).

Fluid-solid thermal coupling is required in order to accurately predict both the maximum Eurofer temperature and the thermal stress across the FCI layer.

From the sensitivity analysis carried out in this study, it can be estimated that, for a maximised liquid metal temperature increment with an inlet velocity of 0.2 m/s, FCI thermal conductance should be around 1 W/m^{2}K. In contrast, for a maximised LM thermal gain, what would imply a reduced thermal stress across the FCI layer, and under the studied design specifications, higher velocities are preferable. However, this second thermal strategy would result in a lower LM temperature increment, which is not desirable for efficiency reasons.

For an accurate assessment of the cooling system requirements, heat losses both at side and Hartmann walls should be predicted. Such analysis could be carried out by 2D simulations of a fully-developed flow across a radial-toroidal plane.

Another interesting pending issue is the analysis of the bend zone, at the bottom of the blanket where the four channels merge, by means of a detailed 3D simulation.

Part V

Appendices

Publications and presentations related to this research

Pb-15.7Li database

Due to the lack of a database for the eutectic Pb-15.7Li, which included all breeding blanket related fluid properties, the first period of the study consisted of building such a database. The obtained database was first presented in two congresses and then, a paper was published.

A1 **Lead-lithium Eutectic material database for Nuclear Fusion Technology**
Journal of Nuclear Materials, vol. 378, issue 3, pp. 353-357. 2008
E. Mas de les Valls, L.A. Sedano, L. Batet, I. Ricapito, A. Aiello, O. Gastaldi and F. Gabriel

P1 **Lead-lithium Eutectic material database for Nuclear Fusion Technology**
IVth Int. Workshop on Materials for HLM Cooled Reactors and Related Technologies, Rome (Italy), 21.23th May, 2007
L.A. Sedano, E. Mas de les Valls, L. Batet, I. Ricapito, A. Aiello, O. Gastaldi and F. Gabriel

P2 **Base de datos del eutéctico Pb-15.7Li para TFN**
33a Reunión Anual de la Sociedad Nuclear Española, Segovia (Spain), 26.28th September, 2007
E. Mas de les Valls, L.A. Sedano, L. Batet, I. Ricapito, A. Aiello, O. Gastaldi and F. Gabriel

Algorithms implemented in OpenFOAM

The implemented algorithms and corresponding validation steps have been presented in 6 workshops or congresses.

P3 **Numerical analysis of buoyancy effects on liquid metal MHD flows**
Workshop on Numerical Simulations of MHD flows, Karlsruhe (Germany), 18-20 October 2010
E. Mas de les Valls, J. Fradera, L. Batet

P4 **Recent MHD activities for blanket analysis at UPC**
36a Reunión Anual de la Sociedad Nuclear Española, Santiago de Compostela (Spain), 6-8 October 2010
E. Mas de les Valls, J. Fradera, L.A. Sedano, S. Badia, R. Planas, L. Batet

P5 **Desarrollo de herramientas computacionales de simulación acoplada de la MHD y el transporte de tritio en los canales de ITER HCLL**
34a Reunión Anual de la Sociedad Nuclear Española, Murcia (Spain), 29-31 October 2008
E. Mas de les Valls, J. Fradera, L. Batet, L. Sedano

P6 **OpenFOAM capabilities for MHD simulation under nuclear fusion technology conditions**
OpenFOAm workshop, Milano (Italy), 10-11 July 2008
E. Mas de les Valls, L. Batet

P7 **Transient algorithm for low magnetic Reynolds number simulations**
MHD Fundamentals, from liquid metals to astrophysics, Brussels (Belgium), 10-11 July 2008
E. Mas de les Valls, L. Batet

P8 **Resistive MHD simulations with OpenFOAM. Algorithm strategies**
International Workshop on Numerical Simulations of Magnetohydrodynamic Flows, Karlsruhe (Germany), 14-15 November 2007
E. Mas de les Valls, L.A. Sedano, L. Batet

Liquid metal flows in Breeding Blankets

The application cases studied in the frame of the present PhD dissertation have been presented in 8 workshops or congresses. Also, 2 papers have been published and 1 has been submitted for peer review.

A2 **Modelling of integrated effect of volumetric heating and magnetic field on tritium transport in a U-bend flow as applied to HCLL blanket concept**
Fusion Engineering and Design, vol. 86, issues 4-5, pp 341-356. June 2011
E.Mas de les Valls, L. Batet, V. de Medina, J. Fradera, L. Sedano

A3 **Qualification of MHD effects in dual-coolant DEMO blanket and approaches to their modelling**
Fusion Engineering and Design, In Press, Corrected Proof, Available online 11 May 2011
E. Mas de les Valls, L. Batet, V. de Medina, J. Fradera, L.A. Sedano

A4 **Influence of thermal performance on design parameters of a He/LiPb dual coolant DEMO concept blanket design**
Submitted to Fusion Engineering and Design, FUSENGDES-D-11-00381
E. Mas de les Valls, L. Batet, V. de Medina, J. Fradera, M. Sanmartí, L.A. Sedano

P9 **Estudio paramétrico de un diseño conceptual de envoltura regeneradora He/LiPb de doble refrigerante para DEMO**
37a Reunión Anual de la Sociedad Nuclear Española, Burgos (Spain), 28-30 September 2011
E. Mas de les Valls, L. Batet, J. Fradera, M. Sanmartí, L.A. Sedano

P10 **Influence of thermal performance on design parameters of a He/LiPb dual coolant DEMO concept blanket design**
International Symposium on Fusion Nuclear Technology (ISFNT-10), Portland (USA), 11-16 September 2011
E. Mas de les Valls, L. Batet, V. de Medina, J. Fradera, M. Sanmartí, L.A. Sedano

P11 **Numerical analysis of MHD-thermofluid flows considering sandwich structures as applied to liquid breeding blankets for fusion technology**
8th PAMIR International Conference, Fundamental and Applied MHD, Corsica (France), 5-9 September 2011
E. Mas de les Valls, L. Batet, V. de Medina, J. Fradera, L.A. Sedano

P12 **MHD modelling for liquid metal banana-shaped channels for Dual-Coolant breeding blanket for DEMO**
26th Symposium on Fusion Technology, SOFT, Porto (Portugal), 27 September - 1 October 2010
E. Mas de les Valls, V. de Medina, L. Batet, J. Fradera, L. Sedano

P13 **TMHD modeling activities at UPC aimed at breeding blanket analysis**
IEA International Workshop on Liquid Metal Breeder Blanket, Madrid (Spain), 23-24 September 2010
E. Mas de les Valls, J. Fradera, R. Codina, S. Badia, R. Planas, L. Sedano, L. Batet

P14 **Flow analysis in the HCLL-TBM ITER channels including MHD and heat transfer**
Eccomas CFD, Lisboa (Portugal), 14-17 June 2010
E. Mas de les Valls, J. Fradera, L. Batet

P15 **Análisis de sensibilidad de los distintos modelados utilizados para los canales de los módulos de ensayo de envoltura ITER HCLL (EU ITER-TBM)**
37a Reunión Anual de la Sociedad Nuclear Española, Sevilla (Spain), 28-30 October 2009
E. Mas de les Valls, J. Fradera, L.A. Sedano, L. Batet

P16 **Boundary layer analysis for coupled mixed convection and MHD flow on tritium permeation in ITER TBM c-shaped channels**
25th Symposium on Fusion Technology, SOFT, Rostock (Germany), 15-19 September 2008
E. Mas de les Valls, F. Gabriel, C. Moreno, J.A. Jiménez, L. Batet, L. Sedano

List of Figures

List of Tables

References

Aiello A, Ciampichetti A and Benamati G 2006 Determination of hydrogen solubility in lead lithium using SOLE device Fusion Engineering and Design **81** 639–644

Aiello A, Gabriel F, Rampal G and Salavy J 2009 A new cooling scheme for the HCLL TBM Fusion Engineering and Design **84** 390–393

Alboussière T, Garandet J and Moreau R 1996 Asymptotic analysis and symmetry in MHD convection Physics of Fluids 8(8) 2215–2226

Aleksandrova S, Molokov S and Reed C 2002 Modeling of liquid metal duct and free-surface flows using CFX Technical report, Argonne National Lab., IL (US) ANL/TD/TM02-30

Authié G, Tagawa T and Moreau. R 2003 Buoyant flow in long vertical enclosures in the presence of a strong horizontal magnetic field. Part 2. Finite enclosures European Journal of Mechanics B/Fluids **22** 203–220

Batet L, Fradera J, de les Valls E M and Sedano L 2011 Numeric implementation of a nucleation, growth and transport model for helium bubbles in lead-lithium HCLL breeding blanket channels. Theory and code development. Fusion Engineering and Design

Bojarevics V, Roy A and Pericleous K 2010 Magnetic Levitation of Large Liquid Volume Magnetohydrodynamics 46(4) 317–329

Brackbill J and Barnes D 1980 The effect of nonzero $\nabla \cdot b$ on the numerical solution of the magnetohydrodynamic equations Journal of Computational Physics 35(3) 426–430

Brigham E 1988 The Fast Fourier Transform and its Applications Prentice-Hall, Inc.

Bühler L 1994 Magnetohydrodynamic flows in arbitrary geometries in strong, nonuniform magnetic fields. A numerical code for the design of fusion reactor blankets Fusion Technology **27** 3–24

Bühler L 1998 Laminar buoyant magnetohydrodynamic flow in vertical rectangular ducts Physics of Fluids 10(1) 223–236

Bühler L, Horanyi S and Arbogast E 2007 Experimental investigation of liquid-metal flows through a sudden expansion at fusion-relevant hartmann numbers Fusion Engineering and Design **82** 2239–2245

Catalán J, Ogando F, Sanz J, Palermo I, Veredas G, Gómez-Ros J and Sedano L 2010 Neutronic analysis of a dual He/LiPb coolant breeding blanket for DEMO In paper ID1759 at SOFT 2011 Conference

Courant R, Friedrichs K and Lewy H 1967 On the partial difference equations of mathematical physics IBM Journal of research and Development 11(2) 215–234

Cramer K and Pai S I 1973 Magnetofluid dynamics for engineers and applied physicists Scripta Publishing Company and McGraw-Hill Book Company

Cuevas S, Picologlou B, Walker J and Talmage G 1997 Liquid metal MHD flow in rectangular ducts with thin conducting or insulating walls: laminar and turbulent solutions Int. J. of Engineering Sciences **35** 485

Davidson P 2001 An introduction to magnetohydrodynamics Cambridge texts in applied mathematics

Davidson P and Pothérat A 2002 A note on Bodewadt-Hartmann layers European Journal of Mechanics B/Fluids 21(5) 545–559

di Piazza I and Bühler L 1999 Numerical simulations of buoyant magnetohydrodynamic flows using the CFX code Fzka 6354, Forschungszentrum Karlsruhe

di Piazza I and Bühler L 2000 A general computational approach for MHD flows usinf CFX code: buoyant flow through a vertical square channel Fusion Science and Technology **38** 180–189

di Piazza I and Ciofalo M 2002a MHD free convection in liquid-metal filled cubc enclosure. I. Differential heating Int. J. of Heat and Mass Transfer **45** 1477–1492

di Piazza I and Ciofalo M 2002b MHD free convection in liquid-metal filled cubc enclosure. II. Internal heating Int. J. of Heat and Mass Transfer **45** 1493–1511

Dousset V and Pothérat A 2008 Numerical simulations of a cylinder wake under a strong axial magnetic field Physics of Fluids **20**

Drazin P 2002 Introduction to Hydrodynamic Stability Cambridge University Press

Egry I, Diefenbach A, Dreier W and Piller J 2001 Conatinerless processing in space - thermophysical property measurements using electromagnetic levitation Int. J. Thermophysics **22** 569–578

Esteban G, na A P, Urra I, Legarda F and Riccardi B 2007 Hydrogen Transport and Trapping in EUROFER'97 **367-370, Part I** 473–477

Evans C and Hawley J 1988 Simulation of magnetohydrodynamic flows: a constrained transport method Journal of Astrophysics **332** 659

Fradera J, Sedano L, Mas de les Valls E and Batet L 2011 Implementation of two-phase tritium models for helium bubbles in HCLL breeding blanket modules

Gabriel F, Escuriol Y, Dabbene F, Gastaldi O, Salavy J and Giancarli L 2007 A 2D finite element modelling of tritium permeation for HCLL DEMO blanket module Fusion Engineering and Design **82** 2204–2211

Garandet J, Alboussiere T and Moreau R 1992 Buoyancy driven convection in a rectangular enclosure with a transverse magnetic field Int. Journal of Heat and Mass Transfer 35(4) 741–748

Gastaldi O, Aizes P, Gabriel F, Salavy J and Giancarli L 2008 Tritium transfers evaluation on ITER HCLL TBM Fusion Science and Technology 54(1) 101–106

Gelfgat A and Molokov S 2011 Quasi two-dimensional convection in a three-dimensional laterally heated box in a strong magnetic field normal to main circulation Physics of Fluids

Graneau P 1989 Electrodynamic Seawater Jet: An Allternative to the Propeller? IEEE Transactions of Magnetics 25(5) 3275–3277

Hartmann J 1937 Hg-Dynamics I. Theory of the laminar flow of an electrically conductive liquid in a homogeneous magnetic field Levin & Munksgaard

Hoffman J 2001 Numerical Methods for Engineers and Scientists, Chapter 7, 10

Hunt J 1965 Magnetohydrodynamic flow in rectangular ducts Journal of Fluid Mechanics 21(4) 577–590

Hunt J and Ludford G 1968 Three-dimensional MHD duct flows with strong transverse magnetic fields. Part 1. Obstacles in a constant area channel Journal of Fluid Mechanics 33(4) 693–714

Jasak H 1996 Error Analysis and Estimation for the Finite Volume Method with Applications to Fluid Flows Ph. D. thesis, Dept. of Mechanical Engineering. Imperial College of Science, Technology and Medicine

Juanas J and Fernández I 2009 Diseño de componentes internos y externos del Programa Consolider TECNO_FUS Technical report, EURATOM-CIEMAT Association Ref: CSD2008-079

Kharicha A, Molokov S, Aleksandrova S and Bühler L 2004 Buoyant convection in the HCLL blanket in a strong, uniform magnetic field FZKA, 6959

Knaepen B and Moreau R 2008 Magnetohydrodynamic Turbulence at Low Magnetic Reynolds Number Annu. Rev. Fluid Mechanics (40) 25–45

Kolesnichenko A 1990 Electromagnetic Processes in Liquid Material in the USSR and Eastern European Countries Iron and Steel Institute of Japan (ISIJ) 30(1) 8–26

konishi S 2010 Overview of the Japanese R&D Programme on Liquid Metal Blanket International Workshop on Liquid Metal Breeder Blankets. 23-24 September, Madrid

Leboucher L 1999 Monotone scheme and boundary conditions for finite volume simulation of magnetohydrodynamic internal flows at high Hartmann number Journal of Computational Physics **150** 181–198

Leveque R 2002 Finite Volume Methods for Hyperbolic Problems, Chapter 8 Cambridge University Press

Lielpeteris J and Moreau R 1989 Liquid Metal Magnetohydrodynamics Kluwer Academic Publishers

Mas de les Valls E, Sedano L, Batet L, Ricapito I, Aiello A, Gastaldi O and Gabrfiel F 2008 Lead-lithium eutectit material database for nuclear fusion technology Journal of Nuclear Materials 376(3) 353–357

McCarthy K and Abdou M 1991 Analysis of liquid metal mhd flow in multiple adjacent ducts using an iterative method to solve the core flow equations Fusion Engineering and Design **13** 363–380

Mergia K and Boukos N 2008 Structural thermal, electrical and magnetic propertiesof Eurofer 97 steel **373** 1–8

Messadek K and Moreau R 2002 An experimental investigation of MHD quasi two-dimensional turbulent shear flows Journal of Fluid Mechanics **456** 137–159

Mistrangelo C 2006 Three-dimensional MHD flow in sudden expansions Ph. D. thesis, Forschungzentrum Karlsruhe

Mistrangelo C 2010 Simulation of MHD flows in OpenFOAM: capabilities and new features Workshop on numerical simulation of MHD flows. 18-20 October, Karlsruhe

Mistrangelo C and Bühler L 2009 Influence of helium cooling channels on magnetohydrodynamic flows in the HCLL blanket Fusion Engineering and Design **84**

1323–1328

Molokov S 1993 Fully developed liquid-metal flow in multiple rectangular ducts in a strong uniform magnetic field European J. of mechanics, B/Fluids **12** 769–787

Molokov S 1997, September 16-18 Towards advanced liquid metal blankets: resolving MHD-related problems In Proceedings of the first workshop on liquid metal blanket experimental activities, pp. 115–118 CEA Headquarters, Paris, France

Molokov S and Bühler L 2003 Three dimensional buoyant convection in rectangular box with thin conducting walls in a strong horizontal magnetic field FZKA, 6817

Molokov S, Bühler L and Stieglitz R 1995 Asymptotic structure of magnetohydrodynamic flows in bends Magnetohydrodynamics 31(3) 357–365

Moreno C and Sedano L 2009, 1-5 June A Pfd-based 1D model for dynamic and transient tritium transfers between ITER HCLL TBM auxiliary systems In SOFE, 23rd IEEE/NPSS Symposium on Fusion Engineering, Sna Diego, USA (2009)

Muck B, Günter C, Müller U and Bühler L 2000 3D MHD flows in rectangular ducts with internal obstacles Journal of Fluid Mechanics **418** 265–295

Müller U and Bühler L 2001 Magnetofluiddynamics in Channels and Containers Springer

Müller U, Mack K, Barleon L and Burr U 1999 The effect of vertical magnetic field on liquid metal Rayleigh-Benard convection Fzka 6267, Forschungszentrum Karlsruhe

Ni M J, Munipalli R, Huang P, Morley N and Abdou M 2007 A current density conservative scheme for incompressible MHD flows at low magnetic Reynolds number. Part II: On an arbitrary collocated mesh Journal of Computational Physics 227(1) 205–228

Northrup E 1907 Some Newly Observed Manifestations of Forces in the Interior of an Electric Conductor Phys. Rev. 24(6) 474–497

Okada K and Ozoe H 1992 Transient Responses of Natural Convection Heat Transfer with Liquid Gallium under an External Magnetic Field in either the x, y, or z Direction American Chemical Society **31** 700–706

Oliver X and de Saracibar C A 2002 Mecanica de Medios Continuos para Ingenieros Edicions UPC

Ozoe H and Okada K 1989 The effect of the direction of the external magnetic field on the three-dimensional natural convection in a cubical enclosures Int. Journal of Heat and Mass Transfer 32(10) 1939–1954

Patankar S 1980 Numerical Heat Transfer and Fluid Flow Hemisphere Publishing Corporation

Pothérat A 2007 Quasi-two-dimensional perturbations in duct flows under transverse magnetic field Physics of Fluids

Pothérat A, Sommeria J and Moreau R 2002 Effective boundary conditions for magnetohydrodynamic flows with thin Hartmann layers Physics of Fluids 14(1) 403–410

Powell K 1994 An Approximate Riemann Solver for MHD That Actually Works in More Than One Dimension ICASE Report No. 94-24, Langley, VA

Rampal G and Aiello G 2006 Design and analyses of the HCLL TBM including design of supporting system and instrumentation integration. report DM2S, SEMT/BCCR/RT/06-004/A Technical report, CEA, Direction de l'Énergie Nucléaire

Reed C, Piclolglou B, Hua T and Walker J 1987, October ALEX results - a comparison of measurements from a round and a rectangular duct with 3D code predictions Technical report, 12th Symposium on Fusion Engineering, Monkey, CA

Reimann J, Barleon L, Bucenieks I, Bühler L, Lenhart L, Malang S, Molokov S, Platnieks I and Stieglitz R 1995 Magnetohydrodynamic investigations of a self-cooled Pb-17Li blanket with poloidal-radial-toroidal ducts Fusion Engineering and Design **27**

Reimann J, Bühler L, Mistrangelo C and Molokov S 2006 Magneto-hydrodynamic issues of the HCLL blanket Fusion Engineering and Design **81**

Reiter F 1991 Solubility and diffusivity of hydrogen isotopes in liquid Pb-17Li Fusion Engineering and Design **14** 207–211

Rodi W 1993 Turbulence Models and Their Application in Hydraulics. A *state-of-the-art* review A.A. Balkema

Salavy J F, Aiello G, David O, Gabriel F, Giancarli L, Girard C, Jonquères N, Laffont G, Madeleine S, Poitevin Y, Rampal G, Ricapito I and Splichal K 2008 The HCLL Test Blanket Module system: present reference design, system integration in ITER and R&D needs Fusion Engineering and Design 83(7-9) 1157–1162

Shercliff J 1953 Steady motion of conducting fluids in pipes under transverse magnetic fields Proc. Cambridge Philosophical Soc. **49** 126

Shinavski R August 12, 2008 Specialized SiC Components for Flow Channel Insert Applications FNST Meeting, UCLA, Los Angeles, CA

Smolentsev S 2009 MHD duct flows under hydrodynamic "slip" condition Theor. Comput. Fluid Dyn. **23** 557–570

Smolentsev S, Cuevas S and Beltrán A 2010 Induced Electric Current-Based Formulation in Computations of Low Magnetic Reynolds Number Magnetohydrodynamic Flows Journal of Computational Physics **229** 1558–1572

Smolentsev S and Moreau R 2006 Modeling quasi-two-dimensional turbulence in MHD duct flows In Proceedings of the Summer Program, CTR, Standford University, pp. 419-430

Smolentsev S and Moreau R 2007 One-equation model for quasi-two-dimensional turbulent magnetohydrodynamic flows Physics of Fluids **19**

Smolentsev S, Moreau R and Abdou M 2008 Characterization of key magnetohydrodynamic phenomena in PbLi flows for the US DCLL blanket Fusion Engineering and Design **83** 771–783

Smolentsev S, Moreau R, Bühler L and Mistrangelo C 2010 MHD Thermofluid Issues of Liquid Metal Blankets: Phenomena and Advances Fusion Engineering and Design **in press**

Smolentsev S, Morley N and Abdou M 2006 Magnetohydrodynamic and Thermal Issues of the SiCf/SiC Flow Channel Insert Fusion Science and Technology **50** 107–119

Smolentsev S, Morley N, Abdou M, Munipalli R and Moreau R 2006 Current approaches to modeling MHD flows in the dual coolant lead lithium blanket Magnetohydrodynamics **42** 225

Smolentsev S and Tananaev A 1994 Development of computer code for analysis of heat transfer in liquid metal MHD flows in ducts In Proceedings of the Second International PAMIR Conference on Energy Transfer in Magnetohydrodynamic Flows, Volume 2, Aussois, France, pp. 551–560

Sommeria J 1988 Electrically driven vortices in a strong magnetic field Journal of Fluid Mechanics **189** 553–569

Sommeria J and Moreau R 1982 Why, how and when MHD turbulence becomes two-dimensional Journal of Fluid Mechanics **118** 507

Sporn P and Kantrowitz A 1959 Magnetohydrodynamics: Future Power Process? Power 103(11) 62–65

Steg L and Sutton G 1960 Prospects of MHD Power Generation Astronautics **5** 22–25

Sterl A 1990 Numerical simulation of liquid-metal mhd flows in rectangular ducts Journal of Fluid Mechanics **216** 161–191

Sze D, Tillack M and El-Guebaly L 2000 Blanket system selection for the ARIES-ST Fusion Engineering and Design **48** 371–378

Tabeling P 1982 Magnetohydrodynamic flows in rectilinear ducts of rectangular cross-section: the question of the corners Journal de Mécanique Théoretique et Appliquée 1(1) 25–38

Tagawa T, Authié G and Moreau. R 2002 Buoyant flow in long vertical enclosures in the presence of a strong horizontal magnetic field. Part 1. Fully-established flow European Journal of Mechanics B/Fluids **21** 383–398

Talmage G and Walker J 1987, Tel-Aviv Three-dimensional laminar MHD-flow in ducts with thin metal walls and strong magnetic fields. 5th Beer-Sheva Seminar on MHD and Turbulence

Temperley D and Todd L 1971 The effect of wall conductivity in magnetohydrodynamic duct flow at high hartmann number Proc. Cambridge Philosophical Society **69** 337–351

Terai T, Nagai S, Yoneoka T and Takahashi Y 1992 Diffusion coefficient of tritium in molten lithium-lead alloy (Li17Pb83) under neutron irradiation at elevated temperatures **187** 247–253

Tillack M and Morley N 1998 Magnetohydrodynamics (14 ed.). McGraw Hill

Tixador P 1994 Magnetic levitation and MHD propulsion J. Phys. III **4** 581–593

Tóth G 1998, June 15-19 Computational magnetohydrodynamics http://hermes.elte.hu/∼gtoth/, Porto Notes for an introductory level course

Tóth G 2000 The $\nabla \cdot \mathbf{B}$ constraint in shock-capturing magnetohydrodynamics codes JCP **161** 605–652

Vetcha N, Smolentsev S and Abdou M 2009 Theoretical study of mixed convection in poloidal flows of DCLL blanket Fusion Science and Technology **56** 851–855

Walker J 1981 Magnetohydrodynamic flows in rectangular ducts with thin conducting walls Journal de Mécanique 20(1) 79–112

Weller H, Tabor G, Jasak H and Fureby C 1998 A tensorial approach to computational continuum mechanics using object oriented techniques Computational Physics **12** 620

Wesson J 2006 The Science of JET Technical report, JET Joint Undertaking

Wong C, Abdou M, Dagher M, Katoh Y, Kurtz R, Malang S, Marriott E, Merrill B, Messadek K, Morley N, Sawan M, Sharafat S, Smolentsev S, Sze D, Willms S, Ying A and Youssef M 2010 An overview of the US DCLL ITER-TBM program Fusion Engineering and Design **85** 1129–1132

Wong C, Abdou M, Dagher M, Smolentsev S, Sharafat S, Morley N, Youssef M, Ying A, Carosella D, Baxi C, Malang S, Rowcliffe A, Sonn D, Tourville S, Sawan M, Sviatoslavsky, Fogart P, Katoh Y, Pint B, Mann T, Zinkle S, Merrill B, Kurtz R, Sze D, reyes S, Willms S, Nygren R, Tanaka T, Youchison D and Ulrickson M 2006 US ITER DCLL TBM Design US-Japan workshop on Fusion High Power Density Components and Systems. 15-17 November, Santa Fe, USA

Yu H, Zhou X, Wang H, Zhao S, Wu Y, huang Q, Zhu Z and Huang Z 2010 2D SiC/SiC composite for flow channel insert (fci) application Fusion Engineering and Design **85** 1693–1696

Zmitko M 2009, Garching, Germany, 29-30 September Test Blanket Modules: Objectives and Programme in ITER Technical Meeting on DEMO